Central exclusive production of χ_c mesons in $\sqrt{s} = 13\,\text{TeV}$ proton-proton collisions

Barak Raimond Gruberg Cazón
Linacre College, University of Oxford

Thesis submitted in partial fulfilment of the requirements for the degree of Doctor of Philosophy at the University of Oxford

Trinity Term 2021

Central exclusive production of χ_c mesons in $\sqrt{s} = 13\,\text{TeV}$ proton-proton collisions

Barak Raimond Gruberg Cazón

Linacre College, University of Oxford

Thesis submitted in partial fulfilment of the requirements for the degree of
Doctor of Philosophy at the University of Oxford

Trinity Term, 2021

Abstract

A measurement is made of the central exclusive production of χ_{c1} and χ_{c2} mesons in proton-proton collisions at a centre-of-mass energy of $\sqrt{s} = 13\,\text{TeV}$, using data collected by the LHCb experiment corresponding to a total single-interaction integrated luminosity of $711\,\text{pb}^{-1}$. The χ_c candidates are reconstructed through their radiative decay into $J/\psi\gamma$, where we use photons that have converted into an electron pair, $\gamma \to e^+e^-$, and reconstruct the J/ψ through its dimuon final state. The High Rapidity Shower Counter sub-detector HeRSChel is used to reduce inelastic background. The product of the cross section and the branching fractions, where the J/ψ muons are measured to be within the pseudorapidity region $2 < \eta < 4.5$, are measured to be,

$$\sigma^{(2<\eta_{\mu^+\mu^-}<4.5)}_{\chi_{c1}\to J/\psi\,[\mu^+\mu^-]\gamma} = 19.5 \pm 15.0(\text{stat}) \pm 15.4(\text{syst})\,\text{pb} \quad [90\%\ \text{C.L.}]$$

$$\sigma^{(2<\eta_{\mu^+\mu^-}<4.5)}_{\chi_{c2}\to J/\psi\,[\mu^+\mu^-]\gamma} = 99.6 \pm 12.7(\text{stat}) \pm 27.7(\text{syst})\,\text{pb},$$

where the first uncertainty is statistical and the second is systematic. The product of the cross section and the branching fractions of χ_{c1} mesons is quoted at a 90% confidence level (C.L.). These results are found to be in agreement with theoretical predictions.

“No man is an island entire of itself; every man
is a piece of the continent, a part of the main;
if a clod be washed away by the sea, Europe
is the less, as well as if a promontory were, as
well as any manner of thy friends or of thine
own were; any man’s death diminishes me,
because I am involved in mankind.
And therefore never send to know for whom
the bell tolls; it tolls for thee.”

— John Donne, *Devotions upon Emergent Occasions*

Acknowledgements

Very few things we accomplish, we accomplish on our own. This thesis would not have been possible without the help of extraordinary people. I would like to recognise them for their guidance, support, and company that have made my DPhil an enjoyable and fruitful experience.

First and foremost, I would like to thank my supervisor, Guy Wilkinson, for welcoming me into the LHCb group and entrusting me early on with a number of projects that allowed me to experience multiple facets of the field. His excellent supervision and feedback has helped me to learn and grow enormously as a researcher. I would like thank him for his patience, honesty, and for championing me and my work.

I would like to extend my gratitude to the people with whom I worked closely, including Paolo Gandini who showed me the ropes during my early days in the Oxford group and guided me through my first projects and the early stages of the analysis presented in this thesis, as well as Nathan Jurik who provided crucial guidance during my stay at CERN and later stages of said analysis. I would also like to acknowledge members of the HeRSCheL group, especially Raphael Dumps, Daniel Johnson, and Heinrich Schindler, with whom I worked with in the replacement and commissioning of the HeRSCheL modules. Of course, the members of the CEP group who have provided fundamental insights and resources that made this analysis possible cannot go unmentioned, in particular Ronan Mcnulty. I am very fortunate to have worked with my fellow gradate students who created an engaging environment in the physics department and made for excellent company during our daily coffee breaks.

A special debt of gratitude goes to Sue Geddes and Kim Proudfoot, the true heart of the Oxford particle physics department, who have gone beyond their call of duty to help me navigate this experience in the most seamless fashion possible during these uncertain times.

I am forever indebted to Linacre College for building a welcoming and diverse environment, which provided an escape from work and ensured the delight of meeting extraordinary people and forming long-lasting friendships. I would like to highlight Conor who I met during my first year at Oxford, quickly became my best friend, and provided invaluable support and comic relief ever since. Ashley is one of the most thoughtful people I have had the pleasure to meet and her friendship, especially during these last few months, has made writing up a delightful experience. I would also like to thank Erich for his life-long friendship, brotherly guidance and support.

Most importantly, I wish to thank Daniella for all her love and patience as my work and I became a permanent feature of the living room. Her unwavering support and encouragement have gotten me through the most challenging parts of this thesis. I would also like to extend my gratitude to her family for welcoming me into their home with open arms.

I also do not wish to forget those who have helped prepare me for this path. I am thankful for my pre-doctoral experience at Creighton University, where my supervisors Janet Seger and Michael Cherney first introduced me to the world of particle physics, gave me the encouragement and opportunity to form part of the STAR and ALICE collaboration, and ultimately ignited my interest and love for the field.

Finally, I would like to thank my parents, sister, and nephew for their life-long love and support. You have always been a driving force in my life in spite of the long distance and I am eternally grateful for all the sacrifices you have made to help me get to where I am today.

Contents

CHAPTER 1

Introduction

It is undeniable that human beings have an inherent desire to make sense of life and the world we live in. Pushing the frontiers of knowledge has always been a continuous and collective endeavour. The field of particle physics is no exception. Today, standing on the shoulders of giants, thousands of members of the particle physics community continue to make an international effort to develop, maintain, and run what is one of the most impressive and ambitious experimental instruments built by humanity, the Large Hadron Collider (LHC). In this thesis, I present my efforts to contribute to our collective goal of advancing the field of particle physics.

The majority of the proton-proton collisions studied at the LHC are inelastic. That is, the incoming protons do not survive the collision and fragment into a large number of particles. The complexity of these events can present an added challenge for event reconstruction, particle identification, and background reduction. However, there is a production mechanism, known as central exclusive production (CEP), where the two incoming protons can interact through the exchange of intermediate particles, produce a single or few low-momentum particles, and remain intact while scattering at small angles. This means that CEP has a distinctive experimental signature where the signal consists of the final-state particles of the produced system in an otherwise empty detector, thus providing a clean environment in which to study resonances and other phenomena.

CEP can be mediated by one of three processes, one of which is purely electromagnetic, another is mediated solely by the strong force, and one mediated by both the electromagnetic and strong force, which give us access to the nature of these forces. Furthermore, the dynamics of CEP, which are approximately independent of the produced system, give rise to unique quantum-number-selection rules that effectively allow us to use this mechanism as a spin quantum-number filter, which in principle enables us to measure and confirm the quantum-number nature of newly discovered objects.

Although the Large Hadron Collider beauty experiment (LHCb) was designed to study CP violation and suppressed decays in the beauty system, it is well equipped for the study of CEP, particularly because of its sensitivity to low momentum and transverse momentum particles. Furthermore, the HeRSCheL sub-detector, which is a system of scintillating planes at high rapidity, has the capability of vetoing inelastic background events. This makes CEP an excellent laboratory for the study of Standard Model states and a discovery tool in the search for unobserved states at LHCb.

The main focus of this thesis is the study of the CEP of χ_c mesons at the LHCb experiment. Although significant advancements have been made on the theoretical front of CEP with the development of the so-called Durham model, additional studies are necessary to validate and further constrain theoretical models. The χ_c states are regarded as the *standard candle* for the CEP processes mediated by the strong force. This study is a crucial benchmark that opens LHCb up to a new frontier of future CEP studies, such as the CEP of the Higgs boson.

We study the production of χ_c mesons through their radiative decay into $J/\psi\,[\mu^+\mu^-]\gamma$. Previous measurements of this decay mode have been limited on account of the resolution of the mass peaks of χ_{c1} and χ_{c2}, which sit within 50 MeV/c^2 of one another. To overcome this problem, we reconstruct the photon using two electrons, known as converted photons, and utilise the momentum resolution of the tracking of the LHCb experiment to improve the χ_c candidates' mass resolution. To this end, we develop a novel method to measure the reconstruction efficiency of converted photons using $D^*(2007)^0 \to D^0\gamma$ decays.

In Chapter 2 we introduce the theoretical background starting with an overview of quantum chromodynamics, the theoretical model of strong interactions responsible for mediating the CEP of χ_c mesons. We then introduce CEP, where we highlight some of the kinematic and dynamic qualities crucial to this analysis before outlining the Durham model. We end with an overview of previous studies and theoretical predictions of the CEP of χ_c mesons. A detailed description of the LHC and the LHCb experiment are presented in Chapter 3 together with an overview of the data acquisition, simulation, and reconstruction framework. We then present the CEP χ_c analysis starting in Chapter 4 with an outline of the data and simulation samples used for the CEP χ_c analysis as well as for the calibration data set necessary for the study of converted photons. We then outline the selection process and criteria applied to each of these samples. In Chapter 5 we present a series of efficiency studies including the efficiency determination of the aforementioned photon-conversions, as well as for the muon reconstruction, detector occupancy, the HeRSChel veto procedure, and other studies associated with selection cuts. Chapter 6 presents a series of background studies and covers the construction of the fit model used to extract the CEP χ_c signal, the fit results of which are presented in Chapter 7 together with a validation study of the model. Chapter 7 also presents the efficiency corrected results, a HeRSChel stability check, the luminosity determination, the calculation of the cross-section, and a summary of systematic studies. We conclude with final remarks and outlook in Chapter 8.

Chapter 2

Theoretical overview

2.1 Quantum Chromodynamics

Quantum chromodynamics (QCD) [1,2] is a well established and successful quantum field theory (QFT) which describes the strong interaction between six spin-$\frac{1}{2}$ fermions, known as quarks, and eight massless, force-carrying spin-1 bosons known as gluons. Unlike quantum electrodynamics, where only the fermions carry the electric charge, in QCD both quarks and gluons carry colour charge (for a total of $N_C = 3$ colour charges), which leads to interesting phenomena unique to the strong force. The quarks are separated into two categories: the first is up-type quarks with electromagnetic charge $+\frac{2}{3}$ (up u, charm c, and top t), with the second being down-type quarks with electromagetic charge $-\frac{1}{3}$ (down d, strange s, and bottom or beauty b). More specifically, QCD is a non-Abelian gauge theory [3] generated by the special-unitary group of degree three, $\mathrm{SU}(3)_C$, where the C highlights the fact that the theory only applies to colour-charge-carrying particles.

In QFT, each elementary particle has a field associated with it that permeates all space-time and these particles are localised, excited states of their underlying quantum fields. These fundamental fields cannot be measured directly, however there are observables related to these fields, such as charge, that are measurable. Different configurations of these fields, or gauges, can result in identical measurements of the observable. If this is the case, the field is said to be gauge invariant under that gauge transformation. These transformations can be global or local. The latter meaning that they can have a dependence on space-time. The dynamics of the theory are specified by the Lagrangian density, $\mathcal{L}$, which is required to be invariant under a continuous group of these local transformations.

2.1.1 QCD Lagrangian

The quark fields ψ_i and anti-quark fields $\bar{\psi}_i$ take the form of a triplet

$$\psi_i = \begin{pmatrix} \psi_1 \\ \psi_2 \\ \psi_3 \end{pmatrix} \quad \text{and} \quad \bar{\psi}_i = \begin{pmatrix} \bar{\psi}_1^* \\ \bar{\psi}_2^* \\ \bar{\psi}_3^* \end{pmatrix}, \tag{2.1}$$

respectively, where the indices $i = \{1, 2, 3\}$ correspond to the three colour charges. The fermion wave-functions transform as

$$\psi(x) \rightarrow \psi'(x) = e^{ig_s\theta^a(x)\cdot T^a}\psi(x) \tag{2.2}$$

where g_s is the bare-strong-coupling constant, $i = \sqrt{-1}$, $\theta^a(x)$ are eight ($a = \{1, ..., N_C^2 - 1 = 8\}$ for each of the eight gluons) phase factors dependent on space-time coordinates, and T_a are known as colour-charge matrices and are the generators of the gauge group. The group generators take the form of 3×3 linearly independent hermitian ($T_a = T_a^\dagger$) matrices related to the Gell-Mann matrices λ_a, such that

$$T^a = \frac{1}{2}\lambda^a. \tag{2.3}$$

The term non-Abelian refers to the fact that the group generators do not commute, such that their commutation relation is given by

$$[T^a, T^b] = if^{abc}T^c, \tag{2.4}$$

where f^{abc} are the $\mathrm{SU}(3)_C$ colour-structure constants with indices a, b, and c, which cycle over the eight colour degrees-of-freedom. The phase transformation described by Eq. 2.2 corresponds to a rotation in colour-space such that the axis of rotation depends on the space-time coordinates.

Maintaining gauge invariance also requires that we satisfy the Dirac equation,

$$i\gamma^\mu\partial_\mu\psi = m\psi, \tag{2.5}$$

where γ_μ are gamma matrices, and $\partial^\mu = (\partial_t, -\vec{\nabla})$ is the four-gradient. This requires the introduction of new gauge fields. These correspond to the gluon fields, which have a time-like and three space-like components, and take the form of an octet A_a^μ. In order to preserve gauge invariance, we modify the four-gradient such that

$$\partial\mu \rightarrow D_\mu = \partial_\mu + ig_sA_\mu^aT^a, \tag{2.6}$$

giving us the covariant derivative D_μ resulting in the quark-quark-gluon interaction vertex, shown in Fig. 2.1 (left).

The gluon field strength tensor $F_a^{\mu\nu}$, which characterises the interaction between quarks and gluons, is given by

$$F_a^{\mu\nu} = \partial^\mu A_a^\nu - \partial^\mu A_a^\mu + g_sf^{abc}A_b^\mu A_c^\nu. \tag{2.7}$$

The third term, $g_sf^{abc}A_b^\mu A_c^\nu$, represents the gluon self-interaction which arises from the fact that the gluons also carry colour charge and the generators of the group do not commute. This gives rise to triple and quartic gluon vertices, shown in Fig. 2.1 middle and right, respectively.

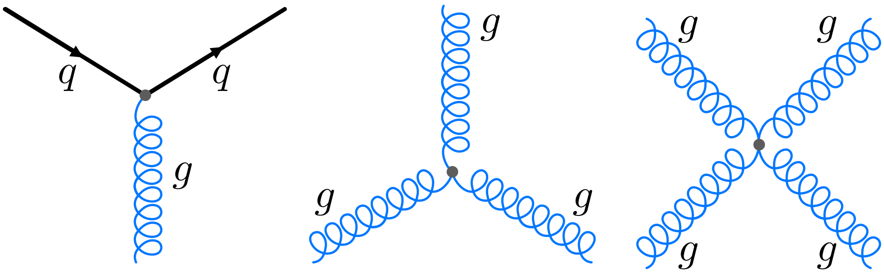

Figure 2.1. Feynman diagram of quark-quark-gluon (left), triple-gluon (middle), and quartic-gluon (right) vertex.

The dynamics of the quark and gluon are given by the QCD Lagrangian density

$$\mathcal{L}_{QCD} = \sum_f \bar{\psi}_f^i (i\gamma_\mu D^\mu - m_f)_{ij} \psi_f^j - \frac{1}{4} F_a^{\mu\nu} F_{\mu\nu}^a, \tag{2.8}$$

where m_f are fermion mass parameters. Note that there are no gluon mass terms of the form $m^2 A^\mu A_\mu$ present in the Lagrangian as these terms violate gauge invariance, explaining the massless nature of the gluon.

2.1.2 Colour confinement

The gluon-gluon self interaction gives rise to a phenomenon known as colour *confinement* that explains why we have not observed freely propagating quarks [1,2]. The strong interaction results in an attractive force between two quarks, and is mediated through the exchange of virtual gluons. Additional gluon-gluon interactions can occur between the virtual gluons, concentrating the colour fields as shown in Fig. 2.2. As a result, a large amount of energy can be stored in the colour fields, or string of colour force, which increases with the distance between the quarks, of about 1 GeV/ fm.

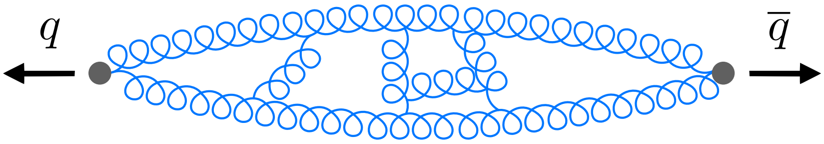

Figure 2.2. Schematic representation of two quarks moving in opposite directions and the concentration of colour fields as a result of additional gluon-gluon interactions between virtual gluons. Adapted from [2].

Naively, it would seem that it would be possible to force a quark from a hadron by applying a sufficiently large force. However, as the distance increases between the nucleon and the quark, the attractive force stored in these colour fields also increases. Given a large enough distance, the stored energy can be sufficiently large to create a quark anti-quark pair before the quark is ever free. This quark anti-quark production process occurs recursively until the energy of the quark pairs is low enough to be bound in a colourless hadronic system of their own. This process is known as hadronisation and results in a collimated burst of particles known as a jet. A schematic representation of the hadronisation process is shown in Fig. 2.3.

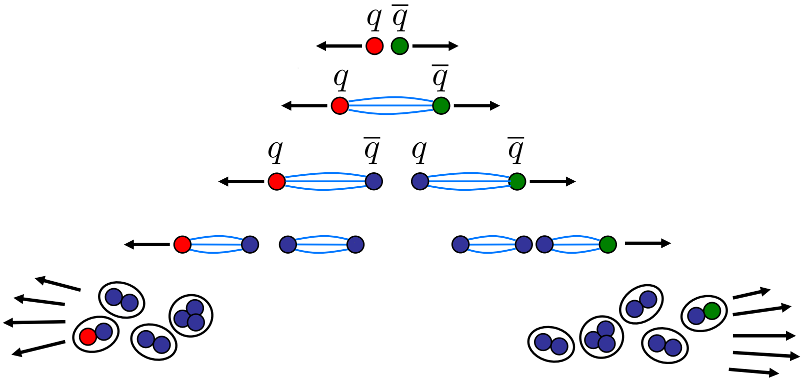

Figure 2.3. Schematic representation of the hadronisation process as two quarks move away from each other at high velocities. The energy stored in gluon tubes results in the recursive production of quark pairs until all quarks are confined in colourless hadrons. Adapted from [2].

As a result of this behaviour, quarks are only found in colour-singlet systems. The parton model [4] classifies hadrons into mesons composed of a quark anti-quark pair ($q\bar{q}$), and baryons composed of three quarks (qqq), or three anti-quarks ($\bar{q}\bar{q}\bar{q}$). In recent years more exotic hadrons have been discovered, which can be explained by tetraquark ($qq\bar{q}\bar{q}$) [5–7] or pentaquark states ($qqqq\bar{q}$) [8–11].

2.1.3 Asymptotic freedom

The strength of the interaction between gluons and quarks is given by the strong-coupling constant. However the value used in Feynman diagram calculations, often referred to as the *bare*-coupling constant, is not the same as the effective-coupling constant measured experimentally.

In QCD, quantum fluctuations in the fermion and boson fields can bring virtual quark and gluons in and out of existence, creating a cloud of electric and colour charge around a quark, as depicted in Fig. 2.4. Due to the electric attraction between the virtual-quark pairs and the probe quark, the anti-quarks in the $q\bar{q}$ pair tend to be closer to the probe quark. This effect is known as vacuum polarisation. This has a *screening* effect which reduces the effective value of g_s at larger distances from the probe quark. The gluon pairs have the opposite effect: they enhance the effective value of g_s at larger distances in what is known as an *anti-screening* effect. It transpires that the anti-screening effect of the gluon pairs dominates, and as a result the strong coupling decreases at shorter distances. Experimentally, small distances translate to large four-momentum transfers $Q^2 = -q^2$ as higher energies are needed to resolve smaller distances. As it turns out, the strong-coupling constant is not constant at all and has a strong dependence on Q^2 and is better described as a *running-coupling* constant.

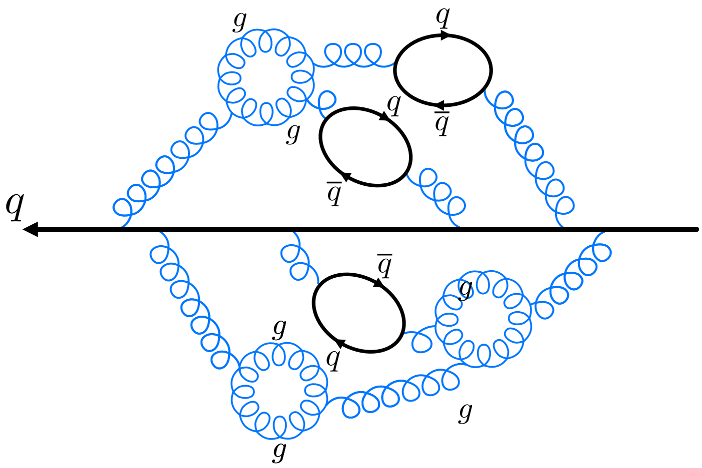

Figure 2.4. Schematic representation of QCD vacuum polarisation.

This behaviour has two interesting phenomenological effects. The first is the concept of confinement which we have already described in Sec. 2.1.2. Essentially, at large distances the coupling becomes so strong that the energy is sufficient for quark pair creation, making the isolation of a quark impossible and forcing quarks to be tightly bound within hadrons. The second is known as asymptotic freedom: at shorter and shorter distances, the strong coupling is smaller and smaller. Experimentally, this means that when probing quarks within a hadron at sufficiently high energy, that is interactions involving high four-momentum transfer entailing large-Q^2 values, the quarks begin to behave more like free particles.

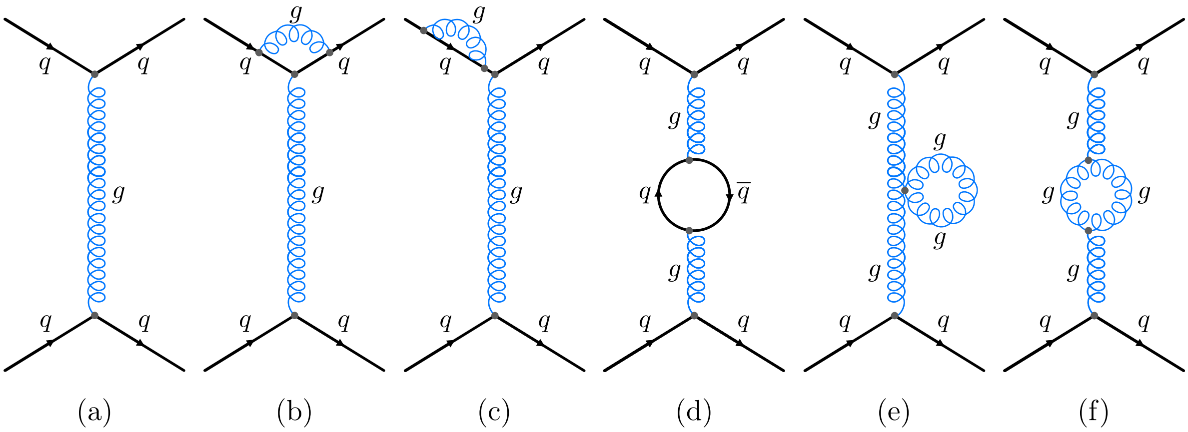

Figure 2.5. Leading order Feynman diagram for gluon exchange (a), corrections to the quark four-vector (b−c), and corrections to the gluon propagator (d−f).

When calculating the vertex of a Feynman diagram, any higher-order corrections can and will contribute to the process. For example, when considering the scattering of two quarks through the exchange of a gluon, the leading-order diagram is given by Fig. 2.5(a). However, the effective-strong coupling will be composed of the sum of all higher-order diagrams which include quark and gluon loops in the propagator known as the gluon self-energy terms or, as hinted above, vacuum polarisation loops. Due to the Ward identity [12], such corrections associated with the quark cancel each other perfectly. These corrections include diverging four-momentum integrals that diverge in the *ultra-violet* as the four-momenta can take large values. These divergences are controlled through the introduction of a cut-off parameter in a process known as *renormalization* [2]. This results in a running-coupling constant

$$\alpha_S(Q^2) = \left[\frac{11N_C - 2N_f}{12\pi}\ln\left(\frac{Q^2}{\Lambda^2}\right)\right]^{-1}, \tag{2.9}$$

where $N_C = 3$ is the number of colour charges, $N_f = 6$ is the number of quarks, Q^2 is the four-momentum transfer squared of the exchanged gluon, Λ is known as the QCD-energy-scale parameter, an experimentally determined parameter ($\sim 100\,\text{MeV}$) which marks the energy scale at which $\alpha_s(Q^2)$, starts to diverge asymptotically. Therefore, Λ loosely marks where perturbative methods are no longer applicable. A summary of strong-coupling constant measurements is shown in Fig. 2.6 as a function of Q.

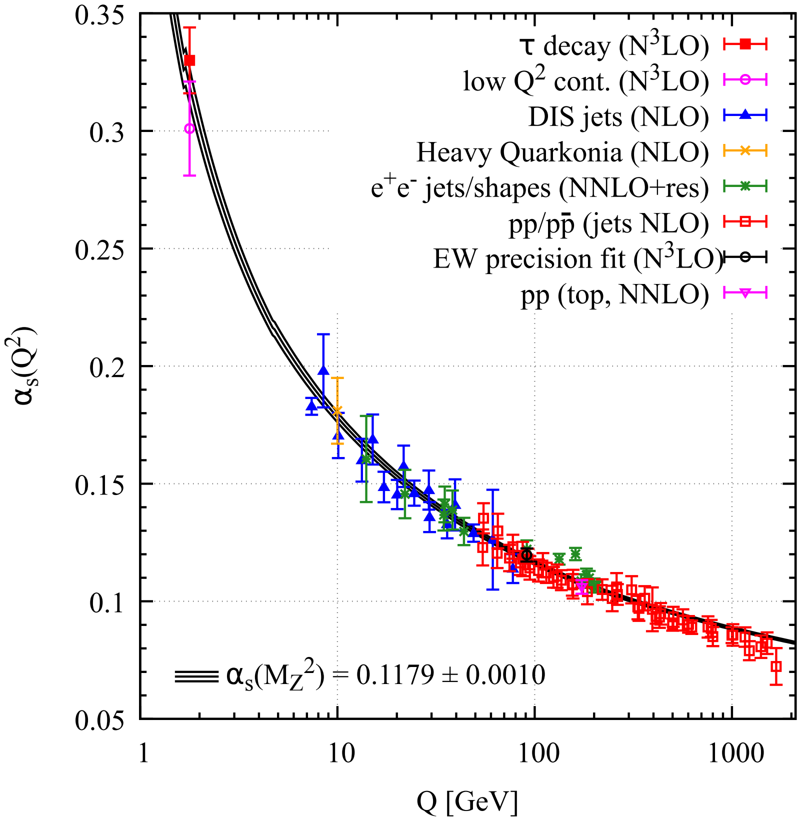

Figure 2.6. Summary of measurements of $\alpha_s(Q^2)$ as a function of the energy scale Q. Reproduced from [13].

2.1.4 Pomeron

In the Durham model, described in Sec. 2.5, and in this text, the word pomeron ($I\!P$) refers to a pair of gluons in a colour-singlet state such that they carry the quantum numbers of the vacuum [14]. That is, it carries no electric charge, zero isospin $I = 0$, natural parity $P = +1$ (even), and even charge-conjugation $C = +1$. As a result, events mediated by a pomeron do not exchange quantum numbers in the reaction.

The word pomeron, coined in honour of the Russian physicist Isaak Yakovlevich Pomeranchuk [15], is inherited from a theoretical model, called Regge theory, developed by Italian physicist Tullio Regge, that predates QCD. Regge theory introduced the use of complex-angular momentum in quantum mechanics. The theory was particularly successful when extended to relativistic particle physics by Chew and Frautschi and then applied to high-energy hadron-hadron and photon-hadron interactions [16].

Regge theory is a t-channel model where the scattering process is mediated through a virtual particle. A Feynman diagram of a t-channel exchange is depicted in Fig. 2.7 (centre). Following the example of the Yukawa hypothesis which states that long-range nucleon interactions are due to the exchange of pions [17], these t-channel interactions were generally modelled through the exchange of virtual mesons, such as the π and ρ mesons which have a definite spin. However, in Regge theory not only can the particles have complex-angular momentum but, to preserve unitarity, processes are mediated through the superposition of a family of resonances known as *Regge trajectories* or *Reggeons* [18]. To obtain agreement between the predicted cross-sections and experimental observations, a new Regge trajectory was added that carries the quantum numbers of the vacuum. This trajectory is what is known as the *pomeron* ($I\!P$).

2.2 Central exclusive production

Central exclusive production (CEP) [19–21] is an interesting phenomenon, where a system of one or two colour-singlet particles, X, are produced in a diffractive-elastic process such that the colliding protons, p, remain intact after the interaction and scatter at small angles. Essentially, the system X is produced in a *central* or near-zero rapidity region relative to that of the outgoing protons, and consists *exclusively* of its decay products and no other hadronic activity. Rapidity, y, is a quantity used to describe the polar coverage of accelerator physics, measured from the interaction point. Differences in rapidity are invariant under longitudinal relativistic transformation. Rapidity is defined such that,

$$y = \frac{1}{2} \ln \left(\frac{E + p_z c}{E - p_z c} \right), \tag{2.10}$$

where E is the total energy of the particle, p_z is the momentum along the beam line, and c is the speed of light in vacuum. A particle with momentum perpendicular to the beam line will have a rapidity of zero, and the rapidity will increase as the momentum becomes more co-linear with the beam line. An alternative variable known as pseudorapidity, η, is calculated, starting from the expression for rapidity, with the assumption that the particle's momentum is much larger than its mass and is defined such that,

$$\eta = -\ln\tan\left(\frac{\theta}{2}\right) \tag{2.11}$$

where θ is the polar angle measured from the beam line.

These conditions result in a unique topology characterised by two large rapidity gaps, defined as a volume of inactivity in the detector and denoted by $\oplus$, between each of the outgoing protons and the system of interest, such that

$$p_1 \oplus p_2 \to p_3 \oplus X \oplus p_4, \tag{2.12}$$

where p_1 and p_2 are the incoming protons and p_3 and p_4 are the outgoing protons. Experimentally, this implies that only the decay products of the produced object of interest are present in an otherwise empty detector, as long as there are no pile-up events[1] or secondary interactions which might break the rapidity-gap criteria. As a result, CEP provides a clean environment in which to study the signal while imposing strict kinematic and dynamic constraints, described in detail in Sec. 2.4, which to a close approximation are independent of the central object produced. In addition, CEP allows us to access spin and parity quantum-number information: a difficult task via inelastic events [22]. Measurements of *standard candles* allow CEP predictions to be tested. When we achieve confidence from the agreement between the theoretical and experimental predictions we can then test properties of other states.

This makes CEP a powerful tool through which to study known resonant and non-resonant Standard Model (SM) states. Additionally, this makes CEP an even more promising discovery tool in the search for unobserved states predicted by the SM, such as the glueball [23], a bound state composed purely of self-interacting gluons and no quarks, and odderon (O) [24, 25], a t-channel exchange of a colour-neutral system composed of an odd number of gluons, as well as states predicted in Beyond the Standard Model (BSM) theories [26]. Not only does CEP provide access to the system, but it also sheds light on the nature of the system and its quantum properties, making CEP a very valuable probe for spectroscopy studies.

2.3 CEP production mechanisms

CEP events are mediated by the t-channel exchange of colour singlets. In t-channel interactions one of the incoming protons can emit an intermediate particle that is absorbed by the second proton. Alternatively, each of the incoming protons can emit an intermediate particle that interact with one another. This allows for interactions where the outgoing protons remain intact, something that is not possible in s-channel and u-channel interactions. Colour singlets are particles, or a system of particles, with a total-colour charge of zero. This means there is no exchange of charge or colour charge during the t-channel exchange. This, in turn, allows the colliding protons to remain intact and preserve the rapidity gap of the final-state particles.

---

[1] Pile-up events have more than one interaction per bunch crossing.

The Feynman diagram for t-channel scattering events is shown in Fig. 2.7 (centre), together with the s-channel (left) and u-channel (right) diagrams. There are three possible mediating mechanisms for CEP: double-photon exchange ($\gamma\gamma \to X$), photo-production ($I\!P\gamma \to X$), and double-pomeron exchange ($I\!P I\!P \to X$).

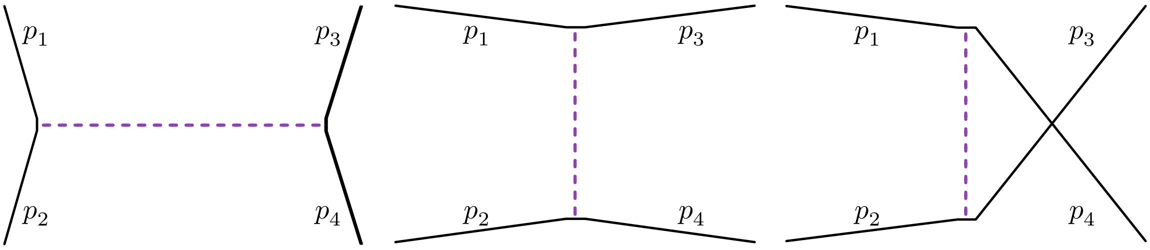

Figure 2.7. Feynman diagrams of different possible scattering channels in proton-proton collisions including the s-channel (left), t-channel (centre), and u-channel (right). Here p_1 and p_2 are incoming particles while p_3 and p_4 are outgoing particles. The exchange of intermediate particles is shown in dashed purple.

2.3.1 Double-photon exchange

In double-photon exchange, also known as two-photon fusion, the event is mediated by a theoretically well-understood Quantum Electrodynamics (QED) process, where each of the protons emits a quasi-real photon (low-Q^2) where q is the four-momentum transfer from the proton to the emitted photon that couples to the electromagnetic charge of the proton. The lowest-order Feynman diagram for this process is shown in Fig. 2.8 (left) for dimuon production.

Through double-photon exchange we are able to study non-resonant states such as light-by-light scattering ($\gamma\gamma \to \gamma\gamma$) [27], di-electron ($\gamma\gamma \to e^+e^-$) [28, 29] and di-muon ($\gamma\gamma \to \mu^+\mu^-$) [30, 31] production, as well as charged-electroweak-gauge boson pair production ($\gamma\gamma \to W^+W^-$) [32]. The CEP $\gamma\gamma$ channel can also be used to study meson production such as $\gamma\gamma \to \eta_c$ [33, 34] as well as double-hadron production ($\gamma\gamma \to hh$). The latter process is of particular interest as it has the potential to shed light on the nature of the odderon [35] as well as glueballs [36].

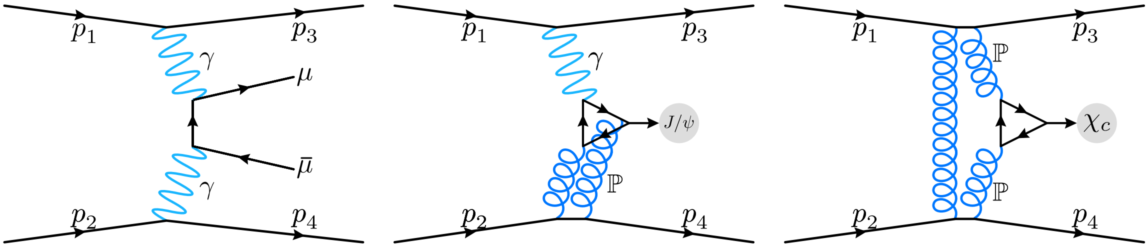

Figure 2.8. Lowest-order Feynman diagrams for three CEP mechanisms: double-photon exchange (left), photo-production (centre), and double-pomeron exchange (right).

2.3.2 Photo-production

A second mechanism involves the exchange of a photon emitted by one of the protons and a pomeron from the other in a process known as photo-production or photon-pomeron fusion. The lowest-order Feynman diagram for J/ψ production is shown in Fig. 2.8 (centre).

The fusion of an odd-charge-conjugate photon and an even-charge-conjugate pomeron implies we are able to produce odd-charge-conjugate objects allowing for the study of spin-1 vector meson final states (1^{--}) such as $\gamma I\!P \to \rho^0$ [37–40]. This also allows for the study of heavy-quarkonia states ($c\bar{c}$ and $b\bar{b}$) such as $\gamma I\!P \to J/\psi$ [41–47], $\psi(2S)$ [42,44,47], and $\gamma I\!P \to \Upsilon(1S)$ [48–50] mesons. These states are particularly interesting as they cover a regime where perturbative QCD applies and serve as a probe of small Bjorken-x, the fraction of the proton momentum carried by the parton (quarks and gluons) involved in the interaction. Quarkonia studies are also of particular interest in searching for the odd-charge-conjugate odderon, O, as it is expected to contribute to the vector-meson-CEP cross-section via an odderon-pomeron interaction ($OI\!P \to X$). The contributions of the odderon can be determined by detecting an excess of these CEP events. In addition to the study of mesons, it is also possible to study the exclusive production of the Z^0 boson via this process [29].

2.3.3 Double-pomeron exchange

The third CEP production mechanism, double-pomeron exchange (DPE) also known as pomeron-pomeron fusion, is mediated purely through QCD and is responsible for the production of $\chi_c(1P)$ mesons. The CEP of χ_c mesons is the main subject of this study and an introduction to the particle is detailed in Sec. 2.7 together with an exposition of previous relevant measurements of this meson. The lowest-order Feynman diagram for the double-pomeron channel for χ_c production is illustrated in Fig. 2.8 (right).

DPE provides a versatile framework through which to study properties of a wide range of SM and BSM physics. Since this channel involves the interaction of two even-charge-conjugate pomerons, it is possible to study the CEP of any even-charge-conjugate particle that couples to gluons. The unique dynamic constraints of CEP limit the process and allows it to behave as a quantum-number filter. The spin-selection rules associated with these production constraints are summarised in Sec. 2.5.3. As a result, this process allows for the study of particles with $J^{CP} = 0^{++},\ 1^{++},\ 2^{++}, ...$ and isospin $I = 0$. For example, this channel is responsible for the production of χ_c mesons, a heavy-charmonium state ($c\bar{c}$). It is also possible to study the CEP χ_b mesons, the heavier bottomonium ($b\bar{b}$) counterparts of χ_c mesons, which are at an energy scale where pQCD predictions might also be more reliable.

DPE is also a promising production mechanism for particle discovery. For example, lattice QCD predicts the lightest glueball state to be a low-mass, $\sim 1700\,\text{MeV}$, scalar with quantum numbers 0^{++} [23,51,52]. This makes $f_0(1500)(0^{++})$ and $f_0(1710)(0^{++})$ prime glueball candidates, and CEP an ideal tool for their study.

The interest of the physics community in CEP physics has been reignited thanks to its inherent ability to measure the spin of the central system and its application to the measurement of the spin for the Higgs boson. The CEP of the Higgs boson is mediated via the DPE [21,22,53–55]. For example, the Higgs boson can be reconstructed through a di-jet decay, $I\!PI\!P \rightarrow H^0 \rightarrow b[\ j\ ]\bar{b}[\ j\ ]$, a final state that can be produced directly through DPE, ($I\!PI\!P \rightarrow jj$) [30]. As a result, the measurement of the cross-section for the CEP of di-jets is an important measurement with which to calibrate our theoretical prediction of the CEP of the Higgs boson. A similar incentive applies for the study of two-photon CEP via double-pomeron,($I\!PI\!P \rightarrow \gamma\gamma$) [56], as this is one of the final states used in the discovery of the Higgs boson by the CMS [57] and ATLAS [58] experiment.

It is important to highlight that observing even a few CEP Higgs events would confirm its 0^{++} nature. As a result, it is essential that we conduct measurements of other resonant states produced exclusively through this mechanism, such as the CEP χ_c mesons, in order to test our theoretical understanding of this process and guide us through these future measurements.

2.4 CEP kinematics and dynamics

2.4.1 Bjorken-x in deep inelastic scattering

In deep inelastic scattering (DIS) [59], a high-energy-charged-probe particle is fired at a nucleon in order to probe the nucleon's internal structure via the exchange of a virtual gauge boson, with four-momentum q. The kinematics of deep inelastic scattering can be described in terms of a few relativistic-invariant quantities, one of which is known as Bjorken-x [60], defined by,

$$x \equiv \frac{Q^2}{2P \cdot q}, \tag{2.13}$$

where Q^2 is the square of the four-momentum of the gauge boson, such that

$$Q^2 = -q^2, \tag{2.14}$$

and P is the momentum of the incoming hadron. The resolving wavelength of the virtual gauge boson is inversely proportional to the magnitude of its four-momentum, as given by the de Broglie relation [61],

$$\lambda = \frac{h}{p}, \tag{2.15}$$

where λ is the wavelength associated with the particle, p is its momentum, and h is Planck's constant. At low-Q^2 values, the wavelength is long compared to the size of the proton. As the wavelength becomes comparable to the size of the proton, the photon begins to resolve the size of the proton. For high-Q^2 values, the wavelength is much shorter than the size of the proton, and is able to resolve the internal structure of the struck proton.

When Bjorken-x is plotted against the spectrum of the probe particle, the distribution has a consistent profile regardless of the collision energy. That is, the scattering process is not determined by the collision energy and therefore the resolving power of the gauge boson. This is known as Bjorken scaling. The independence of the absolute-resolution scale suggests that hadrons behave as a collection of point-like constituents known as partons, quarks and gluons.

2.4.2 Bjorken-x in double-pomeron exchange

When the mass of the central system, m_X, is sufficiently large (*i.e.* in the high-Q^2 regime) the CEP mechanism via double-pomeron fusion can be successfully described by perturbative QCD (pQCD). Here, large m_X is loosely defined in relation to the QCD energy scale Λ_{QCD} such that $Q^2 \gg \Lambda^2_{\mathrm{QCD}}$.

CEP calculations also involve low-Q^2 diffractive physics where perturbation theory breaks down. The physics in this regime is associated with secondary interactions that result in additional hadronic activity which breaks the CEP-double-rapidity-gap criteria, such as in rescattering corrections. CEP physics in this region can be calculated with Regge theory [62, 63]. These soft QCD calculations have a strong sensitivity to low-x and Q^2 gluon parton-distribution functions (PDF), which describe the probability of a parton having a fraction, x, of the proton's energy. These PDFs are extracted from data using global fits and have large uncertainties. The precision of these PDFs plays a fundamental role in studies of SM physics and BSM searches at hadron machines. The sensitivity of DPE to high-Q^2 as well as low-Q^2 physics makes it an ideal mechanism to put perturbative and non-perturbative theoretical frameworks of QCD to the test.

The centre-of-mass energy squared, s, is given by

$$s = (p_1 + p_2)^2, \tag{2.16}$$

where p_1 and p_2 are the momenta of the colliding protons. The parton model is often formulated in a frame where the proton has very high energy. Under the assumption that the proton mass can be neglected, we can also neglect the mass of the quarks and the transverse momentum of the incident partons such that the four-momenta of the partons in the hadron-hadron centre-of-mass frame are given by

$$p_a = \frac{\sqrt{s}}{2}\,(x_a, 0, 0, x_a) \quad \text{and} \quad p_b = \frac{\sqrt{s}}{2}\,(x_b, 0, 0, -x_b)\,, \tag{2.17}$$

where x_a and x_b are the fraction of energy carried by the parton from proton p_1 and p_2 respectively. We apply this approximation to DPE. As a result we can write the square of the mass of the central system, m_X, in terms of the parton momentum such that,

$$m_X^2 = (p_a + p_b)^2 = x_a x_b s. \tag{2.18}$$

It is conventional to define the unitless quantity, τ, such that,

$$\tau = x_a x_b = m_X^2/s. \tag{2.19}$$

We can write the rapidity of the central system in terms of the parton momentum fraction,

$$y = \frac{1}{2}\ln\left(\frac{E+p_z}{E-p_z}\right) = \frac{1}{2}\ln\left(\frac{E\,(x_a+x_b+x_a-x_b)}{E\,(x_a+x_b-x_a+x_b)}\right) = \frac{1}{2}\ln\left(\frac{x_a}{x_b}\right), \tag{2.20}$$

where E is the energy of the central system and p_z is its longitudinal momentum. Making use of Eq. 2.18, we can write the fractional momenta in terms of the centre-of-mass energy and the central system's mass and rapidity such that,

$$x_a = \frac{m_X}{\sqrt{s}}e^{+y} \quad \text{and} \quad x_b = \frac{m_X}{\sqrt{s}}e^{-y}. \tag{2.21}$$

The forward topology of the LHCb experiment allows us to study central systems with a rapidity range $2 < y < 4.5$, giving us access to two Bjorken-x regions that are not accessible through zero rapidity central-barrel experiments: one at low-x and another at high-x. For a central system of mass $m_X = 3.5$ GeV (approximately the mass of a χ_c meson) produced in proton-proton (pp) collisions at a centre-of mass energy of $\sqrt{s} = 13$ TeV, we are able to access fractional momenta (Bjorken-x) of the order 10^{-2} to 10^{-3} and 10^{-5} to 10^{-6} for the case when the colliding gluon belongs to the proton moving in the positive and negative direction, respectively. This provides a unique opportunity to obtain important constraints for PDF fits. The kinematic coverage in (x, Q^2) phase space for pp collisions at a centre-of-mass energy $\sqrt{s} = 13$ TeV for the LHCb experiment is shown in Fig. 2.9, together with the coverage of other experiments including ATLAS, CMS, CDF/D0, HERA, and of fixed-target DIS experiments. The rapidity coverage is shown in red-dashed-diagonal lines.

2.4.3 Characteristically low $p_T^2(X)$ in CEP

The CEP of mesons occurs via the t-channel exchange of a colourless object between the colliding protons, see Fig. 2.7 (centre). In the case of χ_c meson production, this process occurs through a DPE. The differential cross-section of elastic pp scattering as a function of the four-momentum transfer squared at the proton vertex, t, also known as one of the three Mandelstam variables (s, t, and u), falls with increasing values of $|t|$. The four-momentum transfer squared for the t-channel is given by

$$t = (p_1 - p_3)^2 = (p_4 - p_2)^2, \tag{2.22}$$

where p_1 and p_2 are the four momenta of the incident protons and p_3 and p_4 are the four momenta of the scattered protons. To a first approximation, the cross-section dependence on the four-momentum transfer in elastic interactions can be parameterised as an exponential

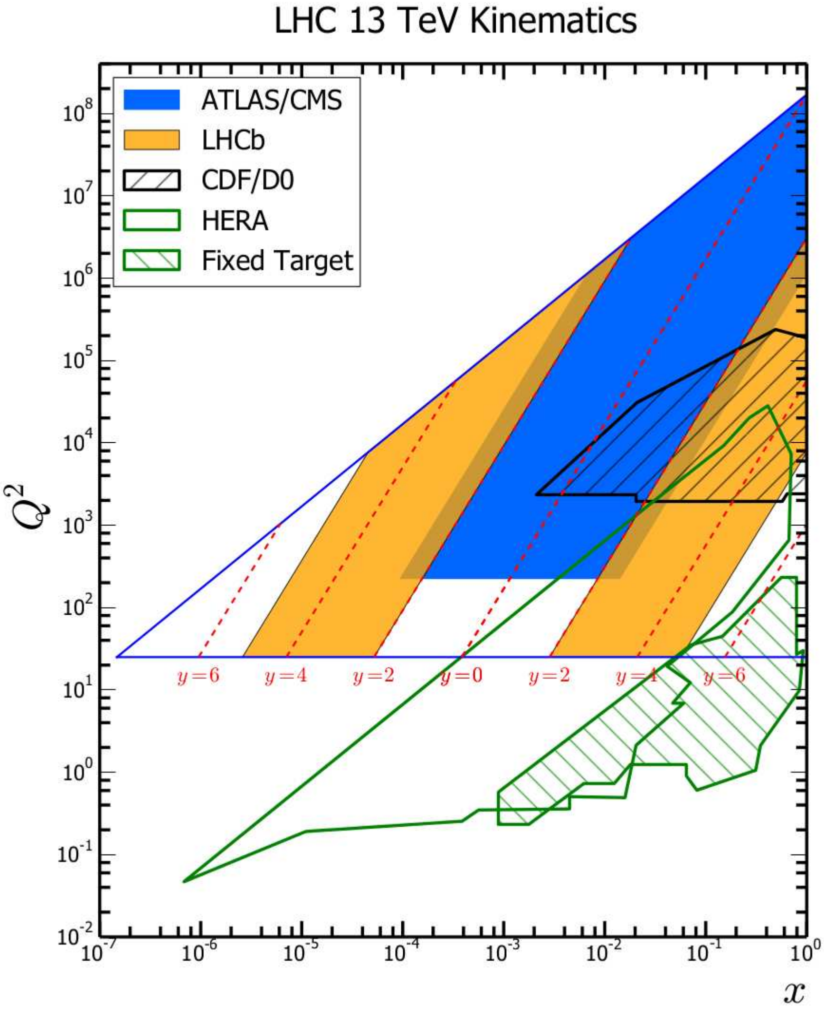

Figure 2.9. Kinematic coverage in (x, Q^2) phase space for pp collisions at a centre-of-mass energy $\sqrt{s} = 13$ TeV in comparison to ATLAS, CMS, CDF/D0, HERA and fixed-target coverage. Image reproduced from [64].

function such that,

$$\frac{d\sigma}{dt} \propto e^{-b_{\mathrm{CEP}}|t|}, \tag{2.23}$$

for small-$|t|$ values, $|t| < 0.5$ GeV/c, and where b_{CEP} is the slope of the exponential, in this case related to the CEP mechanism. Similarly, the differential cross-section for inelastic events with proton dissociation falls as $|t|$ grows. However, it does so at a much lower rate. This is parameterised with a power-law function such that,

$$\frac{d\sigma}{dt} \propto \left(1 + \left(\frac{b_{\mathrm{In.}}}{n}\right)|t|\right)^{-n}, \tag{2.24}$$

where n is the power law's exponent [65, 66]. For low-$|t|$ values, this can be approximated with an exponential that takes the same form as Eq. 2.23,

$$\frac{d\sigma}{dt} \propto e^{-b_{\mathrm{In.}}|t|}, \tag{2.25}$$

where $b_{\mathrm{In.}}$ is the slope of the exponential, in this case related to the inelastic mechanism.

Unfortunately, $|t|$ is not directly accessible experimentally but it can be estimated from the transverse-momentum squared of the central system, X, in the laboratory frame, such that,

$$t \approx -p_{\mathrm{T}}^2(X). \tag{2.26}$$

Therefore, although the invariant-mass distribution of $\chi_c \to J/\psi\,[\mu^+\mu^-]\gamma[e^+e^-]$ in inelastic and CEP events is expected to be similar, CEP events have a characteristically lower transverse-momentum squared compared to their inelastic counterparts, which is a signature that can be used to discriminate between signal and background. The low-momentum exchange between the interacting protons, characteristic of CEP events, stems from the requirement that the protons do not fragment. Therefore, the transverse-momentum squared of the object of interest, X, is also small in CEP events. On the other hand, inelastic interactions result in the fragmentation of one or both of the protons, which does not impose an upper constraint on the momentum exchange, hence producing particles with larger $p_{\mathrm{T}}^2(X)$ on average.

The low-momentum transfer constraint also manifests itself in the low-transverse momentum of the outgoing protons, which typically have $p_T < 1\,\mathrm{GeV}$ for CEP events [20]. In fact, with information about the incoming proton, a measurement of the outgoing proton's kinematics, and law of conservation of four momentum we are able to calculate the mass of the object of interest, m_X, regardless of its decay. This technique is referred to as the missing-mass method [54]. As a result, it is desirable for CEP studies to measure the kinematics of the outgoing proton with high-rapidity spectrometers.

2.5 The Durham model

In this section, we present a summary of the formalism used to calculate the perturbative CEP cross-section, known as the Durham model [20, 67–73]. Theoretical predictions of the cross sections for the processes relevant for this thesis are presented in Chapter 7. The lowest order Feynman diagram for the QCD contribution to CEP, DPE, is shown in Fig. 2.10. As mentioned previously, this occurs through the t-channel exchange of two gluons: a gluon that couples to the central system, X, and and one that is present to ensure the colour singlet interaction between the colliding partons, known as a *screening gluon*. Here p_1 and p_2 are the momenta of the incoming protons, p_3 and p_4 are the momenta of the outgoing protons, q_1 and q_2 are the momenta carried by each of the gluons that couples to the central system, corresponding to the fractional momenta x_1 and x_2 associated with their respective protons, while x' is the fractional momentum carried by the screening gluon. Q is the gluon-loop momentum, and μ and ν are the Lorentz indices associated with their corresponding four-momenta vector.

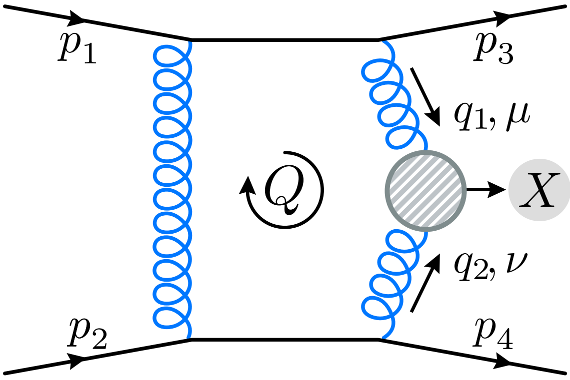

Figure 2.10. Lowest-order Feynman diagrams for the DPE CEP mechanisms for $p \oplus p \to p \oplus X \oplus p$ process in pQCD.

2.5.1 Hard process

The parton-level amplitude, A, of the CEP DPE production mechanism described by Fig. 2.10 is given by

$$\frac{iA}{s} = \frac{8}{N_C^2 - 1}\alpha_s^2 C_F^2 \int \frac{d^2 Q_T}{Q_T^2 q_1^2 q_2^2}\overline{\mathcal{M}}, \tag{2.27}$$

where s is the centre-of-mass energy squared, $i = \sqrt{-1}$, N_C is the number of colour charges, and C_F is known as the colour factor which describes the relative weight of the vertex associated with gluon bremsstrahlung, or the radiation of a gluon from a quark line. In the case of SM QCD, $N_C = 3$ and $C_F = 4/3$. Q_T is the gluon-loop transverse momentum and q_1 and q_2 are the momenta of the fusing gluons, while α_s is the QCD running coupling. The colour-averaged, normalised sub-amplitude $\overline{\mathcal{M}}$ for the $gg \to X$ process is given by

$$\overline{\mathcal{M}} \equiv \frac{2}{m_X^2}\frac{1}{N_C^2 - 1}\sum_{a,b}\delta^{ab} q_{1T}^{\mu} q_{2T}^{\nu} V_{\mu\nu}^{ab}, \tag{2.28}$$

where m_X is the mass of the central system produced in the gluon-fusion vertex, $V_{\mu\nu}^{ab}$, associated with the coupling of the two gluons with the central object produced $gg \to X$. The transverse momenta of the fusing gluons, q_{1T} and q_{2T}, is given by

$$q_{1T} = Q_T - p_{3T} \quad \text{and} \quad q_{2T} = -Q_T - p_{4T}, \tag{2.29}$$

respectively, where p_{3T} and p_{4T} are the transverse momentum of the outgoing protons.

The integral over the momentum loop, in Eq. 2.27, diverges as Q_T approaches zero, which is known as an infrared divergence. This is corrected via higher–order virtual corrections to the leading-order process through the introduction of Sudakov form factors, T_g [74,75]. The Sudakov form factors represent the poisson probability that the gluons involved in the hard process emit non-resolvable parton radiation that might break the exclusivity requirement, and therefore the rapidity gap criteria. Assuming a fixed, strong-coupling constant α_s, for simplicity, the form factor is given by

$$T_g\left(Q_T^2, \mu^2 = m_X^2\right) = \exp\left(-\frac{\alpha_s N_c}{4\pi}\ln^2\left(\frac{Q_T^2}{m_X^2}\right)\right), \tag{2.30}$$

where μ is the hard scale at which the form factor is regularised. In this case, the regularisation occurs at the scale of the central system's mass, $\mu = m_X$. T_g goes to zero as Q_T goes to zero, thus keeping the momentum-loop integral finite and allowing the CEP amplitude in the infrared region to vanish. In the case of the production of χ_c mesons μ is approximately 3 GeV where a significant part of the cross-section calculation falls under the unstable, low-Q_T infrared regime. As a result, corrections described in Sec. 2.5.2 are included to account for these soft processes. The infrared contribution becomes less significant at higher energy scales, such as that of the Higgs boson, $\mu \simeq m_H \sim 125$ GeV [71].

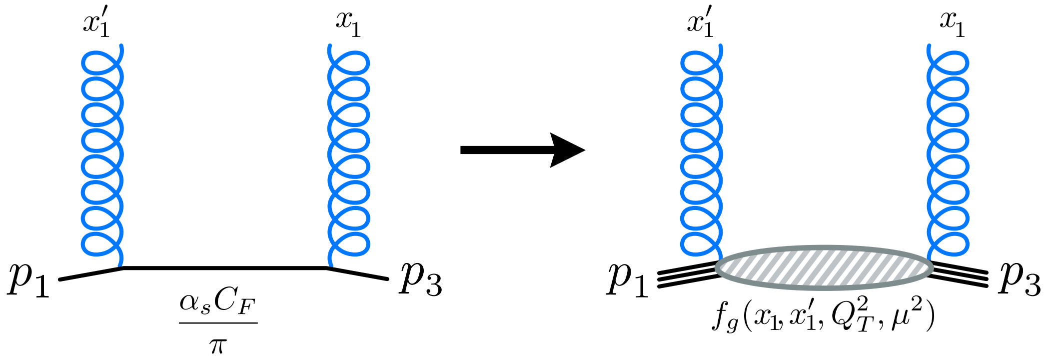

Figure 2.11. Pictorial representation of the replacement of a quark-level treatment, $\alpha_s C_F/\pi$, to a skewed, unintegrated, gluon PDF, $f_g(x, x', Q_T^2, \mu^2)$.

To convert the parton-level amplitude Eq. 2.27 to a hadron-level amplitude, we introduce the replacement of the coupling constant described by Fig. 2.11 as

$$\frac{\alpha_s C_F}{\pi} \rightarrow f_g(x_{1,2}, x', Q_T^2, \mu^2 = m_x^2), \tag{2.31}$$

where f_g is known as the skewed, unintegrated gluon PDF, which describes the probability of finding a gluon with a given momentum fraction, x' is the momentum fraction carried by the screening gluon, and x_i is the momentum fraction carried by the gluon fusing to the central system. Here the term skewed refers to the fact that the momentum fraction carried by the screening gluon can differ from that of the fusing gluon [68, 76, 77] where the longitudinal momentum carried by the gluons satisfy

$$\left(x' \sim \frac{Q_T}{\sqrt{ss}}\right) \ll \left(x_i \sim \frac{M_X}{\sqrt{ss}}\right) \ll 1. \tag{2.32}$$

The skewed, unintegrated gluon PDF includes the Sudakov suppression factor from Eq. 2.30. The final perturbative CEP amplitude is given by,

$$T \equiv \frac{iA}{s} = \pi^2 \int \frac{d^2\vec{Q}_T \overline{\mathcal{M}}}{\vec{Q}_T^2(\vec{Q}_T - \vec{p}_{3T})^2(\vec{Q}_T + \vec{p}_{4T})^2} f_g(x_q, x_1', Q_1^2, \mu^2) f_g(x_2, x_2', Q_2^2, \mu^2) F_p(t_1) F_p(t_2), \tag{2.33}$$

where the t-dependence of the skewed PDFs, f_g, is assumed to factor out as the proton elastic form factors, $F_p(t_1)$ and $F_p(t_2)$. The t dependence, where t corresponds to the t-channel Mandelstam variable, of the proton form factor is not well known and is taken from experimental soft hadronic data and is found to be in agreement with CEP J/ψ studies [41, 43–47, 78]. As hinted in Sec. 2.4.3, this takes the form of $F_p(t) = \exp(bt/2)$. The parameter b is taken from fits of soft hadronic data and is found to be $b \sim 4\,\text{GeV}^{-2}$ [66].

2.5.2 Soft-process corrections

The exclusivity requirement of CEP demands that the event is not accompanied by additional activity. One such source of activity comes from soft, non-perturbative secondary interactions. The Durham model considers two types of rescattering processes associated with the underlying event collectively known as *soft survival effects*, each of which measure the probability that the CEP double-rapidity-gap criteria will *survive* the scattering process.

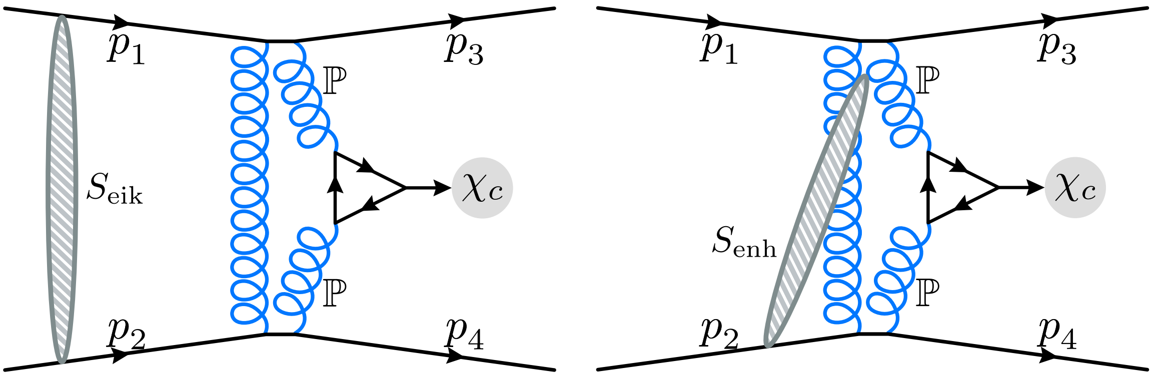

Figure 2.12. A schematic representation of the soft survival factors necessary to correct for soft-rescattering processes that break the rapidity gap including the eikonal survival factor S_{eik} (left) and enhanced survival factor S_{enh} (right).

The first soft survival effect, known as *eikonal survival factor*, S_{eik}, considers pp rescattering and is depicted in Fig. 2.12 (left). Although the survival factor is a soft process that cannot be calculated using perturbative methods, it is possible to measure it from soft hadronic data, such as in single and double diffraction studies [79]. The eikonal survival factor is dependent on the centre-of-mass energy and the transverse momentum of the colliding protons. The dependence on the protons' transverse momentum implies a dependence on the central object's spin and parity, which plays a greater role in the spin selection rules discussed in detail in Sec. 2.5.3. Ignoring the internal structure of the proton, the expected eikonal suppression is given by

$$\langle S^2_{\text{eik}} \rangle = \frac{\int d^2\vec{p}_{1T} d^2\vec{p}_{2T} \; |T(s, \vec{p}_{1T}, \vec{p}_{2T}) + T^{\text{res}}(s, \vec{p}_{1T}, \vec{p}_{2T})|^2}{\int d^2\vec{p}_{1T} d^2\vec{p}_{2T} \; |T(s, \vec{p}_{1T}, \vec{p}_{2T})|^2}, \tag{2.34}$$

where $\langle ... \rangle$ denotes averaging over the proton's transverse momentum, T is the double-pomeron-CEP amplitude, and T^{res} is the pp rescattering amplitude. Although it has a large suppression effect on the CEP cross-section of about two orders of magnitude, there are significant uncertainties associated with its centre-of-mass energy dependence, highlighting the importance of putting our theoretical models to test with this and future studies. The expected suppression factors, $\langle S^2_{\text{eik}} \rangle$, for χ_{c0}, χ_{c1}, and χ_{c2} at a centre-mass-energy $\sqrt{s} = 13\,\text{TeV}$ are expected to be 0.029, 0.091, and 0.072, respectively [67].

The second soft survival effect considers the probability of an additional interaction between one of the protons and one of the partons within the gluon loop. This is known as an *enhanced survival effect*, denoted by S_{enh}, and depicted in Fig. 2.12 (right). Although the magnitude of this effect is not known precisely, it depends mostly on the transverse momentum of the parton and proton, as well as the available rapidity interval for rescattering, which in turn depends on the centre-of-mass energy, $y_X \sim \ln(s/m^2_X)$. The enhanced suppression is expected to have a much smaller effect then the ekional survival factor described above, being about 0.25 at a centre-of-mass energy $\sqrt{s} = 14\,\text{TeV}$ for all $\chi_{c0,1,2}$ states [80].

The differential cross-section for the production of a central object X at rapidity y is given by

$$\frac{d\sigma}{dy} = \langle S^2_{\text{enh}} \rangle \int d^2\vec{p}_{1T} d^2\vec{p}_{2T} \frac{|T(\vec{p}_{1T}, \vec{p}_{2T})^2|}{16^2\pi^5} S^2_{\text{eik}}(\vec{p}_{1T}, \vec{p}_{2T}). \tag{2.35}$$

The final schematic of the Durham model is shown in Fig. 2.13, including representations for the soft survival factors, and gluon PDF. The CEP DPE cross-section has a dependence on the centre-of-mass energy since we expect higher gluon densities at low Bjorken-x to increase the frequency of double pomeron interactions. However, the soft survival effects decrease with centre-of-mass energies due to the increased proton opacity, the matter density of the proton, and the increased size of the rapidity gap available for the enhanced absorption.

2.5.3 Spin selection rules - spin filter

Due to the intact proton requirement, CEP processes satisfy special spin-selection rules that make CEP measurements sensitive to the quantum numbers of new states, particularly spin, parity, and charge conjugation [67], which are not easily accessible in diffractive and inclusive processes. While the production of states with quantum numbers $J_z^{PC} = 1^{++}$ and $J_z^{PC} = 2^{++}$ are possible, DPE predominantly produces central objects with $J_z^{PC} = 0^{++}$ quantum numbers,

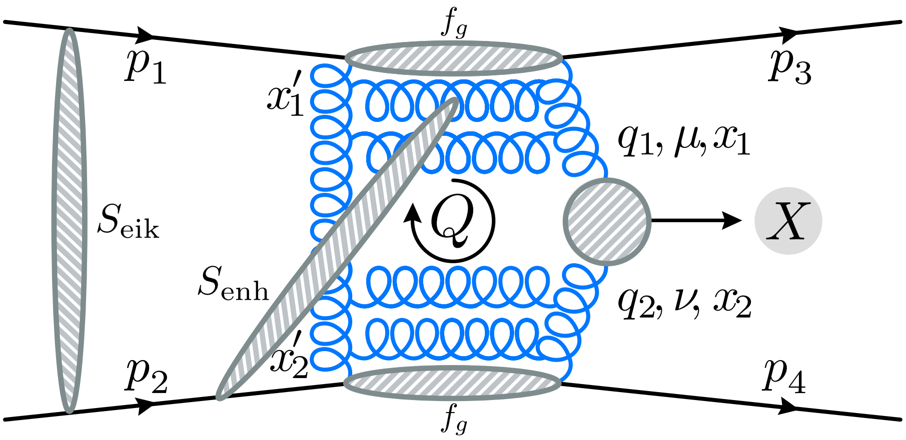

Figure 2.13. A schematic of the perturbative mechanism described by the Durham model for the CEP process $p_1 \oplus p_2 \to p_1 \oplus X \oplus p_2$ through the DPE channel. Here the gluon PDF f_g, the eikonal survival factor S_{eik}, and the the enhanced survival factor S_{enh} are represented symbolically.

where J_z is the projection of the objects' angular momentum on the z-axis. The origin of this selection rule is described below.

As mentioned earlier, DPE includes the interaction of two gluon pairs, one that fuses to the central system and another known as the screening gluon that guarantees the process occurs in a colour-singlet state, even under charge conjugation ($C = +1$). Therefore, the object produced must also be a colour-singlet object with $C = +1$.

In the limit where the protons have no transverse-momentum after the interaction ($p_{3T} = p_{4T} = 0$), there is no angular-momentum transfer between the two protons. Since the orbital-angular momentum of the two proton system is zero, $L_z = 0$, by conservation of angular momentum the central object produced must also have zero angular momentum along the z-axis, $J_z = 0$. In practice, however, there will very likely be some residual momentum transfer between the two colliding protons, such that the net $p_T \neq 0$: this will be small for central-exclusive-elastic reactions, and so will be a small correction to this selection rule.

The transverse momentum of the fusing gluons forms part of the polarisation vectors of the on-shell $g(\lambda_1)g(\lambda_2) \to X$ process. Here, λ_1 and λ_2 are the polarisation modes of the fusing gluons associated with the incoming protons p_1 and p_2, respectively. This can be seen when contracting $p_1^\mu V_{\mu\nu}^{ab} p_2^\nu$ during the calculation of the sub-amplitude $\overline{\mathcal{M}}$, Eq. 2.28, where we find that gauge invariance requires that $q_1^\mu V_{\mu\nu}^{ab} = q_2^\nu V_{\mu\nu}^{ab} = 0$ [81]. Where we have written the four momenta of the gluon in terms of that of the interacting parton, such that $q_i = x_i p_i + q_{iT}$, where $i = 1, 2$ maps to the respective protons. Therefore, we have that

$$p_1^\mu V_{\mu\nu}^{ab} p_2^\nu \approx \frac{q_{1T}^\mu}{x_1} \frac{q_{2T}^\nu}{x_2} V_{\mu\nu}^{ab}. \tag{2.36}$$

As a result, the fusing gluons are effectively transversely polarised, $\varepsilon_i \sim q_{iT}$. Following Eq. 2.29, in the limit where the outgoing protons carry no transverse momentum, we have that $Q_T = -q_{1T} = q_{2T}$. This implies that $\varepsilon_1 = -\varepsilon_2$ and hints at a vanishing angular momentum along the z-axis and therefore at the $j_z = 0$ selection rule.

We take the z-axis to be in the direction-of-motion of the gluons in the gg rest frame, such that the polar angle, θ, is zero. In the on-shell approximation ($q^2 = q_T^2 = 0$), that is a process that satisfies the Einstein energy-momentum relation $E^2 = \vec{p}^{\,2} + m^2$ such that the gluons have zero mass, the z-axis aligns with the beam line in the lab frame up to small corrections, of order q_T^2/m_X^2. Therefore, the momenta of the gluons simplifies to $p_\mu = (p_0,\ 0,\ 0,\ |\vec{p}\,|)$. For a massless boson travelling in the $\hat{z}$ direction, the two transverse polarisation states can be written as

$$\varepsilon_x^\mu = (0,1,0,0) \quad \text{and} \quad \varepsilon_y^\mu = (0,0,1,0). \tag{2.37}$$

We can take their linear combination to get the circular polarisation vectors

$$\varepsilon_\mu^+ = -\frac{1}{\sqrt{2}}(0,1,i,0) \quad \text{and} \quad \varepsilon_\mu^- = \frac{1}{\sqrt{2}}(0,1,-i,0). \tag{2.38}$$

Here, ± are the polarisation modes λ_i, with $+$ corresponding to a right-handed (R) helicity and $-$ corresponding to a left-handed helicity (L). We can then use the inverse of the polarisation vectors to write the gluon transverse-momentum vectors in terms of their helicity vectors, such that

$$q_{1T}^{\lambda_1} q_{2T}^{\lambda_2} \mathcal{M}_{\lambda_1\lambda_2} = \begin{cases} -\frac{1}{2}(\vec{q}_{1T}\cdot\vec{q}_{2T})\,(\mathcal{M}_{++}+\mathcal{M}_{--}) & (J_z^P = 0^+) \\ -\frac{i}{2}|(\vec{q}_{1T}\times\vec{q}_{2T})|\,(\mathcal{M}_{++}-\mathcal{M}_{--}) & (J_z^P = 0^-) \\ +\frac{1}{2}((q_{1T}^x q_{2T}^x - q_{1T}^y q_{2T}^y) + i(q_{1T}^x q_{2T}^y + q_{1T}^y q_{2T}^x))\,\mathcal{M}_{-+} & (J_z^P = +2^+) \\ +\frac{1}{2}((q_{1T}^x q_{2T}^x - q_{1T}^y q_{2T}^y) - i(q_{1T}^x q_{2T}^y + q_{1T}^y q_{2T}^x))\,\mathcal{M}_{+-} & (J_z^P = -2^+), \end{cases} \tag{2.39}$$

where $\mathcal{M}_{\lambda_1\lambda_2}$ are the $g(\lambda_1)g(\lambda_2) \to X$ helicity amplitudes. The parity and angular-momentum-projection quantum numbers shown alongside follow from the possible helicity combinations. The parity eigenstates are given such that

$$\begin{aligned} \psi_+ &= RR + LL \quad (P = +1) \\ \psi_- &= RR - LL \quad (P = -1) \\ \psi_+ &= RL,\ LR \quad\ \ (P = +1), \end{aligned} \tag{2.40}$$

where R and L correspond to right-handed (+) and left-handed (-) helicity states. Similarly, the conditions for the J_z quantum numbers are detailed in Fig. 2.14.

According to the Landau-Yong theorem, spin-1 states cannot decay into two on-shell spin-1 massless bosons [82]. Similarly, two on-shell spin-1 massless bosons cannot fuse into a spin-1 state. We see this reflected in the on-mass-shell calculation where we are missing an $J_z^P = 1^+$ term in

Eq. 2.39, since the term is odd under Q_T and vanishes when integrating over Q_T. However, the Landau-Yang theorem is violated by off-shell virtual effects. As a result, the production of 1^{++} states such as χ_{c1} are not strictly forbidden but instead significantly suppressed.

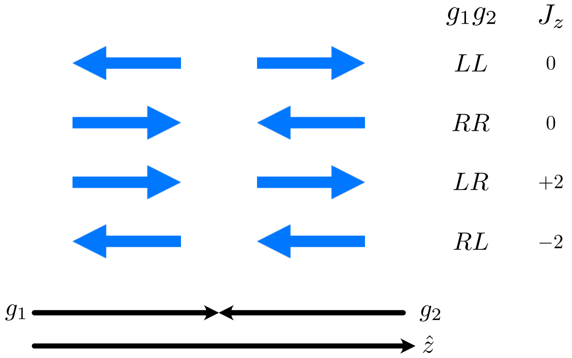

Figure 2.14. Schematic of determination of angular momentum along the z-axis, $J_z = 0$ of the project produced from the fusion of two spin-1 bosons travelling along the z-axis, where R and L corresponds to right-handed and left-handed helicity states.

In addition, when taking the $p_T \to 0$ limit we find that all terms in Eq. 2.39 vanish after the Q_T integral, with the exception of the $J_z^P = 0^+$ state, which results in the $J_z^{CP} = 0^{++}$ selection rule. However, this does not mean that χ_{c1} and χ_{c2} mesons are not produced in CEP DPE interactions, as the production of $J_z^{CP} = 1^{++}$ and $J_z^{CP} = 2^{++}$ systems are still possible due to the small-momentum exchange between the protons, which violates the $p_T \to 0$ assumption and results in small scattering angles. Consequently, CEP will produce predominantly $J_z^{CP} = 0^{++}$ states, with $J_z^{CP} = 1^{++}$ and $J_z^{CP} = 2^{++}$ systems significantly suppressed.

By integrating and squaring the amplitudes $\mathcal{M}_J$ we find rough estimates of the suppression relative to the production of χ_{c0} such that

$$|\mathcal{M}_0|^2 : |\mathcal{M}_1|^2 : |\mathcal{M}_2|^2 \sim 1 : \frac{\left\langle \vec{p}_T^{\,2} \right\rangle}{m_X^2} : \frac{\left\langle \vec{p}_T^{\,2} \right\rangle^2}{\left\langle \vec{Q}_T^2 \right\rangle^2} \sim 1 : \frac{1}{49} : \frac{1}{64}, \tag{2.41}$$

where $\left\langle \vec{Q}_T^2 \right\rangle$ can take values of a few GeV^2, and we have taken $\left\langle \vec{Q}_T^2 \right\rangle \sim 2\,\text{GeV}^2$, $m_X = 3.5\,\text{GeV}$ for the approximate mass of χ_{c1}, and $\left\langle p_{\text{T}}^2 \right\rangle \sim 0.25\,\text{GeV}^2$ is taken from the integral of the proton form factor $F_p(t_i)$. These results suggest we can expect the production of the χ_c mesons to follow a specific hierarchy, where the production of χ_{c1} and χ_{c2} is suppressed relative to that of χ_{c0}. The transverse-momentum dependence of the suppression factors can be exploited to select higher-purity samples of the desired spin system. Although these results provide us with an idea of the χ_c hierarchy and how the suppression scales, these are only approximations and do not take into account the soft-survival effects. The results for the full calculations are presented in Chapter 7 according to SuperChic, a Fortran-based Monte Carlo generator which implements the Durham model for CEP physics [83–85].

2.6 Rapidity-gap-breaking background

As mentioned previously, there are two critical requirements in CEP studies. The first demands that the central object is produced *exclusively* in the absence of any additional activity. The second requires that the colliding protons remain intact after the interaction and continue their trajectory down the beam line. Imposing both criteria implies that there will be two large-rapidity gaps between the outgoing protons and the central object. However, there are processes that mimic the CEP signature by breaking either the low-multiplicity or large-rapidity-gap criterion, without leaving a signature of the proton dissociation or additional activity within the detector acceptance. Here we introduce some of these rapidity-gap-breaking mechanisms.

Figure 2.15 depicts a series of Feynman diagrams for a number of processes considered in this discussion, alongside a typical rapidity-coverage distribution for such events where the forward and backward coverage of the LHCb main spectrometer is marked in green. In addition, the extended rapidity coverage of the newly added HeRSChel modules, described in Sec. 3.8, is marked in blue. This sub-detector, installed for the data collection of Run 2, was designed to detect particle showers at high-rapidity regions. The outgoing protons, if intact after the interaction, are marked in red while the rapidity gaps present in the interaction are marked ($\oplus$) and highlighted in grey. The interactions presented are all mediated through pomeron exchange, with the exception of Fig. 2.15 (c), which represents a hard scattering process. For example, Fig. 2.15 (a) corresponds to CEP through a DPE channel and Fig. 2.15 (b) is elastic proton scattering mediated through the exchange of a pomeron.

In central-exclusive-inelastic processes a central object is produced, much like in CEP, but this time it is accompanied by gluon radiation in one or both directions, as shown in Fig. 2.15 (d−f). This results in additional activity at high-rapidity values, approximately $5 < \eta < 10$, thus falling outside the acceptance of the main spectrometer and therefore leaving no trace of the break in rapidity gap. However, the resulting particles may interact with other accelerator components and induce showers detected by the HeRSChel modules. The presence of such soft interactions are accounted for in the Durham model through the soft-survival factors, as described in Sec. 2.5.2.

If the momentum exchange between the interacting protons is high enough, the dissociation of one or both of the interacting protons can occur in what is respectively known as single and double diffraction, shown in Fig. 2.15 (g−l). As with gluon radiation, these interactions result in high-rapidity fragments that can fall outside of the acceptance of LHCb's main spectrometer since they carry a large-longitudinal fraction of the initial proton's momentum. The particles resulting from the proton dissociation can have a broader rapidity coverage when compared to gluon radiation, spanning between zero and ten in rapidity. Therefore, these processes cannot always be excluded based solely on the no extra track and rapidity-gap requirement in the LHCb experiment. However, the resulting particle showers can be detected by HeRSChel.

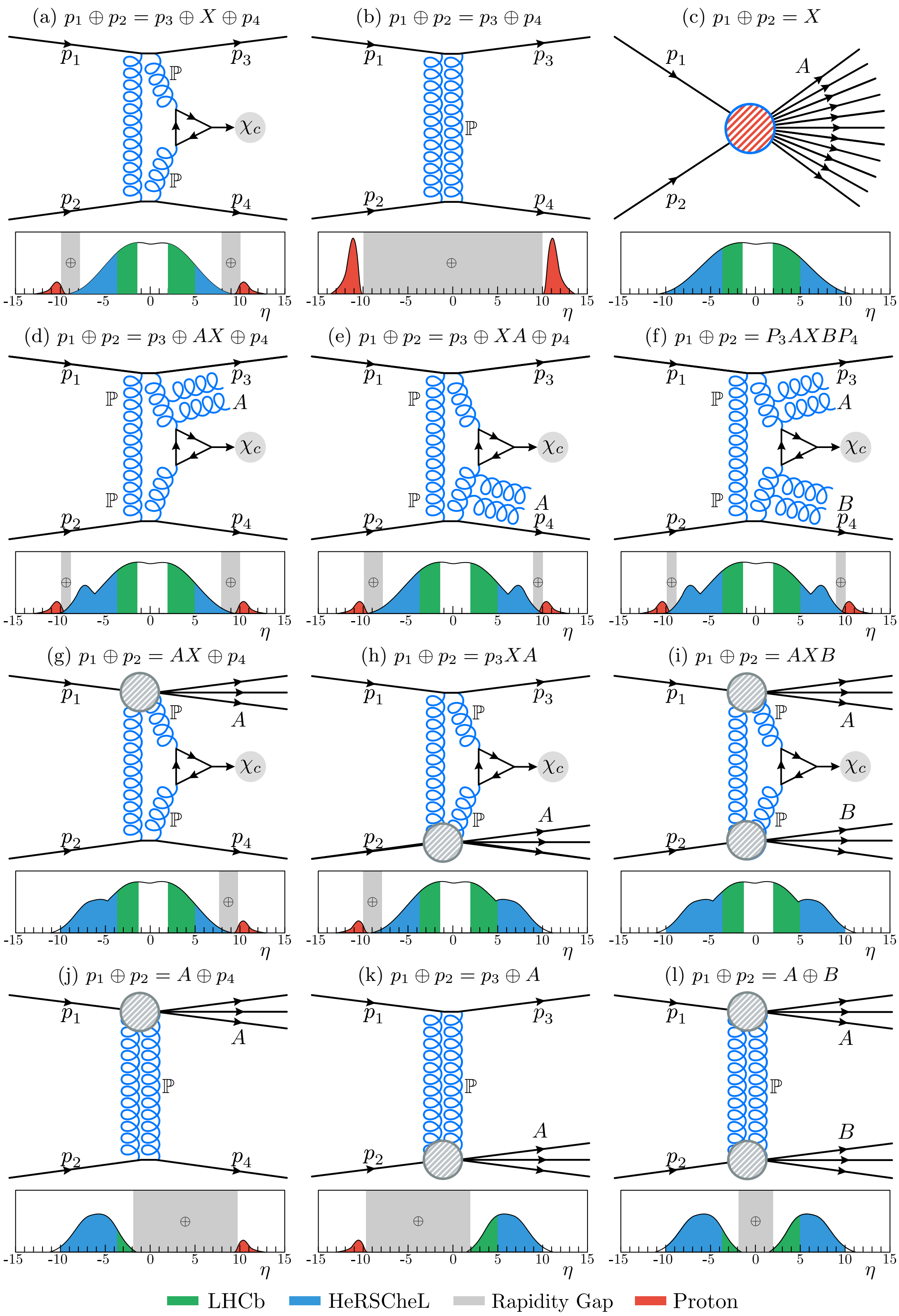

Figure 2.15. Feynman diagrams and pseudorapidity coverage depiction for (a) CEP, (b) proton scattering, (c) hard scattering, (d, e, f) gluon radiation, (g, h) single and (i) double proton dissociation, (j, k) single and (l) double diffraction for double pomeron exchange. The pseudorapidity coverage of the main spectrometer (green), HeRSCheL (blue), intact protons (red), and rapidity gaps (grey) are highlighted.

Table 2.1. Nominal mass and width values for χ_c mesons, as given by the Particle Data Group [86] as well as (J^{CP}) quantum numbers, where I is the isospin, J is the spin, P is the parity and C is the charge-conjugation quantum number, their radiative-decay branching fractions ($\mathcal{B}$) into $\chi_c \to J/\psi\gamma$ and their corresponding mass difference.

Meson	**m(χ_c)** [**MeV/c^2**]	**Width** [**MeV/c^2**]	$I(J^{CP})$	$\mathcal{B}(\chi_c \to J/\psi\gamma)$	$m(\chi_c) - m(J/\psi)$ [**MeV/c^2**]
χ_{c0}	3414.75 ± 0.31	10.8 ± 0.6	$0\ (0^{++})$	1.27 ± 0.06 %	317.85 ± 0.31
χ_{c1}	3519.66 ± 0.07	0.84 ± 0.04	$0\ (1^{++})$	33.9 ± 1.2 %	413.76 ± 0.07
χ_{c2}	3556.20 ± 0.09	1.97 ± 0.09	$0\ (2^{++})$	19.3 ± 0.7 %	459.30 ± 0.09

Events with proton dissociation can come in the form of central-exclusive-inelastic production where a central object is produced alongside proton dissociation, Fig. 2.15 (g–i), or without the production of a central system, Fig. 2.15 (j–l). The latter is characterised by a single large-rapidity gap, which implies an empty detector with signal on either of the HeRSChel modules. Although these events would not be selected directly due to the lack of the central system, they may be selected alongside an elastic CEP event in the presence of pile-up events. As a result, we might wrongly veto an elastic CEP event due to the dissociation of the secondary event. Similarly, elastic CEP events might be wrongly vetoed if accompanied by any secondary pile-up events that leave a signal in the main spectrometer.

2.7 χ_c meson

The χ_c(1P) particles are unstable-hadronic particles known as a meson, which are composed of a quark-antiquark pair. The χ_c(1P) mesons belong to a subset of meson states known as quarkonium, a special case where the quark and antiquark have the same flavour ($q\bar{q}$). In particular, χ_c(1P) mesons are composed of a charm-anticharm quark pair ($c\bar{c}$) and are referred to as charmonium. These characteristics make quarkonium mesons neutral as well as its own anti-particle.

There are three χ_c(1P) mesons, known as χ_{c0}(1P), χ_{c1}(1P), and χ_{c2}(1P), which are close in invariant mass to one another: their masses are 3414.75 ± 0.31, 3519.66 ± 0.07, and 3556.20 ± 0.09 MeV/c^2 respectively, as given by the Particle Data Group [86]. The widths are 10.8 ± 0.6, 0.84 ± 0.04, and 1.97 ± 0.09 MeV/c^2, respectively. In the following, we will refer to these states as χ_{c0}, χ_{c1}, and χ_{c2}, and collectively as χ_c mesons. The nominal values for the invariant mass of the χ_c mesons are summarised in Table 2.1 together with their quantum numbers, the branching fractions of their radiative decay $\chi_c \to J/\psi\gamma$, and the χ_c and J/ψ mass difference.

2.7.1 Quantum numbers

The quarks that make up the χ_c mesons are fermions and have an intrinsic spin of $S = 1/2$. The spins can either be unaligned, forming a spin-0 singlet (*i.e.* vector-length zero with a single-spin projection $S_z = 0$) or the spins can be aligned, resulting in a spin-1 triplet (*i.e.* vector-length one with three possible spin projections, $S_z = -1, 0, 1$). The χ_c mesons are an example of a spin-1 triplet. In addition, χ_c mesons have an orbital-angular-momentum quantum number $L = 1$, which is associated with the angular momentum of their gluon composition. The quantum-number combination of $S = 1$ and $L = 1$ makes the χ_c mesons a set of three $(1P)$ excited-orbital eigenstates of the $c\bar{c}$ system in the QCD potential. These three states are analogous to the three configurations of the p-atomic-electron orbitals. The intrinsic-angular momentum and the orbital-angular momentum can be combined into the total-angular-momentum quantum number J such that it takes any value from $J = |L - S|$ to $J = |L + S|$ in increments of one, inclusive. As a result, χ_{c0}, χ_{c1}, and χ_{c2} mesons have a total-angular-momentum quantum number $J = 0$, $J = 1$, and $J = 2$, respectively.

The parity of the χ_c mesons, a symmetry associated with the sign change of spacial coordinates, is given by $P = (-1)^{L+1} = +1$ (P-even). The charge-conjugate quantum number, a symmetry under the exchange of quantum charges, is $C = +1$ (C-even) such that $|c\bar{c}\rangle = |\bar{c}c\rangle$. Quarkonium systems are also known as flavourless states, since all their quantum numbers associated with flavour are zero (strangeness $S = 0$, charm $C = 0$, bottomness $B = 0$, and topness $T = 0$), which have an isospin $I = 0$ as they have no u-quark or d-quark content. By convention, the notation $I(J^{CP})$ is used to summarise the quantum number of states, as detailed in Table 2.1. Mesons with $J^P = 0^+$, 1^+ and 2^+ such as χ_{c0}, χ_{c1}, and χ_{c2} are known as scalar mesons, pseudovector mesons, and tensor mesons respectively.

2.7.2 χ_c states as a CEP standard candle

As mentioned previously, CEP is a theoretically challenging process sensitive to non-perturbative soft effects, higher-order corrections, and PDF uncertainties. Therefore, it is essential to test our theoretical models, to set a benchmark for new searches and measurements of more exotic systems, and establish this field of study at the LHCb experiment. Naturally, low-mass objects have the largest cross-sections and are easier to access experimentally. In addition, the contribution of soft corrections becomes less significant and the use of perturbative QCD becomes justified when the hard scale is sufficiently high, $\mu \sim m_X \gg Q_T$, and the calculations become infrared stable. The hard-scale for χ_c mesons is approximately $\mu = m_{\chi_c} \sim 3.5\,\text{GeV}$ and sits at the border of the perturbative limit. In addition, the different χ_c states give us access to different J_z^P states and, as a result, the angular distributions of the forward protons and information about the violation of the $J_z = 0$ spin selection rule. This makes the χ_c meson an ideal candidate against which to test our theoretical models for the DPE CEP channel, and consequently is often regarded as the *standard candle* for this mechanism.

2.7.3 χ_c radiative decays

The $J/\psi(1S)$ particle is a neutrally charged $c\bar{c}$ vector meson, making it the second lightest charmonium state after the η_c meson. The J/ψ meson was simultaneously discovered at SLAC and Brookhaven National Laboratories, granting it its unique two-part name. It has a $3096.900 \pm 0.006\,\text{MeV}/c^2$ mass, as given by the Particle Data Group [86], isospin $I = 0$, a total angular momentum $J = 1$, odd parity $P = -1$, and odd charge conjugation $C = -1$, such that

$I(J^{CP}) = 0(1^{--})$. It can decay through either annihilation, or weakly through flavour-changing interactions. As a result, the J/ψ meson is a relatively long-lived particle with a narrow width of $92.9 \pm 2.8\,\text{keV}/c^2$ [86].

Of particular interest to this analysis is the decay of the J/ψ meson into a pair of muons which have a branching fraction of $(5.961 \pm 0.0033)\%$. The CEP of J/ψ mesons has been studied at LHCb through this decay mode together with its excited state $\psi(2S)$ [43, 44]. $\psi(2S)$ is another quarkonium state that shares the same quantum numbers as J/ψ, has an invariant mass of 3686.10 ± 0.06 MeV/c^2 and a width of 294 ± 8 MeV/c^2. Although J/ψ mesons can also decay into an electron pair with a similar branching fraction, $(5.971 \pm 0.032)\%$, the penetrating power of muons makes them easier to identify, they have low background, and tend to be better measured than their electron counterparts as they are less susceptible to energy loss through bremsstrahlung radiation.

χ_c mesons can decay to a J/ψ meson through radiative decay, $\chi_c \to J/\psi\gamma$. The branching fractions to $J/\psi\gamma$ for χ_{c0}, χ_{c1}, and χ_{c2} are $1.27 \pm 0.06\%$, $33.9 \pm 1.2\%$, and $19.3 \pm 0.7\%$ [87]. Given the experience with the study of J/ψ mesons through the dimuon decay, as well as the benefits listed above, this study will focus on the reconstruction of the intermediate J/ψ meson through the dimuon decay. In addition, the well-understood CEP and inelastic production can be easily used to measure the efficiency of the HeRSChel detector as described in Sec. 5.6.

Unfortunately, as will be shown in Sec. 4.1.3, the invariant-mass resolution in LHCb of $\chi_c \to J/\psi\,[\mu^+\mu^-]\gamma$ mesons reconstructed with calorimetric photons (*i.e.* photons that have not undergone pair production, $\gamma \to e^+e^-$) is inadequate to cleanly resolve χ_{c1} and χ_{c2} states, which have means separated by approximately 50 MeV/c^2. However, separation can be achieved through the use of converted photons, $\gamma \to e^+e^-$. This improves the invariant-mass resolution of the χ_c mesons significantly, making the separation of the resonances possible. As a result, this study will focus on the following decay:

$$\chi_c \to J/\psi\,[\mu^+\mu^-]\gamma[e^+e^-]. \tag{2.42}$$

2.8 Previous measurements

2.8.1 CDF II at Tevatron

The CEP of χ_c mesons was first observed in the Collider Detector at Fermilab II (CDF II) detector at the Tevatron, a proton-antiproton collider [42, 88]. CDF was a general-purpose detector with a wide rapidity coverage []. The central barrel had a pseudorapidity coverage of $|\eta| < 5.1$. In addition, CDF was equipped with scintillating pads along the beam line on both sides of the interaction point, extending the coverage to include $5.4 < |\eta| < 7.4$. These pads were designed to detect particle showers at high rapidities originating from proton dissociation. Finally, one side of the detector was equipped with a proton tagger, allowing for the direct detection of one of the emerging protons. The large rapidity coverage, and the ability to identify proton fragmentation, made CDF an excellent experiment with which to study CEP.

The CEP of χ_c mesons was studied in proton-antiproton collisions at centre-of-mass energies $\sqrt{s} = 1.96\,\text{TeV}$ in the $|\eta| < 0.6$ pseudorapidity region through its radiative decay into $J/\psi\gamma$. This subset of the central barrel is instrumented with a tracking system and a drift chamber used to measure the muons from the $J/\psi \to \mu^+\mu^-$ decay. The cross-section was measured with an effective integrated luminosity of $\mathcal{L}_{\text{eff}} = 139 \pm 8\,\text{pb}^{-1}$, accounting for the percentage of bunch crossing with more than one interaction. Unfortunately, the invariant-mass resolution was not high enough to resolve the contributions of each of the χ_c states. The contributions of χ_{c1} and χ_{c2} were taken to be negligible due to the suppression associated with the $J_z = 0$ spin-selection rule described in Chapter 3. Taking χ_{c0} as the only contribution, the cross-section was measured to be $\frac{d\sigma}{dy}|_{y=0}(\chi_{c0}) = 76 \pm 10 \pm 10\,\text{nb}$, where the first uncertainty is statistical and the second is systematic. These results were found to be in agreement with an adjusted theoretical prediction of 90 nb, as described in [42]. The measured cross-section and theoretical predictions are detailed in Table 2.2 together with other results.

2.8.2 LHCb at CERN

Two preliminary CEP χ_c analyses were performed at the LHCb experiment at CERN: one with *pp* data collected during 2010 and another with *pp* data collected during 2011. The LHCb detector, described in great detail in Chapter 3, is a single-arm forward spectrometer fully instrumented in the pseudorapidity range $2 < \eta < 5$. In 2015, LHCb was equipped with a set of scintillating modules that are sensitive to high-rapidity showers from particles originating in proton dissociation, extending the rapidity coverage of LHCb up to $\eta < 10$.

The first $\chi_c \to J/\psi\,[\mu^+\mu^-]\gamma$ analysis at LHCb was performed using *pp* collisions at a centre-of-mass energy $\sqrt{s} = 7\,\text{TeV}$ collected during 2010, exploiting a total integrated luminosity of $37\,\text{pb}^{-1}$ [89]. For this analysis, the photon and the dimuon from the J/ψ decay were required to be within the acceptance of LHCb's main spectrometer $2 < \eta < 4.5$. In this case, the mass resolution is sufficiently good to distinguish the contributions of each χ_c state but not good enough to obtain full resonant separation. The invariant-mass distribution of the $J/\psi\gamma$ system, shown in Fig. 2.16 (left), is fitted using shapes extracted from SuperChic Monte Carlo. An additional shape (yellow) is added to account for background from $\psi(2S)$ *feed-down*, backgrounds where the decay chains of heavier particles may contain the final-state particles of the signal-decay mode. This background was simulated using StarLight [90, 91], a Monte Carlo simulator specialised in ultra-peripheral collisions mediated via two-photon or photonuclear interactions. A single exclusive purity of 0.39 ± 0.13 is calculated for the entire sample by fitting the transverse momentum of the χ_c candidates, thus taking advantage of the lower transverse momentum of CEP compared to inelastic processes. The cross-section-times-branching-fraction is determined to be $(9.3 \pm 4.5)\,\text{pb}$, $(16.4 \pm 7.1)\,\text{pb}$, and $(28.0 \pm 12.3)\,\text{pb}$ for χ_{c0}, χ_{c1} and χ_{c2}, respectively. These are slightly higher than the SuperChic calculations of 4 pb, 10 pb, and 3 pb quoted in the study, which have an uncertainty factor of 4 to 5 [71].

A second preliminary analysis was performed at LHCb, which repeated the previously mentioned measurement with a larger statistical sample corresponding to a total effective integrated luminosity of $222.3\,\text{pb}^{-1}$, collected during 2011 for pp collisions at a centre-of-mass energy of $\sqrt{s} = 7\,\text{TeV}$ [92]. The analysis was performed with the same acceptance criteria. The invariant-mass distribution of the $J/\psi\gamma$ system in Fig. 2.16 (right) together with the *pulls* shown in the lower panel. The pull is given by the ratio of data (d) minus the value given by the total fit (f) to the statistical uncertainty of the data (σ), *i.e.* $(d - f)/\sigma$. This analysis measured a cross-section-times-branching-fraction of $(2.2 \pm 3.0)\,\text{pb}$, $(4.3^{+7.6}_{-9.2})\,\text{pb}$, and $(25.0^{+7.1}_{-9.2})\,\text{pb}$ for χ_{c0}, χ_{c1} and χ_{c2}, respectively: fitting the transverse momentum of the dimuon system, a purity of $23.8 \pm 3.3\%$ is found. Both sets of results suggest there is an enhancement of the χ_{c2} relative to the production of χ_{c1}, in contrast to the expected theoretical hierarchy. However, the cross-section measurements of χ_{c2} are consistent with the theoretical calculations given the large uncertainties. This enhancement can result from the difficulties associated with the invariant-mass and transverse-momentum fits necessary to determine the contribution of the inelastic background and the CEP signal. The experimental and theoretical results for these two analyses are summarised in Table 2.2.

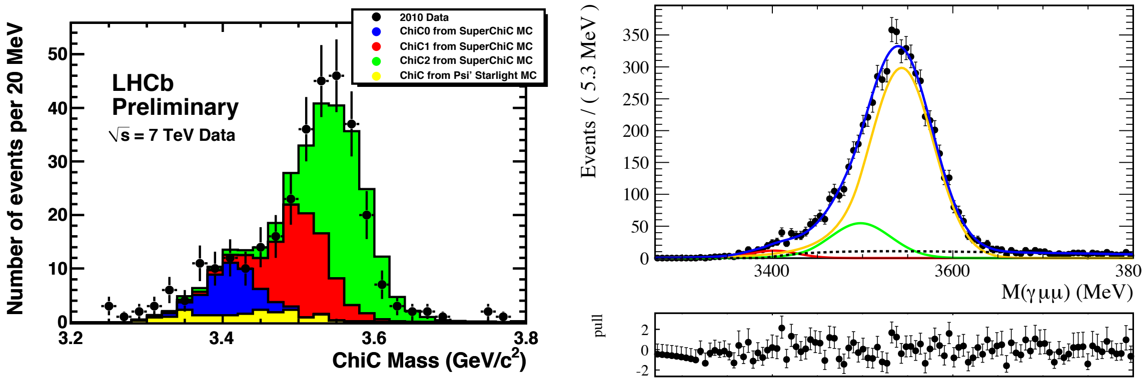

Figure 2.16. Invariant-mass distribution of $\chi_c \to J/\psi\,[\mu^+\mu^-]\gamma$ candidates from pp collisions at a centre-of-mass energy $\sqrt{s} = 7\,\text{TeV}$, from data collected in 2010 (left) and 2011 (right) at the LHCb experiment. Reproduced from Ref. [89] and Ref. [92], respectively. The signal contribution of the latter are shown with solid lines for χ_{c0} (red), χ_{c1} (green), χ_{c2} (yellow) while the background is drawn with a dashed black line, and the total fit is shown in blue. The lower panel shows the pulls relative to the total fit.

Table 2.2. Cross-section measurements for $\chi_c \to J/\psi\,[\mu^+\mu^-]\gamma$ CEP conducted in CDF II at Fermilab Tevatron at a centre-of-mass energy $\sqrt{s} = 1.96\,\text{TeV}$ in proton-antiproton [71, 88] and cross-section-×-branching-fraction at the LHCb experiment with a centre-of-mass energy $\sqrt{s} = 7\,\text{TeV}$ for *pp* collisions collected during 2010 [89] and 2011 [92], as well as theoretical predictions calculated with SuperChic (SC) quoted in each of the analysis [71].

Meson	$\sqrt{s}$ **[TeV]**	η	$\sigma(\chi_{c0})$	$\sigma(\chi_{c1})$	$\sigma(\chi_{c2})$
CDF II	1.96	$-0.6 - 0.6$	$76 \pm 10 \pm 10$ nb	-	-
SC	1.96	$-0.6 - 0.6$	90 nb	-	-
Meson	$\sqrt{s}$ **[TeV]**	η	$\mathcal{B} \times \sigma(\chi_{c0})$	$\mathcal{B} \times \sigma(\chi_{c1})$	$\mathcal{B} \times \sigma(\chi_{c2})$
LHCb 2010	7	$2 - 4.5$	9.3 ± 4.5 pb	16.4 ± 7.1 pb	28.0 ± 12.3 pb
LHCb 2011	7	$2 - 4.5$	2.2 ± 3.0 pb	$4.3^{+7.1}_{-9.2}$ pb	$25.0^{+7.9}_{-9.2}$ pb
SC	7	$2 - 4.5$	14 pb	9.8 pb	3.3 pb

Chapter 3

LHCb detector

Situated on the Franco-Swiss border at the European Organisation for Nuclear Research (CERN), the Large Hadron Collider (LHC) [93] is the world's largest and most powerful particle accelerator, designed to collide protons, pp, at a centre-of-mass energy of $\sqrt{s} = 14\,\text{TeV}$ and luminosity of $1 \times 10^{34}\,\text{cm}^{-2}\,\text{s}^{-1}$. Protons from ionised hydrogen are accelerated through multiple stages of CERN's accelerator complex, a schematic of which is shown in Fig. 3.1. In the final stage of the acceleration the protons are split into two counter-rotating beams and injected into the LHC at an energy of 450 GeV where they are accelerated to the desired collision energy by eight 400 MHz superconducting-radiofrequency cavities cooled to 4.5 K with superfluid helium. To achieve high-luminosity conditions, up to 2808 proton bunches are injected into the LHC storage rings each with $\sim 1.2 \times 10^{11}$ protons. The beams are steered around the 26.7 km ring with 1232 superconducting copper-clad niobium-titanium dipole magnets and focused with 392 quadrupoles. The beams are crossed at four interaction points where the major LHC experiments are located: A Toroidal LHC ApparatuS (ATLAS), Compact Muon Solenoid (CMS), A Large Ion Collider Experiment (ALICE), and the Large Hadron Collider beauty experiment (LHCb).

So far the LHC has had two main periods of operation: Run 1 and Run 2. Run 1, which took place between 2010 and 2012 collisions, occurred at centre-of-mass energies of $\sqrt{s} = 7$ and 8 TeV. In Run 2, which took place between 2015 and 2018, the collision energy was $\sqrt{s} = 13$ TeV.

3.1 LHCb Experiment

LHCb [95, 96] is a single-arm forward spectrometer designed to study heavy-flavour physics through the decay of beauty and charm hadrons. A schematic of LHCb is shown in Fig. 3.2. LHCb adopts a right-handed coordinate system centred on the nominal-interaction point where the positive z-axis points down the beam-line, in the direction of the spectrometer, and the y-axis points upward. In proton collisions b quarks are dominantly produced via gluon fusion. It is stochastically favourable for these interacting gluons to have asymmetric momentum. Therefore, the $b\bar{b}$ pair is boosted along the beam-line. As a result, the main spectrometer is built in a forward direction with a pseudorapidity coverage of $2 < \eta < 5$. Figure 3.3 shows the

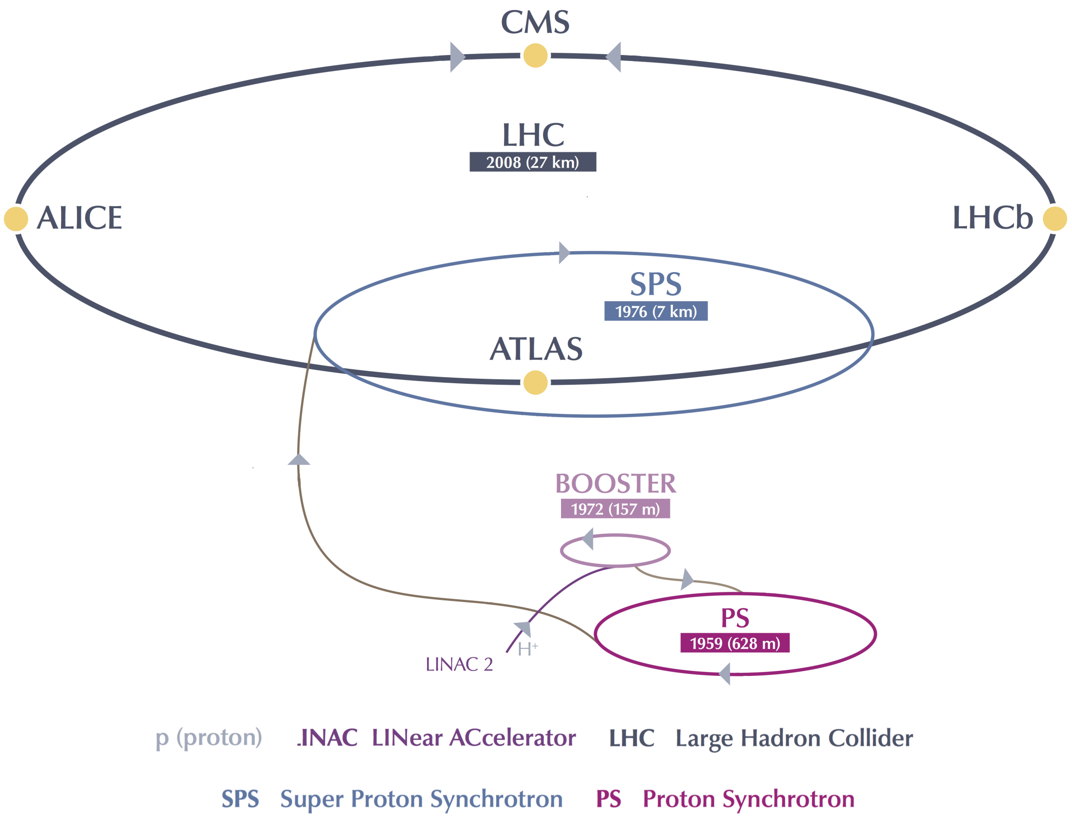

Figure 3.1. Schematic diagram of CERN's accelerator complex. Reproduced from Ref. [94]

relative production cross-section of the produced $b\bar{b}$ pairs as a function of the polar angle of each quark, where the coverage of the LHCb experiment is highlighted in red.

The LHCb main spectrometer is equipped with a number of sub-detectors including the VErtex LOcator (VELO), two Ring Imaging CHerenkov detectors (RICH1 and RICH2), the Tracker Turicensis (TT), the dipole magnet, the inner and outer tracking stations (T1-T3), the Scintillating Pad Detector (SPD), the PreShower (PS), the Electromagnetic CALorimeter (ECAL), the Hadronic CALorimeter (HCAL), and the muon stations (M1-M5) [95, 97]. The sub-detectors are discussed briefly in the following sections. In addition, the HeRsChel detector, a set of forward-scintillating counters designed to increase the coverage of the LHCb experiment, was installed in 2015. This detector will be described in detail in Sec. 3.8.

During the first period of operation (Run 1), from 2010 to the end of 2012, LHCb collected 1.1 fb^{-1} of proton-proton (pp) collisions at $\sqrt{s} = 7\,\text{TeV}$ and 2.1 fb^{-1} at $\sqrt{s} = 8\,\text{TeV}$. During the second period of operation (Run 2), from 2015 to the end of 2018, LHCb collected 5.9 fb^{-1} of pp collisions at $\sqrt{s} = 13\,\text{TeV}$. The LHCb integrated luminosity for pp collisions is summarised in Fig. 3.4. The analysis presented in this thesis uses 2015 and 2016 data corresponding to $1921 \pm 38\,\text{pb}^{-1}$ of integrated luminosity. This data set is chosen for the capabilities provided by the newly installed HeRSChel system.

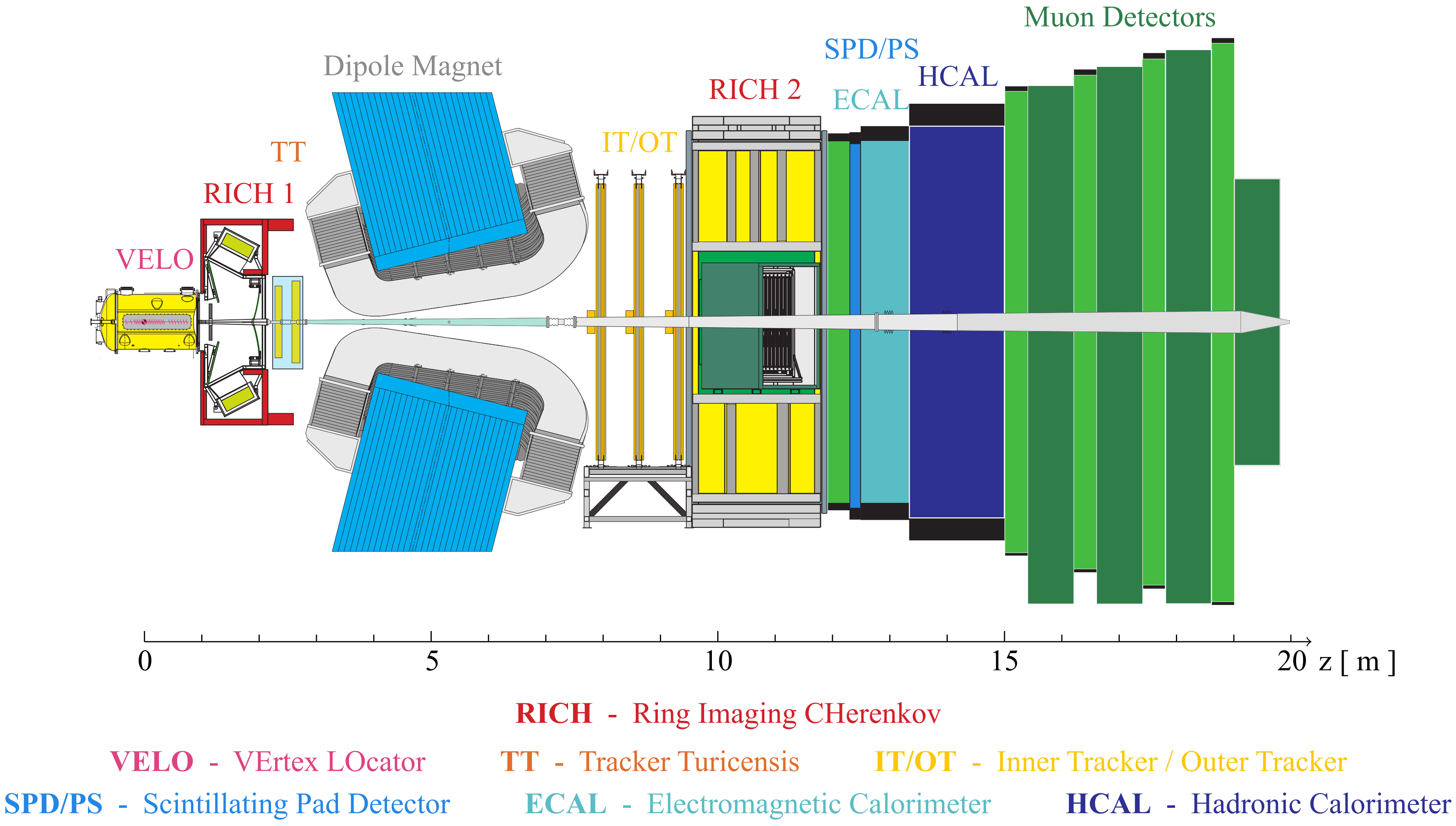

Figure 3.2. Vertical cross–section schematic of LHCb experiment. Reproduced from Ref. [96].

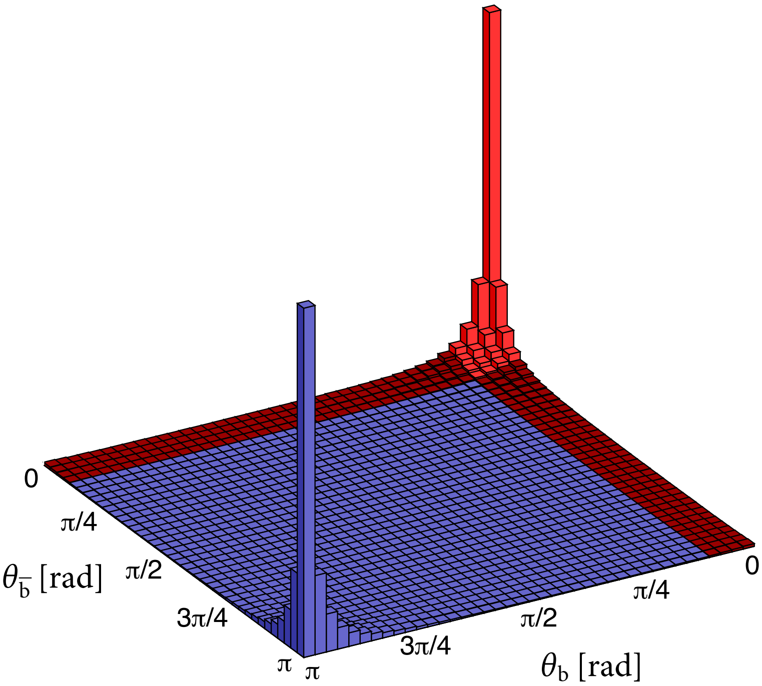

Figure 3.3. Simulation of the relative cross-section of $b\bar{b}$ pair production in pp collisions at $\sqrt{s} = 8\,\text{TeV}$ as a function of the angle between the quark trajectories and the z-axis, θ_1 and θ_2. The LHCb acceptance is highlighted in red. Reproduced from Ref. [98].

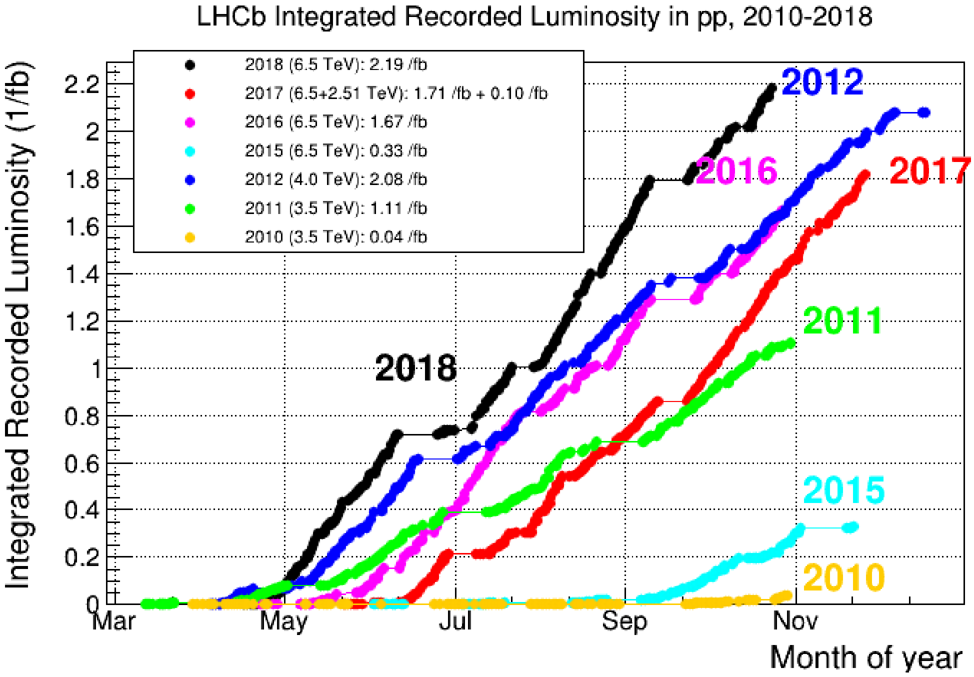

Figure 3.4. LHCb integrated luminosity for pp collisions for 2010 to 2018 runs. Reproduced from Ref. [99].

3.2 Vertex Locator (VELO)

The VELO is the detector closest to the pp interaction point [100, 101]. It uses 21 semicircular-silicon-strip stations distributed along the z-axis to measure the coordinates of energy deposits left by charged particles in order to reconstruct their associated tracks, and from these their production and decay vertices. Figure 3.5 shows the layout of the VELO, which makes clear the positioning of modules relative to the nominal interaction point.

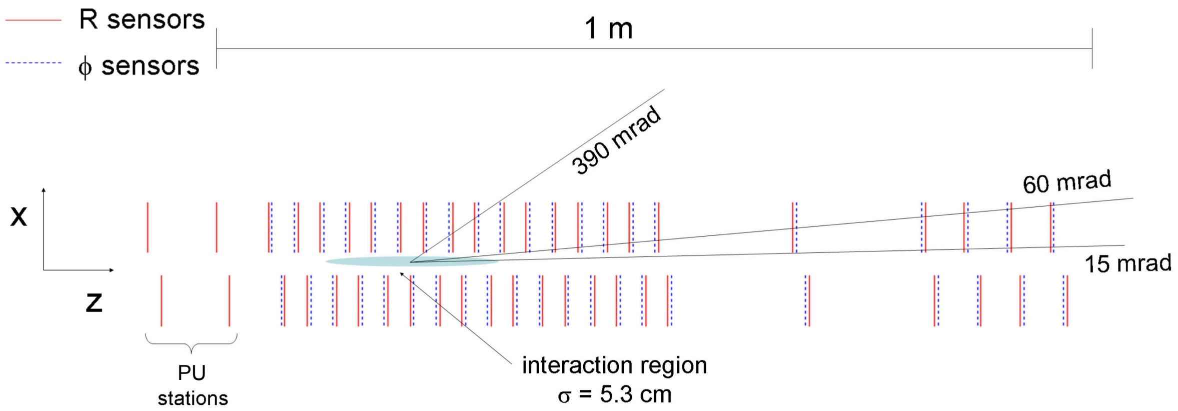

Figure 3.5. Schematic showing the cross-section of the VELO sub-detector and the pile-up system along the $y = 0$ plane showing the position of the silicon-strip modules along the z-axis. The R sensors are depicted in red and ϕ sensors are depicted in blue. Reproduced from Ref. [95].

Each of the modules consists of two sensors, as shown in Fig. 3.6, one with a concentric pattern used to measure the radial distance from the beam (R sensor) and one with a radial pattern designed to measure the azimuthal angle (ϕ sensor) of the track. The VELO provides a forward ($\eta > 0$) coverage of $1.6 < \eta < 4.9$ and a backward ($\eta < 0$) coverage of $-3.5 < \eta < -1.5$ in pseudorapidity.

B mesons, have a typical flight distance of $\mathcal{O}(10)$ mm. Thus, LHCb needs to be able to resolve secondary vertices with high accuracy and precision. To achieve this, the VELO sensors are placed 8.2 mm away from the beam-line during data collection. The VELO is capable of tracking particles with a 10 μm resolution in the perpendicular direction to the beam-line and 50 μm in the parallel direction. The primary vertex resolution as a function of number of tracks, and the impact parameter as a function of $1/p_T$, is shown in Fig. 3.7 for the x-axis and y-axis. Here the impact parameter is defined as the transverse distance of closest approach between the track and its associated primary vertex.

The silicon sensors are placed inside a 0.3 mm thick vacuum-aluminium enclosure, known as the Radio Frequency foil (RF foil). This provides shielding against RF pick-up from the beams while protecting the beams' vacuum from VELO outgassing. The foil is corrugated to allow the sensors to overlap, eliminating inactive detector gaps. To minimise radiation damage,

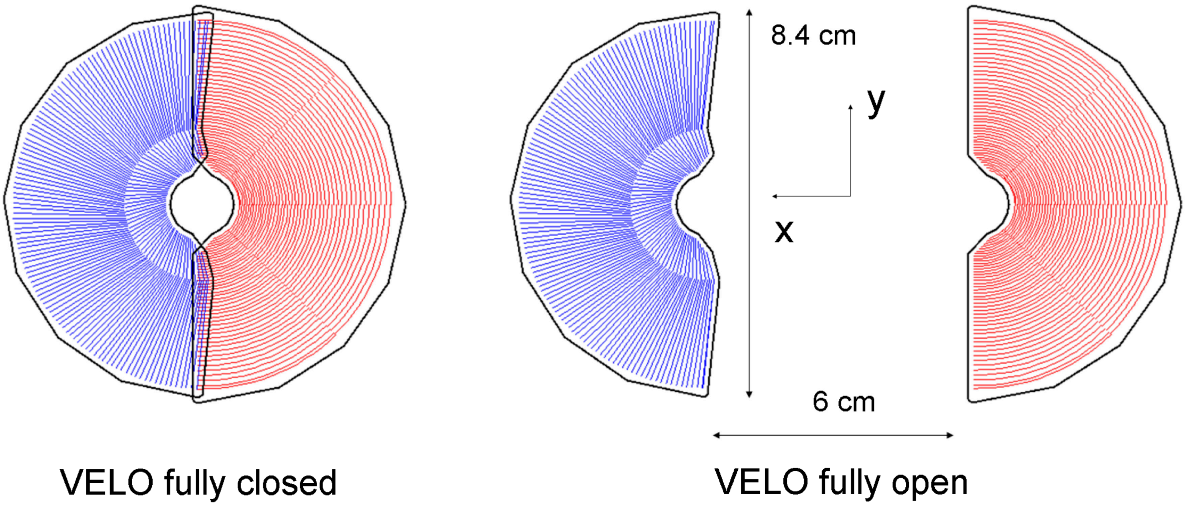

Figure 3.6. Schematic showing the silicon-strip modules in their closed (left) and open position (right). The R sensors are depicted in red and ϕ sensors are depicted in blue. Reproduced from Ref. [95].

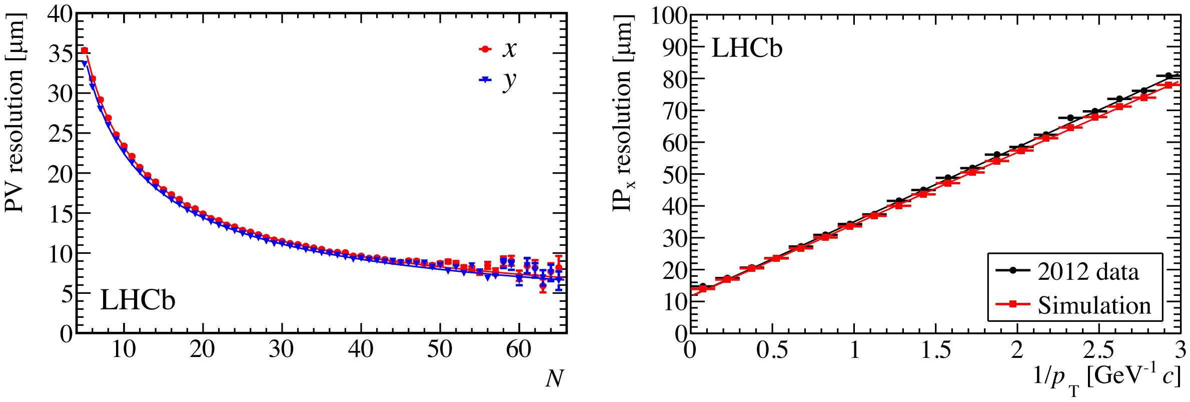

Figure 3.7. Primary vertex resolution as a function of track multiplicity (left) for the x-axis (red) and y-axis (blue) for 2012 data. Impact parameter resolution as a function of $1/p_T$ (right) for 2012 data (data) and Monte Carlo (red). Reproduced from Ref. [97].

the vertex modules are retracted to a position 35 mm away from the beam during injection and periods of unstable beam and kept at $-30\ °C$ with liquid CO_2.

In addition to the 21 stations that compose the main VELO detector, there are two modules upstream of the VELO equipped only with R sensors that constitute the pile-up (PU) system which is used to detect backwards tracks and estimate the number of interactions per bunch crossing. These upstream stations are used to reject backwards tracks during the selection of CEP candidates.

3.3 Dipole magnet

LHCb employs a dipole magnet [102] to curve charged particles in the horizontal plane to allow for the measurement of momentum from each track's radius of curvature. The magnet is made from two water-cooled, non-superconducting, aluminium coils shaped as a trapezoid. The magnet is aligned with the acceptance of the spectrometer and held in a wedge configuration by a 1600 tonne window-frame iron yoke, shown in Fig. 3.2 and Fig. 3.8.

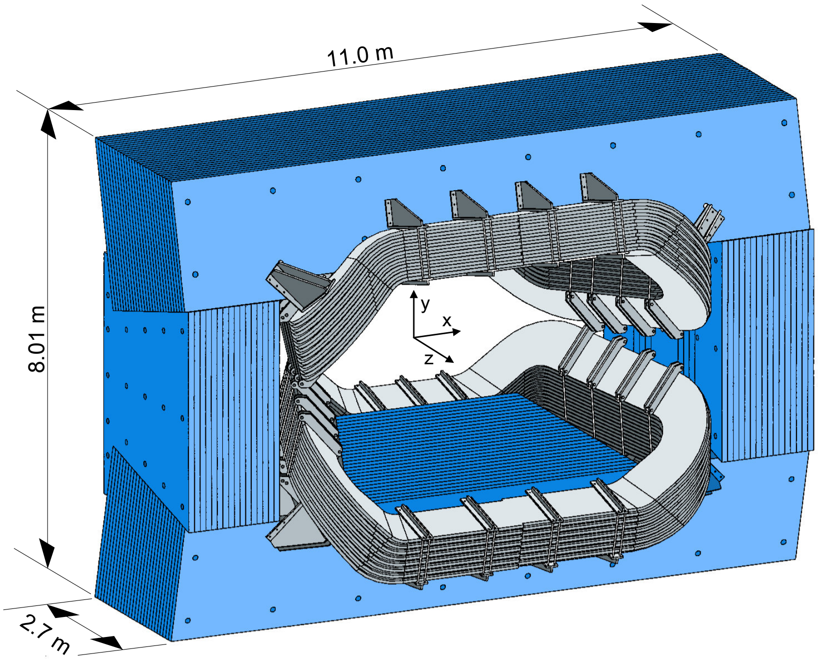

Figure 3.8. Perspective upstream view of the dipole magnet (grey) and yoke (blue). Reproduced from Ref. [102].

The magnet's integrated field is 4 Tm for a 10 m track. To improve the performance of the tracking stations, both immediately before and after the magnet, the dipole is aligned with the spectrometer with a precision of 1 mm and the magnetic field is known with a precision of 1×10^{-4}. The performance of the VELO and RICH detectors is sensitive to external magnetic fields. Straight tracks in the VELO allow for better vertex reconstruction and event triggering. Similarly, the image in the RICH photon detectors are distorted by the presence of a magnetic field. For this reason, not only do both detectors have magnetic shielding but the magnet is designed such that the magnetic field is minimal where these detectors are instrumented and stronger near the tracking stations, see Fig. 3.9.

The CP-violation studies at the LHCb experiment are sensitive to systematic biases from charge asymmetries in the detector. Since positive and negative particles bend in opposite directions within a magnetic field, the polarity of the magnet is periodically inverted to reduce any detector biases.

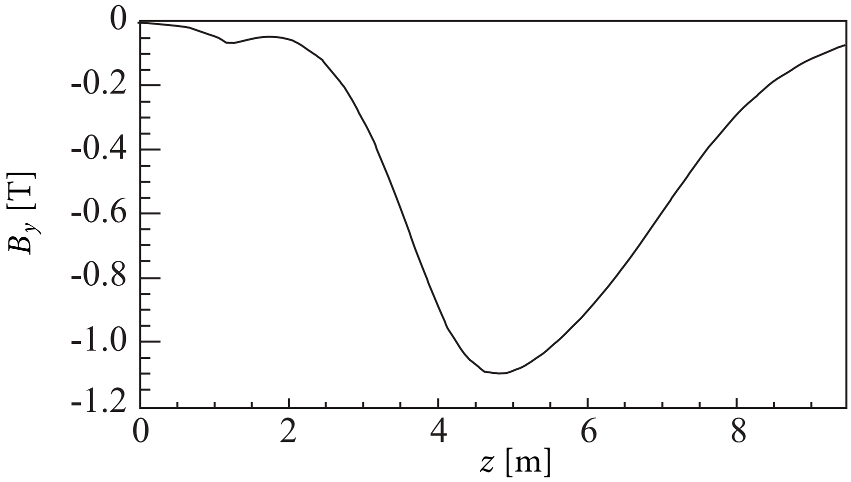

Figure 3.9. The y-component of the dipole-magnetic field as a function of distance along the z-axis of the detector. Reproduced from Ref. [97].

3.4 Tracking system

The LHCb tracking system relies on the VELO, the Tracker Turicensis (TT), dipole magnet and Tracking stations (T1–T3) to map the spatial trajectory of charged particles and measure their momentum.

3.4.1 Tracker Turicensis

Located immediately before the dipole magnet, the TT is composed of four layers of silicon micro-strip sensors with a single-hit spatial resolution of 50 μm that spans the acceptance of the spectrometer. The two inner layers are offset by $-5°$ and $+5°$ relative to the vertical along the x-y plane to provide a *stereo angle* to give some sensitivity to the y-coordinate. A schematic of the third station is shown in Fig. 3.10 (left) illustrating this angular shift. The detector

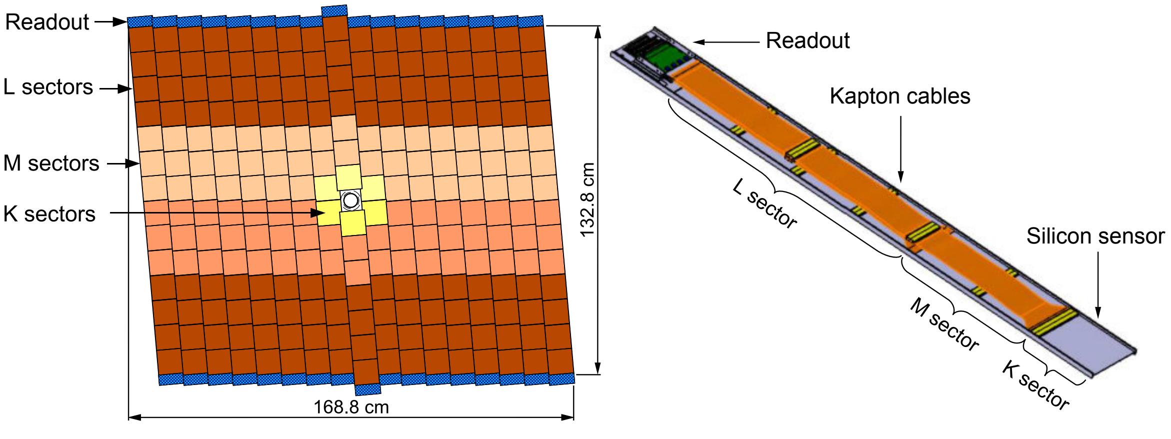

Figure 3.10. Schematic of the third layer of the TT (left). The readout electronics are highlighted in blue, the L sector in brown, the M sector in beige, and the K sector in yellow. A close up schematic of a single TT module (right). Reproduced from Ref. [95].

layers are bifurcated horizontally, and composed of seventeen modules with seven silicon sensors each. The modules closest to the beam-line are separated into three sectors to accommodate for high-track densities, sector L, M, and K. All other modules are separated into two sectors only, sectors L and M. The readout electronics are located at the end of each of the modules. Fig. 3.10 (right) shows the schematic of a module located close to the beam-line. To reduce inactive areas the modules are staggered with an overlap of one centimetre.

3.4.2 Tracking stations

Three Tracking stations (T1-T3) are located immediately after the dipole magnet. To account for the higher track density near the beam-line, each of these stations is separated into an Inner Tracker (IT) instrumented with the same crossed-silicon micro strips as the TT, and an Outer Tracker (OT) instrumented with drift-tube detectors. Each station is composed of four layers with the two internal layers rotated by -5° and $+5^\circ$ with respect to the vertical axis, and overlapping adjacent modules by 4 mm in the z direction and 3 mm in the x direction. Similar to the TT, this increases the sensitivity of the detector in the y-coordinate. The layout of one of the tracking stations is shown in Fig. 3.11 (left) together with a close up of the IT (right). Reproduced from Ref. [103].

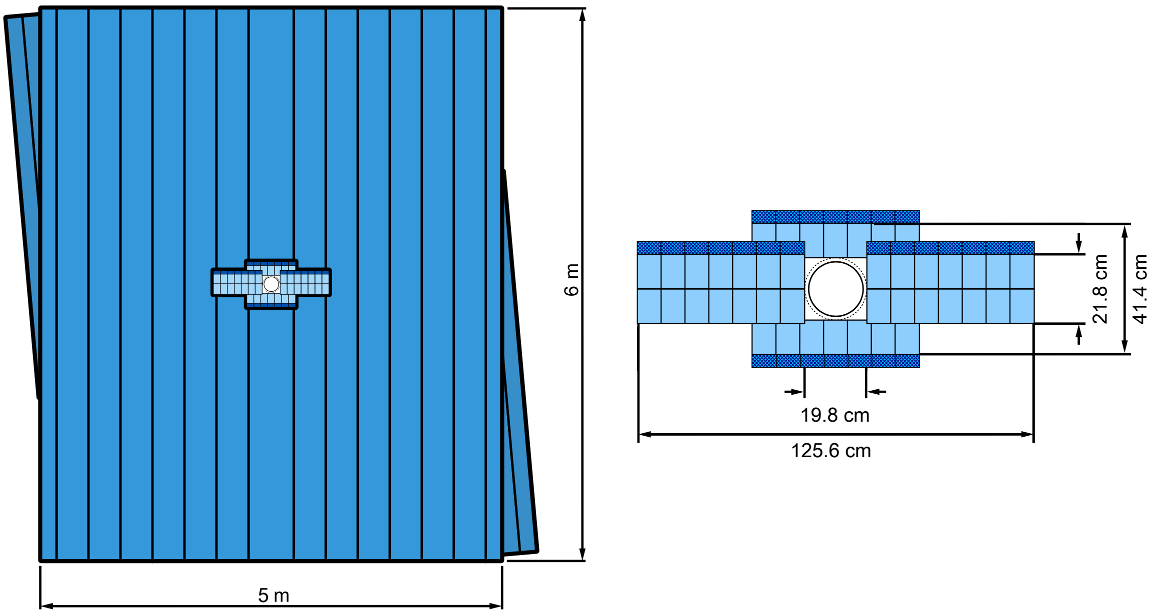

Figure 3.11. Schematic of the Outer Tracker (left) and close up of the Inner Tracker (right). Reproduced from Ref. [95].

Each module of the OT is composed of two layers of the drift-tube detectors filled with a gas mixture composed of 70% argon, 28.5% carbon dioxide and 1.5% oxygen. The OT shares the same four-layer arrangement as the IT, has a drift-coordinate resolution of 200 μm, and a momentum resolution of $\delta p/p \approx 0.4\%$. The track reconstruction procedure is discussed further in Sec. 3.10.1.

3.5 Particle identification

Particle identification (PID) is fundamental for the study of physics involving hadronic decays. Two Ring-Imaging CHerenkov detectors (RICH1 and RICH2) [104] provide charged–particle identification, mainly used to discriminate between kaon, pion, and proton candidates. When a particle passes through a material with refractive index $n > 1$, also known as a radiator, at a velocity (v) greater than the phase velocity of light in the material, it emits a cone of photons known as Cherenkov radiation. These detectors measure the angle of emission of Cherenkov photons (θ_c) defined in Fig. 3.12. The velocity of the particle can then be determined by

$$v = \frac{c}{n\cos(\theta_c)} \ , \tag{3.1}$$

where c is the speed of light in vacuum. The velocity is then combined with the momentum measurement extracted from the radius of curvature of the tracks to determine the mass hypothesis of the particle.

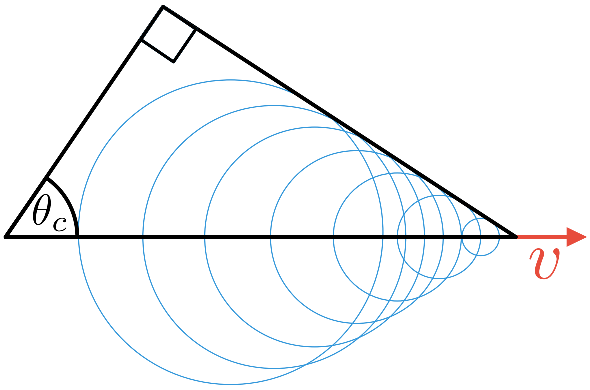

Figure 3.12. The geometry of Cherenkov radiation. The red arrow depicts the velocity of the particle and the blue rings depict the formation of the Cherenkov cone.

Both RICH1 and RICH2 use concave mirrors to focus the Cherenkov rings onto a flat mirror that reflects them onto two layers of Hybrid Photon Detectors (HPD) on either side of the opening window. The HPD are sensitive in the 200 to 600 nm wavelength and enclosed in mu-metalt to reduce magnetic-field distortions. RICH1 is built in a vertical configuration while RICH2 is built in a horizontal configuration, as indicated in Fig. 3.13.

Three different radiator materials are used to provide mass-hypothesis discrimination capabilities across a wide momentum range. Located before the magnet, RICH1 is equipped with an aerogel and C_4F_{10} radiators resulting in optimal performance in the $1 - 60\,\text{GeV}/c$ momentum range. The aerogel radiator, however, was removed before the start of Run 2, a change that only had consequences for very low momentum PID. Since low-momentum particles tend to have larger polar angles, RICH1 has the full coverage of the LHCb acceptance. Conversely, RICH2 is located after the bending magnet and uses a CF_4 radiator optimised for the $50 - 100\,\text{GeV}/c$

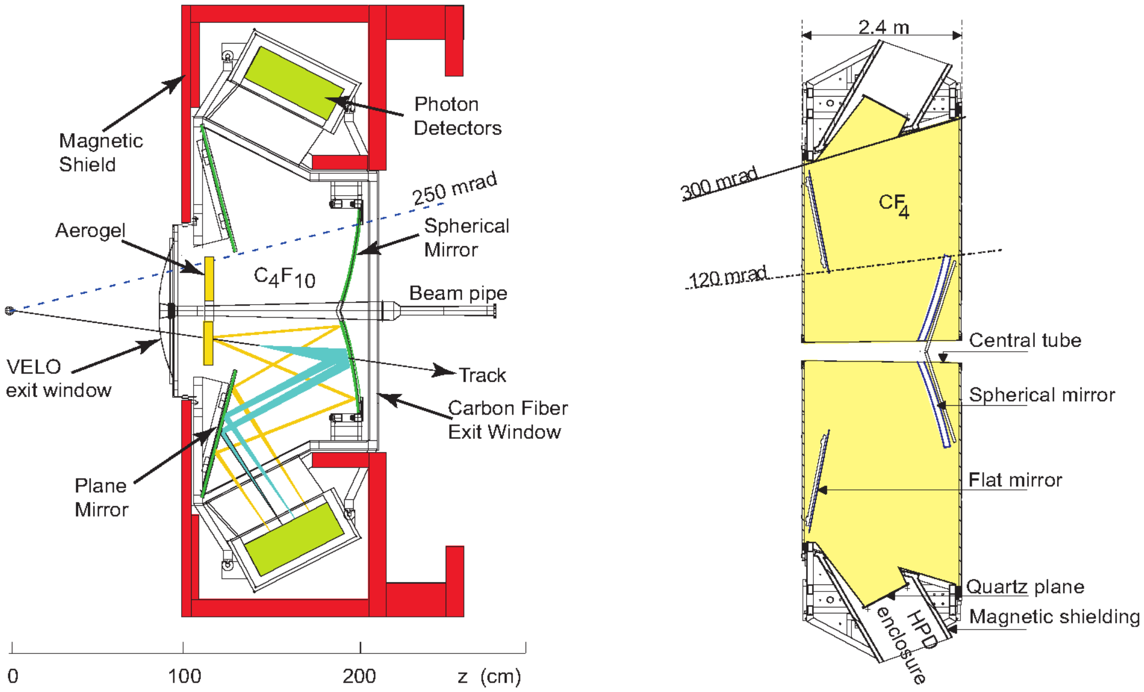

Figure 3.13. Side schematics view of RICH1 (left) and top schematic view of RICH2 (right). Reproduced from Ref. [95].

momentum range and has an acceptance of ±25 mrad to ±300 mrad in the horizontal and ±2500 mrad in the vertical.

Figure 3.14 shows the calculated Cherenkov angle as a function of momentum for the different radiating materials used at LHCb (left) as well as the reconstructed distribution for the C_4F_{10} radiator in RICH1 (right).

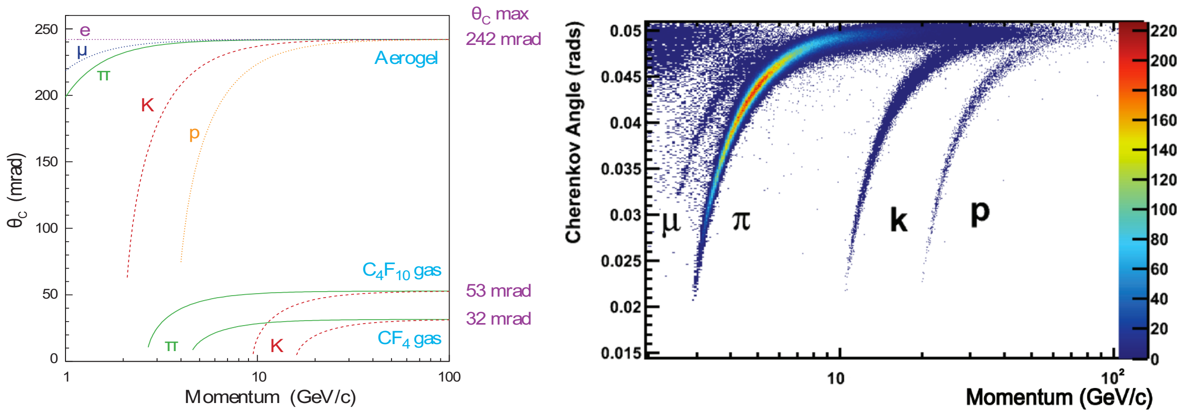

Figure 3.14. Calculated Cherenkov angle as a function of momentum for different RICH radiators: Aerogel, C_4F_{10}, and CF_4 (left). Reconstructed Cherenkov angle for isolated tracks in RICH1 C_4F_{10} radiator (right). The bands are shown for muons (μ), pions (π), kaons (K), protons (p), and electrons (e). Reproduced from Ref. [95] and Ref. [97] respectively.

3.6 Calorimetry

The calorimetry system [105] of LHCb plays an important role in the identification and reconstruction of electrons, photons, and neutral pions (π^0). In addition, it provides occupancy and transverse energy (E_T) information that allows hadrons, electrons, and photons to fire the hardware trigger. This is covered in greater detail in Sec. 3.9.1. Starting from the position closest to the interaction point, the calorimeter system consists of the Scintillating Pad Detector (SPD), the Pre-Shower (PS), the Electromagnetic Calorimeter (ECAL), and the Hadronic Calorimeter (HCAL). The calorimeters are segmented into three regions in the case of the SPD, PS, and ECAL, and two regions in the case of the HCAL with higher granularity towards the beam-line to compensate for two orders of magnitude variation in occupancy along the active plane of the detector. Figure 3.15 illustrates the layout of the SPD/PS and the HCAL.

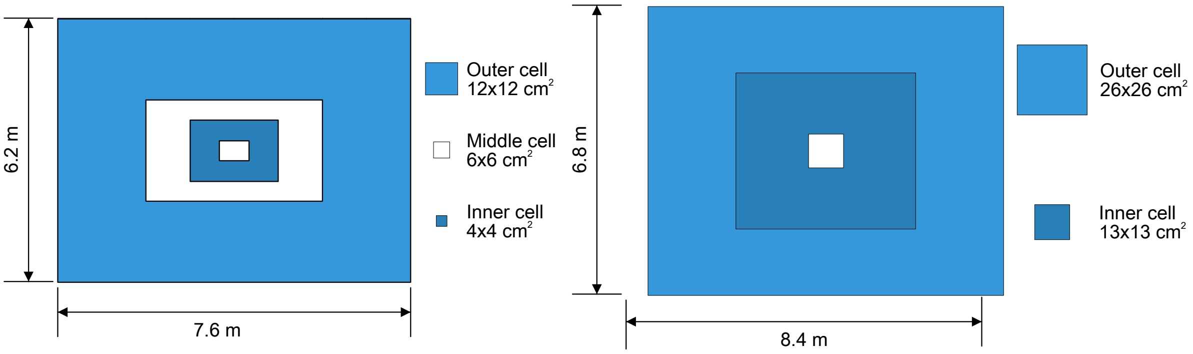

Figure 3.15. Schematic of the SPD (left) and HCAL (right). Each colour region represents a different cell side. The layout of the PS and ECAL are the same as the SPD but scale accordingly to maintain the same acceptance window.

3.6.1 Scintillating Pad and Pre-Shower Detector

The SPD and PS consist of an array of scintillator pads coupled to multi-anode photo multiplier tubes separated by a 15 mm thick layer of lead. Only charged particles interact with the SPD. However, when neutral particles interact with the lead converter a particle shower is induced, leaving a signal in the PS and thus allowing one to distinguish energy depositions left by charged and neutral particles in the ECAL and HCAL. This is exploited in the hardware trigger to provide a rapid separation of electrons, and neutral pions. Figure 3.16 illustrates the detectors involved in the energy measurement of electrons, hadrons, and photons. The hit multiplicity in the SPD also provides a measure of the number of charged particles in an event and plays a crucial role in the low-multiplicity trigger lines used to study CEP.

3.6.2 Electromagnetic Calorimeter (ECAL)

The ECAL is constructed with alternating layers of 2 mm thick lead absorbers and 4 mm scintillators stacked along the z-axis. The cell size of the innermost region of the ECAL ($4 \times 4\,\mathrm{cm}^2$) is close to the Moliere radius, such that most of the shower can be contained in a single cell. Wavelength shifting fibres connect the scintillators to photomultiplier tubes. A

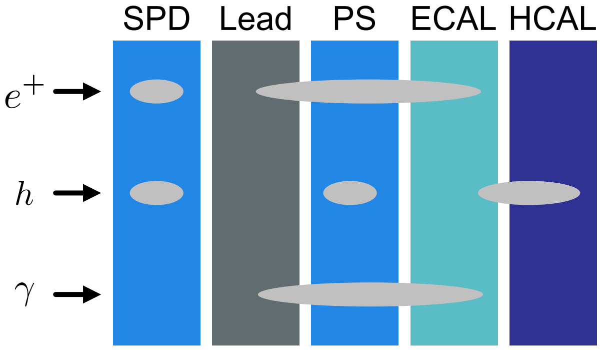

Figure 3.16. Schematic of energy depositions in the calorimetry system for electron, hadrons, and photons.

schematic of an ECAL module is shown in Fig. 3.17 (left). The energy resolution for the ECAL can be modelled as

$$\frac{\sigma_E}{E} = \frac{9\ \%}{\sqrt{E}} \oplus 0.8\ \% \ , \tag{3.2}$$

where E is in GeV and the symbol $\oplus$ indicates a quadratic sum. The first term on the right–hand side describes the stochastic-resolution effect and the second term gives the energy-independent contribution.

3.6.3 Hadronic Calorimeter (HCAL)

Similar to the ECAL, the HCAL is a sampling calorimeter with alternating 3 mm scintillator tiles and 1 cm iron absorbers connected to photomultiplier tubes via wavelength shifting absorbers. However, the plates are placed perpendicular to the ECAL plates along the x-axis. Since hadronic showers are larger, the granularity of the HCAL does not need to be as fine as that of the ECAL. A schematic of an HCAL module is shown in Fig. 3.17 (right). The energy resolution for the HCAL is described by

$$\frac{\sigma_E}{E} = \frac{69\ \%}{\sqrt{E}} \oplus 9\ \% \ , \tag{3.3}$$

where E is in GeV. The first term on the right–hand side describes the stochastic-resolution effect and the second term gives the energy-independent contribution.

3.7 Muon system

The muon system is composed of five stations (M1–M5). To keep the detector occupancy uniform, the modules are segmented into four regions, R1 to R4, with R1 having the smallest granularity, being the region closest to the beam-line. All stations are equipped with multi-wire proportional counters (MWPC) with the exception of station M1 region R1, which is equipped with gas electron multipliers (GEM). Figure 3.18 (left) shows a the front view of one of the quadrants of a muon station.

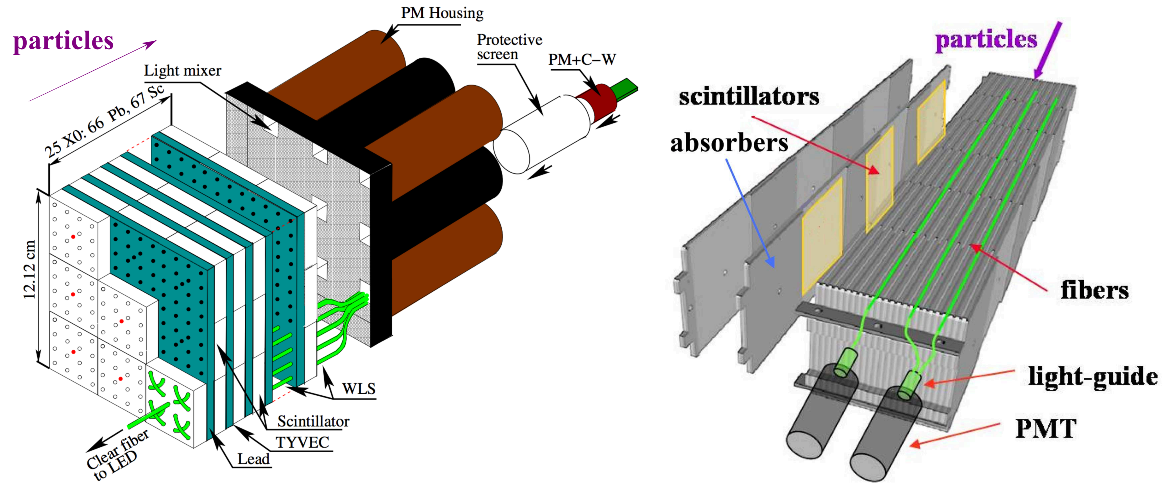

Figure 3.17. Blown-up schematic of an ECAL (left) and HCAL (right) module. The approximate direction of motion of incoming particles is indicated by a violet arrow. Reproduced from Fig. [95]

The first module, M1 is located between RICH2 and the calorimetry system to improve the transverse-momentum calculation in the earliest trigger level, while M2-M5 are located at the end of the calorimetry system. The M2-M5 modules are each separated by an 80 cm iron absorber preventing hadrons that punch through the HCAL from entering into the muon system. This results in a momentum resolution of 20%. See Fig. 3.18 for a schematic of the muon station positioning.

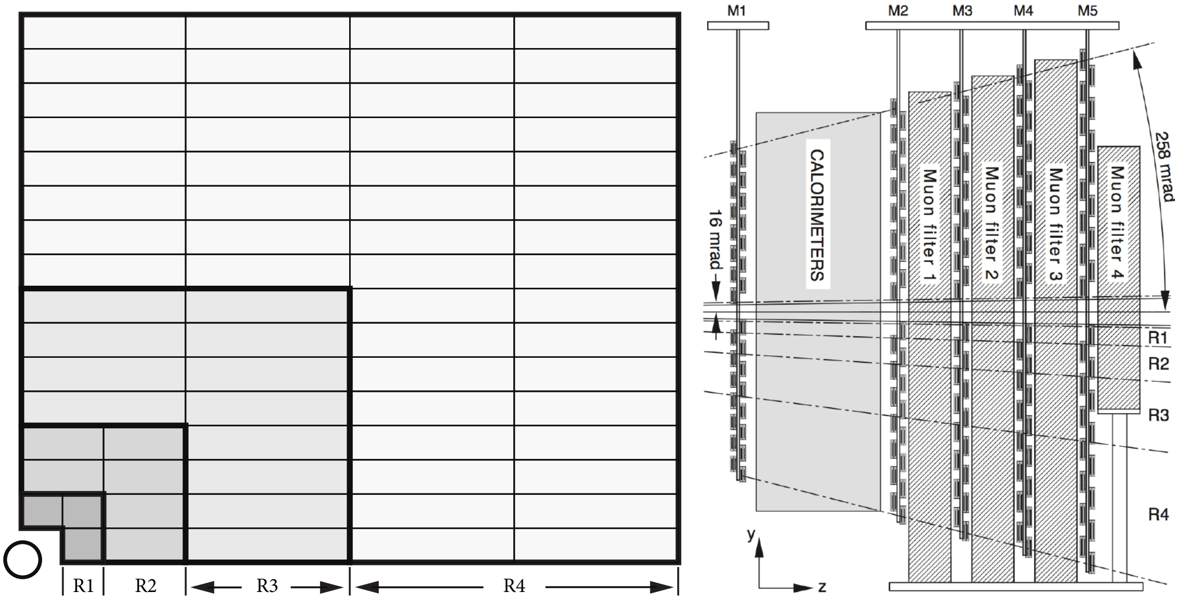

Figure 3.18. Front view schematic of a quadrant of a muon station (left) and side view of the muon system (right). Reproduced from Ref. [95]

3.8 HeRSCheL

HeRSCheL (High Rapidity Shower Counter for LHCb) [106] is a sub-detector system installed for Run 2, which began in 2015. The modules are designed to detect particle showers induced by the interaction of high-rapidity particles, which fall outside the acceptance of the main spectrometer, with the beampipe as well as structural and machine elements of the particle collider. It is composed of five shower-counter modules, F0, F1, B0, B1, and B2, installed around the beamlines inside the accelerator tunnel: two in the forward direction of the interaction point, downstream, and three in the backwards direction, upstream. Each module is segmented into four quadrants of 300 mm × 300 mm × 20 mm EJ-200 [107] plastic scintillating pads tightly fitted around the beam pipe. EJ-200 has a peak emission wavelength of 425 nm and a yield of 10^4 photons per 1 MeV electron. Energy from incident particles is absorbed in the form of ionisation and released as light in the de-excitation process.

To detect and amplify the scintillating light, each pad is equipped with a 51 mm diameter Hamamatsu R1828-01 photo-multiplier tube [108] connected to the scintillating pad via a fishtail-plexiglass light guide, which is read synchronously with the LHCb spectrometer. These PMTs are characterised by a high-response time of 1.3 ns necessary to keep up with the high collision rate of the LHC as well as a large range in gain. The latter allows for operation at high gain during calibration using single-particle cosmic-ray interactions as well as low gain necessary to cope with the high-multiplicity particle showers present during regular operation. For fire safety regulations, and as a means to shield the scintillators from external light leaks, each module is wrapped with a 1 mm thick aluminium sheet. A module schematic is shown in Fig. 3.19 together with the schematic of one of the stations.

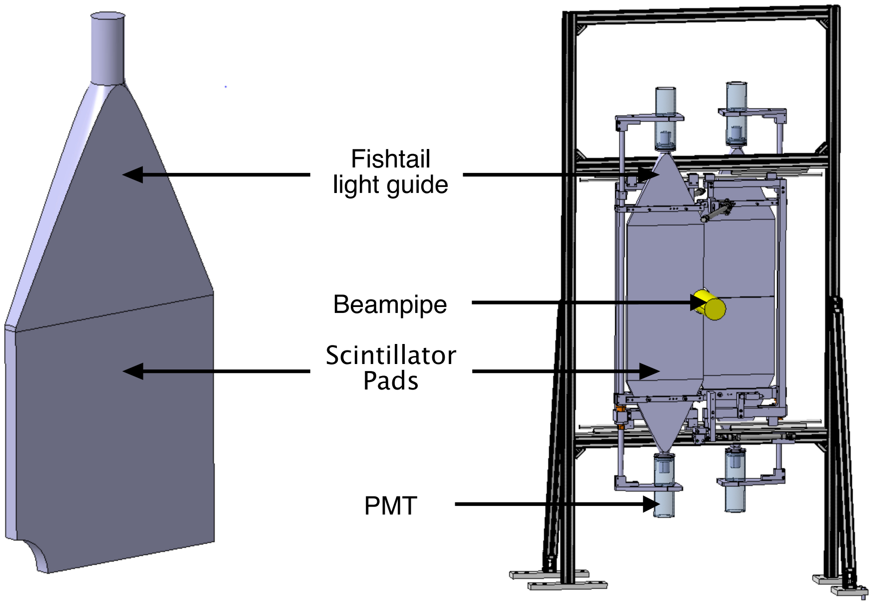

Figure 3.19. Schematic design of a scintillator and light guide of a single HeRSCheL quadrant (left) and a full station (right). Reproduced from Ref. [106]

The stations are placed behind large and dense accelerator components, such as beam screens and collimating magnets, where particle showers might be initiated. In the forward direction (positive z relative to the interaction point), we find stations F1 and F2 at $z \sim 20.0\,\mathrm{m}$ and $z \sim 114.0\,\mathrm{m}$, respectively. In the backwards direction (negative z), we find stations B0, B1, and B2 at $z \sim -7.5\,\mathrm{m}$, $z \sim -19.7\,\mathrm{m}$, and $z \sim 114.0\,\mathrm{m}$, respectively. Figure 3.20 shows a schematic of the system. The HeRSCheL modules extend the sensitivity of the main spectrometer from $2 < \eta < 5$, in the forward direction, and $-3.5 < \eta - 1.5$, in the backwards direction, to a maximum pseudorapidity of ten on either side. A simulation of the energy deposits from forward showers originating from proton dissociation in pp collisions is reproduced in Fig. 3.21, showing the pseudorapidity coverage of each HeRSCheL module.

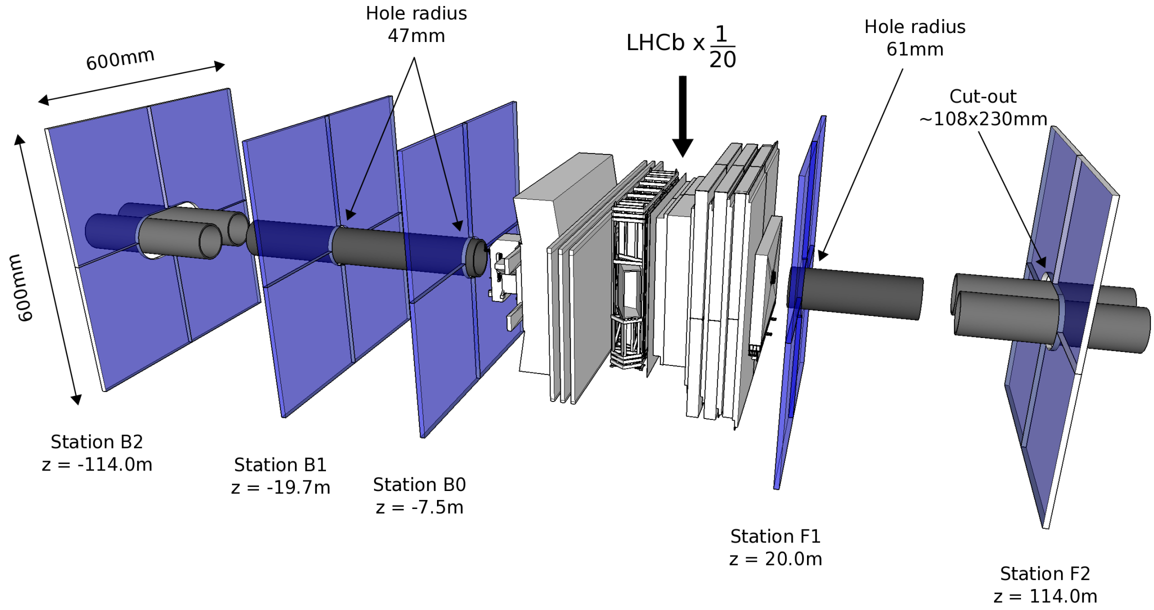

Figure 3.20. Layout of the active area of HeRSCheL stations. The stations are scaled by a factor of 20 and the z-axis is not to scale. Reproduced from Ref. [106]

The increased sensitivity at high rapidities provides valuable information for the classification of diffractive processes, such as single and double diffraction, by providing information about the presence or absence of a rapidity gap. For example, in a CEP event and in the absence of pile-up, the interacting protons would remain intact and continue their trajectory down the beam line, resulting in a signature in the HeRSCheL modules consistent with background noise. While in inelastic events, the primary background of CEP, the resulting high-rapidity particles from the proton-dissociation interact with machine elements and produce particle showers, breaking the rapidity gap and leaving an excess of signal in the HeRSCheL modules. This signature allows us to use this information to veto the primary source of background in CEP studies. In addition, HeRSCheL is also sensitive to the presence of inelastic events originating from secondary interactions that can occur alongside a CEP event during pile-up.

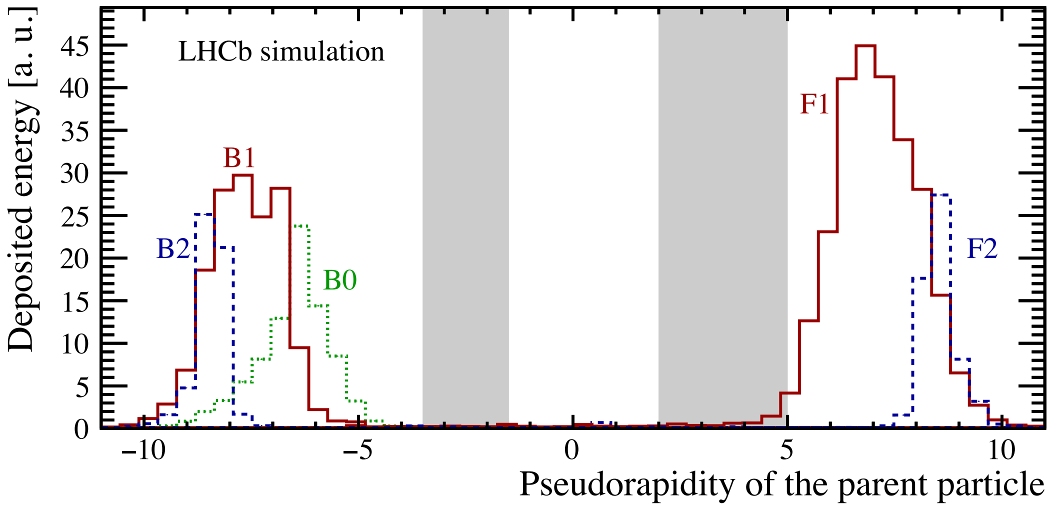

Figure 3.21. Energy deposits on the HeRSCheL modules as a function of pseudorapidity. The pseudorapidity coverage of LHCb is highlighted in grey. Reproduced from Ref. [106]

Although HeRSCheL is able to identify the presence of these rapidity-gap-breaking showers it is unable to distinguish their source.

The integrated analogue signal from the PMT is digitised by a 10-bit analogue-to-digital converter (ADC). A typical detector signal is shown in Fig. 3.22 for station B0 for the first 100 ADC counts. The pedestal, shown in red, corresponds to an empty detector and is representative of the absence of activity we expect in CEP-like events. It is determined by reading the detector during an empty crossing following the last of a series of *pp* crossings known as a train. Events with activity, shown in black, are read during *pp* crossings and are characterised by a long tail at higher ADC counts. An efficiency study of the HeRSCheL module for 2015 and 2016 data is detailed in Sec. 5.6 using dimuon continuum data.

3.9 Trigger system

The LHC bunch crossing frequency is 40 MHz. However, it is unfeasible to permanently store every event. Composed of a hardware, Level-0 (L0), and a software component, High Level Trigger (HLT), the trigger system [109] is a two stage process designed to identify and store events containing signatures of interesting physics as well as select events for calibration.

3.9.1 Level-0 trigger

The earliest trigger level, L0, operates synchronously with LHC's 40 MHz bunch crossings and reduces the data bandwidth to 1 MHz, the rate at which the entire detector can be read out. Given how quickly the initial decision needs to be made, only a subset of the detectors are used at this stage. This includes the Pile-Up, the calorimetry, and muon systems. The PU system distinguishes events with multiple interactions by measuring the multiplicity of backward tracks. The calorimetry provides multiplicity information in the forward direction and calculates the total transverse energy, E_T, for electrons, photons, and hadrons in 2×2 cell clusters. The muon

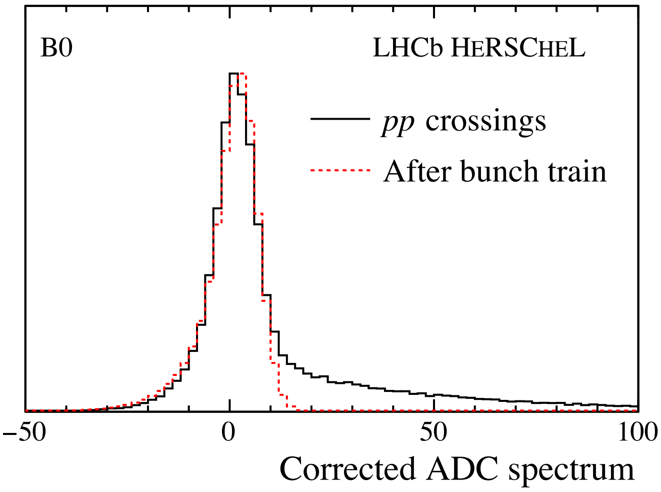

Figure 3.22. Example of corrected HeRSCheL signal for station B0 for pp crossings (black) and for empty crossings following a pp crossing (red). Reproduced from Ref. [106]

decision uses all five stations to calculate the transverse momentum, p_T, and selects the two muons with the highest p_{T} per quadrant. This information is then combined and compared with decision criteria or trigger lines. Those events that meet these criteria are placed in a buffer to be processed by the hardware stage. Dedicated low-multiplicity trigger lines are used for the study of CEP physics. The specific trigger lines used to collect the data for the analysis presented in this thesis will be described in detail in Chapter 4.

3.9.2 High Level Trigger (HLT)

The second trigger level, HLT, is a software-based C++ application executed in the Event Filter Farm (EFF), which is a large ensemble of CPUs, and employs information from the entire detector to reduce the 1 MHz L0 output to a bandwidth of 12.5 kHz. This is achieved in two steps: HLT1 where the event with tracks that have large impact parameters or matching hits in the muon arm are reconstructed, and HLT2 where the event is fully reconstructed. During HLT1, vertex tracks are reconstructed to calculate impact parameters as well as primary and secondary vertices. These are combined with information of the tracking system to reconstruct the entire track. The track reconstruction process is explained in detail in Sec. 3.10.1.

3.10 Reconstruction

3.10.1 Track reconstruction

LHCb's data-processing software is centred around Gaudi, an event-processing framework for particle physics experiments [110, 111]. As part of this framework, Brunel [112] is specialised in track reconstruction and particle identification. During track reconstruction, the signal from all the tracking sub-detectors are combined to determine each particle's trajectory. The process starts with energy depositions from the VELO and the T stations. Since the magnetic field is weakest for these stations, they have relatively straight tracks. A Kalman filter is then used to account for multiple scattering, and energy loss as intermediate data points are iteratively added to construct the track. The event display of a typical inelastic event is shown in Fig. 3.23 with the overlapping tracks. HLT2 uses the fully reconstructed event and is able to apply kinematic cuts to individual particles as well as combine tracks and apply cuts to mass and vertex fits.

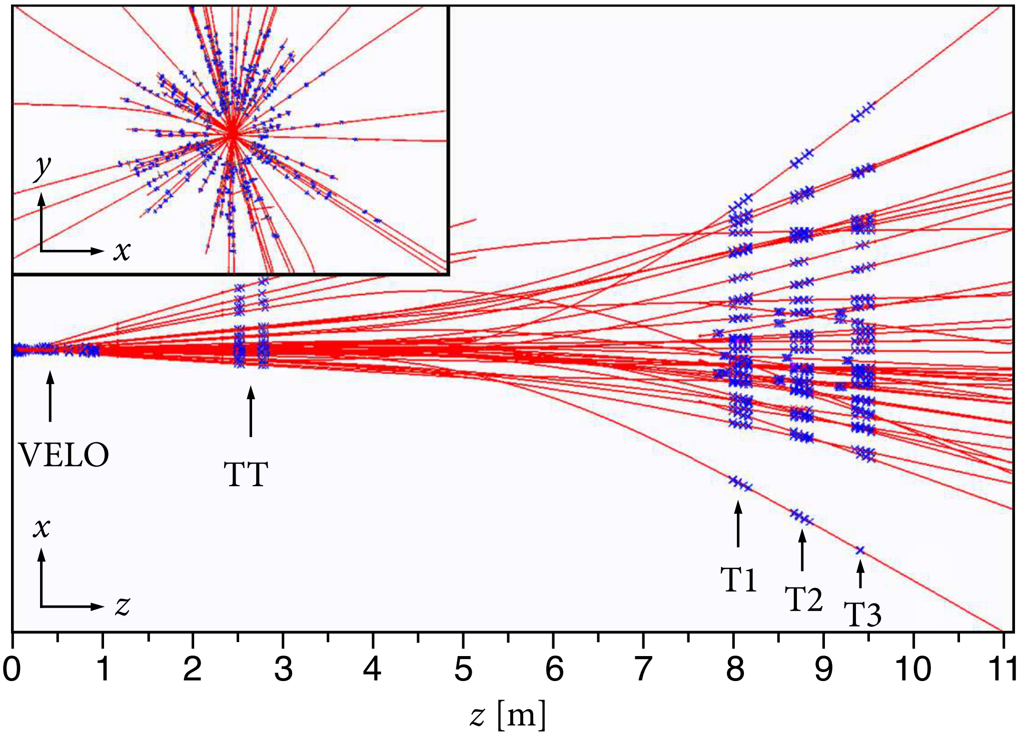

Figure 3.23. Reconstructed tracks (red) and energy detector hits (blue). Reproduced from Ref. [95]

The tracks are then classified according to the detectors with energy deposits associated with that track:

- **VELO Tracks** traverse only the VELO, tend to have large angles relative to the horizontal, and are normally used for vertex reconstruction.
- **Upstream Tracks** traverse the VELO and TT, tend to be low momentum with poor momentum resolution, and are deflected outside the acceptance of the spectrometer by the bending magnet.
- **Long Tracks** traverse all tracking stations and tend to have the best momentum resolution.
- **Downstream Tracks** traverse the TT and T stations and tend to be decay products of particles that decay outside of the VELO.
- **T Tracks** traverse only the T station.

- **Backwards Tracks** traverse through the VELO and PU. These particles have a negative rapidity and do not make it into the main spectrometer.

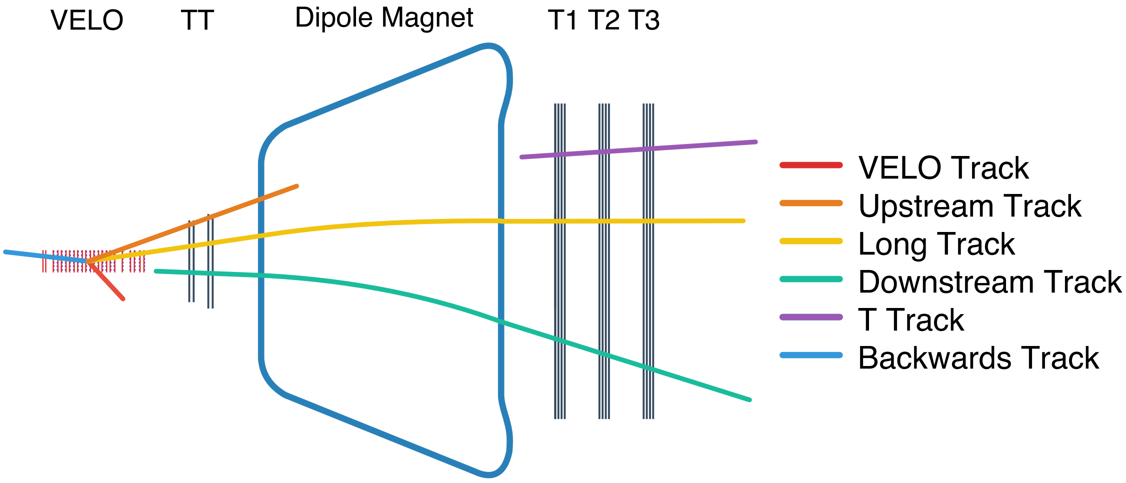

Figure 3.24. Schematic of the LHCb tracking system with representative examples of track types: VELO (red), upstream (orange), long (yellow), downstream (green), T (purple), and backward tracks (blue).

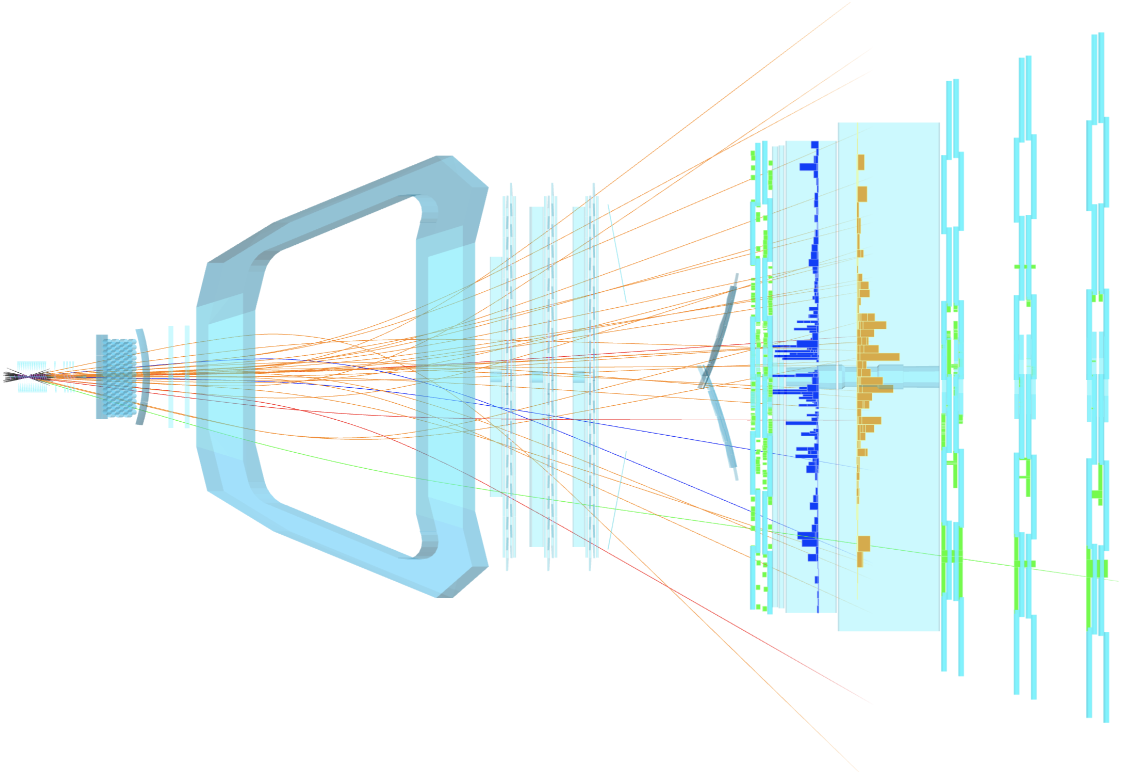

Figure 3.25. Event display top view of a typical event showing tracks for pions (orange), kaons (red), protons (violet), electrons (blue), and muons (green) together with energy depositions in the calorimeters and muon arm.

3.10.2 Particle identification

Neutrals

Neutral particles are distinguished by the absence of tracks associated with energy depositions in the calorimetry system. To identify neutral particles, all reconstructed tracks are extrapolated to the calorimetry system and matched with a cluster. In the ECAL, a cluster is defined as a 3×3 cell pattern centred around the cell with the largest energy deposit. The match is evaluated by comparing the track and cluster coordinates at the energy-weighted centre of the cluster along the z direction according to a χ^2_{2D} metric,

$$\chi^2_{2D} = (\vec{r}_{track} - \vec{r}_{cluster})^T (C_{track} + S_{cluster})^{-1} (\vec{r}_{track} - \vec{r}_{cluster}) \ , \tag{3.4}$$

where $\vec{r}_{track}$ and $\vec{r}_{cluster}$ are the local coordinates of tracks and clusters respectively, C_{track} is the covariant matrix of $\vec{r}_{track}$ and $S_{cluster}$ is the cluster energy spread matrix. Neutrals are identified as being associated to clusters with a large value of χ^2. The isolation criteria for photon candidates are satisfied by selecting events with $\chi^2_{2D} > 4$.

The energy of non-converted photons is calculated from the total energy deposition in the ECAL and the PS. The photon direction is calculated according to its assumed point of origin. Photons can also be reconstructed from electron-positron pairs when they convert before the bending magnet. Electron-positron candidates within 3σ of cluster extent and 200 mm in the vertical plane are paired and the energy is corrected by including associated bremsstrahlung photons.

Neutral pions are reconstructed with two well-separated photons. However, for transverse momentum greater than 2 GeV the photon clusters tend to overlap with one another. The energy deposited in overlapping cells is accounted for by fitting the energy distribution of the two photons according to simulation. To prevent the misidentification of high-energy neutral pions and photons a neural network trained on $B^0 \to K^{*0}\gamma$ is used to distinguish energy-deposit patterns.

Hadrons

Charged hadrons are mainly identified through a global pattern-recognition algorithm that matches the patterns left by Cherenkov radiation in the photo detectors of RICH1 and RICH2 with the expected signature of a reconstructed track under a given mass hypothesis. The mass hypothesis with the highest likelihood is found by cycling through all potential candidates (pion, kaon, proton, electron or muon) for all reconstructed tracks and finding the best match. For each track, the log-liklihood difference is calculated relative to the pion mass hypothesis, the most abundant hadron produced, such that

$$\Delta \log \mathcal{L}_{X-\pi} = \log \mathcal{L}_X - \log \mathcal{L}_\pi \ , \tag{3.5}$$

where $\mathcal{L}_X$ is the likelihood of a given mass hypothesis X and $\mathcal{L}_\pi$ is the likelihood given the π mass hypothesis.

Muons

Muons are identified by extrapolating reconstructed tracks and associating them with signals recorded in the muon system. Signals are searched at each station within a window centred around the coordinates of the extrapolated reconstructed tracks. The window as well as the number of stations involved in the particle-identification algorithm are energy dependent since a minimum-momentum of 3 GeV is needed to reach the M2 and M3 stations and 6 GeV to reach all five stations. Similarly to the ECAL cluster-track matching, a χ^2_{2D} metric that quantifies the cluster-track proximity is minimised.

Combined particle identification

Two methods are used to combine particle identification information from each subsystem to form a more powerful identification. The first adds the log likelihood of each sub-system linearly to obtain a combined likelihood $\Delta \log \mathcal{L}_{combined}(X - \pi)$. A second method uses Toolkit for Multivariate Data Analysis with ROOT (TMVA) [113] to combine PID information and other parameters to calculate the probability for a given mass hypothesis.

3.10.3 Stripping and Turbo

Stripping can be considered as an offline trigger. Pre-selections are applied to the recorded events, and the saved samples are grouped in streams according to their physics potential. In the stripping process, the latest alignments and calibrations are used to fully reconstruct the recorded events. This high-precision tracking, vertex, and PID information is used for the study of independent decay channels. The reconstruction of composite particles and loose selection criteria are specified in dedicated stripping lines. This first selection pass is designed to reduce the data set to a manageable size while maintaining flexibility of the selection criteria for a broad number of analyses.

During the LHC long shut down, 2013 to 2014, the processing power and storage of the EFF computing system was upgraded allowing for a 5.2 PB of buffer space. This corresponds to about ten days of continuous data taking. As a result, the HLT decision can be postponed until after data taking, and fully calibrated events can be reconstructed, providing analysis-ready data to be used as part of the trigger decision. Turbo [114] is a class of output stream with fully reconstructed decay-specific dedicated streams immediately ready for analysis. Fig. 3.26 depicts a direct comparison of the conventional trigger system (left) and the Turbo stream system (right).

The data in the Turbo and Stripping streams are ready for analysis. Part of the analysis process is conducted with DaVinci [115], a component of the Gaudi analysis framework where particles can be combined from the decay chain and a first pass of cuts can be applied. At this stage specialised tools and algorithms can be implemented and tailored for the analysis.

The remainder of the analysis is done with custom software based around the ROOT analysis framework [116].

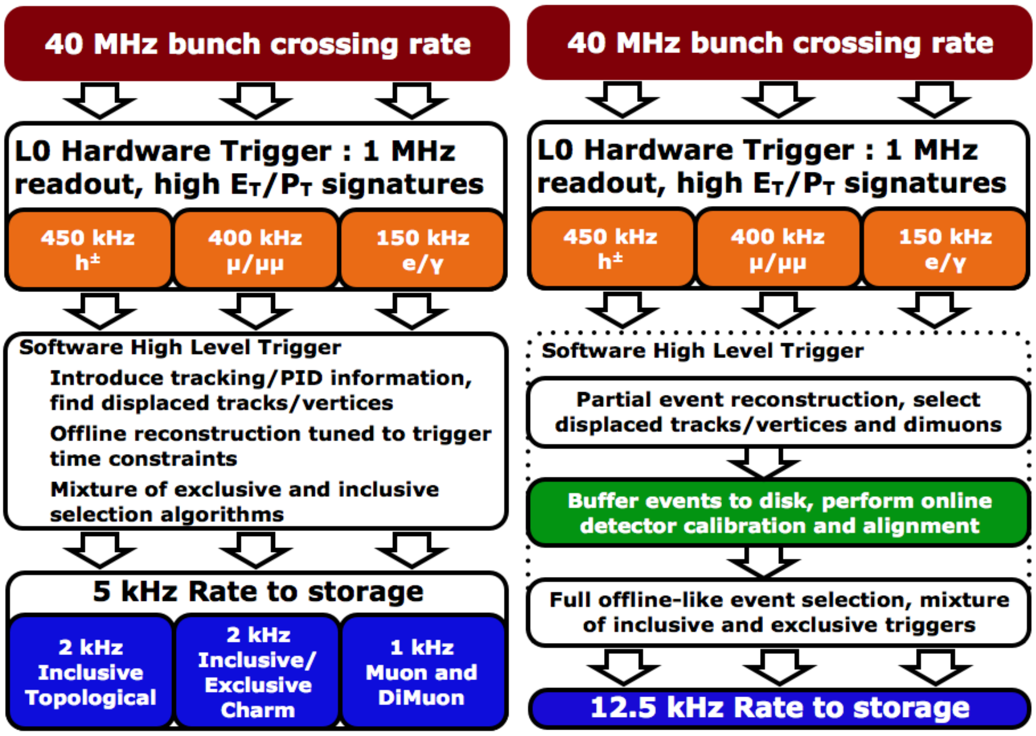

Figure 3.26. LHCb trigger decision flow for Run 1 (left) and Run 2 (right). Reproduced from Ref. [117].

3.11 Simulation

Monte Carlo studies play an essential role in the study of signal modes, efficiencies, detector response, and background studies. The first stage of simulation is run using Gauss [118–120]. This takes care of the generation and particle propagation. The analysis presented in this thesis relies on SuperChic v2 [83] to generate χ_c signal samples as well as $\psi(2S)$ background samples. The output of SuperChic v2 is incorporated in the simulation framework via a *particle gun* method. This method generates χ_c particles by sampling the momentum distribution generated by SuperChic v2 and decays them using EvtGen [121] and models final-state radiation with Photos [122]. The decay particles are then propagated through the detector by Geant4 [123], which simulates multiple scattering throughout the detector material. The second set of generators used are Pythia 6 [124] and Pythia 8 [125], pp collision simulators, which are fully implemented into the LHCb simulation framework. The Pythia generators are used to simulate D^{*0} decays necessary for the calculation of the photon-conversion efficiency described in Sec. 4.2.4. Boole [126] models the detector response and front-end electronics. The trigger software is then run, Moore [127], to simulate the hardware and software triggers. At this point, the Monte Carlo can be reconstructed with Brunel [112] and analysed with DaVinci [115] in the same fashion as data.

Chapter 4

Event selection

In this chapter we present the selection of the collision data sets for the two major components of this analysis: the CEP χ_c sample used for the cross-section measurements of CEP χ_{c1} and χ_{c2} mesons as well as the D^{*0} sample necessary to measure the photon-conversion efficiency. The trigger, stripping, and offline-selection criteria applied to each of the samples are outlined in detail. Finally, we present the samples of Monte Carlo simulation data necessary for the measurements.

4.1 CEP χ_c study: data sets, selection criteria, and simulation

4.1.1 CEP χ_c data sets

This analysis is performed with *pp* collision data collected with the LHCb detector at a centre-of-mass energy of $\sqrt{s} = 13\,\text{TeV}$, during the 2015 and 2016 runs. The data collected correspond to an integrated luminosity of $\mathcal{L}_{\text{int}}^{2015} = 328\,\text{pb}^{-1}$ and $\mathcal{L}_{\text{int}}^{2016} = 1665\,\text{pb}^{-1}$ for a total of $\mathcal{L}_{\text{int}}^{2015+2016} = 1993\,\text{pb}^{-1}$. Only events where all sub-detectors were operational are used in the analysis. However, due to commissioning downtime of the trigger lines and the newly installed HeRSChel detector during the early parts of the 2015 run, only 86.6% of the 2015 data meets the trigger lines and HeRSChel requirements for this analysis while 98.2% of the 2016 data satisfies these requirements. In addition, to isolate CEP candidates the exclusivity requirement demands that we examine events with a single interaction per bunch crossing, that is, in the absence of pile-up. Approximately 35.7% of the total-integrated luminosity meets this criterion. The determination of the effective integrated luminosity for single-interaction events is described in Sec. 7.5. The reconstruction and stripping conditions used are summarised in Table 4.1 together with the data pipeline utilised in the analysis. Each of the steps within the data-selection process is described in detail in Sec. 4.1.2 and Sec. 4.1.3.

It is worthwhile mentioning that there are two additional data samples of similar size to the 2016 data set. The data collected during the 2017 and 2018 *pp* runs have an integrated luminosity of $\mathcal{L}_{\text{int}}^{2017} = 1609\,\text{pb}^{-1}$ and $\mathcal{L}_{\text{int}}^{2018} = 2185\,\text{pb}^{-1}$, respectively. Although we have conducted preliminary studies with the 2017 sample, these two data sets have been excluded from this study as the data necessary to perform the photon-conversion-efficiency measurement is missing for these two data sets. This is explained further in Sec. 4.2.1.

Table 4.1. Summary of the trigger reconstruction and stripping information.

Data pipeline	
L0	`L0DiMuon,lowMult` || `L0Muon,lowMult`
HLT1	`Hlt1NoPVPassThrough`
HLT2	`Hlt2LowMultDiMuon` || `Hlt2LowMultMuon`
Stripping Line	`LowMultDiMuon` || `LowMultMuon`

4.1.2 CEP χ_c online-selection criteria

L0 trigger criteria

To be considered, the events must pass the requirements specified by either the `Muon,lowMult` or `DiMuon,lowMult` lines in L0, the earliest hardware-trigger level. As the name suggests, these trigger lines are designed to select events with one or two muons in a low-multiplicity environment. The `Muon,lowMult` trigger requires a single muon with a transverse momentum above 400 MeV/c for 2015, and above 800 MeV/c for 2016. The `DiMuon,lowMult` trigger requires two muons, each with a transverse momentum above 200 MeV/c.

The low-multiplicity criteria are met by selecting events with less than 30 hits in the SPD for 2015, and less than 20 hits for the 2016 data set. The distribution of SPD hits for $\chi_c \to J/\psi\,[\mu^+\mu^-]\gamma[e^+e^-]$ is expected to have approximately one hit from each muon and slightly over one hit for each electron, as bremsstrahlung radiation can result in additional hits. Other than the hits from the final-state particles, we expect activity in the SPD from noise and spillover. A study of this SPD requirement is presented in Sec. 5.1.6 and the L0 trigger criteria are summarised in Table 4.2.

Table 4.2. Configuration for the `L0DiMuon,lowMult` and `L0Muon,lowMult` L0 trigger line.

Variable	Units	L0DiMuon,lowMult		L0Muon,lowMult	
Year	-	2015	2016	2015	2016
SPD hits	-	< 30	< 20	< 30	< 20
μ_1 p_T	MeV/c	> 200	> 200	> 400	> 800
μ_2 p_T	MeV/c	> 200	> 200	n/a	n/a
Prescale	-	1.0	1.0	1.0	1.0

HLT trigger criteria

Events that pass the hardware-line requirements are forwarded to the first software-trigger level, HLT1. In this case, the events are evaluated by the `Hlt1NoPVPassThrough` trigger line, which has two unique characteristics pertaining to CEP events. Firstly, since CEP events have a low multiplicity, the resources required to process these events are low compared to typical inelastic events and so they can therefore be processed directly by HLT2, in the lines `Hlt2LowMultDiMuon` or `Hlt2LowMultMuon`. The second is that this line, unlike those for inelastic events, does not require the reconstruction of a primary vertex (PV).

The `Hlt2LowMultDiMuon` line requires two muons with transverse momentum greater than 400 MeV/c and the `Hlt2LowMultMuon` line requires a single muon with transverse momentum greater than 400 MeV/c. The configurations for these HLT2 trigger lines are summarised in Table 4.3.

Table 4.3. Configuration for `Hlt2LowMultDiMuon` and `Hlt2LowMultMuon` trigger lines.

Variable	**Units**	**Hlt2LowMultDiMuon**		**Hlt2LowMultMuon**	
Year	-	2015	2016	2015	2016
$\mu_1\ p_T$	MeV/c	> 400	> 400	> 400	> 400
$\mu_2\ p_T$	MeV/c	> 400	> 400	n/a	n/a
$m_{\mu^+\mu^-}$	MeV/c^2	> 0.0	> 0.0	n/a	n/a
Prescale	-	1.0	1.0	1.0	1.0
Postscale	-	1.0	1.0	1.0	1.0

4.1.3 CEP χ_c offline-selection criteria

Approximately a fifth of the photons at the LHCb experiment convert into an electron-positron pair before they reach the dipole magnet due to their interactions with detector material. These photons are known as *converted photons*. More specifically, we categorised photons into three subgroups. The first set is known as *long converted photons*, which undergo conversion in the first part of the VELO. The electron tracks in this sub-group will leave energy deposits in the VELO, TT, and T-stations and as a result will be classified as long tracks. In the second group, known as *downstream converted photons*, the conversion occurs in the later portion of the VELO or after the VELO, primarily in the TT. These electrons will leave energy deposits in the TT and T-stations, and will be classified as downstream tracks. Finally, we define a third group, *calorimetric photons*, composed of unconverted photons detected at the ECAL and photons that convert into an electron-positron pair after the dipole magnet.

The use of converted photons has two major consequences: a low reconstruction efficiency and an improved energy resolution. The low reconstruction efficiency is due to the fact that electrons with energies lower than 2 GeV are deflected outside of the detector acceptance by the dipole magnet and never reach the ECAL. In addition, the electrons scatter en route to the calorimeters and lose energy to bremsstrahlung radiation, reducing the reconstruction efficiency further. On the other hand, there is a significant improvement in energy resolution in converted photons. This stems from the added tracking information traversing most of the magnetic field. Downstream tracks have an average momentum resolution of $\delta p/p \approx 0.43\%$, which compares to an energy resolution of $\sigma_E/E \approx 9\%/\sqrt{E} \oplus 0.8\%$ from the ECAL [95]. The improvement in energy resolution of the photons translates into a better invariant-mass resolution of particles reconstructed with these converted photons, making it particularly appealing for studies such as that of the χ_c mesons, which require the χ_{c1} and χ_{c2} resonances to be resolved within $50\,\mathrm{MeV}/c^2$ of each other. Throughout this analysis we use the difference between the reconstructed invariant mass of the χ_c candidates and of the intermediate J/ψ meson such that,

$$\Delta m_{\chi_c} = m(J/\psi\gamma) - m(J/\psi). \tag{4.1}$$

Using the Δm_{χ_c}, a quantity we shall sometimes refer to as *delta mass*, partially cancels the experimental uncertainty in the reconstruction of the J/ψ meson and improves the mass resolution of the χ_c candidates, therefore allowing us to better resolve the different χ_c resonances. The Δm_{χ_c} distribution in 2016 data is shown in Fig. 4.1 for χ_c mesons using calorimetric and downstream converted photons. The distributions are shown prior to the application of the exclusivity cuts described later in the section to increase the sample size and better appreciate the differences between the two photon-reconstruction methods. In the case of calorimetric photons, the signal distributions for χ_{c1} and χ_{c2} mesons overlap completely, whereas they are easily distinguished when we use downstream converted photons. As a result, we use converted photons in this study.

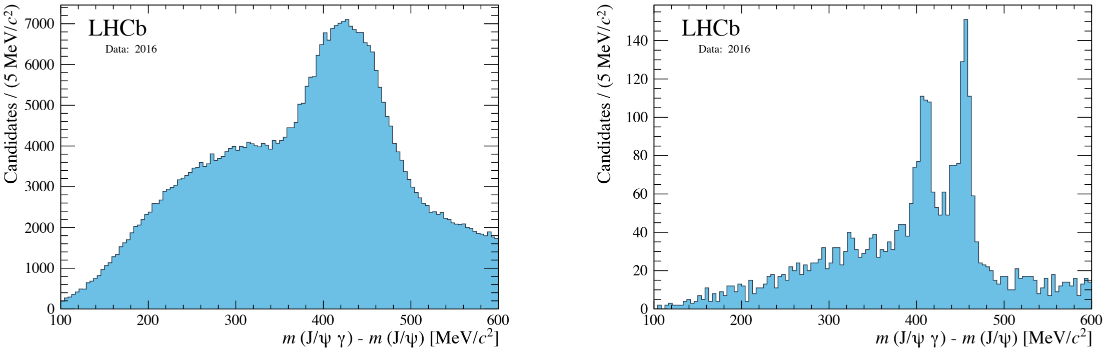

Figure 4.1. Invariant-mass difference of χ_c candidates reconstructed with calorimetric photons (left) and downstream converted photons (right) in 2016 data.

In particular, we prefer downstream converted photons over long converted photons since, on average, the electrons from long converted photons have longer distances to traverse and thus tend to radiate more secondary photons compared to downstream converted photons. The higher sensitivity of long converted photons to bremsstrahlung effects make correcting for this effect more difficult and, on average, results in poorer resolution. In addition, the electrons from long converted photons are more likely to be deflected from the spectrometer acceptance by the magnetic field making their detection and full reconstruction more difficult. The reconstruction efficiency of long conversions is further hindered since the energy deposits from conversions that occur early in the VELO can be reconstructed as a single VELO track. As a result, electron pairs that should be reconstructed as two long tracks can be reconstructed as a single long track and a downstream track. Such events are not considered as candidates. Overall, downstream converted photons give rise to a better χ_c mass resolution, produce lower levels of background, and provide larger data samples compared to long converted photons. Consequently, we use downstream converted photons in this study.

CEP χ_c stripping-selection criteria

Stripping, described in Sec. 3.10.3, provides another software-based mechanism for data reduction. This level of selection allows for fine tuning in a non-destructive form, that is, the events that do not pass the criteria set by a stripping line are not deleted. However, they are also not available for analysis.

We use the `LowMultDiMuonLine` and `LowMultMuon` stripping lines, which take in the output of `Hlt2LowMultDiMuon` and `Hlt2LowMultMuon` trigger lines described above, respectively. In 2015 and 2016, these trigger lines did not impose new cuts to the HLT2 output. However, they do run data-quality checks and make the data available for offline analysis. The decision not to impose new cuts is possible with low-multiplicity muon events because of the data samples' size and the simplicity of the muon experimental signature. In addition, this allows for the greatest flexibility by expanding the range of applicability of these data sets.

CEP χ_c offline-selection criteria

The offline-selection criteria in this analysis focus on two main goals. The first is to select $\chi_c \to J/\psi[\mu^+\mu^-]\gamma[e^+e^-]$ candidates and the second is to ensure there are no signatures of additional rapidity-gap-breaking activity.

The intermediate J/ψ candidates are reconstructed using two oppositely charged long tracks, which are required to match energy deposits in the muon chambers and be consistent with the muon hypothesis. In order to reduce fake tracks, commonly known as *ghost tracks* that are composed of mismatched hits and do not correspond to a true particle, we impose a loose cut on the *track ghost probability*, such that $P_{\text{Track}}^{\text{Ghost}} < 0.9$. This is a discriminating variable based on a neural network multivariate classifier designed to reduce fake tracks [128, 129]. The classifier takes in twenty-two tracking variables and produces an output between zero and one, where values closer to zero tend to be more signal-like.

We require that both muons be within the acceptance of the main spectrometer, $2 < \eta(\mu^+\mu^-) < 4.5$. To reduce contamination from dimuon-combinatorial background we apply a $100\,\text{MeV}/c^2$ J/ψ mass-window cut centred around the J/ψ nominal mass, which is $3096.916\,\text{MeV}/c^2$ according to the PDG [86]. Figure 4.2 shows the invariant mass of the J/ψ mesons in the χ_c sample as well as the selection mass window. The J/ψ mass distribution is slightly skewed to the left due to the muons' loss of energy as they traverse the different layers of the spectrometer. The combinatorial background and mass fit is addressed in detail in Sec. 6.1.

The J/ψ meson is then paired with a downstream converted photon, which is reconstructed by selecting energy cluster pairs in the ECAL associated with downstream electron tracks of opposite charge. The clusters must be at most 200 mm or within 3σ of each other in the

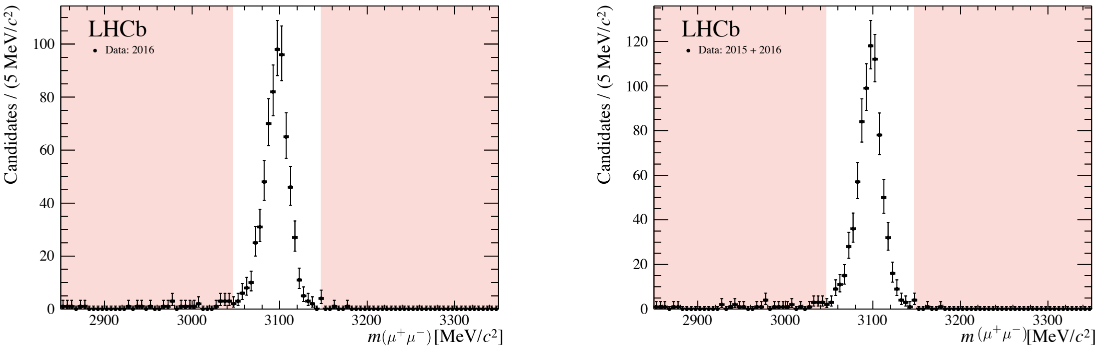

Figure 4.2. Invariant mass of J/ψ mesons from $\chi_c \to J/\psi\,[\mu^+\mu^-]\gamma[e^+e^-]$ candidates for the 2016-only (left), and combined 2015 and 2016 (right) data. The veto mass windows are highlighted in red.

vertical direction. The tracks are then extrapolated and the vertex is reconstructed using the *Runge-Kutta* method, which uses iterative-numeric integration to trace tracks through non-uniform magnetic fields such as the one in LHCb [130]. Convergence is reached when the vertex z-position, $z_{\gamma_{\rm conv}}$, varies no more than 100 mm within two iterations.

To account for the electrons' energy loss to bremsstrahlung radiation, we apply a recovery procedure which systematically adds low-energy photons, $p_{\rm T}(\gamma_{\rm Brem}) > 75$ MeV/c, detected in the calorimeter. The ECAL clusters that fall between the linearly extrapolated energy deposits in the TT from the dielectron pair are selected as bremsstrahlung candidates. The kinematic restrictions on the electrons and photons are left as loose as possible.

Another useful tool for background suppression is the two-dimensional distribution of the di-electron invariant mass $m(e^+e^-)$ and $z_{\gamma_{\rm conv}}$. A photon needs to interact with material in order to convert into a pair of electrons. By allowing some dependence on $z_{\gamma_{\rm conv}}$, we are able to efficiently eliminate events with non-physical vertices, combinatorial background and poorly reconstructed photons. For these reasons, events that satisfy one of the following requirements are rejected:

$$m(e^+e^-)\left[\mathrm{MeV}/c^2\right] - 0.00001\left[\frac{\mathrm{MeV}/c^2}{\mathrm{mm}^2}\right] z^2_{\gamma_{\rm Conv}}\left[\mathrm{mm}^2\right] > 20\left[\mathrm{MeV}/c^2\right] \;, \tag{4.2}$$

$$m(e^+e^-)\left[\mathrm{MeV}/c^2\right] - 0.04\left[\frac{\mathrm{MeV}/c^2}{\mathrm{mm}}\right] z_{\gamma_{\rm Conv}}\left[\mathrm{mm}\right] > 20\left[\mathrm{MeV}/c^2\right] \;, \tag{4.3}$$

$$m(e^+e^-) > 50\left[\mathrm{MeV}/c^2\right] \;. \tag{4.4}$$

We will refer to these cuts collectively as the γ two-dimensional (2D) cut. The $m(e^+e^-)$ and $z_{\gamma_{\rm conv}}$ distribution is shown in Fig. 4.3 before and after the the γ two-dimensional cut is applied.

These same cuts are studied with the larger $D^*(2007)^0 \to D^0[K^\pm\pi^\mp]\gamma[e^+e^-]$ data set used to calculate the photon-conversion efficiency, described in greater detail in Sec. 4.2.3.

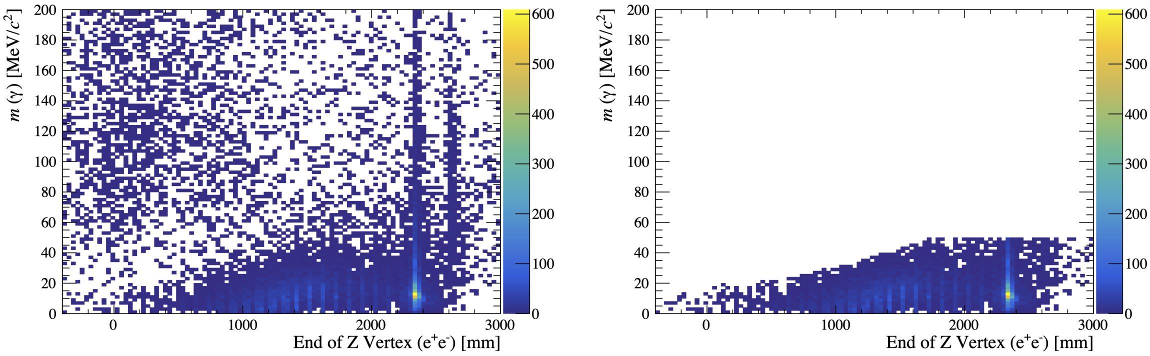

Figure 4.3. Downstream converted photon invariant-mass vs. photon Z-Vertex before (left) and after the (right) the two-dimensional cut given by Eq. 4.2–4.4 is applied.

To meet the exclusivity CEP requirement in the main spectrometer, we select events that have tracks associated with our final-state particles in an otherwise empty detector. This enhances the CEP component of the sample by enforcing the rapidity-gap criteria within the main spectrometer. We achieve this by selecting events with two oppositely charged, long muon tracks necessary to reconstruct our intermediate J/ψ candidates and two downstream, oppositely charged electron tracks used to reconstruct the converted photon. In addition, we request that there are no tracks, backwards tracks, or track stubs in the VELO as well as no additional long, muon or downstream tracks. The full set of offline-selection criteria are summarised in Table 4.4.

HeRSCheL selection

As mentioned in Sec. 2.6, there are diffractive processes that can mimic the CEP signature where one or both of the colliding protons dissociate outside of the main spectrometer's acceptance. The HeRSCheL detector is thus employed to reduce this background. This is done via a figure-of-merit variable, the HeRSCheL discriminant $\ln(\chi^2_{\rm HRC})$, which is related to the amount of activity in each of the forty HeRSCheL modules. To account for spill-over effects, the pedestal is characterised by extracting the mean (μ) and the root-mean-squared (σ) from the first non-beam-beam event after a train of beam-beam collisions. With these calibration constants we define the figure-of-merit value such that,

$$\chi^2_{\rm HRC} = \sum_{i=1}^{40} \left(\frac{x_i - \mu_i}{\sigma_i} \right)^2 , \tag{4.5}$$

where x_i is the HeRSCheL signal in channel i. CEP-like events will show little activity in the HeRSCheL modules and as a result will have low values of $\ln(\chi^2_{\rm HRC})$ compared to events with proton dissociation.

Table 4.4. J/ψ candidate offline-selection criteria.

Variable	**Cut**	**Units**
	$\boldsymbol{J/\psi\,[\mu^+\mu^-]}$	
$p(\mu^\pm)$	> 1000	MeV/c
$P_{\rm Track}^{\rm Ghost}$	< 0.9	–
μ_1, μ_2 isMuon	True	–
$\eta(\mu_1)$, $\eta(\mu_2)$	$\in [2, 4.5]$	–
J/ψ mass window	$\lvert m_{J/\psi} - 3096.916\rvert < 50$	MeV/c^2
	$\boldsymbol{\gamma[e^+e^-]}$	
$e^\pm$ track type	Downstream	–
ECAL position	$\Delta y < 3\sigma \mid\mid \Delta y_{max} < 20$ [cm]	-
$p_{\rm T}(\gamma)$	$\in [0, 1600]$	MeV/c
$p_{\rm T}(e^\pm)$	> 0	MeV/c
$p_{\rm T}(\gamma_{\rm Brem})$	> 75	MeV/c
γ 2D cut	Eq. 4.2 || Eq. 4.3 || Eq. 4.4	–
	CEP track criteria	
Nº upstream tracks	0	–
Nº VELO tracks	0	–
Nº backward tracks	0	–
Nº downstream tracks	2 (e^+e^-)	–
Nº long tracks	2 ($\mu^+\mu^-$)	–
	HeRSChel	
$\ln(\chi^2_{\rm HRC})$	< 5	–

The figure-of-merit is shown in Fig. 4.4 for the CEP $\chi_c \to J/\psi\,[\mu^+\mu^-]\gamma[e^+e^-]$ candidates in 2016, and combined 2015 and 2016 data. The distribution is shown before (left) and after (right) the rapidity-gap selection is applied. The distribution on the right corresponds to events with the CEP-track selection applied: two long muon tracks and two downstream tracks. Before this selection is applied we see that the sample is dominated by inelastic-like events which have high values of $\ln(\chi^2_{\rm HRC})$. After the CEP criteria are applied, the mean of the distribution reduces as the proportion of inelastic background is reduced. We select events with $\ln(\chi^2_{\rm HRC}) < 5$. The efficiency of the HeRSChel figure-of-merit is studied in detail in Sec. 5.6. The Δm_{χ_c} distribution of the final CEP χ_c selection is shown in Fig. 4.5 before and after the HeRSChel cut is applied.

4.1.4 Simulation samples for the CEP χ_c analysis

Monte Carlo simulations play an essential role in this analysis. They help us guide our decisions on selection criteria, provide valuable information for background and signal modelling, and help us to determine efficiencies and systematic uncertainties. In addition, they give us access to state-of-the-art theoretical predictions with which to compare our experimental results, thus

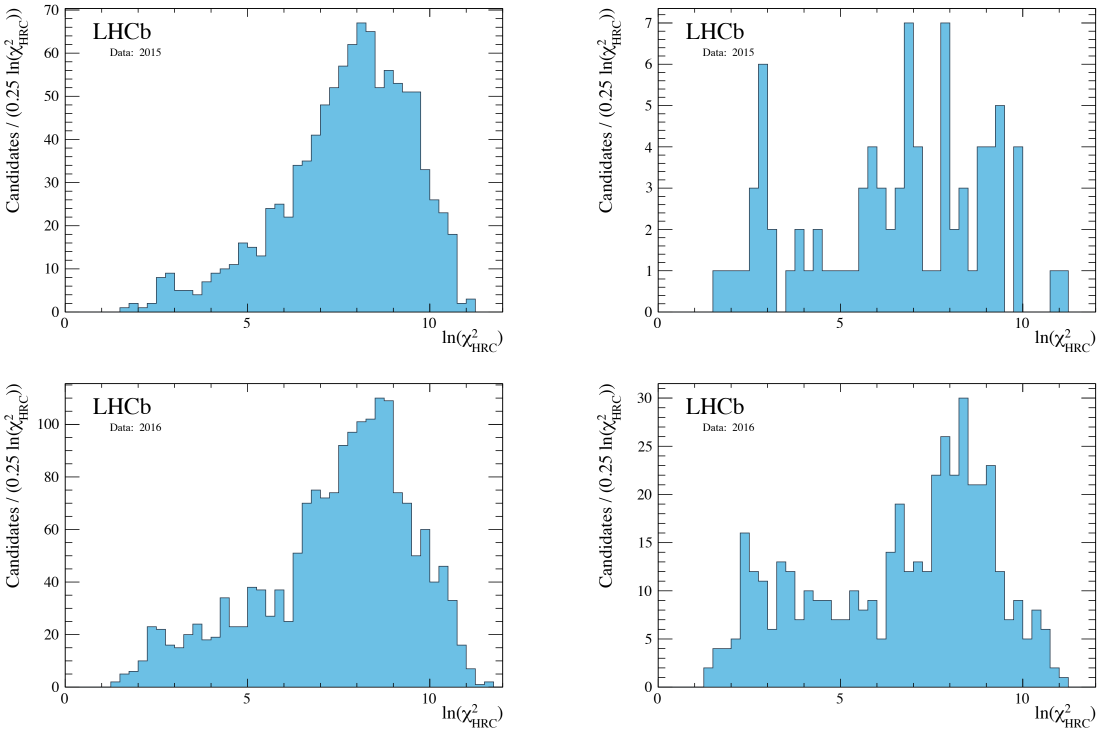

Figure 4.4. Logarithm distribution of the HeRSChel discrimination variable, $\ln(\chi^2_{\mathrm{HRC}})$, for $\chi_c \to J/\psi\,[\mu^+\mu^-]\gamma[e^+e^-]$ candidates before (left) and after (right) the CEP-rapidity-gap-track selection is applied in 2015 (top) and 2016 (bottom).

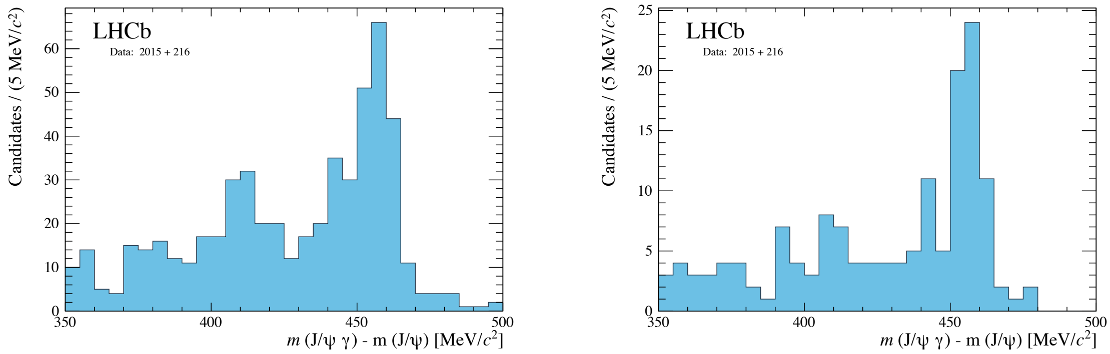

Figure 4.5. Delta-mass distribution of CEP χ_c selection before (left) and after (right) the HeRSChel cut is applied.

allowing us to put our understanding of fundamental physics to test. In this section, we introduce the Monte Carlo samples used throughout this analysis.

CEP χ_c Monte Carlo

Approximately one million $\chi_{c1,2} \to J/\psi\gamma$ events were generated using the LHCb central-production framework for Monte Carlo simulations for each of the χ_{c1} and χ_{c2} mesons, as well as each of the magnet polarities using the *particle gun* (`pGun`) method in conjunction with

SuperChic v2. The number of events generated for each configuration are summarised in Table 4.5. The pGun method is fully incorporated into the LHCb simulation framework. It is capable of generating one or several particles coming from the same vertex according to a specified PDG particle ID and a set of momentum distributions taken as input. The vertex is randomly spread around the nominal-interaction point according to a Gaussian distribution that is representative of a typical collision at LHCb.

Table 4.5. Summary of the number of CEP $\chi_c \to J/\psi\gamma$ Monte Carlo events generated for 2015 and 2016 run conditions.

Magnet Polarity	**Year**	χ_{c1}	χ_{c2}
Up	2015	1,311,819	1,169,524
Up	2016	1,128,492	1,006,600
Down	2015	1,081,398	1,170,477
Down	2016	1,296,204	1,201,728

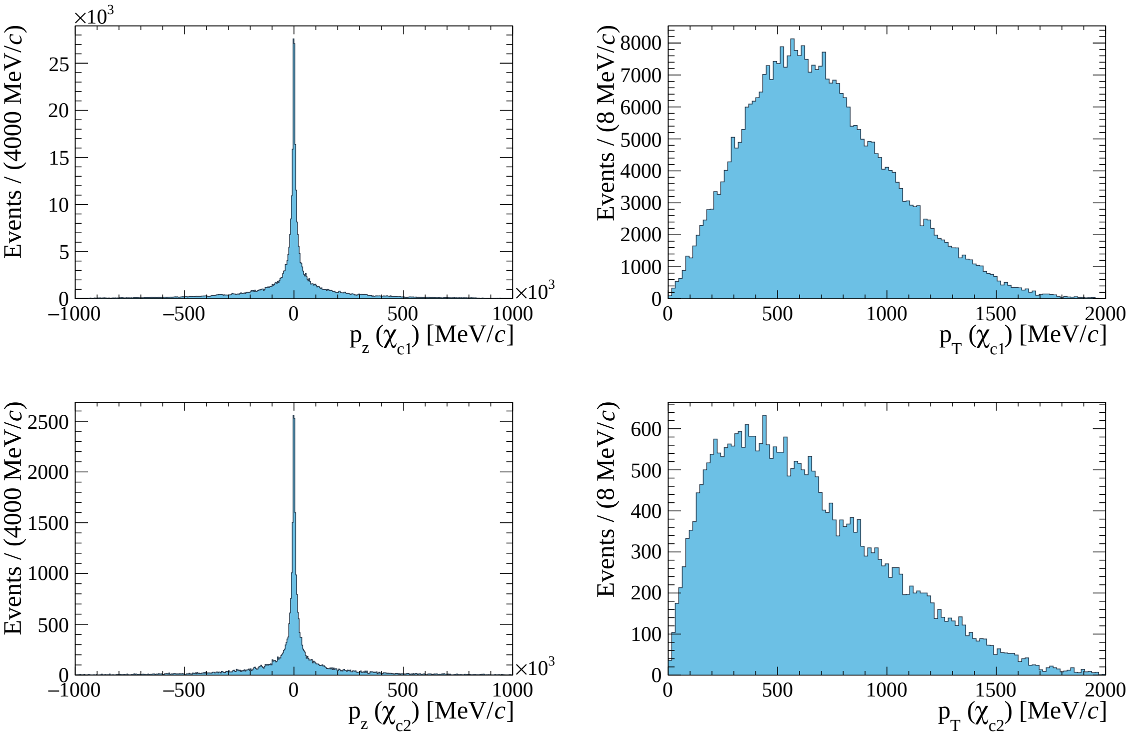

Figure 4.6. Generator-level p_z distribution (left), and p_T (right) for χ_{c1} (top), and χ_{c2} (bottom). These distributions were generated by SuperChic v2 for pp collisions with a centre-of-mass energy $\sqrt{s} = 13\,\text{TeV}$.

The momentum distribution of the χ_c mesons, show in Fig. 4.6, is calculated using the SuperChic v2.03 [83–85, 131] generator, described in Sec. 3.11, with the `MMHT2014lo68cl` ($\alpha_S(M_Z^2) = 0.135$) [132] PDF set. We select a leading-order (LO) PDF to match the $gg \to \chi_c$ vertex calculation which is calculated to leading order by SuperChic. The generator implements four versions of the two-channel eikonal model as described in Ref. [79] to describe proton dissociation. The simulations are run with "soft-survival model four", which describes the interaction via an effective pomeron and allows its coupling to the diffraction eigenstates to depend on the collider energy. This model successfully describes diffraction into low and high-mass systems at the LHC. The number of events generated for each of the run conditions is summarised in Table 4.5.

After the event generation, the χ_c mesons are forced to decay into a $J/\psi\gamma$ with the J/ψ decaying into a pair of muons that fall within the acceptance of the main LHCb spectrometer. The events are then propagated through the LHCb simulation framework, described in Sec. 3.11. This includes the propagation of particles, material interactions, detector response and signal digitisation. After digitisation the Monte Carlo can be treated as standard data and propagated through the trigger and stripping pipe-line.

$\psi(2S)$ feed-down Monte Carlo

To calculate the contribution of $\psi(2S)$ feed-down background, we use a *cocktail* sample of $100,000$ simulated CEP $\psi(2S) \to J/\psi X$ events generated with SuperChic for pp collisions at a centre-of-mass energy $\sqrt{s} = 13$ TeV. Here X represents all possible decay products in a $\psi(2S)$ decays containing a J/ψ meson. The contribution of each decay is proportional to the decay branching fractions, summarised in Table 4.6.

Table 4.6. Branching fractions of relevant $\psi(2S) \to J/\psi X$ decays, taken from the PDG [86].

Variable	**Value**
$\mathcal{B}(\psi(2S) \to \chi_{c0}\gamma)$	(9.79 ± 0.27) %
$\mathcal{B}(\psi(2S) \to \chi_{c1}\gamma)$	(9.75 ± 0.20) %
$\mathcal{B}(\psi(2S) \to \chi_{c2}\gamma)$	(9.52 ± 0.24) %
$\mathcal{B}(\psi(2S) \to J/\psi\gamma\gamma)$	(0.031 ± 0.010) %
$\mathcal{B}(\psi(2S) \to J/\psi\eta)$	(3.37 ± 0.05) %
$\mathcal{B}(\psi(2S) \to J/\psi\pi^0)$	(0.1268 ± 0.0032) %
$\mathcal{B}(\psi(2S) \to J/\psi\pi^0\pi^0)$	(18.24 ± 0.31) %
$\mathcal{B}(\chi_{c0} \to J/\psi\gamma)$	(1.4 ± 0.05) %
$\mathcal{B}(\chi_{c1} \to J/\psi\gamma)$	(34.3 ± 1.0) %
$\mathcal{B}(\chi_{c2} \to J/\psi\gamma)$	(19.0 ± 0.5) %
$\mathcal{B}(J/\psi(1S) \to \mu^+\mu^-)$	(5.961 ± 0.033) %
$\mathcal{B}(\eta \to \gamma\gamma)$	(39.41 ± 0.2) %
$\mathcal{B}(\pi^0 \to \gamma\gamma)$	(98.823 ± 0.034) %

The $\psi(2S)$ mesons are generated according to the assumed shape for the hadronic form factor, reflecting the size and shape of the proton described in Sec. 2.5.1. The $\psi(2S)$ mesons are also produced according to a flat distribution in the azimuthal angle (ϕ), and restricted to rapidities within the LHCb acceptance, $2 < \eta < 4.5$. The $\psi(2S)$ mesons are then decayed using Pythia version 6.205, with the J/ψ forced to decay into a pair of muons. These events are then processed by the LHCb detector simulation, digitisation, and reconstruction chain for 2015 run conditions.

4.2 Converted-photon study: data sets, selection criteria, and simulation

Having a good understanding of the photon-conversion efficiency is crucial for the success of the CEP χ_c study. Moreover, the determination of this photon-conversion efficiency is particularly challenging as we are dealing with low-momentum photons, a characteristic which stems from the low-energy transfer required to avoid proton dissociation by CEP. As a result, we have developed a new method through which we are able to measure the photon-conversion efficiency of soft-photons at the LHCb using $D^{*0} \to D^0[K^\pm\pi^\mp]\gamma$ radiative decay, described in Sec. 5.1. Although the approach is primarily data driven, simulation input is required for some aspects. In the following sections we introduce the data and simulation samples required for this study, followed by a description of the event-selection criteria. A schematic of the $D^{*0} \to D^0[K^\pm\pi^\mp]\gamma$ decay is shown in Fig. 4.7 depicting the characteristic displaced vertex of the long-lived D^0 meson.

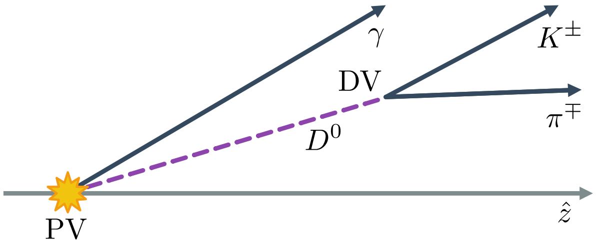

Figure 4.7. Schematic depicting the production of a $D^{*0} \to D^0[K^\pm\pi^\mp]\gamma$ meson including the primary vertex (PV) of the pp collision and the displaced vertex of the long lived D^0.

4.2.1 D^{*0} and D^0 data set

We use pp collisions at a centre-of-mass energy $\sqrt{s} = 13\,\text{TeV}$, collected during the 2016 run comprising of a total integrated luminosity of $\mathcal{L}_{\text{int}}^{2016} = 1665\,\text{pb}^{-1}$. The photon-conversion efficiency measurement requires both a $D^{*0} \to D^0[K^\pm\pi^\mp]\gamma$ and a $D^0[K^\pm\pi^\mp]$ inclusive sample. In both samples, the D^0 candidates originate from the `Hlt2CharmHadD02KmPipTurbo` Turbo-stream line and are selected identically. As a reminder, a Turbo stream is a data-processing stream that uses fully reconstructed information as part of the event selection during the software-trigger stage, as is described in Sec. 3.10.3. The online data selection pipe-line is summarised in Table 4.7 and described in Sec. 4.2.2.

The photon-conversion-efficiency study is performed exclusively with 2016 data since the HLT2 line necessary for the study, `Hlt2CharmHadD02KmPipTurbo`, was not run during 2015. In addition, during 2016, if the requirements were met for a given trigger the entire event was stored. Changes to the nature of the stored information means that this analysis cannot be performed on the 2017 and 2018 data.

Table 4.7. Summary of the data set used in the photon-conversion-efficiency study.

	Data pipeline
`L0`	`L0Hadron`
HLT1	`Hlt1TrackMVA` || `Hlt1TwoTrackMVA`
HLT2 `/Turbo`	`Hlt2CharmHadD02KmPipTurbo`

4.2.2 D^{*0} and D^0 online-selection criteria

To study the converted-photon reconstruction efficiency in an unbiased manner we make sure that the trigger criteria are independent of the photon. The D^0 mesons are required to pass the `L0Hadron` trigger decisions, either `Hlt1TrackMVA` or `Hlt1TwoTrackMVA` decision lines, and the `Hlt2CharmHadD02KmPipTurbo` Turbo stream.

D^{*0} and D^0 L0 trigger-selection criteria

The `L0Hadron` trigger has two main criteria. The first selects events with a cluster in the hadronic calorimeter, a group of 2×2 cells, with transverse energy greater than 3.7 GeV. This threshold is chosen to meet the finite rate at which the detector channels can be read, and to select b- and c-hadron decays, which have a characteristically high transverse energy. The threshold value was adjusted slightly throughout the 2016 data collection period. At this stage, the transverse energy is estimated by summing over the energy deposits, E_i, in the cluster's i^{th} cell and over all calorimeter layers, while accounting for the polar angle, θ_i, which measured from the interaction point such that

$$E_T = \sum_{i=1}^{4} E_i \sin\theta_i. \tag{4.6}$$

The second criterion limits the event multiplicity by placing a cap of 450 on the number of SPD hits. The `L0Hadron` selection criteria are summarised in Table 4.8.

D^{*0} and D^0 HLT1 trigger-selection criteria

At the HLT1 level, the events must pass either the `Hlt1TrackMVA` or the `Hlt1TwoTrackMVA` trigger lines [128]. In the case of `Hlt1TrackMVA`, at least one of the mesons from the $D^0 \to K^{\pm}\pi^{\mp}$ decay is required to result in a well-reconstructed track, which is characterised by a large transverse momentum and a significant impact parameter (IP) relative to the primary vertex (PV). A schematic depicting the IP of a track is shown in Fig. 4.8 alongside other important parameters to the discussion of the software trigger requirements.

The track-reconstruction-quality requirement is met through two reconstruction-quality cuts: $\chi^2_{\text{Track}}/\text{dof} < 2.5$ and $P^{\text{Ghost}}_{\text{Track}} < 0.2$. The former is the χ^2 per degrees-of-freedom associated to the track fit. The latter is the probability that a track is fake, as previously described in Sec. 4.1.3.

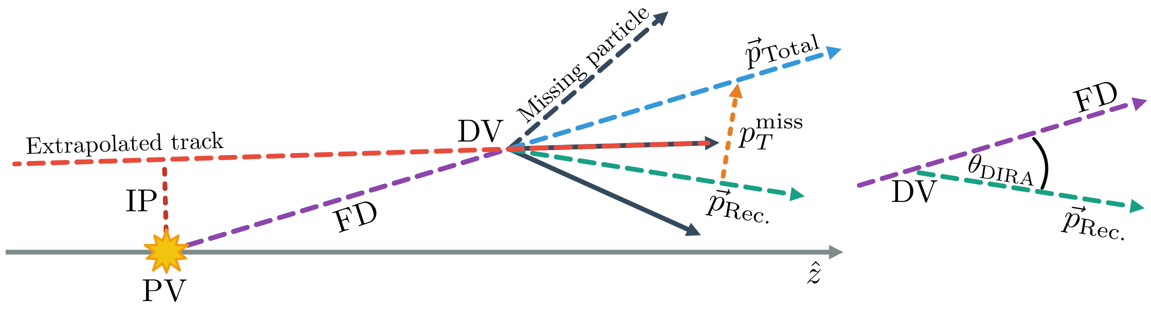

Figure 4.8. Schematic depicting parameters of events with long-lived particles produced at the primary vertex (PV in yellow), which decays after a flight distance (FD in dashed purple) into a three-particle final state (in black) with a summed three-momentum $\vec{p}_{Total}$ and displaced vertex (DV). Two of the particles are reconstructed (solid black) with summed three-momentum $\vec{p}_{\text{Rec.}}$ (dashed green) while one particle is not reconstructed (dashed black) with transverse momentum p_T^{miss}. The track of one of the reconstructed particles is extrapolated (dashed red) and the shortest distance to the PV, known as the impact parameter (IP), is marked (dashed-dark red). The angle between the $\vec{p}_{Total}$ and the vector formed by the PV and the DV, known as the directional angle θ_{DIRA}, is shown on the right.

The remainder of the criteria focuses on selecting tracks that are likely to originate from long-lived particles, such as the D^0 meson. This is achieved by identifying potential displaced vertices (DV). A fit of the PV is performed with and without the track considered and the difference between these fits results in a χ^2_{IP} value. Particles originating from secondary vertices tend to have large χ^2_{IP} values. A two-dimensional cut of this variable is then performed in tandem with the tracks' transverse momentum such that

$$p_{\text{T}} > 25 \quad \text{and} \quad \chi^2_{\text{IP}} > 7.4, \tag{4.7}$$

or

$$1 < p_{\text{T}} < 25 \quad \text{and} \quad \chi^2_{\text{IP}} > \ln(7.4) + \frac{1}{(p_{\text{T}} - 1)^2} + 1.2\left(1 - \frac{p_{\text{T}}}{25}\right), \tag{4.8}$$

where the transverse momentum is measured in GeV/c.

Alternatively, both of the hadrons from the D^0 decay can meet the criteria of `Hlt1TwoTrackMVA`, which requires two long, oppositely charged, well-reconstructed, high-momentum tracks. We define well-reconstructed tracks according to the track fit χ^2, requiring $\chi^2_{\text{Track}}/\text{dof} < 2.5$. A cut is applied to the track momentum, $p > 5$ GeV/c, the transverse momentum, $p_{\text{T}} > 500$ MeV/c, and the sum of the transverse momentum of the two tracks, $\sum p_{\text{T}} = p_{\text{T}}(h^+) + p_{\text{T}}(h^-) > 2$ GeV/c). The two tracks are required to originate from a DV by considering their displacement relative to the PV, $\chi^2_{\text{IP}} > 2.5$.

A set of cuts is also applied to the combined h^+h^- system. The D^0 candidate is required to have a rapidity within the acceptance of the main spectrometer, $2 < \eta < 5$. The mass of D^0

meson candidates, m_{D^0}, is corrected with respect to particle-flight direction such that

$$m_{\text{corr}} \equiv \sqrt{m_{D^0}^2 + |p_{\text{T}}^{\text{miss}}|^2} + p_{\text{T}}^{\text{miss}}, \tag{4.9}$$

where p_T^{miss} is the missing momentum transverse to the direction of flight of the D^0. This correction is used to account for missing-transverse momentum from partially reconstructed decays, such as those that include neutrinos, which might result in a lower-mass reconstruction of the parent particle. The directional angle, θ_{DIRA}, is the angle between the line drawn from the PV to the DV, and the three-momentum sum of the D^0 candidate's decay products. We expect θ_{DIRA} to be zero for particles originating from primary vertices, and non-zero for both secondary decays and partially reconstructed decays. At this stage, the cosine of the angle is expected to be greater than zero which prevents the DV from being behind the PV. The quality of the vertex fit using the two tracks is evaluated by requesting a $\chi^2_{\text{Vertex}} < 10$.

Additionally, a boosted-decision-tree (BDT) classifier is used with the following inputs: the flight distance between the PV and the DV (χ^2_{FD}), $\sum p_{\text{T}}$, the number of tracks with $\chi^2_{\text{IP}} > 16$, and the the χ^2_{DV} of the displaced-vertex fit. A threshold of 0.96 is set on the BDT figure-of-merit. The entire selection criteria of these trigger lines are specified in Table 4.8.

D^{*0} and D^0 HLT2 trigger-selection criteria

At the HLT2 level, events are selected by the `Hlt2CharmHadD02KmPipTurbo` line, which is designed to identify and select $D^0 \to K^{\pm}\pi^{\mp}$ mesons with displaced vertices. This selection tightens the minimum transverse-momentum requirement of the hadron tracks to 800 MeV/c and one of the daughters is required to have p_{T} larger than 1500 MeV/c. Particle identification is applied to the $K^{\pm}$ and $\pi^{\pm}$ candidates such that the log-likelihood difference relative to the pion hypothesis (described in Eq. 3.10.2) is $\Delta \log \mathcal{L}_{K-\pi} > 5$ and $\Delta \log \mathcal{L}_{K-\pi} < 5$, respectively. The efficiency and fake rate for this cut is shown in Fig. 4.9 as a function of the meson's momentum.

A series of cuts associated with the D^0 DV is then applied. The χ^2 distance between a track and the PV is expected to be greater than four, the distance of closest approach (DOCA) of each track to the DV is required to be within 0.1 mm, and the minimum χ^2_{FD}-distance between the PV and the DV is required to be greater than 25. The contribution of secondary charm mesons produced from B-meson decays is low and is reduced to negligible levels by requiring that the D^0 candidate point back to the primary vertex. To this end, the angle θ_{DIRA} (described above) is capped at 17.3 mrad. Finally, the minimum transverse momentum of the D^0 candidate is set at 2 GeV/c and its invariant-mass window is limited to the $1715 < m(D^0) < 2015$ MeV/c^2 range. The selection criteria of these trigger lines are specified in Table 4.8.

4.2.3 D^{*0} and D^0 offline-selection criteria

Unlike the CEP χ_c sample, events processed by Turbo are directly available for analysis and stripping is not required. To ensure that the data sample is not biased, we require that the trigger decision is based on the D^0 meson, or three daughter hadrons, and is independent of

Table 4.8. Summary of the trigger-level-selection criteria used for the reconstruction of $D^0 \to K^{\pm}\pi^{\mp}$ and $D^*(2007)^0 \to D^0[K^{\pm}\pi^{\mp}]\gamma[e^+e^-]$ decay modes for 2016 data .

Variable	**Cuts**	**Units**
	`L0Hadron`	
$E_{\mathrm{T}}(h^{\pm})$	> 3.7	GeV
SPD Hits	< 450	–
Prescale	1	–
	`HLT1TrackMVA`	
$p_{\mathrm{T}}(h^{\pm})$, χ^2_{IP}	Eq. 4.7 || Eq. 4.8	GeV/c, –
$\chi^2_{\mathrm{Track}}/\mathrm{DoF}$	< 2.5	–
$P^{\mathrm{Ghost}}_{\mathrm{Track}}$	< 0.2	–
	`HLT1TwoTrackMVA`	
$p(h^{\pm})$	> 5000	MeV/c
$p_{\mathrm{T}}(h^{\pm})$	> 500	MeV/c
χ^2 track distance to PV	> 4	–
χ^2_{IP}	> 2.5	MeV/c
$\chi^2_{\mathrm{Track}}/\mathrm{DoF}$	> 4.0	MeV/c
$\eta(h^+h^-)$	$\in [2, 5]$	–
m_{corr}	$\in [1, 10^6]$	GeV/c^2
θ_{DIRA}	> 0	–
Σp_{T}	> 2	GeV/c
Vertex χ^2	< 10	–
BDT threshold	0.96	–
	`Hlt2CharmHadD02KmPipTurbo`	
$\Delta \log \mathcal{L}_{K-\pi}(K^{\pm})$	> 5	–
$\Delta \log \mathcal{L}_{K-\pi}(\pi^{\pm})$	< 5	–
$p(h^{\pm})$	> 5000	MeV/c
$p_{\mathrm{T}}(h^{\pm})$	> 800	MeV/c
$p_{\mathrm{T}}(h^+)$ || $p_{\mathrm{T}}(h^-)$	> 1500	MeV/c
$K^{\pm}\pi^{\mp}$ pair `DOCA`	< 0.1	mm
χ^2 track distance to PV	> 4	–
D^0 χ^2_{FD}	> 25	–
θ_{DIRA}	< 17.3	mrad
Vertex χ^2	< 10	–
$p_{\mathrm{T}}(D^0)$	> 2000	MeV/c
m(D^0)	$\in [1715, 2015]$	MeV/c^2

the photon reconstruction for all L0 and HLT1 physics lines. The offline-selection criteria are summarised in Table 4.9.

The D^0 invariant-mass is restricted to a 50 MeV/c^2 window centered around the D^0 nominal mass. The transverse momentum of the D^0 mesons is constrained within the range of 2 to

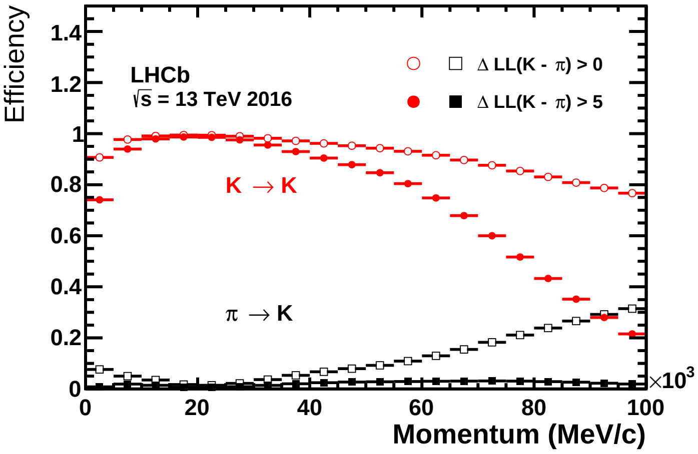

Figure 4.9. Kaon identification efficiency and pion misidentification rate as a function of track momentum using RICH information for two different PID requirements (open and filled marker) for 2016 proton-proton collisions at a centre-of-mass energy of $\sqrt{s} = 13\,\text{TeV}$. Reproduced from [133].

15 GeV/c and a fiducial cut is applied such that the daughters of the D^0 mesons have a pseudorapidity between 2 and 4.5. At this point the D^0 selection is complete and approximately 139 million D^0 candidates pass the selection. Their invariant-mass distribution is shown in Fig. 4.10. However in the case of D^{*0} we apply an additional set of selections associated with the photon and the reconstructed D^{*0} candidate.

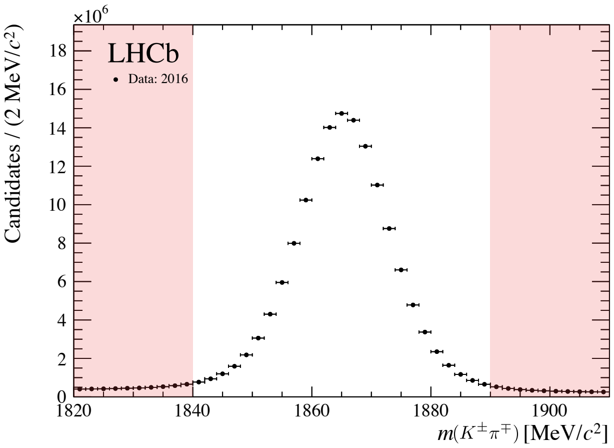

Figure 4.10. Invariant-mass distribution of D^0 candidates. The veto windows are highlighted in red.

To form the D^{*0} candidates, the converted photons are selected and reconstructed with the same requirements as the CEP χ_c meson analysis, see Sec. 4.1.3. The effects of the two-dimensional cuts are shown in Fig. 4.11, along with the accepted (blue) and rejected (red) $m(D^0\gamma) - m(D^0)$ distributions showing that this cut is effective at removing background. The two vertical lines around 2300 and 2600 mm correspond to the two TT tracker planes, where most of the conversions occur. Events to the left of the nominal interaction point are clearly non-physical and tend to have large measurement uncertainties. A comparison of truth-matched Monte Carlo and data shows that events with high $m(e^+e^-)$ and $z_{\gamma_{\text{Conv}}}$ are combinatorial background. High $m(e^+e^-)$ values correspond to background or they must be poorly reconstructed signal. The transverse momentum of the converted photons is capped at a maximum of 1600 MeV/c, which fully covers the kinematic range of the photons in the χ_c sample. We restrict our selection to D^{*0} mesons with a mass within 1900 and 2100 MeV/c^2.

Table 4.9. Offline-selection criteria for $D^{*0} \to D^0[K^\pm\pi^\mp]\gamma[e^+e^-]$ and $D^0 \to K^\pm\pi^\mp$ samples.

Variable	**Cut**	**Units**
	$\boldsymbol{D^0[K^\pm\pi^\mp]}$	
$p_{\mathrm{T}}(D^0)$	$\in [2, 15]$	GeV/c
$\eta(D^0)$	$\in [2, 4.5]$	–
m(D^0)	$\in [1840, 1890]$	MeV/c^2
	$\boldsymbol{\gamma[e^+e^-]}$	
$e^\pm$ track type	Downstream	–
ECAL position	$\Delta y < 3\sigma \; \| \; \Delta y_{max} < 20$ [cm]	–
$p_{\mathrm{T}}(e^+e^-)$	< 1600	MeV/c
$p_{\mathrm{T}}(e^\pm)$	> 0	MeV/c
γ 2D cut	Eq. 4.2 || Eq. 4.3 || Eq. 4.4	–
	$\boldsymbol{D^{*0}}$	
m(D^{*0})	$\in [1900, 2100]$	MeV/c^2

4.2.4 Simulation samples for converted-photon study

This photon-conversion-efficiency calculation requires three different Monte Carlo samples. The first is a $D^{*0} \to D^0[K^\pm\pi^\mp]\gamma$ Monte Carlo sample that consists of 64 million events, with equal proportions for each magnet polarity setting produced with the pGun method, described in Sec. 4.1.4. The kinematic phase space for the D^{*0} mesons was calculated using Pythia 8 for its production in pp collisions at a centre-of-mass energy of $\sqrt{s} = 13$ TeV. The events are decayed with EvtGen and then processed by the LHCb simulation framework under 2016 run conditions. We use this sample to extract invariant-mass-difference distributions for different photon transverse-momentum ranges. We also use the generator-level information to model the photon transverse-momentum dependence of the total number of D^{*0} mesons, as described in Sec. 5.1.5. The second sample, generated using the same method, consists of 84 million $D^{*0} \to D^0[K^\pm\pi^\mp]\pi^0[\gamma\gamma]$ events, with equal parts for each magnet polarity setting. This sample is used to model the background for our $D^{*0} \to D^0[K^\pm\pi^\mp]\gamma$ selection where one of the photons from the π^0 decay is not reconstructed.

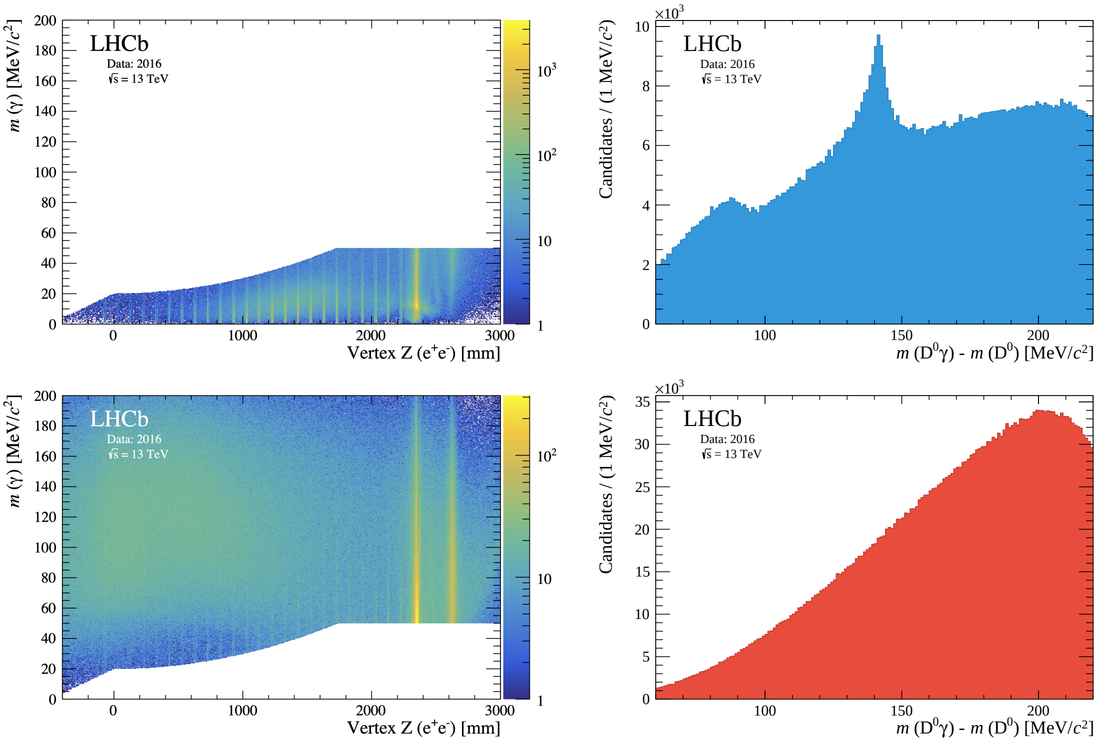

Figure 4.11. Two dimensional cut of the di-electron invariant mass vs. photon Z-Vertex (left) and invariant-mass-difference distribution (right) of selected (top) and rejected (bottom) D^{*0} meson candidates from the 2016 data set, based on a two-dimensional cut.

The third sample consists of a centrally produced D^{*0} Monte Carlo generated with PYTHIA 6 [124] for pp collisions at a centre-of-mass energy $\sqrt{s} = 13\,\text{TeV}$ under 2015 run conditions for each of the magnet polarities. In this sample the D^{*0} mesons are forced to decay into $D^0\pi^0$ and $D^0\gamma$ but only the latter component is used for this study. Meanwhile, the D^0 mesons are forced to decay into $K^{\pm}\pi^{\mp}$. The sample consists of 5,840,161 events, of which 2,943,685 are simulated with the magnetic field of the dipole magnet pointing up and 2,896,476 events with the magnetic field pointing down. This sample is used to validate the method by which we calculate the photon transverse-momentum dependence of the total number of D^{*0} mesons, described in Sec. 5.1.5. This sample is statistically limited and, as we will see, the photon-conversion efficiency for low-momentum photons is very low. Consequently, we are unable to use that sample to extract reliable invariant-mass-difference distributions for different photon transverse-momentum ranges, and instead rely on the sample described above for this.

Chapter 5

Efficiency determination

In this chapter we present a series of studies used to determine reconstruction and selection efficiencies at different stages of the CEP χ_c analysis. In Sec. 5.1 we present the photon-conversion-efficiency study as a function of the transverse momentum of the photon as well as its dependence on the event multiplicity, followed by the study of the efficiency associated with the muon reconstruction and selection in Sec. 5.2. The efficiency of the J/ψ mass-window and the χ_c mass-difference-window cut are discussed in Sec. 5.3 and Sec. 5.4, respectively. The efficiency of the low-multiplicity requirement at the hardware-trigger level is discussed in Sec. 5.5, followed by a study of the performance of the HeRSCheL figure-of-merit in Sec. 5.6.3.

5.1 Determination of the photon-conversion efficiency

Although the combined conversion probability and reconstruction efficiency of photons ($\varepsilon_{\gamma\to e^+e^-}$) at the LHCb experiment has been studied in the past, a couple of factors make the determination for photons from CEP events non-trivial. Previous $\varepsilon_{\gamma\to e^+e^-}$ studies have not been performed for photons with transverse momenta as low as those observed in the CEP χ_c selection. Furthermore, $\varepsilon_{\gamma\to e^+e^-}$ has a significant dependence on the transverse momentum of the photon, which makes the extrapolation of previous measurements into our soft regime unreliable. Previous studies have been performed on hard-scattering events [134,135]. Although these types of events provide a statistical advantage, they are characterised by a high detector occupancy. In comparison, the low-multiplicity of CEP events provides a favourable environment for the reconstruction of the electron tracks associated with the photon, which should result in a higher efficiency for a given photon's transverse momentum.

5.1.1 Strategy for the determination of the photon-conversion efficiency

The probability for a photon conversion to occur and the efficiency for it to be reconstructed by the LHCb spectrometer can be written as follows:

$$\epsilon_{\gamma\to e^+e^-} = \frac{N_{\gamma\to e^+e^-}}{N_{\gamma_{\rm All}}}, \tag{5.1}$$

where $N_{\gamma\to e^+e^-}$ is the number of photons within a sample that undergo photon conversion into an electron-position pair and are fully reconstructed by LHCb, while $N_{\gamma_{\rm All}}$ is the initial number of photons in the same data sample, whether or not they have converted.

To take advantage of LHCb's excellent performance at reconstructing charmed mesons, we use a data-driven approach using $D^*(2007)^0$ mesons to calculate the photon-conversion efficiency. In particular, we use $D^*(2007)^0 \to D^0[K^\pm\pi^\mp]\gamma[e^+e^-]$ decays. Henceforth, D^{*0} should be taken to mean $D^*(2007)^0$ mesons, and when we speak of D^{*0} candidates it should be assumed that we speak of $D^{*0} \to D^0[K^\pm\pi^\mp]\gamma$ decays. Of course, there is some inefficiency associated with the reconstruction of the $D^0 \to K^\pm\pi^\mp$ decay itself. Thus, we seek to measure

$$\epsilon_{\gamma\to e^+e^-} = \frac{N_{\text{Conv}}(D^{*0})}{N_{\text{All}}(D^{*0}|D^0)} , \tag{5.2}$$

where $N_{\text{Conv}}(D^{*0})$ denotes the number of reconstructed and selected D^{*0} mesons using downstream converted photons, and $N_{\text{All}}(D^{*0}|D^0)$ denotes the number of D^{*0} decays in which the D^0 mesons would be reconstructed and selected given the criteria presented in Sec. 4.2, independent of the photon detection.

To calculate the number of D^{*0} mesons produced in our sample, we invoke isospin symmetry and take advantage of the results from a previous LHCb measurement of inclusive cross-section measurement of D^{*+} and D^0 mesons at a centre-of-mass energy of $\sqrt{s} = 13\,\text{TeV}$ [136]. By isospin symmetry we expect the same number of D^{*0} as D^{*+} to be produced in the LHCb detector. Therefore, we can use the number of all D^0 mesons in the sample $N(D^0)$ to calculate $N_{\text{All}}(D^{*0}|D^0)$ within the LHCb acceptance such that,

$$N_{\text{All}}(D^{*0}|D^0) = N(D^0) \cdot \frac{\mathcal{B}(D^{*0} \to D^0\gamma)}{\mathcal{B}(D^{*+} \to D^0\pi^+)} \cdot r(D^{*+}/D^0), \tag{5.3}$$

where $\mathcal{B}(D^{*0} \to D^0\gamma) = (35.3 \pm 0.9)\%$ and $\mathcal{B}(D^{*+} \to D^0\pi^+) = (67.7 \pm 0.5)\%$ are the branching fractions of their corresponding decays as given by the PDG [86], and $r(D^{*+}/D^0)$ is the ratio of the cross-sections times their corresponding branching fraction of $D^{*+} \to D^0[K^\pm\pi^\mp]\pi^+$ and $D^0 \to K^\pm\pi^\mp$ as calculated in the LHCb paper referenced above.

The ratio $r(D^{*+}/D^0)$ has been measured in bins of the charmed meson rapidity, in the $2.0 < y < 4.5$ range, and its transverse momentum, in the $p_{\text{T}} < 15$ GeV/c range. These results are tabulated in Table 5.1 and are plotted in Fig. 5.1. Here we observe evidence of significant variation with the transverse momentum of D^0, but less so with its rapidity. We weight these $r(D^{*+}/D^0)$ values by the transverse momentum and rapidity distributions of the D^0 mesons in our inclusive D^0 selection, to calculate a $r(D^{*+}/D^0)$ central value that is representative of our sample.

The average transverse momentum of a photon in $D^{*0} \to D^0\gamma$ decays is higher than that of photons from CEP $\chi_c \to J/\psi\gamma$ decays. Since the kinematics of the photon in D^{*0} decays are strongly correlated to the kinematics of the D^0 meson, we are able to better match the kinematics of the D^{*0} photons to those in our CEP χ_c sample by placing an upper limit cut on the transverse momentum of the D^0. As a result, we require that the transverse momentum of

Table 5.1. The ratios of differential production cross-section-times-branching-fraction for prompt $D^{*+} \to D^0[K^{\pm}\pi^{\mp}]\pi^+$ and $D^0 \to K^{\pm}\pi^{\mp}$ mesons, $r(D^{*+}/D^0)$, in bins of (p_{T}, y). The first uncertainty is statistical and the second is systematic. All values are given in percent [136] .

			y		
p_{T} [GeV/c]	**[2.0, 2.5]**	**[2.5, 3.0]**	**[3.0, 3.5]**	**[3.5, 4.0]**	**[4.0, 4.5]**
[0.0 – 1.0]	-	-	-	-	$21.9^{+3.0+6.7}_{-3.0-6.3}$
[1.0 – 1.5]	-	$18.3^{+0.8+2.0}_{-0.8-2.0}$	$22.6^{+0.3+1.3}_{-0.3-1.6}$	$20.3^{+0.3+1.4}_{-0.3-1.5}$	$25.5^{+0.8+3.7}_{-0.8-3.1}$
[1.5 – 2.0]	-	$26.3^{+0.5+1.8}_{-0.4-1.6}$	$26.4^{+0.2+1.3}_{-0.2-1.9}$	$24.7^{+0.3+1.5}_{-0.3-1.9}$	$25.5^{+0.6+2.5}_{-0.6-2.0}$
[2.0 – 2.5]	$26.8^{+2.4+5.7}_{-2.4-6.0}$	$26.5^{+0.3+1.9}_{-0.3-1.1}$	$27.4^{+0.2+1.3}_{-0.2-1.8}$	$25.7^{+0.2+1.6}_{-0.2-1.6}$	$25.5^{+0.5+2.6}_{-0.5-2.1}$
[2.5 – 3.0]	$26.8^{+0.9+2.9}_{-0.9-3.1}$	$27.1^{+0.3+1.2}_{-0.3-1.7}$	$27.0^{+0.2+1.6}_{-0.2-1.5}$	$26.0^{+0.2+1.7}_{-0.3-1.7}$	$26.6^{+0.6+1.8}_{-0.6-2.0}$
[3.0 – 3.5]	$27.2^{+0.7+2.2}_{-0.7-2.5}$	$28.3^{+0.2+1.2}_{-0.2-1.9}$	$28.6^{+0.2+1.7}_{-0.2-1.4}$	$25.5^{+0.3+1.8}_{-0.3-1.8}$	$25.9^{+0.6+2.7}_{-0.6-2.2}$
[3.5 – 4.0]	$28.9^{+0.6+2.1}_{-0.6-2.5}$	$29.8^{+0.3+1.4}_{-0.3-2.1}$	$28.9^{+0.2+1.8}_{-0.2-1.4}$	$27.2^{+0.3+1.9}_{-0.3-1.7}$	$27.9^{+0.8_{2}.7}_{-0.8-2.7}$
[4.0 – 5.0]	$28.8^{+0.4+1.4}_{-0.4-2.3}$	$29.2^{+0.2+1.3}_{-0.2-2.0}$	$28.5^{+0.2+1.6}_{-0.2-1.4}$	$28.2^{+0.3+2.0}_{-0.3-1.5}$	$30.2^{+0.9+2.3}_{-0.9-2.2}$
[5.0 – 6.0]	$27.3^{+0.4+1.3}_{-0.4-2.3}$	$29.4^{+0.2+1.4}_{-0.2-2.0}$	$29.9^{+0.3+1.7}_{-0.3-1.3}$	$32.2^{+0.4+2.3}_{-0.5-1.6}$	$31.5^{+2.1+4.1}_{-2.0-3.7}$
[6.0 – 7.0]	$30.9^{+0.5+1.8}_{-0.5-2.6}$	$30.8^{+0.3+1.6}_{-0.3-2.1}$	$29.8^{+0.4+1.7}_{-0.4-1.5}$	$29.5^{+0.6+2.2}_{-0.6-2.2}$	$38.0^{+10.0+24}_{-8.0-17.0}$
[7.0 – 8.0]	$33.1^{+0.7+2.0}_{-0.7-2.9}$	$29.6^{+0.4+1.7}_{-0.4-2.3}$	$31.7^{+0.5+2.2}_{-0.5-1.6}$	$36.8^{+1.3+4.4}_{-1.2-4.3}$	-
[8.0 – 9.0]	$32.3^{+0.8+2.2}_{-0.8-2.9}$	$29.9^{+0.5+1.9}_{-0.5-2.3}$	$31.4^{+0.7+2.8}_{-0.7-1.7}$	$28.0^{+1.8+4.1}_{-1.7-3.4}$	-
[9.0 – 10.0]	$21.8^{+0.7+1.2}_{-0.7-1.7}$	$30.9^{+0.7+1.6}_{-0.7-2.1}$	$30.2^{+0.8+1.6}_{-0.8-1.5}$	$40.6^{+4.8+6.1}_{-4.3-7.0}$	-
[10.0 – 11.0]	$31.8^{+1.2+1.6}_{-1.1-2.2}$	$32.1^{+0.9+1.6}_{-0.9-2.1}$	$34.6^{+1.4+1.8}_{-1.3-1.8}$	$34.0^{+10.0+13.0}_{-8.0-11.0}$	-
[11.0 – 12.0]	$30.8^{+1.3+1.6}_{-1.4-2.5}$	$30.16^{+1.1+1.4}_{-1.1-2.0}$	$31.2^{+1.8+1.6}_{-1.7-1.7}$	-	-
[12.0 – 13.0]	$33.0^{+1.8+2.1}_{-1.8-3.1}$	$32.2^{+1.4+1.6}_{-1.4-2.2}$	$32.8^{+2.5+2.2}_{-2.4-1.8}$	-	-
[13.0 – 14.0]	$34.0^{+2.1+1.8}_{-2.1-3.0}$	$27.6^{+1.6+1.5}_{-1.6-2.0}$	$41.2^{+4.7+3.1}_{-4.3-3.4}$	-	-
[14.0 – 15.0]	$29.7^{+2.5+1.9}_{-2.4-2.4}$	$34.0^{+2.5+2.3}_{-2.3-2.5}$	$27.8^{+5.6+6.7}_{-4.8-5.7}$	-	-

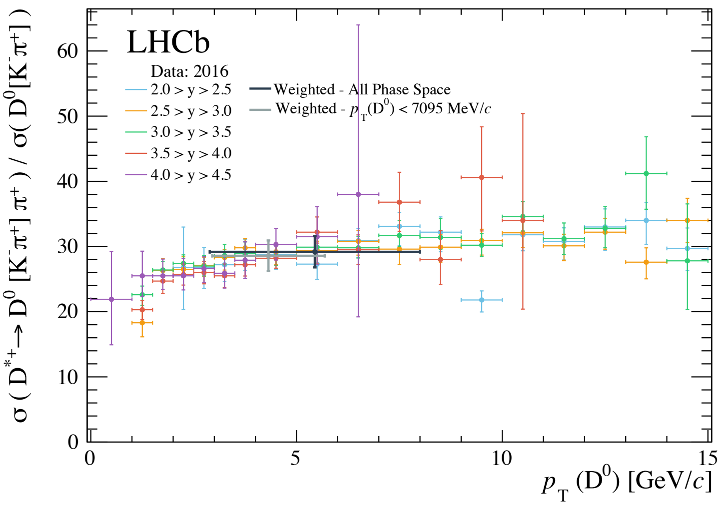

Figure 5.1. The ratios of differential production cross-section-times-branching-fraction for prompt D^{*+} and D^0 mesons as a function of the D^0 meson's transverse momentum and rapidity as determined in Ref. [136]. In addition, we show the ratio averaged over our D^0 meson candidates with $p_{\mathrm{T}} < 7.095\,\mathrm{GeV}$ (in grey) and over the entire D^0 kinematic range in (black).

the D^0 mesons used in the ratio calculation be less than 7.095 GeV/c in order to match the mean of the transverse-momentum distribution of the photons in the χ_c sample.

In a few cases, near the edge of phase space, the uncertainties in the measured cross-section ratios are larger than ten percent. To reduce the effect of these larger uncertainties, we average the value of that (p_{T}, η) bin with that of the nearest bin in p_{T}, then merge the result into a single larger bin. Any event with kinematics for which a ratio has not been calculated is assigned the value of the nearest neighbour in p_{T}.

This procedure results in a value of $r(D^{*+}/D^0) = (28.6 \pm 2.3)\%$, which then can be used in Eq. 5.3 as part of the photon-conversion efficiency calculation. The value is marked in Fig. 5.1 in grey. Here we assign a systematic uncertainty of a relative eight percent which is the combined statistic and systematic uncertainty determined for the average ratio quoted in the prompt-charm paper. (This compares to $(29.19 \pm 2.4)\%$, marked in Fig. 5.1 in black, where the ratio is averaged over the entire D^0 p_{T} kinematic range, 1.8 to 15.0 GeV/c. In this figure, the error bar along the x-axis for these two values are set by the root-mean-squared value of the D^0 transverse-momentum distribution used in each calculation.)

5.1.2 Study of the photon acceptance in the calibration and signal samples

To ensure photons in our D^{*0} calibration sample are representative of those in our CEP χ_c sample in all phase space, we compare the density plots of the photons' pseudorapidity and the logarithm of the photons' transverse momentum. We start with the photons in the D^{*0} sample in Fig. 5.2 (top left) where we observe a clear boundary in the photons' phase space. Low-momentum electrons tend to be deflected out of the spectrometer's acceptance. The electrons closest to the detector's edge are more likely to be expelled from the detector. This boundary can be described empirically with the line overlaid in red such that,

$$\log(p_{\mathrm{T}}(\gamma)) = -0.46 \cdot \eta(\gamma) + 4.1. \tag{5.4}$$

From the χ_c signal sample (top right), we see that all events fall above this boundary and their phase space is well represented by the calibration sample. We observe the same in fully reconstructed and truth-matched Monte Carlo events for χ_{c1} (middle left) and χ_{c2} (middle right) mesons. The differences in the density-plot distributions between the CEP χ_c data sample and the Monte Carlo are attributed to both reconstruction and resolution differences between data and Monte Carlo, specifically due to the bremsstrahlung correction and the contribution of inelastic background events in the data which typically have higher energies. In addition, we look at the generator-level phase-space distribution of the photon in Monte Carlo within our fiducial acceptance, given the reconstruction of a J/ψ. To do this, we reconstruct only the J/ψ mesons from the CEP χ_c Monte Carlo using the same criteria pertaining to the J/ψ from the CEP χ_c selection and save the generator-level information of the accompanying photon. The phase-space-density plots of these photons are shown in Fig. 5.2 for χ_{c1} (bottom left) and χ_{c2}

(bottom right) Monte Carlo, from which we find that approximately 46 (49) percent of $\chi_{c1}(\chi_{c2})$ events fall below this phase space boundary.

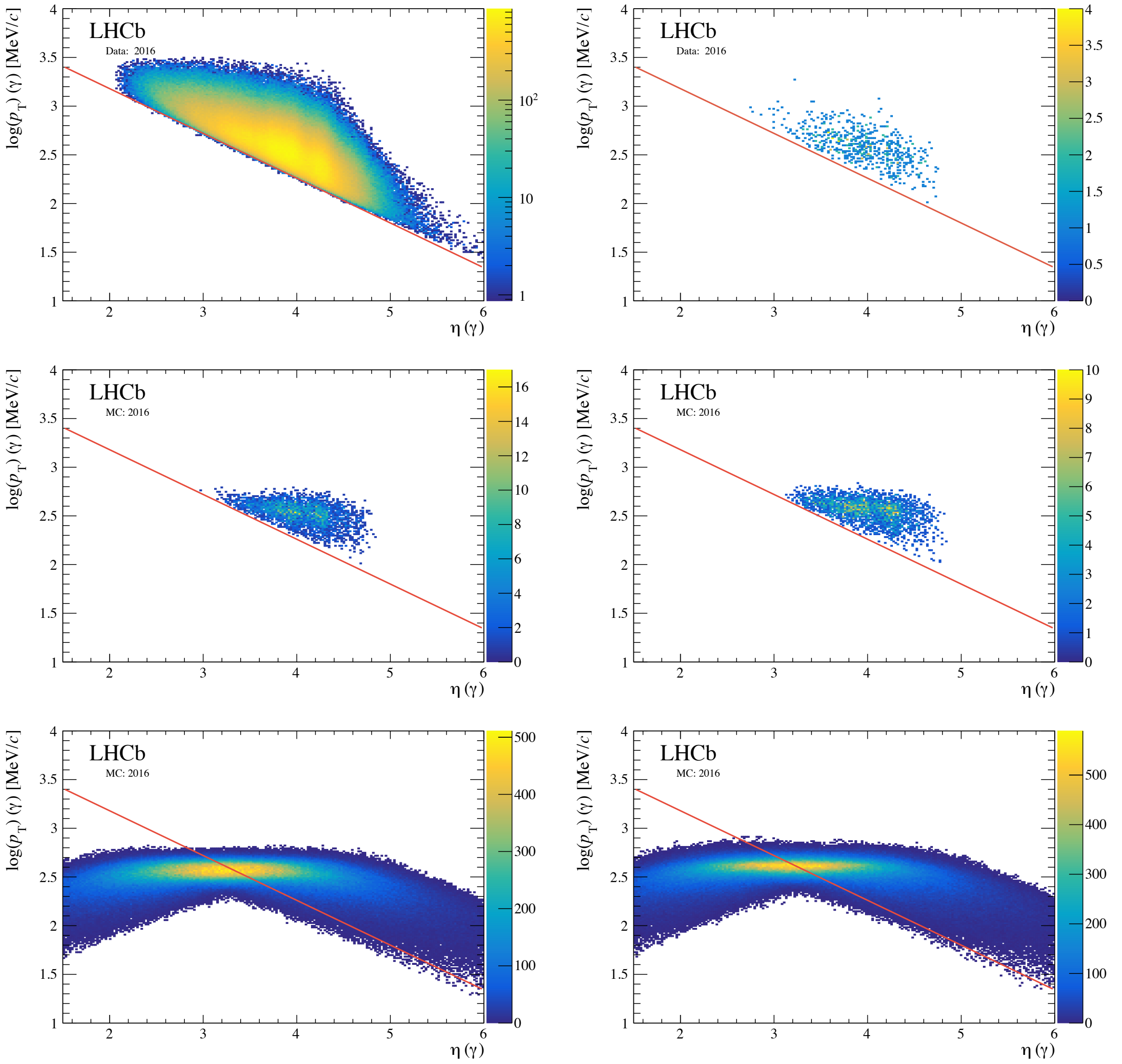

Figure 5.2. Density plots of the photons' pseudorapidity and the logarithm of its transverse momentum for photons from $D^{*0} \to D^0[K^{\pm}\pi^{\mp}]\gamma[e^+e^-]$ candidates (top left), χ_c candidates (top right), χ_{c1} reconstructed Monte Carlo (middle left), χ_{c2} reconstructed Monte Carlo (middle right), χ_{c1} generator-level Monte Carlo (bottom left), and χ_{c2} generator-level Monte Carlo (bottom right). A linear fit is overlaid to show the kinematic limit for the reconstruction of photons in red.

5.1.3 Determination of D^0 yields

To calculate $N(D^0)$ for Eq. 5.3, we fit the mass distribution of $D^0 \to K^{\pm}\pi^{\mp}$ candidates in the $1820 < m(D^0) < 1910\,\text{MeV}/c^2$ mass range. For the signal we use two Gaussian distributions, which share the same mean parameter, and we use a first-order Chebyshev polynomial for the background. The fit results are shown in Fig. 5.3 and the parameter values are detailed in Table 5.2. As is evident from the distribution, this sample has very low combinatoric background, however to suppress it further we count the number of D^0 candidates within a window of ±25 MeV/c^2 around its nominal mass value given by the PDG, $1864.83 \pm 0.05\,\mathrm{MeV}/c^2$. From the fit we find $139,404,920 \pm 14,931$ signal and $8,616,519 \pm 5,628$ background events within the mass window, which corresponds to a purity of 94.18 ± 0.01 %.

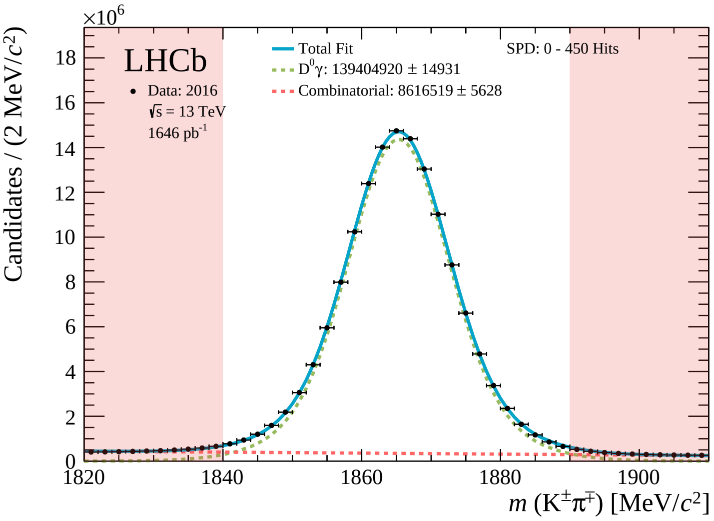

Figure 5.3. Invariant-mass distribution of $D^0 \to K^{\pm}\pi^{\mp}$ mesons for pp collisions at a centre-of-mass energy $\sqrt{s} = 13\,\mathrm{TeV}$ from 2016 data. The D^0 signal is fitted with two Gaussian distributions with a common mean in green and the background is fitted with a first-order Chebyshev polynomial in red. The total fit is shown in blue. The region excluded by the mass-window cut is highlighted in red.

Table 5.2. Fit parameters for D^0 invariant-mass fit for 2016 data where μ is the mean shared by the two Gaussian distributions, σ_1 and σ_2 are their widths, Y_1/Y_2 is the fraction of the yields of the Gaussian distributions, Y_{Signal} is the number of D^0 candidates, a_1 is the parameter of the first-order Chebyshev polynomial, and $Y_{\mathrm{Background}}$ is the number of background events.

Parameter	**Value**	**Units**
μ	1865.3266 ± 0.0008	MeV/c^2
σ_1	11.35 ± 0.01	MeV/c^2
σ_2	6.751 ± 0.003	MeV/c^2
Y_1/Y_2	0.507 ± 0.003	-
Y_{Signal}	139,404,919 ± 14930	-
a_1	-0.2885 ± 0.0005	-
$Y_{\mathrm{Background}}$	8,616,519 ± 5627	-

5.1.4 Determination of D^{*0} yields

We use the difference between the reconstructed invariant mass of the D^{*0} candidates and the intermediate D^0 meson throughout this analysis to partially cancel out the experimental error in the reconstruction of the D^0 meson such that,

$$\Delta m_{D^{*0}} = m(D^0\gamma) - m(D^0). \tag{5.5}$$

Modelling $D^{*0} \to D^0[K^\pm\pi^\mp]\gamma[e^+e^-]$ invariant-mass difference

The shape of the $\Delta m_{D^{*0}}$ distribution is determined from the large, fully reconstructed Monte Carlo described in Sec. 4.2.4. The same selection criteria used in the D^{*0} data are applied to the Monte Carlo sample. After truth-matching the Monte Carlo a double-sided Crystal Ball [137] is used to fit the $\Delta m_{D^{*0}}$ distribution, shown in Fig. 5.4, where all the parameters are left floating during the fit. A double-sided Crystal Ball has a Gaussian core with two different power-law tails, which allow for an adequate description of the asymmetric $\Delta m_{D^{*0}}$ shape. This shape has a total of six free parameters: a mean (μ), a width (σ), two parameters that describe the distance to the left (α_{Left}) and right (α_{Right}) of the mean where the Gaussian core becomes a power law, and two parameters for the exponent of the power-law component of each tail (n_{Left} and n_{Right}). We then separate the sample in $p_{\text{T}}(\gamma)$ bins of 200 MeV/c, and fit the $\Delta m_{D^{*0}}$ distribution in each range up to 1600 MeV/c. These fits are shown in Fig. 5.5 and their fitting-parameter values are summarised in Table 5.3.

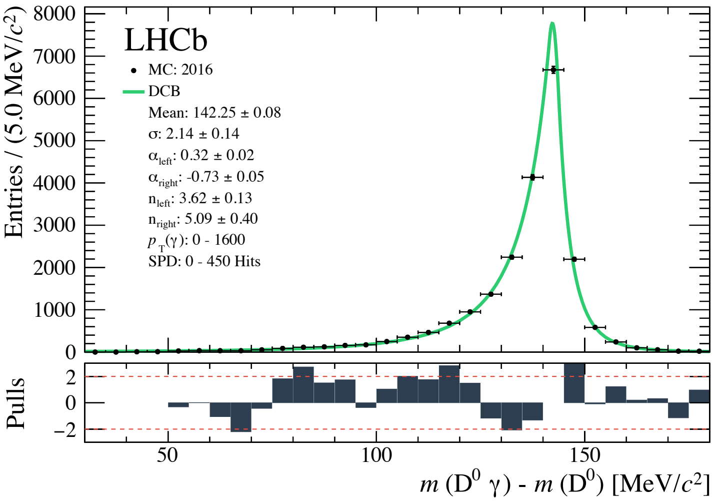

Figure 5.4. Fit of the $\Delta m_{D^{*0}}$ distribution of truth-matched $D^{*0} \to D^0[K^\pm\pi^\mp]\gamma[e^+e^-]$ mesons for pp collisions at a centre-of-mass energy $\sqrt{s} = 13$ TeV from 2016 Monte Carlo for converted photons with transverse momentum in the 0 to 1600 MeV/c range. The distribution is fitted with a double-sided Crystal Ball with all parameters floated (green). The lower panel shows the pulls.

Modelling $D^{*0} \to D^0[K^\pm\pi^\mp]\pi^0[\gamma\gamma]$ background

D^{*0} mesons can decay into a $D^0\pi^0$ pair with a branching fraction of $64.7 \pm 0.9\%$, where the π^0 decays into a pair of photons $98.923 \pm 0.034\%$ of the time. This compares to the $35.3 \pm 0.9\%$ branching fraction of $D^{*0} \to D^0\gamma$ decays. $D^0\pi^0$ events reconstructed with a single missing photon have a lower invariant-mass signature than $D^0\gamma$ events, with the majority of events

Table 5.3. Fit parameters and yields for D^{*0} invariant-mass fit for Monte Carlo in bins of $p_{\mathrm{T}}(\gamma)$.

Parameter	**Unites**	**Value**				
$p_{\mathrm{T}}(\gamma)$	MeV/c	$0-1600$	$0-200$	$200-400$	$400-600$	$600-800$
μ	MeV/c^2	142.25 ± 0.08	142.4 ± 0.7	143.0 ± 0.2	142.30 ± 0.02	142.1 ± 0.2
σ	MeV/c^2	2.1 ± 0.1	2.11 ± 0.5	1.4 ± 0.5	1.56 ± 0.01	2.5 ± 0.3
α_{Left}	-	0.32 ± 0.02	0.13 ± 0.05	0.11 ± 0.04	0.21 ± 0.01	0.40 ± 0.05
α_{Right}	-	-0.73 ± 0.05	-0.6 ± 0.2	-0.4 ± 0.1	-0.50 ± 0.01	-0.9 ± 0.1
n_{Left}	-	3.6 ± 0.1	2.12 ± 0.7	5.8 ± 0.8	5.1 ± 0.2	5.6 ± 0.7
n_{Right}	-	5.09 ± 0.4	3.0 ± 1.6	9.8 ± 3.1	6.5 ± 0.4	4.3 ± 0.7
$p_{\mathrm{T}}(\gamma)$	MeV/c		$800-1000$	$1000-1200$	$1200-1400$	$1400-1600$
μ	MeV/c^2		142.2 ± 0.2	142.1 ± 0.3	142.3 ± 0.2	142.4 ± 0.3
σ	MeV/c^2		2.2 ± 0.3	2.8 ± 0.5	0.7 ± 0.5	3.4 ± 0.3
α_{Left}	-		0.44 ± 0.07	0.5 ± 0.1	0.2 ± 0.1	0.7 ± 0.1
α_{Right}	-		-0.9 ± 0.2	-1.4 ± 0.3	-0.5 ± 0.3	-2.0 ± 0.3
n_{Left}	-		4.4 ± 0.5	5.7 ± 1.3	3.7 ± 0.7	5.7 ± 2.7
n_{Right}	-		3.7 ± 0.9	2.5 ± 0.7	2.8 ± 0.7	1.0 ± 0.5

falling between 50 and 100 MeV/c^2 in the $\Delta m_{D^{*0}}$ distribution. Due to the negative-skewed distribution of the $D^0\gamma$, the tails overlap slightly and, as a result, it is important to include this lower-mass region as part of the data fit.

To model this background, we use the $D^{*0} \to D^0\pi^0$ Monte Carlo sample described in Sec. 4.2.4. The fully reconstructed events are processed with the same selection criteria as the D^{*0} data. As with the D^{*0} signal model, we need to understand how the $D^0\pi^0$ background changes with the photon's transverse momentum. The $\Delta m_{D^{*0}}$ shape of this background varies significantly with $p_{\mathrm{T}}(\gamma)$. As a result, we use a one-dimensional *kernel estimation* (KE) PDF [138], a flexible, non-parametric method which models each data point as a Gaussian kernel. The width of the Gaussian is proportional to the local density of events and contributes to $1/N$ of the total integral, where N is the total number of events in the distribution. The fit for photons with a transverse momentum in bins of 200 MeV/c is shown in Fig. 5.6. The fit results are saved as templates for later use in the data fits.

D^{*0} combinatorial-background model

The combinatorial background in the $\Delta m_{D^{*0}}$ distribution has a characteristic shape, which goes to zero at threshold. To model the combinatorial background, where D^0 mesons are wrongly matched with a photon, we use an empirical density function designed to model $D^{*0} \to D^0 X$ decays, which is defined in the $\Delta m_{D^{*0}} - \Delta m_0 > 0$ region as follows,

$$f(\Delta m_{D^{*0}}) = \left(\frac{\Delta m_{D^{*0}}}{\Delta m_0}\right)^A \left[1 - \exp\left(\frac{-(\Delta m_{D^{*0}} - \Delta m_0)}{C}\right)\right] + B\left(\frac{\Delta m_{D^{*0}}}{\Delta m_0} - 1\right), \tag{5.6}$$

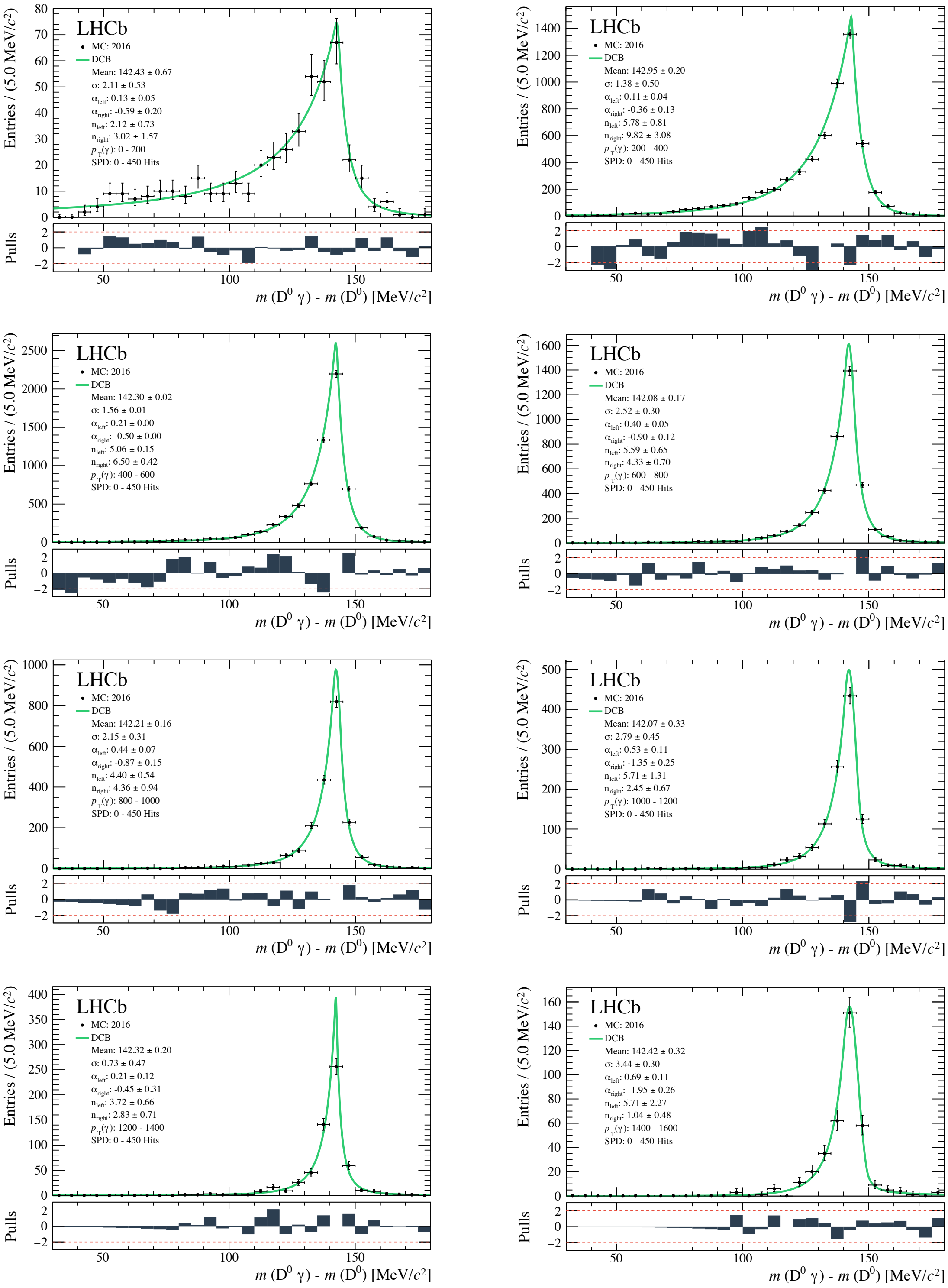

Figure 5.5. Fit of the $\Delta m_{D^{*0}}$ distribution of truth-matched $D^{*0} \to D^0[K^{\pm}\pi^{\mp}]\gamma[e^+e^-]$ Monte Carlo for pp collisions at a centre-of-mass energy $\sqrt{s} = 13\,\text{TeV}$ for 2016 data in increments of 200 MeV/c in p_{T} (γ) from left to right. The distributions are fitted with a double-sided Crystal Ball with all parameters floated. The lower panels show the pulls.

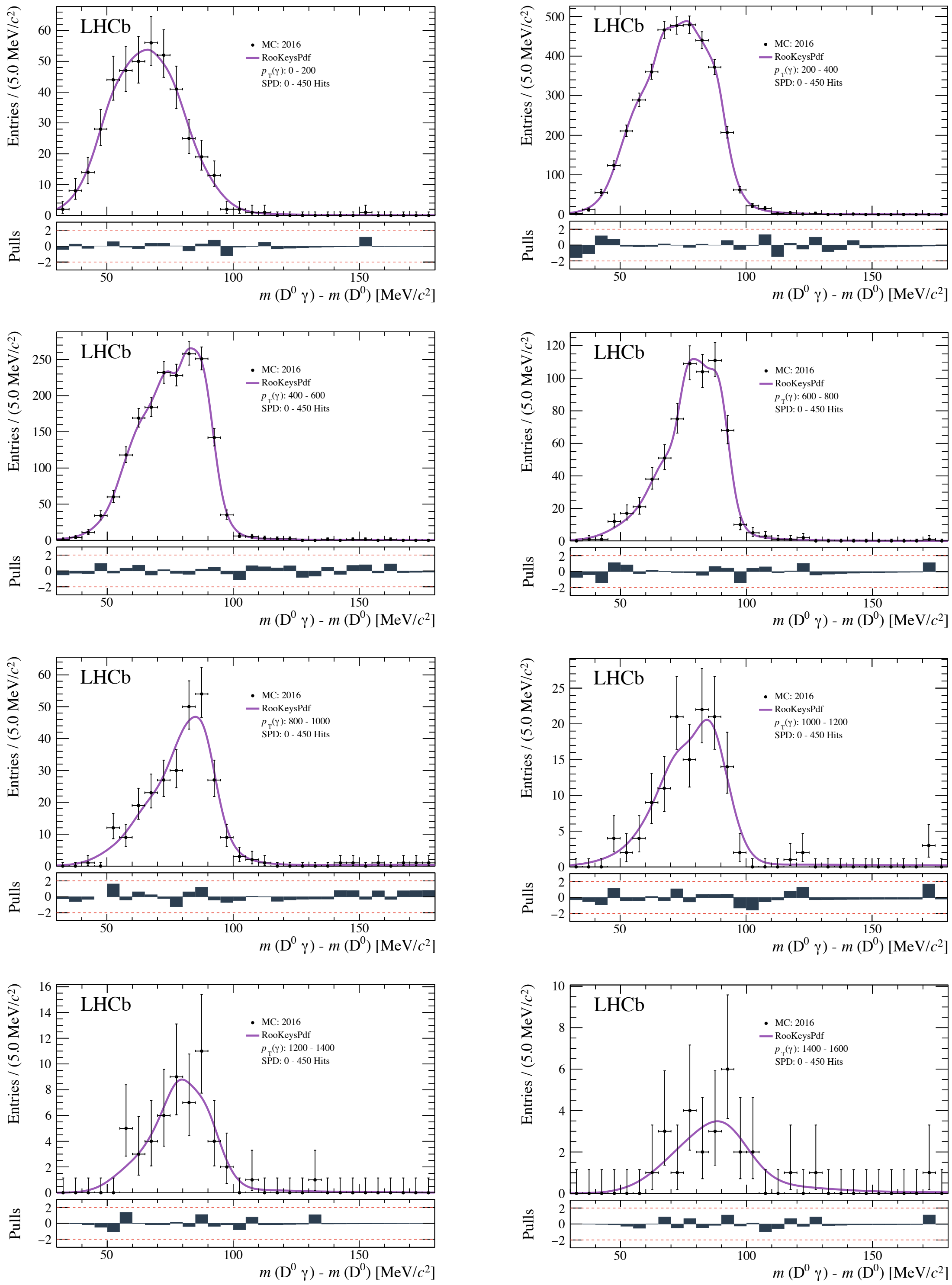

Figure 5.6. Fit of the $\Delta m_{D^{*0}}$ distribution of truth-matched $D^{*0} \to D^0[K^{\pm}\pi^{\mp}]\gamma[e^+e^-]$ events reconstructed from $D^{*0} \to D^0[K^{\pm}\pi^{\mp}]\pi^0[\gamma\gamma]$ Monte Carlo for pp collisions at a centre-of-mass energy $\sqrt{s} = 13\,\text{TeV}$ for 2016 data run conditions in increments of 200 MeV/c in $p_{\mathrm{T}}(\gamma)$ from left to right. The distributions are fitted with a kernel-estimator PDF. The lower panels show the pulls.

where Δm_0, A, B, and C are shape parameters. The parameter Δm_0 defines the kinematic threshold below which the function evaluates to zero. Parameters A and B determine the curvature of the distribution at large $\Delta m_{D^{*0}}$ values while C determines the curvature at small $\Delta m_{D^{*0}}$ values. All parameters are floated during the fit.

D^{*0} data fit

To fit the $\Delta m_{D^{*0}}$ distribution in the 2016 calibration data, we fix the $D^0\gamma$ signal parameters associated with the tails of the double-sided Crystal Ball to match the results of the Monte Carlo fits for each $p_{\mathrm{T}}(\gamma)$ range, while allowing the mean value to float. In addition, we use a Gaussian convolution on the signal shape as an empirical correction to account for differences in resolution between data and Monte Carlo. We allow the mean and width of the Gaussian to float in the fit of the data spanning a wide photon kinematic range, 0 to 1600 MeV/c, and fix the parameters according to these results for the fits in 200 MeV/c bin intervals. The KE PDFs of the $D^0\pi^0$ background is used for the corresponding $p_{\mathrm{T}}(\gamma)$ selection. This background has a much wider distribution than that of the $D^0\gamma$ signal and, as a result, is not as susceptible to the resolution effects. Therefore, no additional correction is applied to the shapes extracted from Monte Carlo. Finally, we allow all the combinatorial-background parameters to float. The fit result in the $p_{\mathrm{T}}(\gamma) < 1600$ MeV/c range is shown in Fig. 5.7 and for the individual 200 MeV/c bin increments in Fig. 5.8. The peak of D^{*0} candidates is barely visible at low values of $p_{\mathrm{T}}(\gamma)$ and steadily grows with higher $p_{\mathrm{T}}(\gamma)$. The corresponding yields and fit parameters are summarised in Table 5.4. The $D^{*0}{}_{\mathrm{Yield}}$ or $N_{\mathrm{Conv}}(D^*(2007)^0)$ is plotted as a function of the photon's transverse momentum in Fig. 5.9. This is the numerator of our efficiency calculation described in Eq. 5.2.

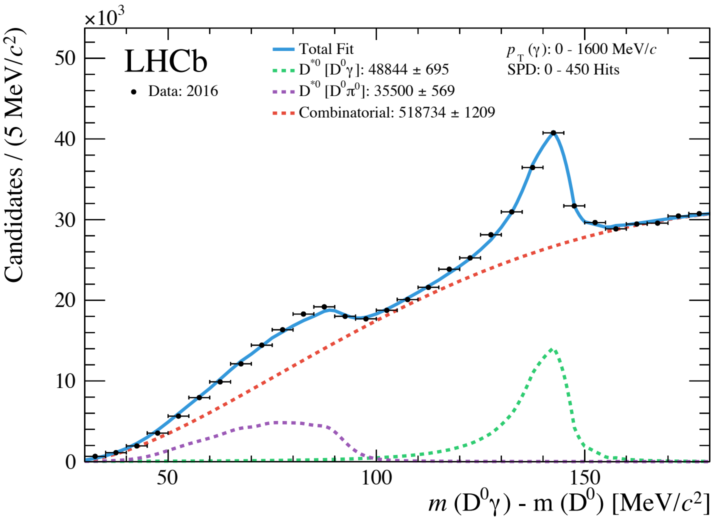

Figure 5.7. Fit of the $\Delta m_{D^{*0}}$ distribution of $D^{*0} \to D^0[K^\pm\pi^\mp]\gamma[e^+e^-]$ candidates for 2016 data with photons with transverse momentum between 0 to 1600 MeV/c. The D^{*0} signal is fitted with a double-sided Crystal Ball convoluted with a Gaussian (green), the $D^{*0} \to D^0[K^\pm\pi^\mp]\pi^0[\gamma\gamma]$ background is fitted with a KE template from Monte Carlo (purple), and the combinatorial background is fitted with Eq. 5.6.

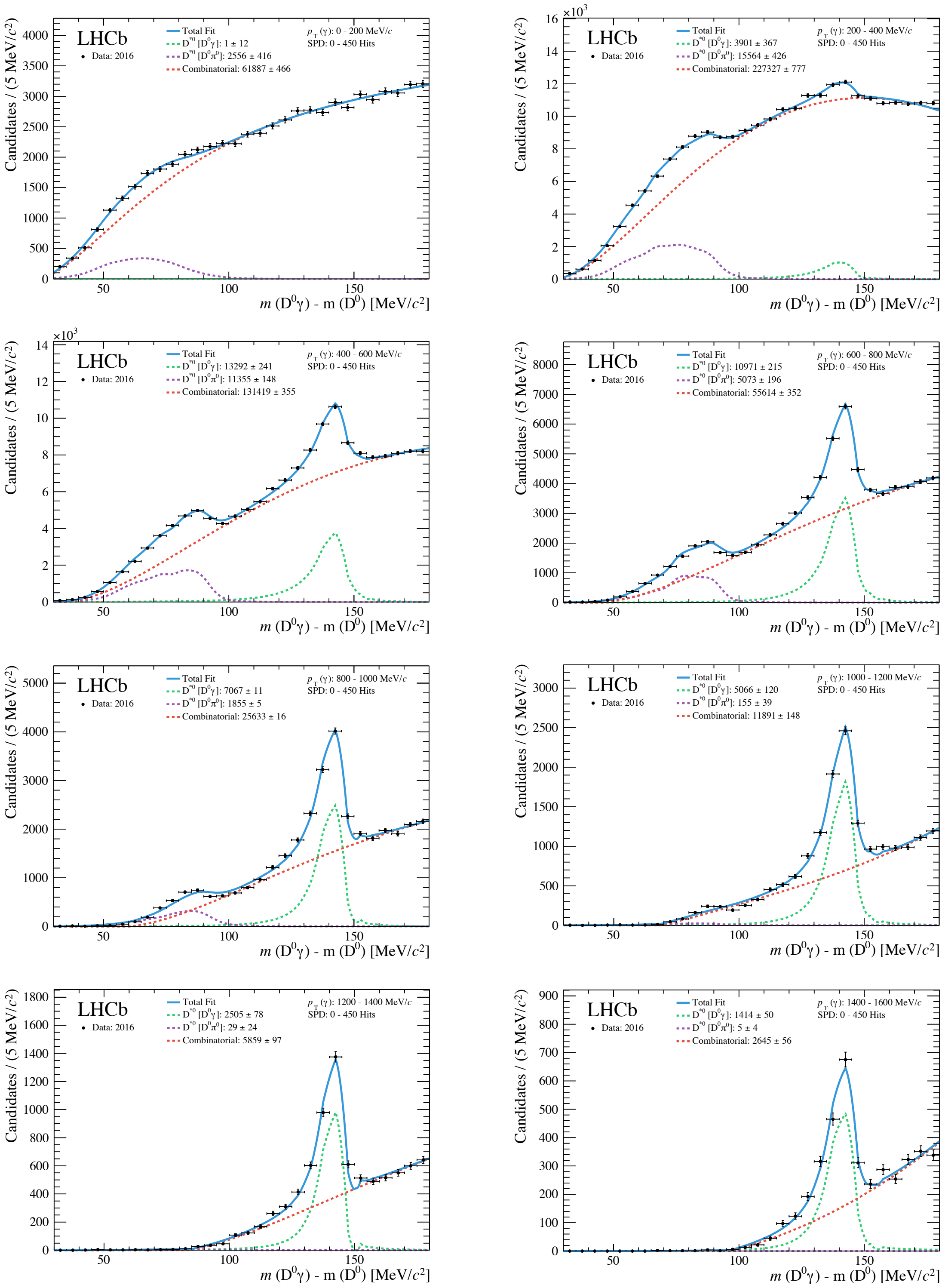

Figure 5.8. Fit of the $\Delta m_{D^{*0}}$ distribution of $D^{*0} \to D^0[K^{\pm}\pi^{\mp}]\gamma[e^+e^-]$ candidates for 2016 data in increments of 200 MeV/c in $p_{\mathrm{T}}(\gamma)$. The D^{*0} signal is fitted with a double-sided Crystal Ball convoluted with a Gaussian (green), the $D^{*0} \to D^0[K^{\pm}\pi^{\mp}]\pi^0[\gamma\gamma]$ background is fitted with a KE template from Monte Carlo (purple), and the combinatorial background is fitted with Eq. 5.6.

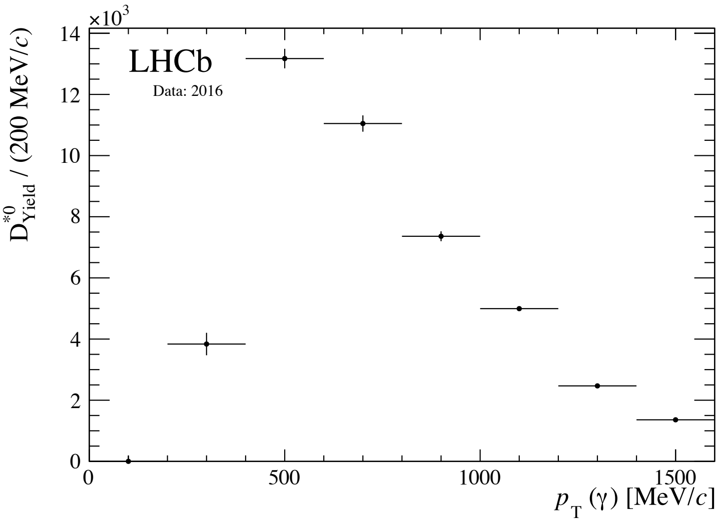

Figure 5.9. ${D^{*0}}_{\text{Yield}}$ in 200 MeV/c bins of the photon's transverse momentum for 2016 data.

Table 5.4. Fit parameters and yields for $\Delta m_{D^{*0}}$ mass fit for 2016 data for photons with transverse momentum in the 0 to 1600 MeV/c range and in increments of 200 MeV/c. The μ_{Gauss} and σ_{Gauss} parameters are related to the Gaussian convolution to the signal used to apply the empirical correction to the data.

Para.	**Units**	**Value**				
$p_{\text{T}}(\gamma)$	MeV/c	$0-1600$	$0-200$	$200-400$	$400-600$	$600-800$
μ_{Gauss}	MeV/c^2	0.002 ± 0.0005	-	-	-	-
σ_{Gauss}	MeV/c^2	0.12 ± 0.01	-	-	-	-
μ_{Signal}	MeV/c^2	142.9 ± 0.2	140 ± 6	141.6 ± 0.4	143.6 ± 0.1	142.8 ± 0.2
Y_{Signal}	-	48843 ± 695	1 ± 179	3901 ± 367	13292 ± 241	10970 ± 215
m_0	MeV/c^2	26.0 ± 0.3	25 ± 0.5	25.8 ± 0.7	31 ± 2	45.95 ± 0.04
A	-	0.486 ± 0.002	0.93 ± 0.07	0.57 ± 0.02	0.641 ± 0.004	0.62 ± 0.02
B	-	-0.263 ± 0.001	-0.73 ± 0.14	-0.39 ± 0.02	-0.42527 ± 0.00004	-0.42 ± 0.02
C	-	99.4 ± 0.4	28 ± 4	67 ± 3	76.909 ± 0.008	97 ± 3
Y_{Bkg}	-	518734 ± 1209	61887 ± 465	227327 ± 777	131419 ± 355	55613 ± 352
Y_{π^0}	-	35499 ± 569	2556 ± 415	15563 ± 426	11355 ± 148	5073 ± 196
$p_{\text{T}}(\gamma)$	MeV/c		$800-1000$	$1000-1200$	$1200-1400$	$1400-1600$
μ_{Signal}	MeV/c^2		142.03 ± 0.02	143.011 ± 0.001	142.03 ± 0.09	142.1 ± 0.2
Y_{Signal}	-		7066 ± 11	5065 ± 0.01	2505 ± 78	1414 ± 50
m_0	MeV/c^2		49 ± 2	42.2645 ± 0.00002	55 ± 6	29 ± 5
A	-		1.17 ± 0.04	1.4113 ± 0.0002	1.03 ± 0.06	1.715 ± 0.007
B	-		-1.0341 ± 0.0006	-2.1000 ± 0.0002	-1.04 ± 0.03	-3.27 ± 0.04
C	-		53.0145 ± 0.0008	24 ± 18	66 ± 3	19 ± 13
Y_{Bkg}	-		25633 ± 15	11891.5 ± 0.01	5859 ± 97	2645 ± 56
Y_{π^0}	-		1854 ± 5	155.472 ± 0.002	29 ± 24	5 ± 4

5.1.5 Efficiency denominator

D^0 kinematic re-weight method and validation

We now discuss the calculation of the denominator of Eq. 5.2, $N_{\mathrm{all}}(D^{*0}|D^0)$. As has been explained, the inclusive cross-section measurements, $\sigma(pp \to D^{*+}X)$ and $\sigma(pp \to D^0X)$ [136], are used together with our inclusive D^0 sample to provide a normalisation. However, we also need the $p_{\mathrm{T}}(\gamma)$ dependence of $N_{\mathrm{all}}(D^{*0}|D^0)$. Driven by the correlations of the D^0 and γ kinematics, the selection requirements imposed on the D^0 will change the $p_{\mathrm{T}}(\gamma)$ distribution, even if there are no requirements imposed on the photon. The effect of the D^0 selections on the photon p_{T} can be reproduced by considering the changes in the $\eta(D^0)$ and $p_{\mathrm{T}}(D^0)$ distributions with respect to their unbiased distributions, *i.e.* prior to any selection and reconstruction effects. Therefore, to obtain the $p_{\mathrm{T}}(\gamma)$ dependence of $N_{\mathrm{all}}(D^{*0}|D^0)$ before selection and reconstruction effects of the photon, we use the centrally produced $D^{*0} \to D^0[K^{\pm}\pi^{\mp}]\gamma$ Monte Carlo described in Sec. 4.2.4 and weight the generator-level events such that their $\eta(D^0)$ and $p_{\mathrm{T}}(D^0)$ distributions are aligned with those observed in our inclusive D^0 data selection.

This procedure is tested with our reconstructed, centrally-produced $D^{*0} \to D^0[K^{\pm}\pi^{\mp}]\gamma$ Monte Carlo to check the assumption that reweighting the generator-level $D^{*0} \to D^0[K^{\pm}\pi^{\mp}]\gamma$ Monte Carlo in $\eta(D^0)$ and $p_{\mathrm{T}}(D^0)$ is sufficient to reproduce the p_{T} distribution of the not yet selected photons. To do this, reconstructed Monte Carlo events are selected with the requirement that the D^0 is reconstructed, and with no requirement on the reconstruction of a photon. Using the Monte Carlo truth information, we check if the reconstructed D^0 is associated with a $D^{*0} \to D^0[K^{\pm}\pi^{\mp}]\gamma$ decay. If it is, then the generator-level information of the photon is saved.

We then re-weight the generator-level D^{*0} Monte Carlo to match the kinematics of the D^0 mesons in the reconstructed Monte Carlo. It is checked and shown in Fig. 5.10 that $\eta(D^0)$ (top left), $p_{\mathrm{T}}(D^0)$ (top right), and $p(D^0)$ (bottom left) are brought into agreement by this procedure, as expected. The photon transverse momentum of the re-weighted generator-level D^{*0} Monte Carlo is then compared with that of reconstructed photons from the fully-reconstructed $D^{*0} \to D^0[K^{\pm}\pi^{\mp}]\gamma$ Monte Carlo. This is shown in Fig. 5.10 (bottom right), where good agreement is seen between the two distributions, indicating that the method works.

D^0 kinematic re-weight and efficiency calculation

With the method validated, we next re-weight the generator-level Monte Carlo to now match the kinematics of all the D^0 mesons in the inclusive D^0 sample. The comparison between re-weighted, generator-level Monte Carlo and the data is shown in Fig. 5.11. After this procedure, the $p_{\mathrm{T}}(\gamma)$ of the re-weighted, generator-level Monte Carlo gives the $p_{\mathrm{T}}(\gamma)$ dependence of $N_{\mathrm{All}}(D^{*0}|D^0)$. After normalising it using Eq. 5.3, we have obtained the denominator of our efficiency calculation, shown in Fig. 5.12.

By dividing the reconstructed $N(D^{*0})$, shown in Fig. 5.9, and $N_{\mathrm{All}}(D^{*0}|D^0)$ in bins of the photon's transverse momentum, we obtain the efficiency of detecting a photon through

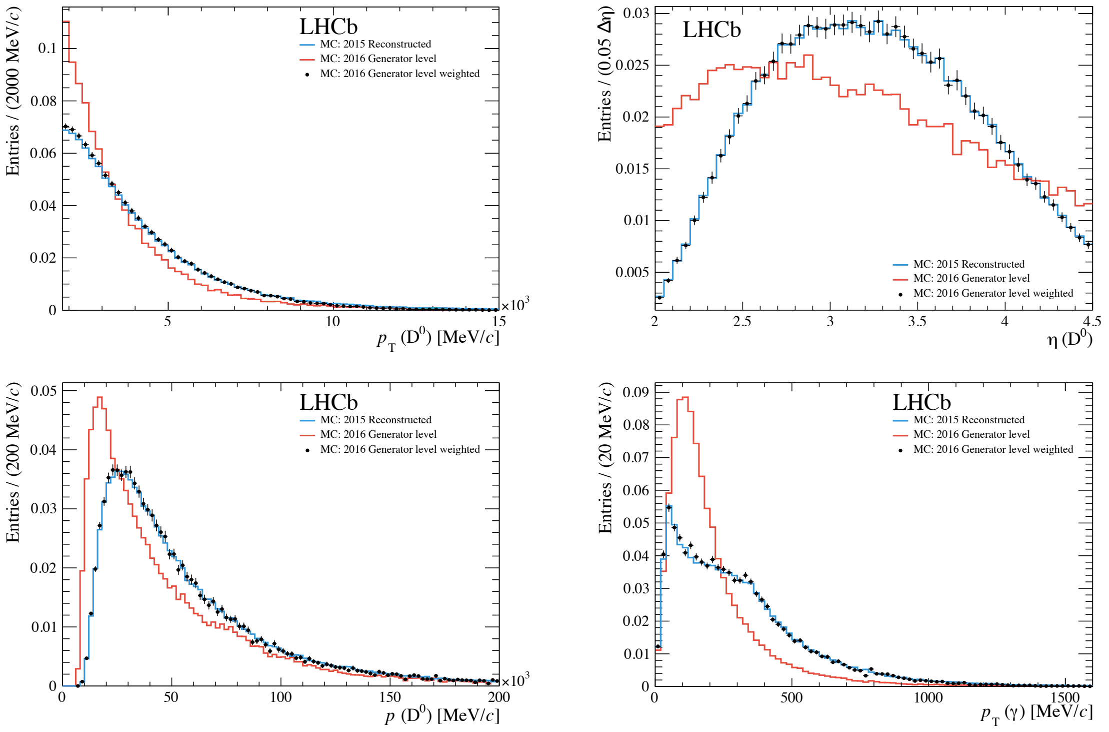

Figure 5.10. $D^0 \to K^{\pm}\pi^{\mp}$ kinematics in the fully reconstructed Monte Carlo (blue) and generator-level $D^{*0} \to D^0[K^{\pm}\pi^{\mp}]\gamma$ before (red) and after re-weighting (black markers). Weights are applied to D^0 transverse momentum (top left) and η (top right) that successfully reproduce the D^0 momentum distribution (bottom left) and the photon's transverse momentum (bottom right).

conversion versus $p_{\rm T}(\gamma)$, shown in Fig. 5.13. The efficiency is compatible with zero below 200 MeV/c and rises steadily to 1% at around 1300 MeV/c.

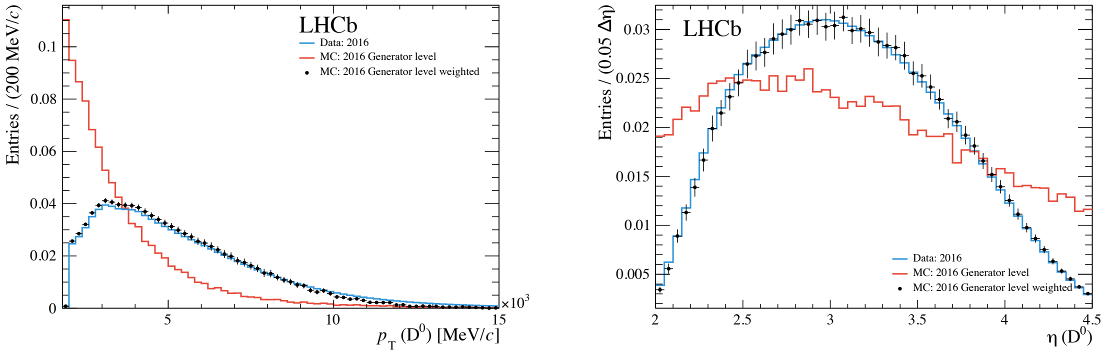

Figure 5.11. $D^0 \to K^{\pm}\pi^{\mp}$ kinematics from 2016 data (blue) and generator level $D^{*0} \to D^0[K^{\pm}\pi^{\mp}]\gamma$ before (red) and after re-weighting (black markers). Weights are applied to the D^0 transverse momentum (left) and pseudorapidity (right).

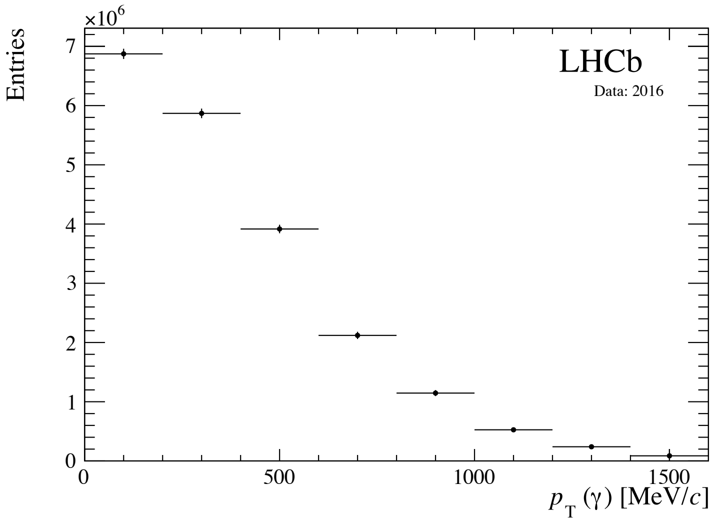

Figure 5.12. $N_{\text{All}}(D^{*0}|D^0)$ as a function of the photon's transverse momentum. The distribution is normalised according to the number of reconstructed D^0 mesons and the ratio of $pp \to D^{*+}$ and $pp \to D^0$ cross-sections.

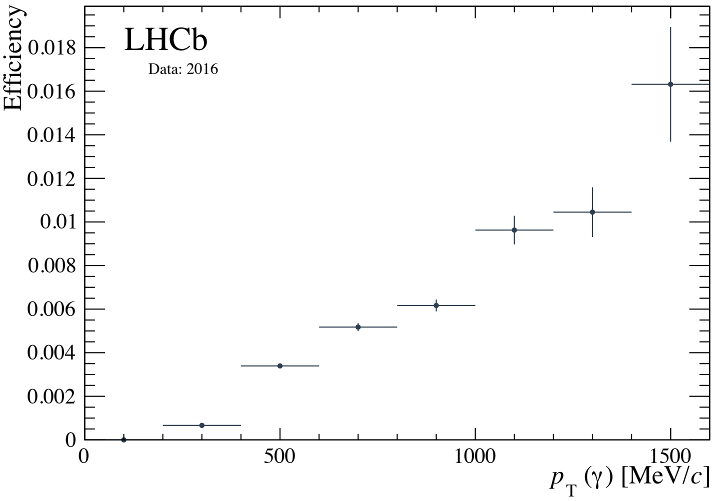

Figure 5.13. Photon-conversion efficiency as a function of photon's transverse momentum in bins of 200 MeV/c for 2016 run conditions.

5.1.6 Dependence of efficiency on detector occupancy

The detector environment for events in the D^{*0} samples is not properly representative of the CEP environment, where we expect to see only particles associated with our decay mode in an otherwise empty detector. As detector occupancy can affect pattern-reconstruction efficiency in the tracking, we expect this difference to have consequences for the photon-reconstruction efficiency. The amount of activity in the detector can be estimated using the number of hits in the SPD. A typical CEP event, after accounting for spill over, will have less than 20 or 30 SPD hits, depending on the decay's final state. In contrast, the D^{*0} and D^0 events used for the calibration studies are generally produced in inelastic collisions where the detector occupancy is much higher: see Fig. 5.14 for a comparison of the SPD distribution from CEP χ_c and inelastic D^{*0} events from 2016 data. It is expected that the reconstruction efficiency will vary as a function of the detector occupancy, as tracking and vertex reconstruction tends to improve with lower multiplicities. Therefore, to better understand the effect of the detector occupancy on $\varepsilon_{\gamma\to e^+e^-}$, we repeat the procedure detailed above and calculate the photon-conversion efficiency using subsets of the calibration sample separated into bins of SPD hits.

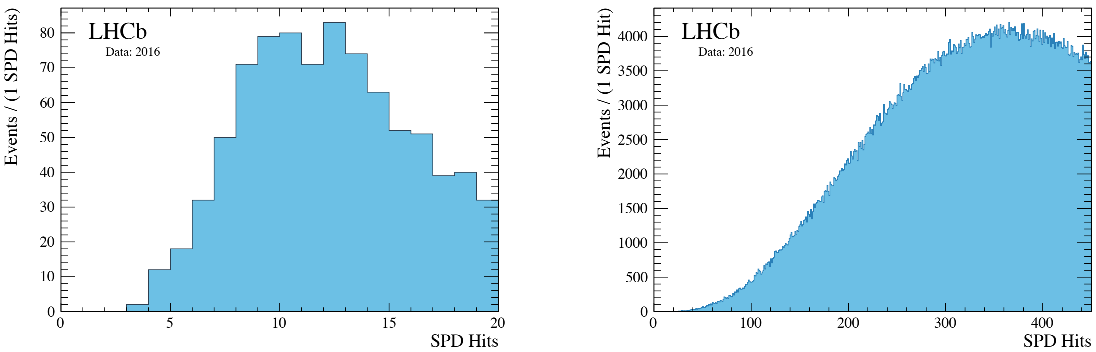

Figure 5.14. Distribution of the number of SPD hits in the CEP χ_c sample (left) and the inelastic D^{*0} (right) sample for 2016 data.

Therefore, we separate the D^0 and D^{*0} data sets into subsets of SPD bins while keeping the whole converted-photon transverse momentum range, 0 to 1600 MeV/c. For systematic checks several binning schemes are considered: SPD bin widths of 75, 90, 112.5, and 150 SPD hit increments. The photon-conversion efficiencies as a function of $p_\mathrm{T}(\gamma)$ for these four data sets are shown in Fig. 5.15.

As expected, from these distributions we learn that the photon-conversion efficiency increases with a lower detector occupancy. However, the overall shape of the distribution with respect to $p_\mathrm{T}(\gamma)$ appears to be essentially independent of SPD multiplicity. We demonstrate this by fitting the efficiency calculated with the calibration sample spanning the entire SPD range, 0 to 450, with a quadratic polynomial,

$$a + b \cdot p_\mathrm{T} + c \cdot p_\mathrm{T}^2, \tag{5.7}$$

with all parameters floating. We then apply the same fit, with all parameters fixed, except for the normalisation constant a, to each of the photon-conversion efficiency distributions calculated using the calibration sample that is separated into 75 SPD hit intervals. These fits are shown in Fig. 5.16. The first bin, 0 to 200 SPD hits, is excluded from these fits as its inclusion leads to instabilities, particularly for efficiencies calculated using subsets with a smaller sample size. It is seen that the shape of the efficiency distribution fitted on the inclusive sample, *i.e.* using the whole SPD rage, describes all of the sub-samples, separated in SPD bins, well. This

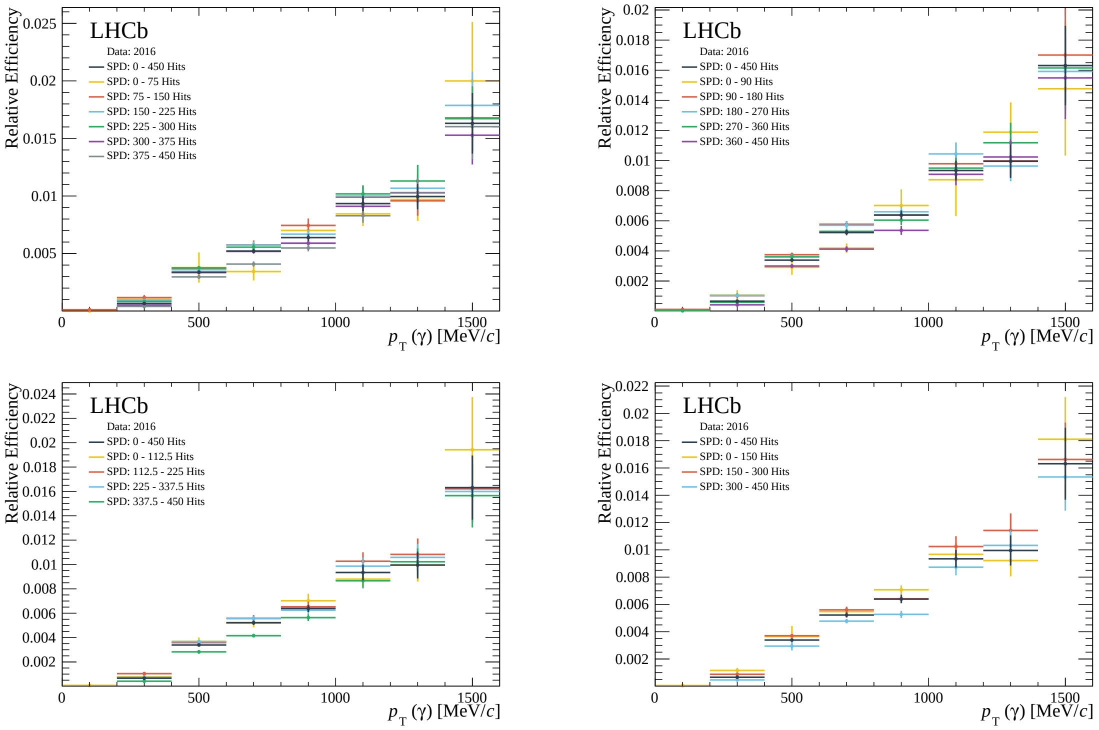

Figure 5.15. Photon-conversion efficiency as a function of the photon's transverse momentum in bins of 200 MeV/c for 2016 run conditions for 75 (top left), 90 (top right), 112.5 (bottom left), and 150 (bottom right) SPD hit increments.

indicates that it is reasonable to factorise $p_{\mathrm{T}}(\gamma)$ and multiplicity dependence when measuring the photon-conversion efficiency.

To extrapolate the photon-conversion efficiency to the low-multiplicity regime of CEP events we take the sample of CEP χ_c candidates and correct for the photon-conversion efficiency to calculate the number of χ_c candidates prior to photon conversion. We repeat this exercise using the different photon-conversion efficiency results calculated using the calibration samples separated into different bins of SPD multiplicity. The corrected number of CEP χ_c candidates is plotted in Fig. 5.17 (first two rows) using the set of photon-conversion efficiencies determined with the calibration sample separated into bins of 75 SPD hits. The points are plotted at the mean of the SPD distribution of the calibration sample for each range, with an error bar corresponding to the RMS of this distribution. As expected, the dependence of the photon-conversion efficiency on event multiplicity means that the corrected number of candidates is not constant. Rather, the corrected number of CEP χ_c candidates increases with multiplicity, reflecting the higher photon-conversion efficiency in low-multiplicity events.

To deduce the true number of CEP candidates we fit the distribution described above and extrapolate to zero multiplicity, which is representative of CEP conditions. To this end, we fit a quadratic function over the entire SPD range, 0 to 450, with the minimum fixed at zero SPD

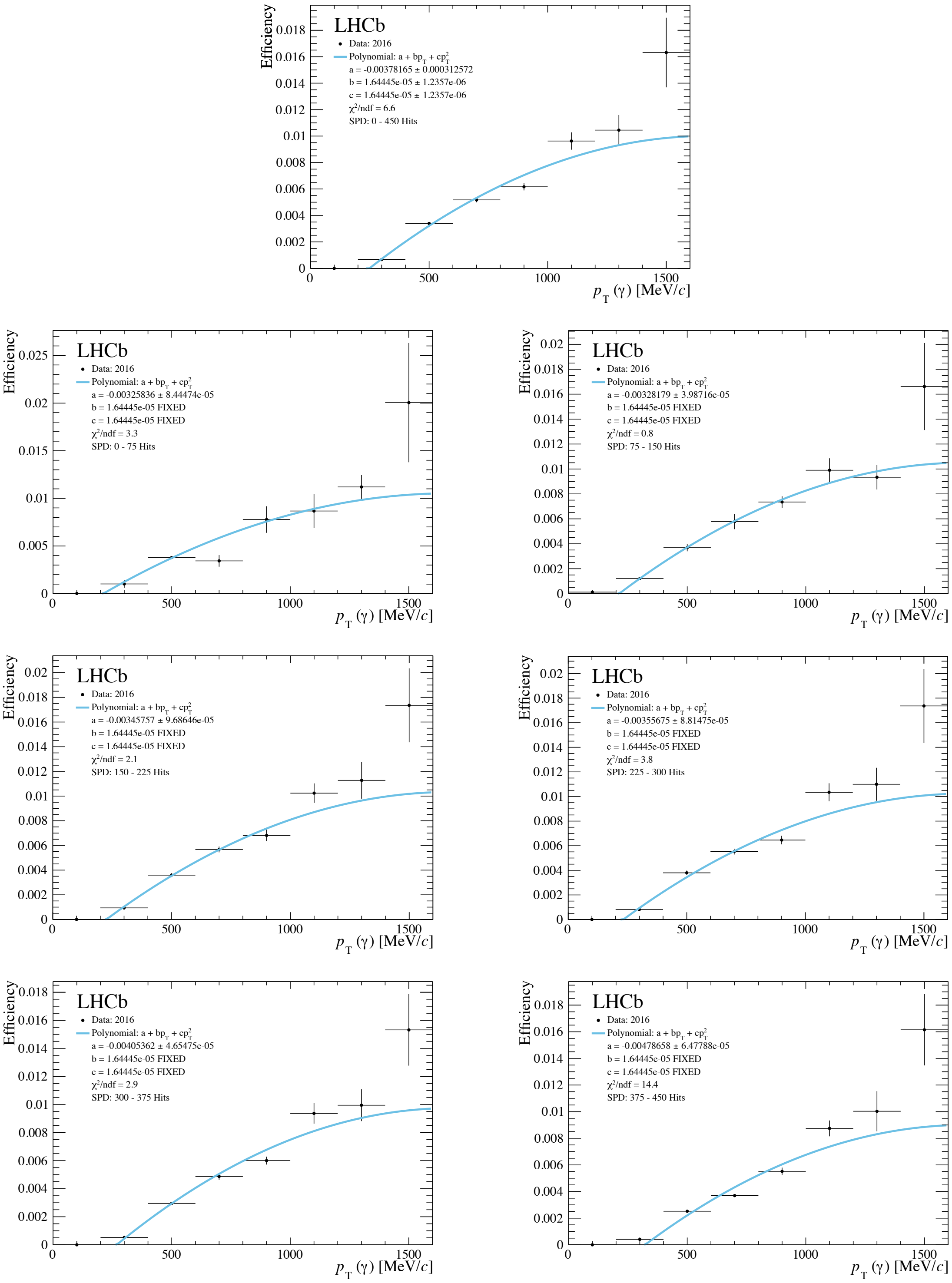

Figure 5.16. Photon-conversion efficiency as a function of the photon's transverse momentum in bins of 200 MeV/c for 2016 run conditions in 75 SPD hit increments. The distributions are fitted with a quadratic polynomial (blue). The top plot shows the results for the inclusive distribution.

hits: $a + b \cdot x^2$. The fit results are shown in Fig. 5.17 (first row) for the 2016-only, and combined

2015 and 2016 data. The fit parameters are summarised in Table 5.5. We obtain the expected number of efficiency corrected χ_c candidates from the intercept parameter a.

As a systematic check, we repeat the fit using the quadratic model over the first four points, 0 to 300 SPD hits, which are both well measured and lie closest to the CEP regime. This fit is shown in Fig. 5.17 (second row) for the 2016-only, and combined 2015 and 2016 data. The fit model is also substituted for a first-order polynomial and the fit is performed over both the entire range and the first four points, see Fig. 5.18 (first two rows). In addition, we repeat the procedure described above using the other two calibration sample subsets described above, *i.e.* using 90 and 112.5 SPD bin width subsets. The quadratic and linear fits are shown in Fig. 5.17 (third and fourth row) and Fig. 5.18 (third and fourth row), respectively. The fit parameters are summarised in Table 5.5.

In addition, we calculate the total number of expected χ_c candidates using our nominal efficiency distribution ($Y_{\mathrm{All\,SPD}}$), calculated using the entire SPD range. This value is marked in orange in both Fig. 5.17 and Fig. 5.18. As with the other data points, this point is placed at the mean of the SPD distribution and has an error corresponding to the RMS of the distribution. To correct our nominal photon-conversion-efficiency distribution calculated using the entire SPD range, 0 to 450 SPD hits, for the difference in multiplicity between the calibration sample and typical CEP samples, we take the ratio between our extrapolation into low SPD, a, and $Y_{\mathrm{All\,SPD}}$. These ratios are summarised in Table 5.5 for the different extrapolation methods and calibration sample subsets. The set of ratios calculated using the quadratic fits tend to have a smaller uncertainty and variance when compared to those calculated using the linear extrapolation. From considering the precision of these fits, and inspecting the variation in central values of the ratios, we estimate a correction factor of 0.50 ± 0.10.

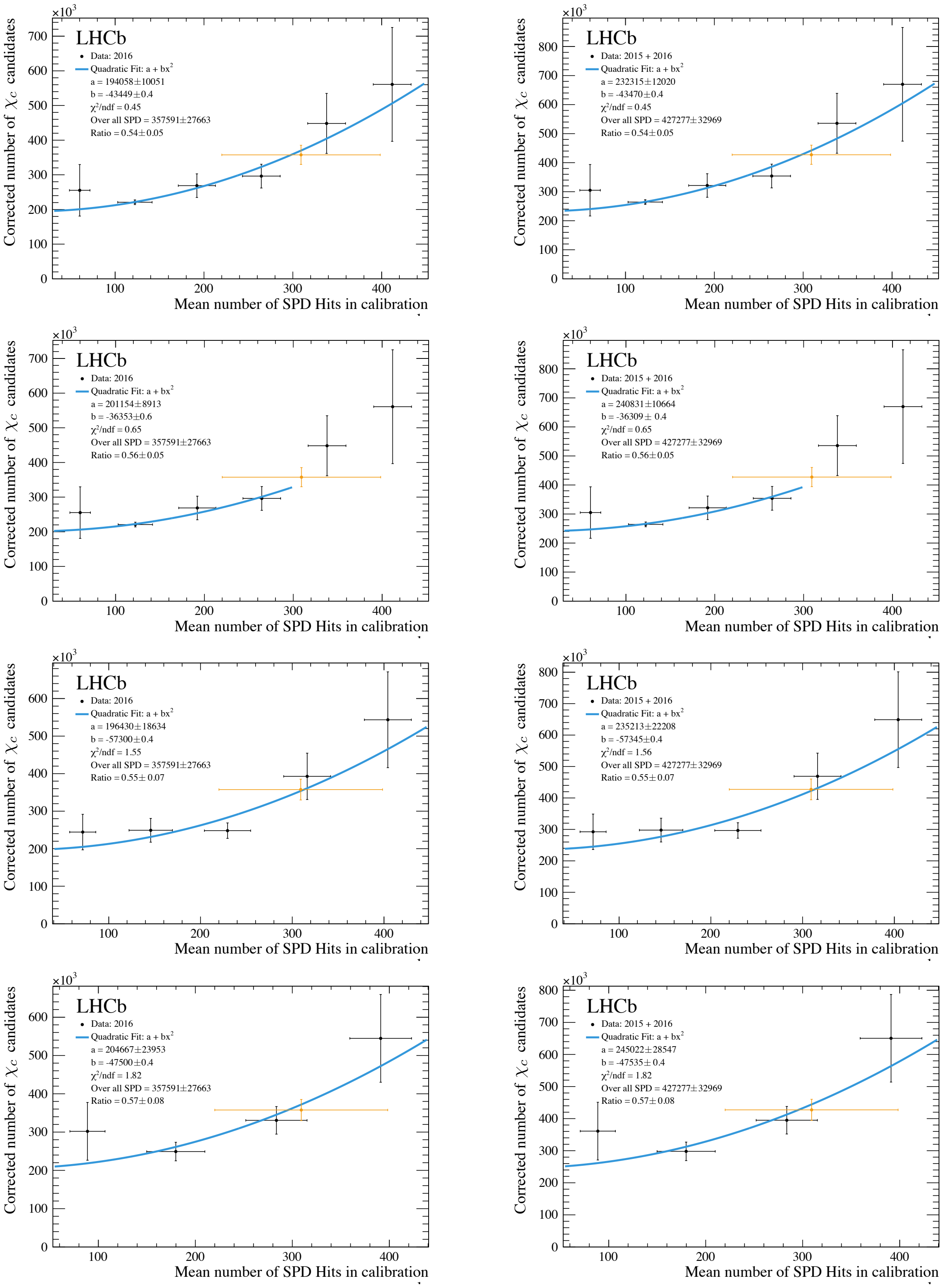

Figure 5.17. Number of χ_c candidates corrected for the photon-conversion efficiency using different calibration sample subsets for the 2016-only (left), and combined 2015 and 2016 (right) data. The distributions are fitted with a quadratic function centred at zero, $a + b \cdot x^2$. In the first and second row, the calibration samples used are separated into 75 SPD hit intervals but the fit is performed using the full range and the first four points, respectively. In the third and fourth row, the fit is performed using the full range but the calibration samples are separated into 90 and 112.5 SPD hit intervals, respectively. Each point is placed at the mean number of SPD hits in the calibration sample and has an uncertainty equal to the RMS of that sample. The number of corrected candidates calculated with the complete calibration sample, 0 to 450 SPD hits, is overlaid in orange. The ratio of the extrapolated low SPD, a, and the total number of expected χ_c candidates as calculated using the whole SPD range, $Y_{\text{All SPD}}$, is included in the legend.

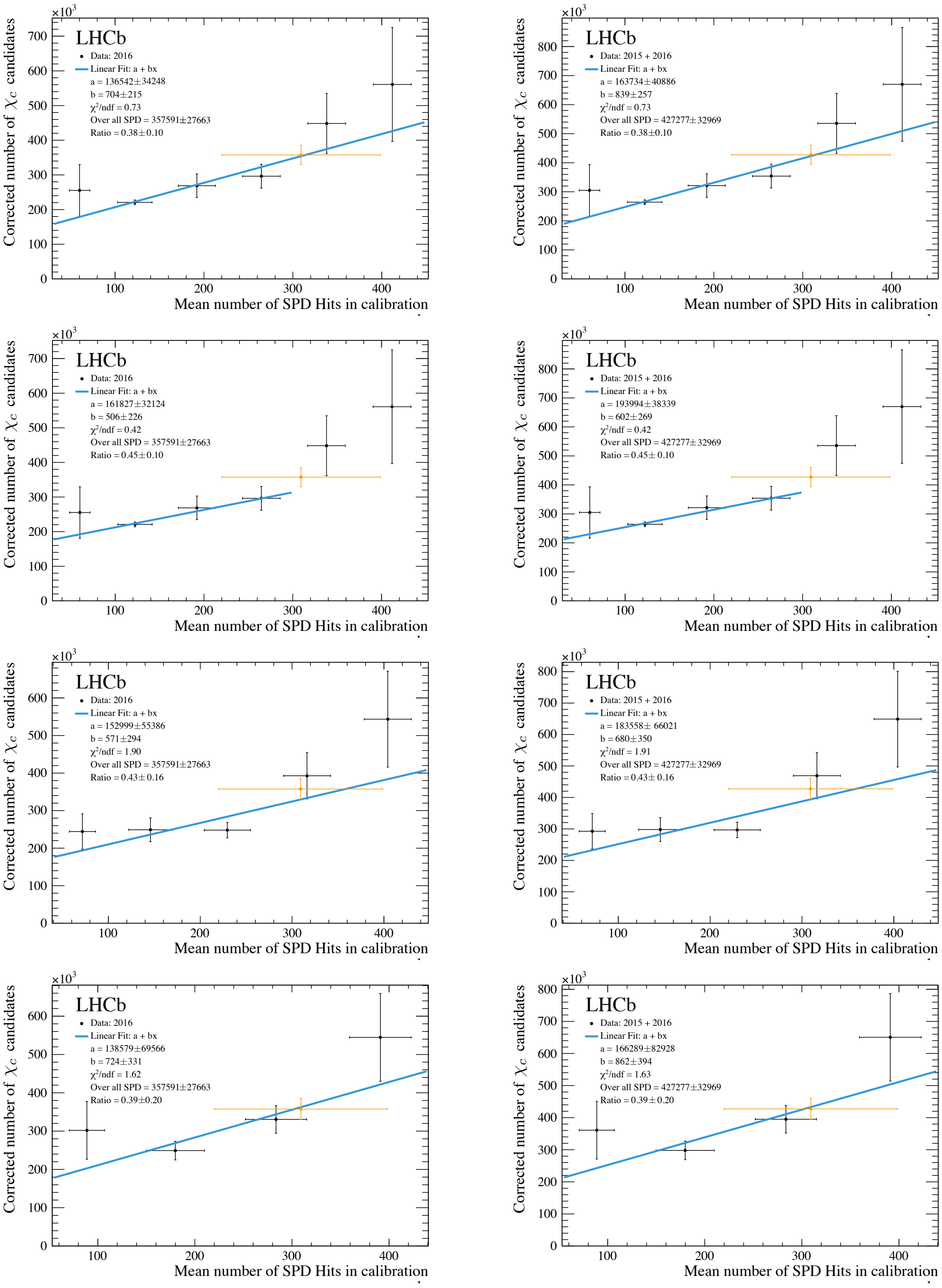

Figure 5.18. Number of χ_c candidates corrected for the photon-conversion efficiency using different calibration sample subsets for the 2016-only (left), and combined 2015 and 2016 (right) data. The distributions are fitted with a first-order polynomial, $a + b \cdot x$. In the first and second row, the calibration samples used are separated into 75 SPD hit intervals but the fit is performed using the full range and the first four points, respectively. In the third and fourth row, the fit is performed using the full range but the calibration samples are separated into 90 and 112.5 SPD hit intervals, respectively. Each point is placed at the mean number of SPD hits in the calibration sample and has an uncertainty equal to the RMS of that sample. The number of corrected candidates calculated with the complete calibration sample, 0 to 450 SPD hits, is overlaid in orange. The ratio of the extrapolated low SPD, a, and the total number of expected χ_c candidates as calculated using the whole SPD range, $Y_{\text{All SPD}}$, is included in the legend.

Table 5.5. Summary of the fit parameters used to extrapolate the number of expected χ_c candidates corrected for photon conversions for linear and quadratic fits at two SPD intervals for 2016-only, and combined 2015 and 2016 data.

Model	**SPD Hits**	**SPD Bins**	**Parameter**	**2016**	**2015 + 2016**
$a + b \cdot x^2$	0 - 450	6	a	194058 ± 10051	232315 ± 12020
			b	-43449 ± 0.4	-43470 ± 0.4
			$a/Y_{\mathrm{All\,SPD}}$	0.54 ± 0.05	0.54 ± 0.05
$a + b \cdot x^2$	0 - 300	6	a	201154 ± 8913	240831 ± 10664
			b	-36353 ± 0.6	-36309 ± 0.4
			$a/Y_{\mathrm{All\,SPD}}$	0.56 ± 0.05	0.56 ± 0.05
$a + b \cdot x^2$	0 - 450	5	a	196430 ± 18634	235213 ± 22208
			b	-57300 ± 0.4	-57345 ± 0.4
			$a/Y_{\mathrm{All\,SPD}}$	0.55 ± 0.07	0.55 ± 0.07
$a + b \cdot x^2$	0 - 450	4	a	204667 ± 23953	245022 ± 28547
			b	-47500 ± 0.4	-47535 ± 0.4
			$a/Y_{\mathrm{All\,SPD}}$	0.57 ± 0.08	0.57 ± 0.08
$a + b \cdot x$	0 - 450	6	a	136542 ± 34248	163734 ± 40886
			b	704 ± 215	839 ± 257
			$a/Y_{\mathrm{All\,SPD}}$	0.38 ± 0.10	0.38 ± 0.10
$a + b \cdot x$	0 - 300	6	a	161827 ± 32124	193994 ± 38339
			b	506 ± 226	602 ± 269
			$a/Y_{\mathrm{All\,SPD}}$	0.45 ± 0.10	0.45 ± 0.10
$a + b \cdot x$	0 - 450	5	a	152999 ± 55386	183558 ± 66021
			b	571 ± 294	680 ± 350
			$a/Y_{\mathrm{All\,SPD}}$	0.43 ± 0.16	0.43 ± 0.16
$a + b \cdot x$	0 - 450	4	a	138579 ± 69566	166289 ± 82928
			b	724 ± 331	862 ± 394
			$a/Y_{\mathrm{All\,SPD}}$	0.39 ± 0.20	0.39 ± 0.20

5.1.7 Summary of photon-conversion efficiency studies

By studying the photons from $D^{*0} \to D^0[K^\pm\pi^\mp]\gamma$ decays we have been able to calculate the photon-conversion efficiency (defined to be the product of the conversion probability and reconstruction efficiency) for downstream tracks in bins of the photon's transverse momentum, $p_{\mathrm{T}}(\gamma)$. A significant dependence on $p_{\mathrm{T}}(\gamma)$ is observed, with negligible efficiency below $\sim 300\,\mathrm{MeV}/c$, rising steeply thereafter. This behaviour affects the reconstruction of χ_{c0} mesons the most, for which the photons in CEP events are very soft. As a result, we conclude our sample in the χ_{c0} mass region is background dominated and have excluded it from the study.

To account for the unique low-multiplicity environment conditions of CEP, we have studied the effect of the detector occupancy on the photon-conversion efficiency. By determining the evolution of the efficiency in bins of event multiplicity, quantified in the number of SPD hits, we are able to extrapolate the performance into the low-multiplicity regime of CEP physics. In conclusion, we shall correct our observed χ_{c1} and χ_{c2} CEP signal by the photon-conversion efficiency vs. $p_{\mathrm{T}}(\gamma)$ distribution of Fig. 5.13. The dominant systematic uncertainty in this procedure is a relative $\pm 8\%$ associated with the knowledge of the produced number of D^{*0} mesons in the sample. We shall then apply a further correction factor to the corrected yield of 0.50 ± 0.10 to account for the difference in multiplicity between the calibration and signal samples.

5.2 Muon-reconstruction efficiencies

The muon-pair reconstruction efficiencies have been calculated for CEP conditions using 2015 data in an earlier study of J/ψ and $\psi(2S)$ production [44]. This study employed the same muon trigger lines and muon fiducial cut, $2 < \eta < 4.5$, used in our CEP χ_c analysis. In the CEP J/ψ and $\psi(2S)$ study, the reconstruction efficiency, $\varepsilon_{\mathrm{Rec}}$, is defined such that,

$$\varepsilon_{\mathrm{Rec}} = \varepsilon_{\mathrm{Track}} \times \varepsilon_{\mu\mathrm{Acc}} \times \varepsilon_{\mu\mathrm{ID}} \times \varepsilon_{\mathrm{Trig}} \times f_{\mathrm{Rec}}, \tag{5.8}$$

where $\varepsilon_{\mathrm{Track}}$ is the tracking efficiency for two tracks to be reconstructed inside the fiducial region, $2 < \eta < 4.5$, $\varepsilon_{\mu\mathrm{Acc}}$ is the efficiency for both of the tracks to be inside the muon chamber acceptance, $\varepsilon_{\mu\mathrm{ID}}$ is the muon-identification efficiency, given by the fraction of muons traversing the muon chamber that are reconstructed as muons, and $\varepsilon_{\mathrm{Trig}}$ is the trigger efficiency, which is defined as the fraction of events with two identified muons that fire the relevant hardware and software triggers. Throughout this study, we will refer to the product of these efficiencies as the *dimuon efficiency*. In Ref. [44] these efficiencies were calculated as a function of the J/ψ rapidity using simulation and were then corrected to bring Monte Carlo and data into agreement using a rapidity-dependent scale factor, f_{Rec}, obtained from a 'tag-and-probe' study performed on data. The efficiencies and correction factors are tabulated in Table 5.6, with their distributions shown in Fig. 5.19. We use this 2015 efficiency as a reference point in our analysis. However, we must adjust this measurement slightly to be suitable for the conditions of the 2015 and 2016 χ_c study.

Table 5.6. Summary of the track ($\varepsilon_{\text{Track}}$), muon-chamber acceptance ($\varepsilon_{\mu\text{Acc}}$), muon identification ($\varepsilon_{\mu\text{ID}}$), and trigger ($\varepsilon_{\text{Trig}}$) efficiencies calculated using SuperChic Monte Carlo of exclusive J/ψ production for 2015 run conditions, and the scaling factor (f_{Rec}) applied to the simulation in order to match data and calculate the muon data-reconstruction efficiency (ε_{Rec}). These values are reproduced from Ref. [44]. There follow quantities determined in the current analysis: the total dimuon efficiencies in data for this analysis (including all the contributions above) for 2015, $\varepsilon_{\mu\mu 15} = f_{\mu\varepsilon 15} \times \varepsilon_{\text{Rec}}$, and 2016 data, $\varepsilon_{\mu\mu 16} = \varepsilon_{\mu\mu 15} \times R_{\mathcal{L}} \ / \ R_N$, where $f_{\mu\varepsilon 15}$ is the ratio of the yield of J/ψ events selected in our 2015 sample and those of the earlier study, $R_{\mathcal{L}}$ is the integrated-luminosity ratio of 2015 to 2016 data of single interaction crossings, and R_N is the J/ψ yield ratio from 2015 and 2016 data.

$\boldsymbol{y}$	$\mathbf{[2.0, 2.25]}$	$\mathbf{[2.25, 2.5]}$	$\mathbf{[2.5, 2.75]}$	$\mathbf{[2.75, 3.0]}$	$\mathbf{[3.0, 3.25]}$
$\varepsilon_{\text{Track}}$	0.624 ± 0.018	0.770 ± 0.009	0.812 ± 0.007	0.861 ± 0.005	0.877 ± 0.005
$\varepsilon_{\mu\text{Acc}}$	0.789 ± 0.019	0.860 ± 0.009	0.896 ± 0.006	0.907 ± 0.005	0.887 ± 0.005
$\varepsilon_{\mu\text{ID}}$	0.986 ± 0.006	0.979 ± 0.004	0.966 ± 0.004	0.952 ± 0.004	0.944 ± 0.004
$\varepsilon_{\text{Trig}}$	0.790 ± 0.022	0.797 ± 0.011	0.805 ± 0.008	0.797 ± 0.007	0.820 ± 0.006
f_{Rec}	1.070 ± 0.063	1.016 ± 0.042	0.981 ± 0.032	0.952 ± 0.026	0.934 ± 0.024
ε_{Rec}	0.410 ± 0.031	0.524 ± 0.024	0.555 ± 0.020	0.564 ± 0.017	0.562 ± 0.016
$f_{\mu\varepsilon 15}$	0.973 ± 0.086	0.930 ± 0.042	0.955 ± 0.034	1.004 ± 0.030	1.044 ± 0.029
R_N	0.143 ± 0.007	0.151 ± 0.004	0.148 ± 0.003	0.158 ± 0.003	0.165 ± 0.003
$\varepsilon_{\mu\mu 15}$	0.399 ± 0.046	0.488 ± 0.032	0.530 ± 0.027	0.566 ± 0.024	0.586 ± 0.023
$\varepsilon_{\mu\mu 16}$	0.485 ± 0.061	0.562 ± 0.039	0.622 ± 0.034	0.622 ± 0.029	0.617 ± 0.026

$\boldsymbol{y}$	$\mathbf{[3.25, 3.5]}$	$\mathbf{[3.5, 3.75]}$	$\mathbf{[3.75, 4.0]}$	$\mathbf{[4.0, 4.25]}$	$\mathbf{[4.25, 4.5]}$
$\varepsilon_{\text{Track}}$	0.897 ± 0.004	0.916 ± 0.004	0.925 ± 0.005	0.913 ± 0.007	0.900 ± 0.013
$\varepsilon_{\mu\text{Acc}}$	0.871 ± 0.005	0.850 ± 0.006	0.818 ± 0.007	0.779 ± 0.011	0.763 ± 0.020
$\varepsilon_{\mu\text{ID}}$	0.935 ± 0.004	0.932 ± 0.004	0.921 ± 0.006	0.905 ± 0.009	0.888 ± 0.017
$\varepsilon_{\text{Trig}}$	0.869 ± 0.006	0.902 ± 0.005	0.925 ± 0.006	0.935 ± 0.008	0.950 ± 0.012
f_{Rec}	0.924 ± 0.023	0.915 ± 0.024	0.911 ± 0.026	0.914 ± 0.030	0.893 ± 0.037
ε_{Rec}	0.587 ± 0.016	0.599 ± 0.017	0.587 ± 0.019	0.550 ± 0.021	0.517 ± 0.029
$f_{\mu\varepsilon 15}$	1.030 ± 0.029	1.068 ± 0.032	1.099 ± 0.096	1.065 ± 0.122	1.126 ± 0.099
R_N	0.166 ± 0.003	0.171 ± 0.003	0.171 ± 0.003	0.164 ± 0.004	0.171 ± 0.008
$\varepsilon_{\mu\mu 15}$	0.604 ± 0.023	0.639 ± 0.027	0.645 ± 0.060	0.586 ± 0.071	0.583 ± 0.061
$\varepsilon_{\mu\mu 16}$	0.633 ± 0.027	0.650 ± 0.029	0.657 ± 0.0624	0.622 ± 0.077	0.592 ± 0.068

By comparing the yield of J/ψ events we select in 2015, $N(J/\psi)_{\text{B}}$, with those of the earlier analysis, $N(J/\psi)_{\text{A}}$, we are able to determine the efficiency of our selection, since the muon-reconstruction efficiency for our 2015 sample is given by $\varepsilon_{\mu\mu 15} = f_{\mu\varepsilon 15} \times \varepsilon_{\text{Rec}}$, where $f_{\mu\varepsilon 15} = N(J/\psi)_{\text{B}} / N(J/\psi)_{\text{A}}$. The selection criteria in the earlier paper are summarised in Table 5.7. In our analysis we replace the software trigger requirements, which are conditional on the state of the low-multiplicity hadron trigger decision called `L0Hadron,lowMult`, with a pass on either the `Hlt2LowMultDimuon` or `Hlt2LowMultMuon` trigger line detailed in Table 4.3 in order to match our χ_c analysis requirement. In performing this study we also need to reproduce as closely as possible the HeRSCheL working point adopted in the earlier analysis. The aforementioned paper used a different method and calibration to calculate $\ln(\chi^2_{\text{HRC}})$. Therefore, using our HeRSCheL figure-of-merit efficiency results presented later in Sec. 5.6, we select a threshold

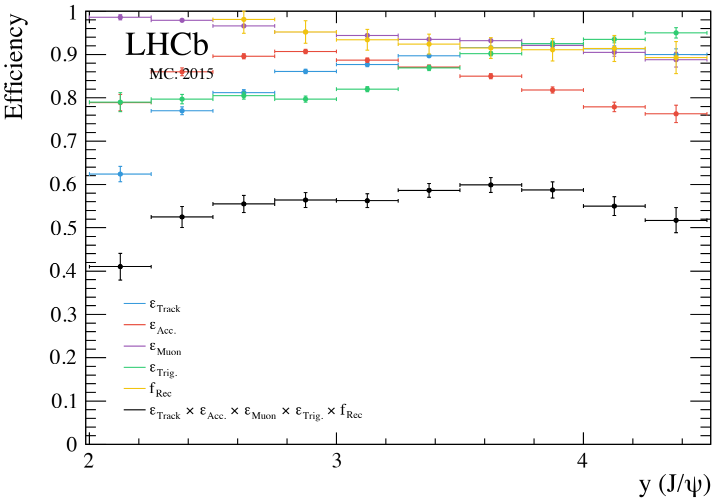

Figure 5.19. Track ($\varepsilon_{\text{Track}}$ in blue), muon chamber acceptance ($\varepsilon_{\mu\text{Acc}}$ in red), muon identification ($\varepsilon_{\mu\text{ID}}$ in purple), and trigger efficiencies calculated ($\varepsilon_{\text{Trig}}$ in green) using SuperChic Monte Carlo of exclusive J/ψ production for 2015 run conditions and the global scaling factor (f_{Rec} in yellow) applied to the simulation in order to match data and calculate the muon data-reconstruction efficiency (ε_{Rec} in black). These efficiencies are taked from Ref. [44].

of $\ln(\chi^2_{\text{HRC}}) < 5$. This is the same requirement used in the main χ_c analysis, which has an efficiency of 0.704 ± 0.018 (see Sec. 5.6), to match the $\ln(\chi^2_{\text{HRC}}) < 3.5$ cut used in the CEP J/ψ analysis, which in turn has an efficiency of 0.723 ± 0.008.

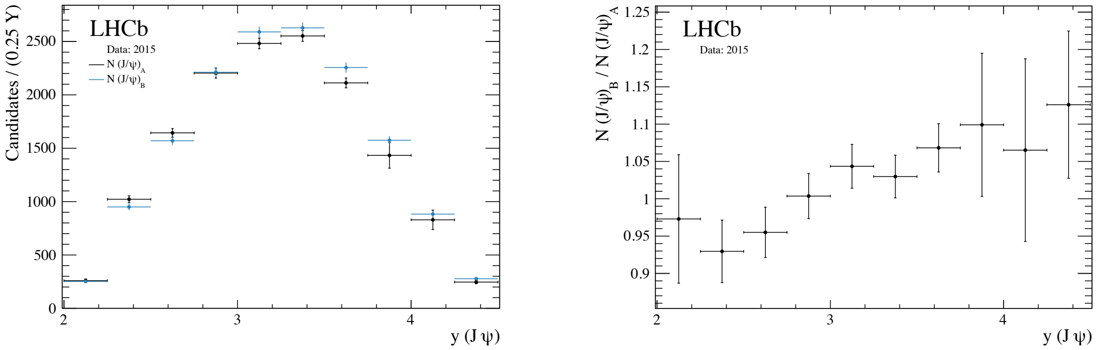

Figure 5.20. J/ψ yield as a function of rapidity (left) from the CEP J/ψ results [44], $N(J/\psi)_{\text{A}}$ in black, together with the results from our modified selection, $N(J/\psi)_{\text{B}}$ in blue, for 2015 data, run numbers 164524 to 167136. Correction factor for 2015 data, $f_{\mu\varepsilon 15}$ (right).

The J/ψ yields, $N(J/\psi)_{\text{B}}$ and $N(J/\psi)_{\text{A}}$, are shown in Fig. 5.20 in bins of rapidity alongside their ratio, $f_{\mu\varepsilon 15}$, and their values are tabulated in Table 5.6. We see that there is a difference in the total selection efficiency between the two analyses that varies with rapidity and does not exceed 10% throughout most rapidity bins. Globally, the yields integrated over all rapidity bins for each sample is $N(J/\psi)_{\text{A Total}} = 14783 \pm 122$ and $N(J/\psi)_{\text{B Total}} = 15193 \pm 123$, making

Table 5.7. Summary of the selection criteria used in CEP J/ψ analysis paper from Ref. [44] and the selection applied to 2015 data only, to closely match the selection from the CEP J/ψ paper and compare their results. The slightly tighter selection applied to both 2015 and 2016 data for the comparison of the muon-reconstruction efficiency between the two years is also summarised.

Trigger Level		**J/ψ paper**	**2015 J/ψ**	**2015, 2016 J/ψ**
L0 Trigger		`L0Muon,lowMult` or `L0DiMuon,lowMult`	`L0Muon,lowMult` or `L0DiMuon,lowMult`	`L0Muon,lowMult` or `L0DiMuon,lowMult`
HLT1		Pass through	Pass through	Pass through
HLT2		If `!L0Hadron,lowMult` then `Hlt2LowMultMuon` If `L0Hadron,lowMult` then `Hlt2LowMultChiC2HH`	`Hlt2LowMultMuon` or `Hlt2LowMultDiMuon`	`Hlt2LowMultMuon` or `Hlt2LowMultDiMuon`
Variable	**Units**	**Cut**		
$m_{\mu^+\mu^-}$ window	MeV/c^2	$\lvert m_{\mu^+\mu^-} - 3097\rvert < 65$	$\lvert m_{\mu^+\mu^-} - 3097\rvert < 65$	$\lvert m_{\mu^+\mu^-} - 3097\rvert < 50$
Nº photons	-	0 with $E_T > 200\,\text{MeV}$	0 with $E_T > 200\,\text{MeV}$	0 with $E_T > 200\,\text{MeV}$
Nº upstream tracks	-	0	0	0
Nº VELO tracks	-	0	0	0
Nº backward tracks	-	0	0	0
Nº downstream tracks	-	0	0	0
Nº long tracks	-	2 ($\mu^+\mu^-$)	2 ($\mu^+\mu^-$)	2 ($\mu^+\mu^-$)
Nº muon tracks	-	2 ($\mu^+\mu^-$)	2 ($\mu^+\mu^-$)	2 ($\mu^+\mu^-$)
Muon ID	-	True	True	True
$p_{\mathrm{T}}^2(\mu^+\mu^-)$	$[\,\text{GeV}/c]^2$	< 0.8	< 0.8	< 0.5
$\eta(\mu)$	-	$\in [2, 4.5]$	$\in [2, 4.5]$	$\in [2, 4.5]$
$\ln(\chi^2_{\text{HRC}})$	-	< 3.5	< 5	< 5
$p_{\mathrm{T}}(\mu)$	MeV/c	-	-	> 200 or Max > 800
Nº SPD Hits	-	-	-	< 20

our selection more efficient. The corrected muon-reconstruction efficiency for 2015 is shown in Fig. 5.21 (black).

It is now necessary to understand whether there are differences between the selection efficiency for 2015 and 2016. To determine if this is the case, we apply the same nominal selections to both years and compare the ratio of reconstructed CEP-like J/ψ events between the years with the ratio of their integrated luminosities. If the efficiency is the same, we expect these ratios to be the same. To account for any differences, the dimuon efficiency for 2016 is given by $\varepsilon_{\mu\mu 16} = \varepsilon_{\mu\mu 15} \times R_{\mathcal{L}} \,/\, R_N$, where $R_{\mathcal{L}}$ is the integrated-luminosity ratio of 2015 to 2016 data of single interaction crossings [1], and R_N is the J/ψ yield ratio from 2015 and 2016 data.

We use a similar selection as the one detailed above with a few exceptions: we tighten the J/ψ mass-window cut to match the one used in our χ_c study, and we tighten the upper cut on the

---

[1] We assume there is negligible uncertainty on this ratio, as the bulk of the luminosity systematic will be fully correlated between years.

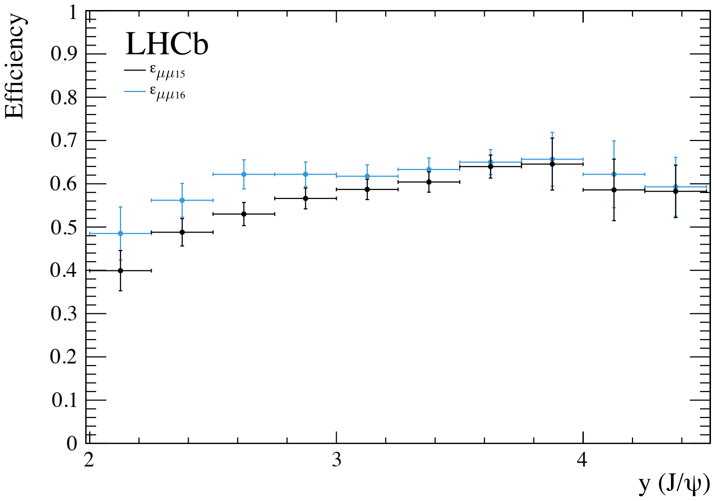

Figure 5.21. Dimuon-reconstruction efficiency for 2015 (black), $\varepsilon_{\mu\mu 15}$, and 2016 (blue), $\varepsilon_{\mu\mu 16}$, run conditions.

$p_{\mathrm{T}}^2(J/\psi)$ to increase the CEP purity of the sample. In addition, some changes were implemented to the hardware trigger for the 2016 runs. This included the tightening of the number of SPD hit requirements from < 30 to < 20 hits for both `L0DiMuon,lowMult` and `L0Muon,lowMult` trigger lines. The `L0Muon,lowMult` trigger line requires a muon with a momentum greater than 800 MeV/c compared to 400 MeV/c. As a result, we apply these tighter cuts on the 2015 sample to have a uniform selection between samples. The J/ψ selection is summarised in Table 5.7.

We find that the global value of R_N is 0.1624 whereas $R_{\mathcal{L}}$ is 0.1739. Hence the 2016 efficiency is seen to be 7% more efficient than 2015. The J/ψ yield for 2015 and 2016 is shown in Fig. 5.22 alongside their ratio in bins of J/ψ rapidity. As the rapidity dependence is significant, we apply the correction factor to go from 2015 to 2016 efficiency in bins of this quantity. The corrected muon reconstruction efficiency for 2016 is shown in Fig. 5.21 (blue) and the values are tabulated in Table 5.6.

To calculate a global dimuon efficiency, $\varepsilon_{\mu\mu}^{Global}$, which accounts for the distribution in rapidity, we correct each χ_c signal candidate for efficiency according to its rapidity bin, and then divide the number of candidates in the original sample by the corrected total. This yields a global dimuon efficiency of 0.611 (0.635) with the HeRSCheL cut applied for 2015 (2016) data and 0.607 (0.635) without. This corresponds to a global dimuon efficiency of 0.631 for the combined data set both with and without the HeRSCheL cut applied, once these individual numbers are weighted by the integrated luminosities of each year.

The systematic uncertainties of the dimuon efficiency, as determined in Ref. [44], has two major systematic uncertainties: one associated with the method used to evaluate the muon identification corresponding to an uncertainty of 0.4%, and another associated with the method used to evaluate the muon trigger corresponding to an uncertainty of 0.2%. However, the

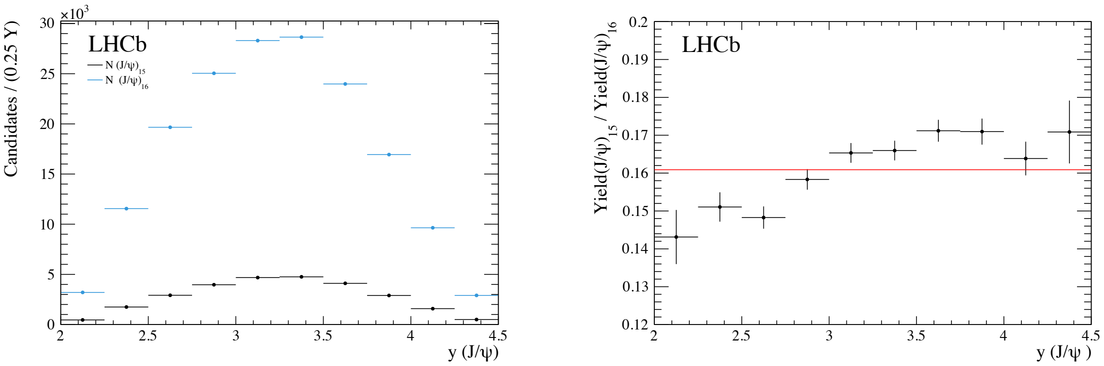

Figure 5.22. J/ψ yield as a function of rapidity (left) for two muon-track events for 2015, $N(J/\psi)_{15}$ in black, and 2016, $N(J/\psi)_{16}$ in blue, together with their ratio R_N (right). The horizontal red line marks the global value of R_N at 0.1626.

uncertainty we assign is necessarily larger, and is dominated by the change in efficiency between 2015 and 2016, which is not fully understood. We assign the full value of this change as a systematic uncertainty in the 2016 analysis, which then corresponds to an uncertainty of 5% on the combined 2015 and 2016 analysis.

5.3 J/ψ mass-window efficiency

We apply a J/ψ mass-window cut, $|m(J/\psi) - 3096.916| < 50\ \text{MeV}/c^2$, to reduce contamination from di-muon continuum background. Since there is a slight difference in the J/ψ mass resolution in Monte Carlo and data, we use a data-driven method to calculate the efficiency associated with this cut, $\varepsilon_{m(J/\psi)}$. We employ a similar J/ψ selection as the one used for the 2015 and 2016 muon-reconstruction efficiency comparison tabulated in Table 5.7. However, we omit the SPD and muon transverse-momentum requirements, since these cuts were only intended to make a one-to-one comparison between 2015 and 2016 data samples and are not part of the χ_c analysis. Similarly, we omit the photon cut as we expect to see extra photons in $\chi_c \to J/\psi\,[\mu^+\mu^-]\gamma[e^+e^-]$ events from bremsstrahlung radiation.

To fit the J/ψ mass distribution, we use a Gaussian and a double-sided Crystal Ball with a shared mean value. The ratio of the Gaussian yield and the double-sided Crystal Ball yield is fixed according to the results of these fits on CEP $\chi_{c1,2} \to J/\psi\,[\mu^+\mu^-]\gamma[e^+e^-]$ Monte Carlo described in Sec. 4.1 while keeping all other parameters free. Applying this constraint, we perform an unbinned-maximum-likelihood fit of the data samples over the 2750 to 3450 MeV mass range, the results of which are shown in Fig. 5.23. This fit method estimates the parameters, θ, of our model PDF, $f(x_i, \theta)$, by maximising the likelihood function given by

$$L(x_1, ..., x_n|\theta) = \prod_{i=1}^{n} f(x_i, \theta), \tag{5.9}$$

where x_i are data points in a sample of size n. In the case of a binned-maximum-likelihood fit, the observed events in each bin are assumed to have a Poisson distribution. The fit does a

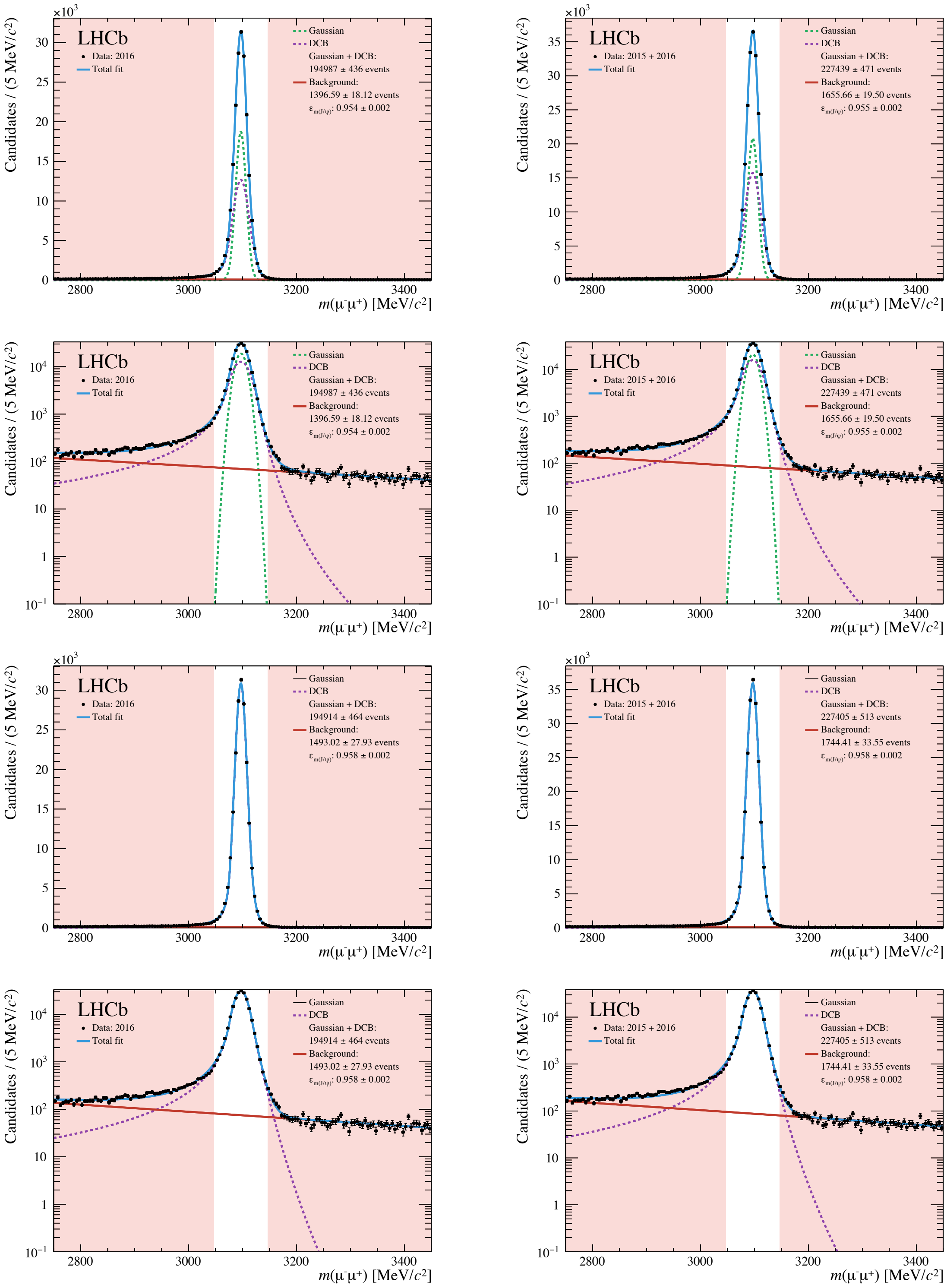

Figure 5.23. Invariant mass of CEP like $J/\psi \rightarrow \mu^+\mu^-$ mesons from proton-proton collisions at a centre-of-mass energy $\sqrt{s} = 13$ TeV for the 2016-only (left), and combined 2015 and 2016 (right) data in linear (first and third row) and logarithmic (second and fourth row) scale. In the first and second row the signal is fitted with the combination of a double-sided Crystal Ball (dashed purple) and a Gaussian (dashed green) while in the third and fourth row it is fitted with a double-sided Crystal Ball. The continuum-combinatorial background is fitted with an exponential (dotted red). Integrals for events within our selection mass window are shown and the veto region is highlighted in red.

good job at describing the slightly skewed shape of the J/ψ resonance. The normalised integral of the J/ψ signal shape within our selection mass window is 0.954 ± 0.002 (0.955 ± 0.002) for 2016 (2015 and 2016).

As a systematic check, we repeat the fit using a single double-sided Crystal Ball to model the J/ψ signal while maintaining a single exponential to model the background. The fit results are shown in Fig. 5.23 for 2016-only, and the combined 2015 and 2016 data samples. The normalised integral of the J/ψ signal shape over our selection mass window is 0.958 ± 0.002 (0.958 ± 0.002) for 2016 (2015 and 2016). We take the difference between the two sets of results as the systematic uncertainty, corresponding to 0.4% (0.3%) for the 2016 (2015 and 2016) data.

5.4 χ_c invariant-mass-difference window-selection efficiency

As part of our analysis, we apply a cut to the mass difference between the χ_c candidate and the intermediate J/ψ meson, $350 < \Delta m_{\chi_c} < 500$. Therefore, when measuring the χ_{c1} and χ_{c2} yields we have to account for the cut efficiency for each meson, $\varepsilon_{\Delta m_{\chi_{c1}}}$ and $\varepsilon_{\Delta m_{\chi_{c2}}}$ respectively. To calculate the efficiency, we use the reconstructed CEP χ_c Monte Carlo, described in Sec. 4.1.4, with our CEP χ_c selection applied. The Δm_{χ_c} distribution of the selected events is shown in Fig. 5.24 for the 2016-only, and combined 2015 and 2016 run conditions together with the delta-mass vetoed regions highlighted in red.

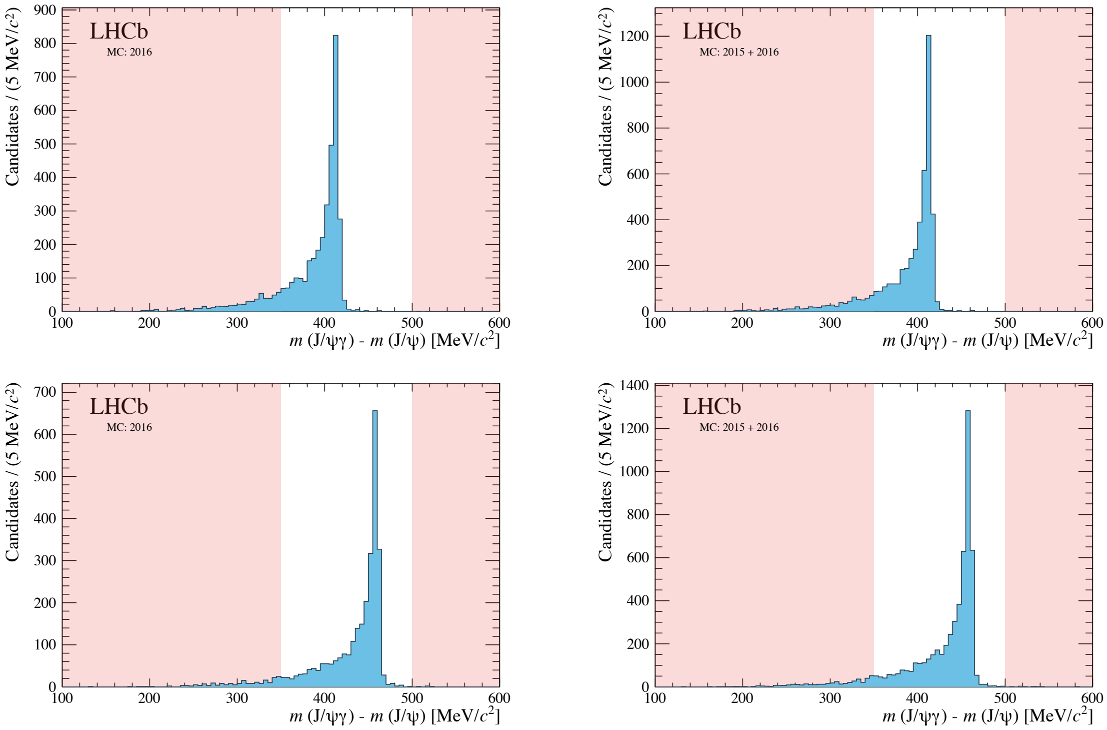

Figure 5.24. Delta-mass distribution from reconstructed CEP χ_{c1} (top) and χ_{c2} (bottom) Monte Carlo generated with SuperChic v2 for the 2016-only (left), and combined 2015 and 2016 (right) run conditions. The delta-mass veto region is highlighted in red.

It is important to note that these distributions correspond to reconstructed events, and it is possible for the reconstruction efficiency of converted photons to be different in Monte Carlo and data. The efficiency of the photon reconstruction varies with transverse momentum. If the p_T distribution of those events below the cut in delta mass is different from those events within the window, and if the dependence of the reconstruction efficiency with p_T is different between data and Monte Carlo, then the determination of the window-selection efficiency will be biased. To account for any differences, we calculate the photon-conversion efficiency using the Monte Carlo, the distributions of which are shown as a function of the photon's transverse momentum in Fig. 5.25 for 2016-only, and combined 2015 and 2016 run conditions. The photon-conversion efficiency determined from data, shown in Fig. 5.13, grows more steeply than that of the Monte Carlo. We then correct the delta-mass distribution for the Monte Carlo photon-conversion efficiency and apply the efficiency determined using the data-driven method described in Sec. 5.1, such that the distribution is now representative of that reconstructed in data. By integrating the Δm_{χ_c} distribution within our selection window we determine the cut to have an efficiency of 0.885 ± 0.017 (0.892 ± 0.015) for χ_{c1} mesons and 0.944 ± 0.021 (0.948 ± 0.015) for χ_{c2} for the 2016-only (combined 2015 and 2016) data.

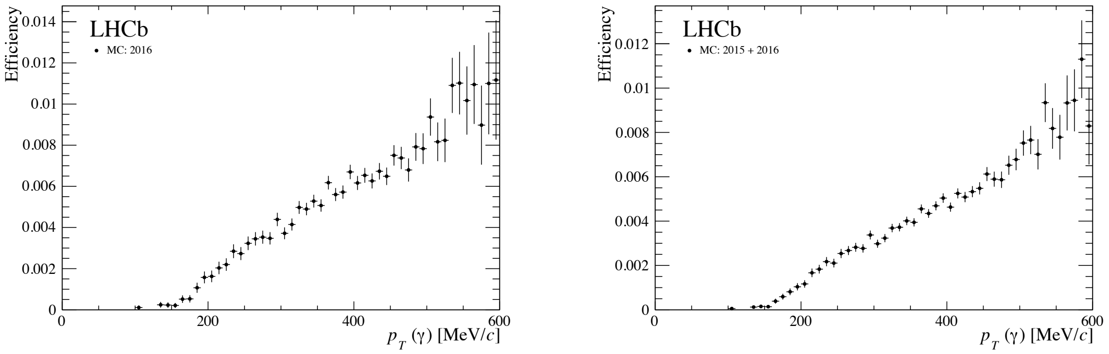

Figure 5.25. Photon-conversion efficiency as a function of the photon's generator-level transverse momentum using combined CEP χ_{c1} and χ_{c2} Monte Carlo for the 2016-only (left), and combined 2015 and 2016 (right) run conditions.

As a systematic check we determine the mass-window efficiency directly from Monte Carlo, that is with the photon-reconstruction efficiencies displayed in Fig. 5.25. By taking the fraction of events that fall within our selection window we determine the window cut efficiency to be 0.851 ± 0.014 (0.856 ± 0.012) for χ_{c1} mesons and 0.928 ± 0.017 (0.923 ± 0.012) for χ_{c2} for the 2016-only (combined 2015 and 2016) data. As a result, we assign an uncertainty of 3.8% (4.0%) for χ_{c1} and 1.7% (2.7%) for χ_{c2} for the 2016-only (combined 2015 and 2016) data.

A further source of possible bias would be if the χ_c resolution of the Monte Carlo is significantly different from that in the data. This is not the case, as can be seen in Fig. 5.26, where we compare the function fitted to the data with the χ_{c1} and χ_{c2} Monte Carlo distributions. Although the fit undershoots the Monte Carlo at the core, the tail is well described. Nonetheless, exercises are performed in which additional smearing is introduced to the Monte Carlo, such that the agreement with data remains tolerable. No significant change in the fraction of events in the veto region is observed.

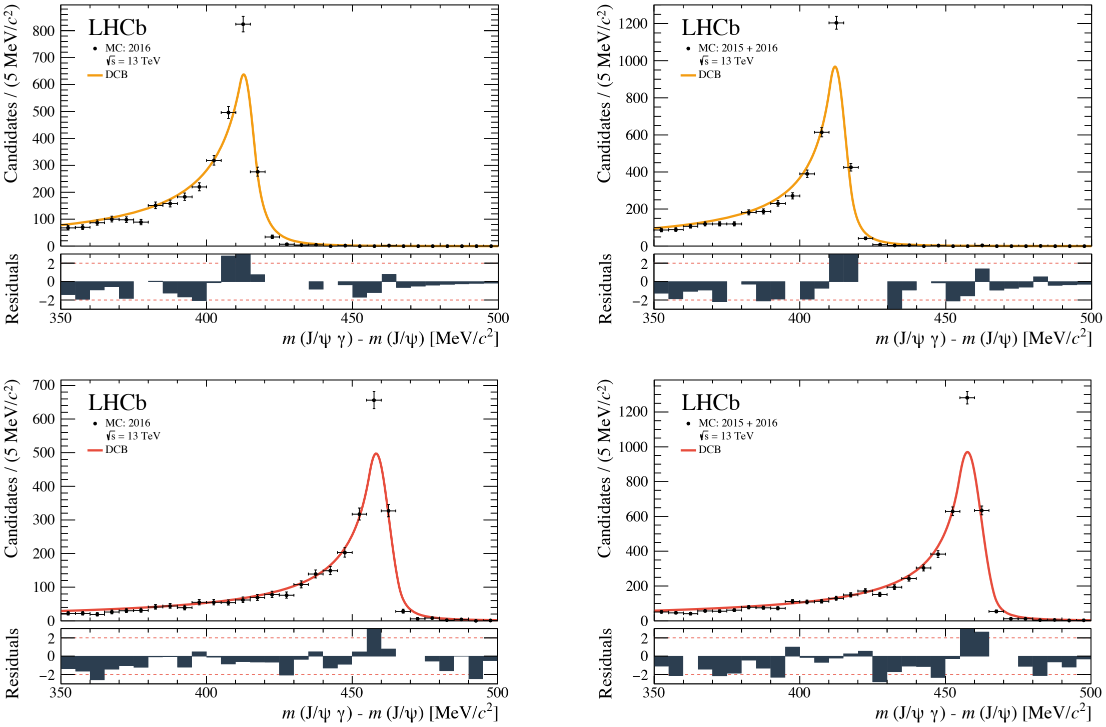

Figure 5.26. Delta-mass distribution from χ_{c1} (top) and χ_{c2} (bottom) Monte Carlo for the 2016-only (left), and combined 2015 and 2016 (right) run conditions. The distributions are fitted with the functions fitted to data. The lower panels show the pulls.

5.5 SPD efficiency

As part of the low-multiplicity hardware trigger lines, we use the number of SPD hits as an indicator of the detector occupancy. Characteristically, CEP events have a low number of final-state particles and will leave few SPD hits. However, due to the short 25 ns bunch spacing, this detector is sensitive to remnant signatures from collisions of adjacent beam crossings, known as spill-over and pre-spill. The `L0Muon,lowMult` and the `L0DiMuon,lowMult` hardware trigger lines require less than thirty SPD hits for 2015 data and less than twenty for 2016. To estimate the impact of the SPD cut on the efficiency of our χ_c selection, we model the SPD distribution of an empty detector, as well as the separate contribution of muons from the J/ψ decay and electrons from the photon conversion.

To estimate the extra activity in the detector (detector noise, spill-over, and pre-spill), we use randomly-triggered events and select those with zero reconstructed tracks and photons. The SPD distribution for these empty events is shown in Fig. 5.27 for 2016 data in linear and logarithmic scale. We expect muons to leave about one hit in the SPD. To model this, we assume a Poisson distribution with a mean of one ($\lambda_\mu = 1$) for each muon and add it to the noise distribution extracted from the minimum-bias sample. We check the model against the

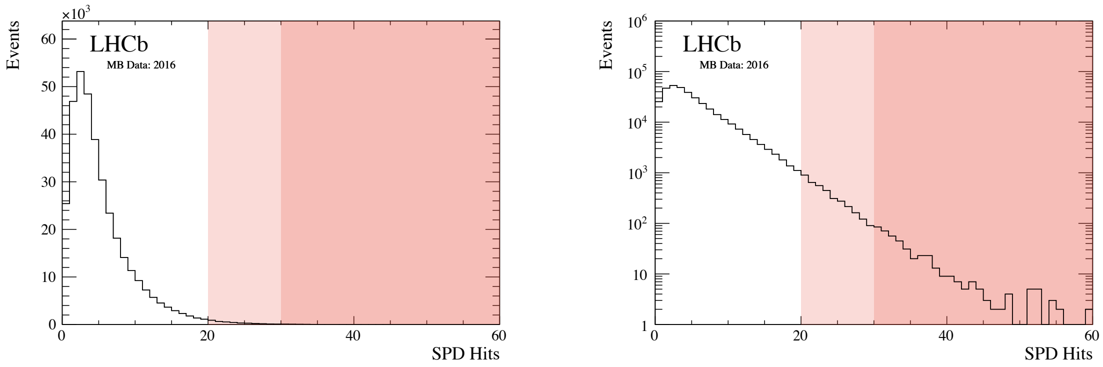

Figure 5.27. Distribution of SPD hits in randomly triggered empty events with zero tracks and photons in linear (left) and logarithmic scale (right) for 2016 data. The SPD veto regions for the `L0Muon,lowMult` and `L0DiMuon,lowMult` trigger lines is highlighted in red for 2015 and pink for 2016 run conditions.

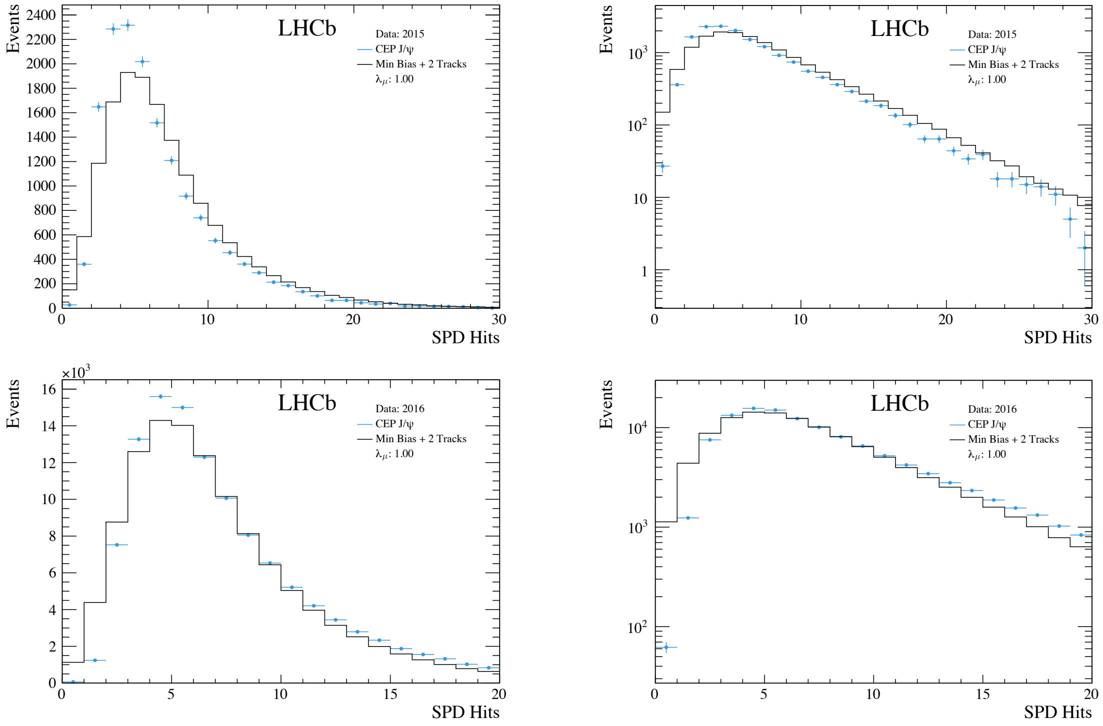

Figure 5.28. Distribution of SPD hits of CEP J/ψ candidates (blue) and of randomly triggered events with zero tracks and photons, added to a simple model that describes the interaction of muons assuming a Poisson distribution with a mean of one (black) for 2015 (top) and 2016 (bottom) data shown in linear (left) and logarithmic (right) scale.

CEP J/ψ sample used to compare the muon reconstruction efficiency of 2015 and 2016 data described in Table 5.7 but with the additional requirement that there are no photons in the event. The SPD distribution of this sample and our SPD model are shown in Fig. 5.28. This method adequately models the right tail region, where our interest lies, although less well so for lower SPD hit values.

We expect electrons to generate more hits on the SPD than muons because of bremsstrahlung radiation and material interactions. We can estimate the number of hits expected from electrons using Monte Carlo, where we expect this aspect of the SPD response to be adequately described. We use the truth matched $\chi_{c1,2} \to J/\psi\,[\mu^+\mu^-]\gamma[e^+e^-]$ Monte Carlo, described in Sec. 4.1, with our CEP χ_c selection applied. The SPD distribution for this selection is shown in Fig. 5.29. Note that this distribution has less of a spillover tail than that of Fig. 5.28 due to the absence of noise, pre spill, and spill over in the simulated sample. Given our previous determination of approximately one SPD hit per muon, we estimate an additional average of two hits per electron is required to model the distribution.

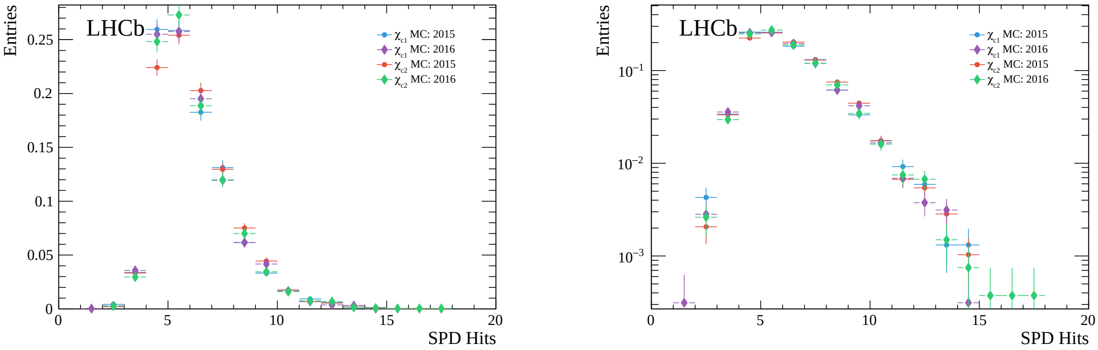

Figure 5.29. Normalised distribution of SPD hits of CEP χ_{c1} (blue and purple) and χ_{c2} (red and green) candidates from 2015 (dots) and 2016 (diamonds) Monte Carlo with CEP χ_c selections applied, in linear (left) and logarithmic (right) scale.

Table 5.8. SPD efficiencies for the reconstruction of CEP-like χ_c events using different λ_μ and λ_e values in our SPD distribution model for 2015 and 2016 hardware trigger requirements.

λ_μ	λ_e	< 20 SPD Hits	< 30 SPD Hits
0.75	1	0.970 ± 0.001	0.997 ± 0.001
	2	0.949 ± 0.001	0.995 ± 0.001
	3	0.914 ± 0.001	0.992 ± 0.001
1	1	0.966 ± 0.001	0.997 ± 0.001
	2	0.942 ± 0.001	0.995 ± 0.001
	3	0.902 ± 0.001	0.991 ± 0.001
1.25	1	0.961 ± 0.001	0.996 ± 0.001
	2	0.933 ± 0.001	0.994 ± 0.001
	3	0.888 ± 0.001	0.989 ± 0.001

With this in mind, we repeat the procedure detailed above and add a Poisson distribution with a mean of two ($\lambda_e = 2$) for each electron in the χ_c decay to the J/ψ plus additional-activity model. The resulting model for χ_c events is presented together with the SPD hit distribution from χ_c data for 2015 and 2016 samples, shown in Fig. 5.30. We obtain a reasonable description

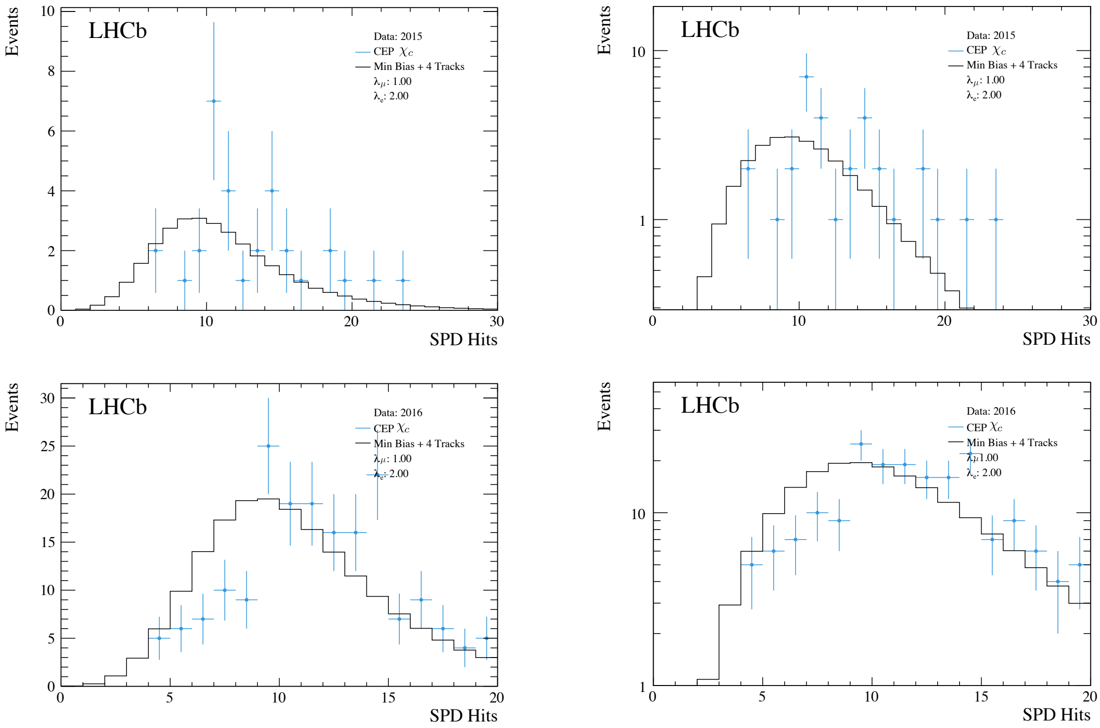

Figure 5.30. Distribution of SPD hits of CEP χ_c candidates (blue) and a model composed of randomly triggered 2016 events with zero tracks and photons added to a model that describes the interaction of muons assuming a Poisson distribution with a mean of one (black), and that of electrons with a Poisson distribution with a mean of two for 2015 (top) and 2016 (bottom) data shown in linear (left) and logarithmic (right) scale.

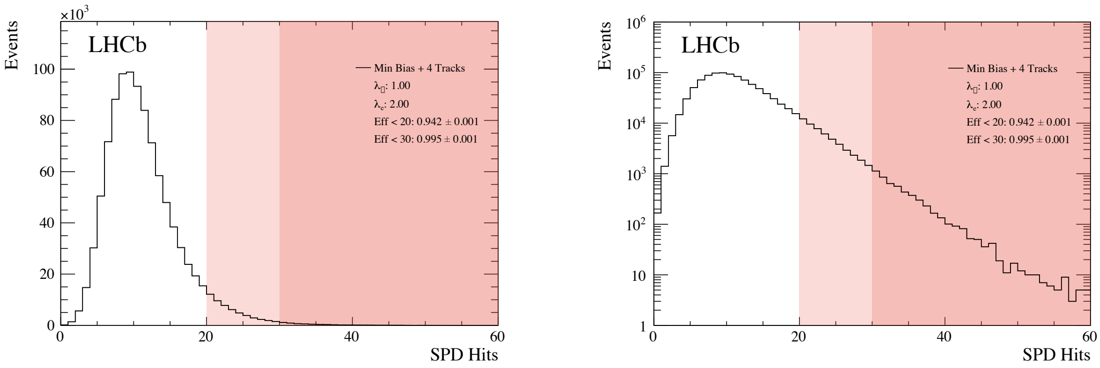

Figure 5.31. Distribution of SPD hits model based on randomly triggered 2016 events with zero tracks and photons added to a model that describes the interaction of muons assuming a Poisson distribution with a mean of one (black), and that of electrons with a Poisson distribution with a mean of two in linear (left) and logarithmic (right) scale.

of the right tail. We then generate a large sample with one million events, shown in Fig. 5.31, and take a normalised integral from zero to thirty (twenty) to calculate an SPD efficiency, ε_{SPD}, of 0.995 ± 0.001 (0.942 ± 0.001) for 2015 (2016). We weight the efficiency of each year by its corresponding single-interaction luminosity, the calculation of which is described in Sec. 7.5, to yield a SPD efficiency of $\varepsilon_{\text{SPD}} = 0.950 \pm 0.001$ for the combined 2015 and 2016 data set.

As a systematic check we vary the mean number of hits for muons by ±0.25 and electrons by ±1, the results for which are summarised in Table 5.8. We assign a systematic uncertainty of ±0.005 (±0.05) for 2015 (2016) data. This corresponds to a combined uncertainty of ±0.04 for the combined 2015 and 2016 data set.

5.6 HeRSCheL efficiency

To combine the response of all twenty HeRSCheL counters, four for each of the five modules, we construct a figure-of-merit quantity, $\ln(\chi^2_{\text{HRC}})$, as defined in Eq. 4.5, where low values correspond to CEP-like events and high values correspond to non-CEP background. To better understand the efficiency of the figure-of-merit, ε_{HRC}, and inform the placement of an upper limit for the χ_c analysis, we study the efficiency with a continuum-dimuon sample as it offers a large CEP data set. The dimuon CEP is mediated through two-photon exchange.

5.6.1 Dimuon-data selection

For this efficiency study, we select two samples: one with a high-CEP purity and another inelastic sample that breaks the rapidity-gap criteria. Henceforth, these samples will be referred to as the CEP-dimuon and non-CEP-dimuon samples. For the high-CEP purity sample we use a similar selection as the one presented in Table 5.7 for the comparison of the J/ψ yield between 2015 and 2016 data sets. However, we omit the SPD and muon transverse-momentum requirements, since these cuts were only intended to make a one-to-one comparison between the two data sets. In addition, the dimuon invariant mass is limited to the window $1500 < m(\mu^+\mu^-) < 8000$ MeV/c^2 where the resonant-mass windows of the J/ψ, $2700 < m(J/\psi) < 3200$ MeV/c^2, and $\psi(2S)$, $3500 < m(\psi(2S)) < 3800$ MeV/c^2, are excluded from the study. We choose to exclude these resonant contributions because CEP J/ψ and $\psi(2S)$ meson production is mediated by a different mechanism, photon-pomeron exchange, than that of CEP-dimuon production, which is mediated by double-photon exchange. The veto-windows around the resonant peaks are asymmetric in width to fully exclude the tail associated with energy loss via bremsstrahlung radiation. A total of $14,357$ and $86,918$ events pass the selection for 2015 and 2016 data respectively. The statistics for this sample are summarised in Table 5.9. The invariant-mass distribution for this sample is shown in Fig. 5.32 (left) for 2015 and 2016 data sets, where the vetoed resonance regions are highlighted in red. The transverse-momentum distribution, excluding data from the invariant-mass-veto regions, is shown in Fig. 5.33 (left).

For the non-CEP-dimuon sample, the track selection is modified to break the rapidity-gap criteria by requesting that the event has at least one extra track or any type of photon activity in the calorimeter. This assures the sample corresponds to non-CEP background. A total of $2,158,100$ and $2,712,653$ events survive the selection for 2015 and 2016 data respectively, summing to a total of $4,870,753$ events. The statistics for this sample are also summarised in Table 5.9. The invariant-mass distribution for the non-CEP-dimuon sample is shown in Fig. 5.32

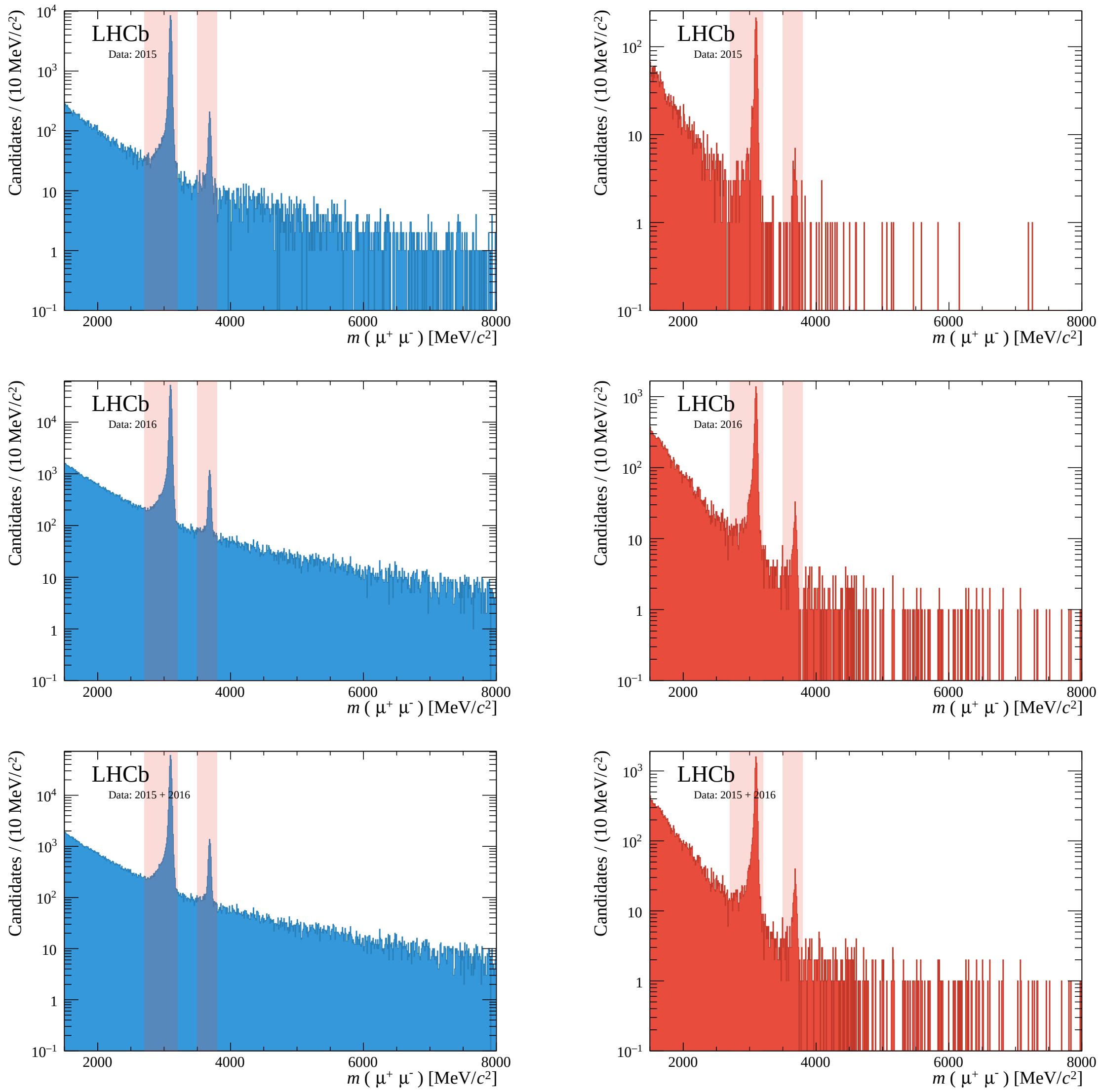

Figure 5.32. Dimuon invariant-mass distribution for the CEP (left) and non-CEP (right) dimuon selection for the 2015 (top), 2016 (middle), and combined 2015 and 2016 (bottom) data in logarithmic scale. The veto region of resonant J/ψ and $\psi(2S)$ mesons is highlighted in red.

(right) for the 2015, 2016, and combined 2015 and 2016 data sets. The transverse-momentum-squared distribution, excluding data from the invariant-mass-veto regions, is shown in Fig. 5.33 (right). We use these histograms as templates for the PDF of the transverse-momentum-squared distributions of non-CEP-dimuon production, which is necessary to describe the background of our CEP-dimuon sample.

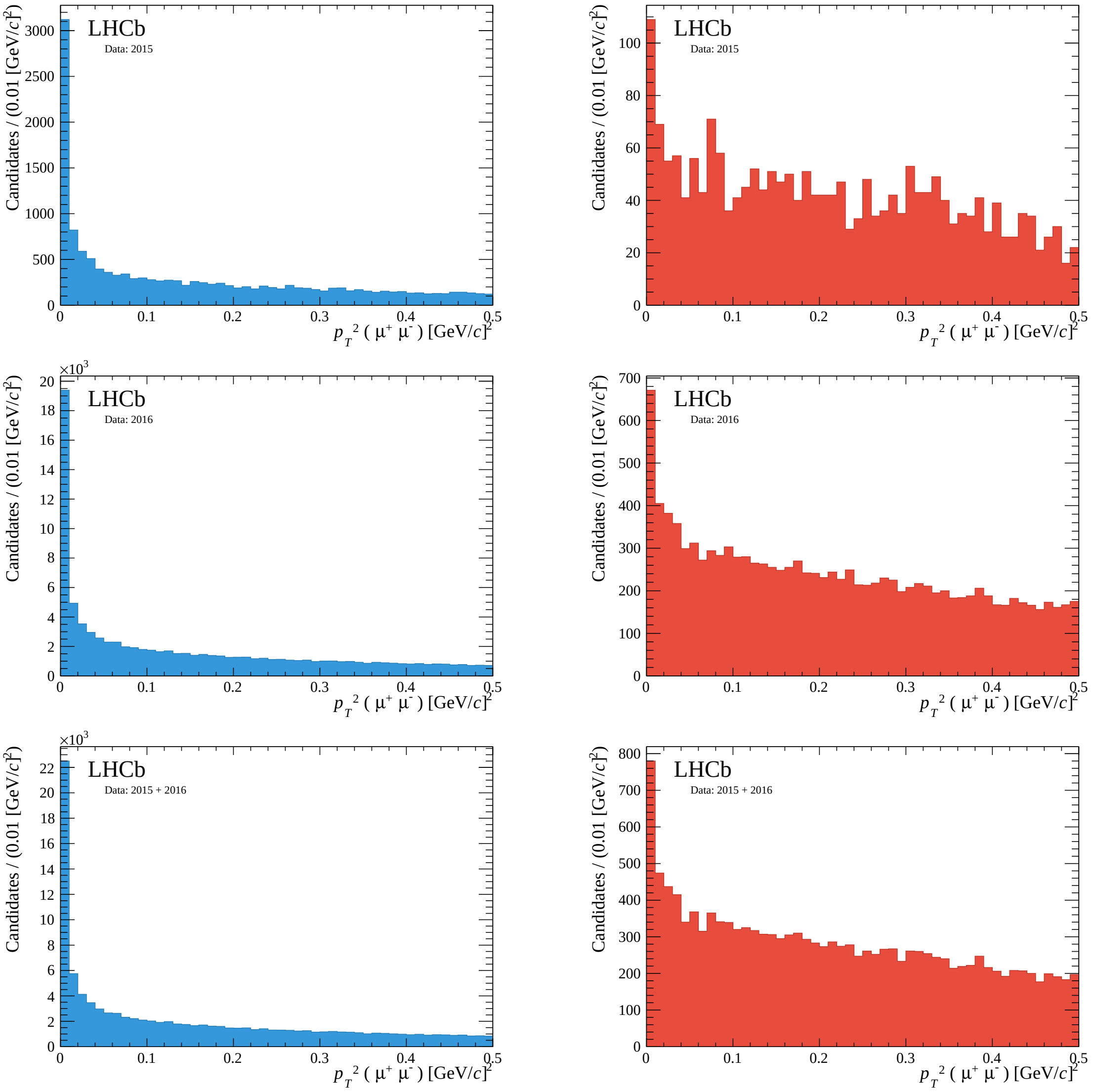

Figure 5.33. Dimuon transverse-momentum-squared distribution for the CEP (left) and non-CEP (right) dimuon selection for the 2015 (top), 2016 (middle), and combined 2015 and 2016 (bottom) data.

Table 5.9. Summary of CEP and non-CEP dimuon samples for the 2015, 2016, and combined 2015 and 2016 data as well as the LPair dimuon Monte Carlo for 2016.

Mechanism	**2015**	**2016**	**2015 + 2016**
CEP	$14,357$	$86,981$	$101,275$
Non-CEP	$2,158,100$	$2,712,653$	$4,870,753$
MC	-	$18,166$	-

5.6.2 Dimuon transverse-momentum fit model

To model the signal we use LPair [139], a Monte Carlo generator devoted to the process of electromagnetic production of lepton pairs, to generate 100,000 CEP-dimuon events for 13 TeV proton-proton collisions. After the reconstruction process, we apply the same selection criteria as in the CEP-dimuon data sample and use generator-level information to check we reconstructed the correct muons. A total of $18,166$ events pass our selection. The invariant-mass distribution of the dimuon system is shown in Fig. 5.34 where the veto-mass windows corresponding to the J/ψ and $\psi(2S)$ resonance regions have been highlighted in red and the transverse-momentum-squared distribution of the dimuon system is shown in Fig. 5.35. The events in the veto have been excluded from this distribution. We can now use the transverse-momentum-squared histogram as a PDF for the CEP signal in the fit of our CEP-dimuon sample.

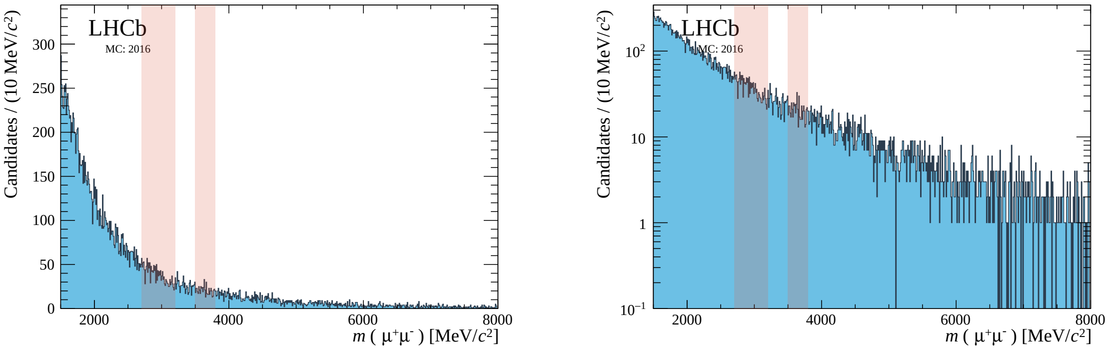

Figure 5.34. Dimuon invariant-mass distribution for the CEP-dimuon Monte Carlo for proton-proton collisions at a centre-of-mass energy $\sqrt{s} = 13$ TeV for 2016 run conditions in linear (left) and logarithmic scales (right). The veto region of resonant J/ψ and $\psi(2S)$ mesons is highlighted in red.

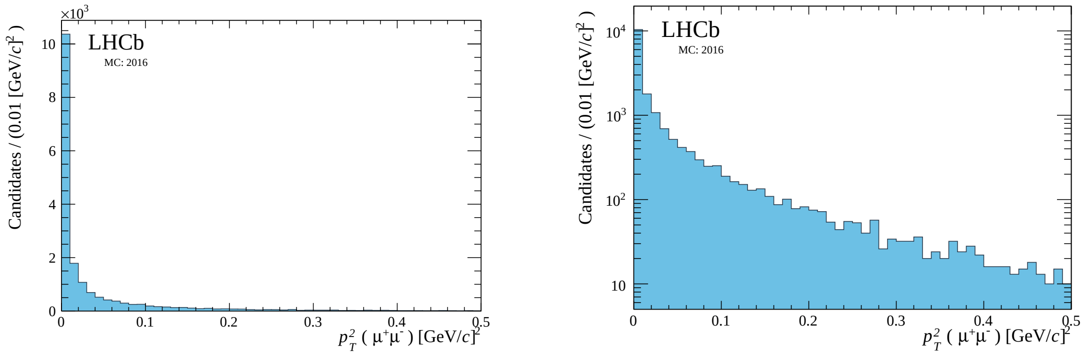

Figure 5.35. Dimuon transverse-momentum-squared distribution for the CEP dimuon Monte Carlo for proton-proton collisions at a centre-of-mass energy $\sqrt{s} = 13$ TeV for 2016 run conditions in linear (left) and logarithmic scales (right).

5.6.3 HeRSChel efficiency calculation

The $\ln(\chi^2_{\mathrm{HRC}})$ distribution is shown in Fig. 5.36 for the CEP (blue) and non-CEP (red) sample. To better showcase the discriminatory power of the HeRSChel detector, we tighten the transverse-momentum-squared cut of the CEP sample, such that $p_{\mathrm{T}}^2(\mu^+\mu^-) < 0.01$ GeV/c, to increase the CEP purity. Similarly, we can increase the inelastic purity of the non-CEP sample by requiring that there are more than five long tracks in the main spectrometer. The $\ln(\chi^2_{\mathrm{HRC}})$ distributions for these enhanced purity samples are shown alongside our nominal selection in Fig. 5.36. The non-CEP samples have a tail which extends to low $\ln(\chi^2_{\mathrm{HRC}})$ values: these are background events where all additional activity associated with proton dissociation or secondary interactions lies outside the HeRSCheL acceptance. Similarly, the CEP enhanced-purity sample has a small fraction of events that have high $\ln(\chi^2_{\mathrm{HRC}})$ values: we attribute this feature to small levels of residual background and also occasions where secondary proton interactions may occur, producing activity outside of the main spectrometer but within that of HeRSCheL. Prior to October 1st 2015, HeRSCheL was under commission. As a result, the HeRSCheL response was less stable during this period, thus explaining the worse separation compared to 2016.

To measure a signal efficiency for a given $\ln(\chi^2_{\mathrm{HRC}})$ cut we perform an unbinned-maximum-likelihood fit on the dimuon-transverse-momentum-squared distribution of our CEP-dimuon sample with the $\ln(\chi^2_{\mathrm{HRC}})$ cut applied. The fit enables us to determine how the true signal content of the CEP sample varies with p_{T}^2. We use a PDF composed of a CEP-signal shape extracted from the LPair Monte Carlo, and a non-CEP-background shape extracted from data, as described above. An example of such a fit is shown in Fig. 5.37 for $\ln(\chi^2_{\mathrm{HRC}}) < 5$. The signal peaks at low p_{T}^2 values, a feature characteristic of CEP events, while the background has a much wider profile and extends to higher p_{T}^2 values.

The effect of the HeRSCheL activity on a CEP-dimuon sample can be quantified by an efficiency given by the ratio of the CEP-signal yield after the $\ln(\chi^2_{\mathrm{HRC}})$ cut is applied to the CEP-signal yield prior to the $\ln(\chi^2_{\mathrm{HRC}})$ cut. Similarly, we are able to calculate the effect HeRSCheL activity has on the non-CEP background surviving the cut. The background rejection rate is given by subtracting the background-efficiency rate from one. The CEP-dimuon-signal efficiency distribution and the non-CEP-background rejection are shown Fig. 5.38. The efficiency distributions are shown for the interval of greatest change in efficiency, $2 < \ln(\chi^2_{\mathrm{HRC}}) < 5$, alongside the full-range versions. The uncertainties are calculated from the fit-yield uncertainties. while the values and uncertainties between intervals are linearly interpolated. The signal-efficiency and background-rejection values are tabulated in Table 5.10.

Our working $\ln(\chi^2_{\mathrm{HRC}})$ upper limit for the χ_c analysis, marked in Fig. 5.38 by a grey-vertical-dashed line, is $\ln(\chi^2_{\mathrm{HRC}}) < 5$. With this cut the signal efficiency is $70.4 \pm 1.8\%$, $85.1 \pm 0.8\%$, and $83.0 \pm 0.8\%$ for 2015, 2016, and combined 2015 and 2016 data respectively, while the background rejection is $71.9 \pm 2.1\%$, $67.6 \pm 0.8\%$, and $68.2 \pm 0.7\%$. It should be stressed, however, that the proportion of background that is suppressed is dependent on the exact nature of the background, and so the values found are not necessarily representative of the background in the χ_c analysis sample. As stated previously, the difference in performance between 2015 and 2016 is due to a period of commissioning during 2015.

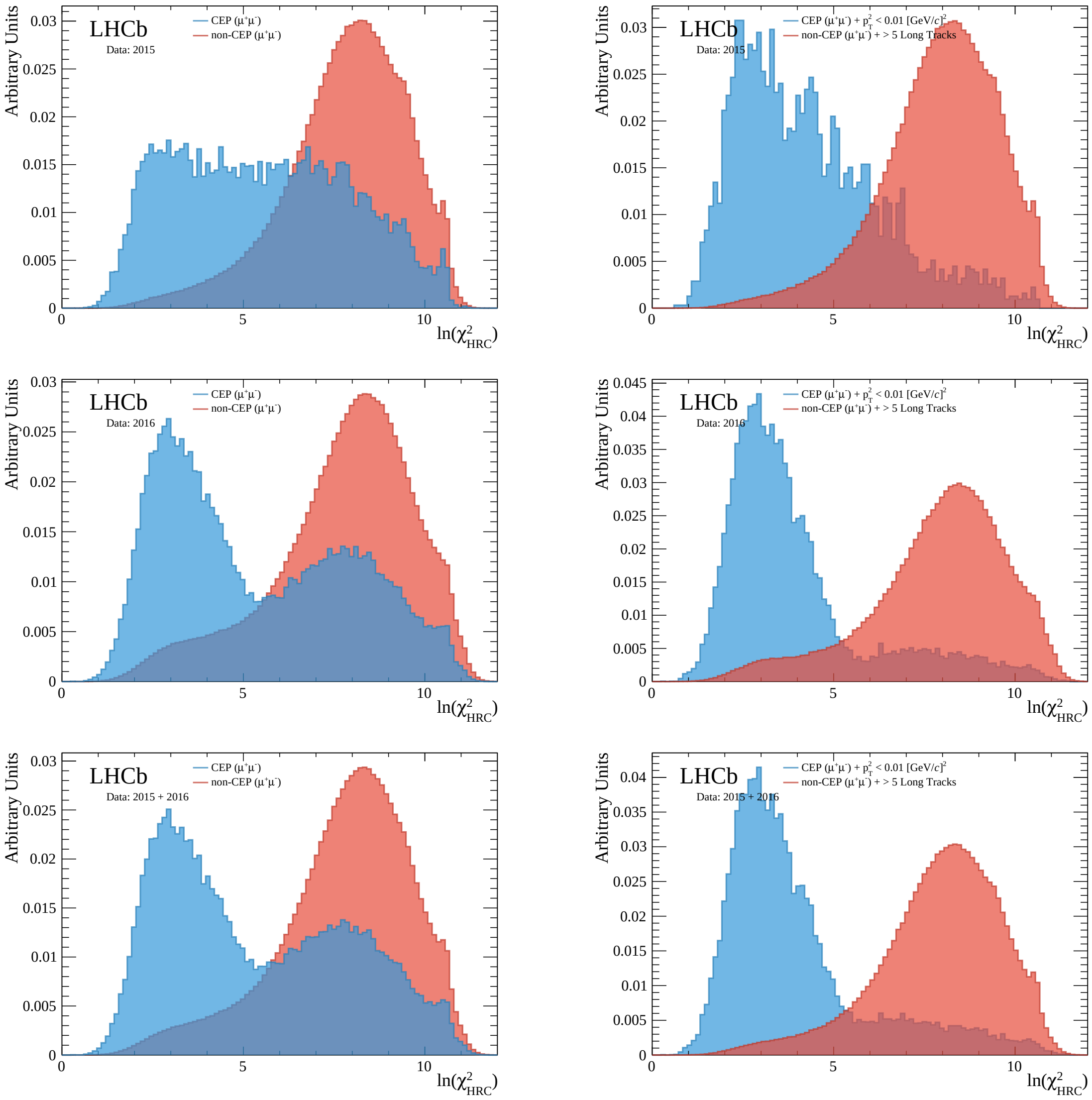

Figure 5.36. Distribution, normalised to unit area, of the discriminating $\ln(\chi^2_{\text{HRC}})$ variable that is related to the activity in HeRSCheL for the 2015 (top), 2016 (middle), and combined 2015 and 2016 (bottom) data. The response is shown for the CEP (blue) and non-CEP (red) sample in the left column and again on the right column with tighter CEP, $p_{\text{T}}^2(\mu^+\mu^-) < 0.01$ GeV/c, and non-CEP, number of long tracks ≥ 6, requirements respectively.

To assess the systematic uncertainty associated with the dimuon transverse-momentum fit used to calculated the HeRSCheL efficiency, we independently vary the background and signal fit model, then recalculate the efficiency at our working point $\ln(\chi^2_{\text{HRC}}) < 5$ for each of the new configurations. As an alternative model of the background we use a shape suggested in a HERA analysis [140] associated with the inelastic proton form factor, which takes the form

$$B(p_T^3) = \frac{p_0}{(1 + (a/n)p_T^2)^n}, \tag{5.10}$$

where n and a are free parameters and the $n = 1.79$ is fixed to the experimental value taken from the HERA paper. The fit results are shown in Fig. 5.39 in linear and logarithmic scale. With this model we obtain an efficiency of $(85.5 \pm 0.8)\%$ and $(83.6 \pm 0.7)\%$ for the 2016-only, and combined 2015 and 2016 data, respectively. This corresponds to a difference of 0.4% and 0.7%, respectively, with respect to the default fit.

Similarly, we replace the signal shape for the sum of two exponentials while keeping the background shape model unchanged such that

$$p_0 e^{p_1 p_t^2} + p_2 e^{p_3 p_t^2}. \tag{5.11}$$

As before, we repeat the fit procedure, the fits for which are shown in Fig. 5.39, and find an efficiency of $(80.2 \pm 1.1)\%$ and $(78.9 \pm 1.0)\%$ for the 2016-only, and combined 2015 and 2016 data. This corresponds to a difference of 5.7% and 4.9%, respectively, with respect to the default fit. We take the largest effect as the systematic uncertainty, and assign a 6% to the 2016-only data and 5% for the combined 2015 and 2016 data.

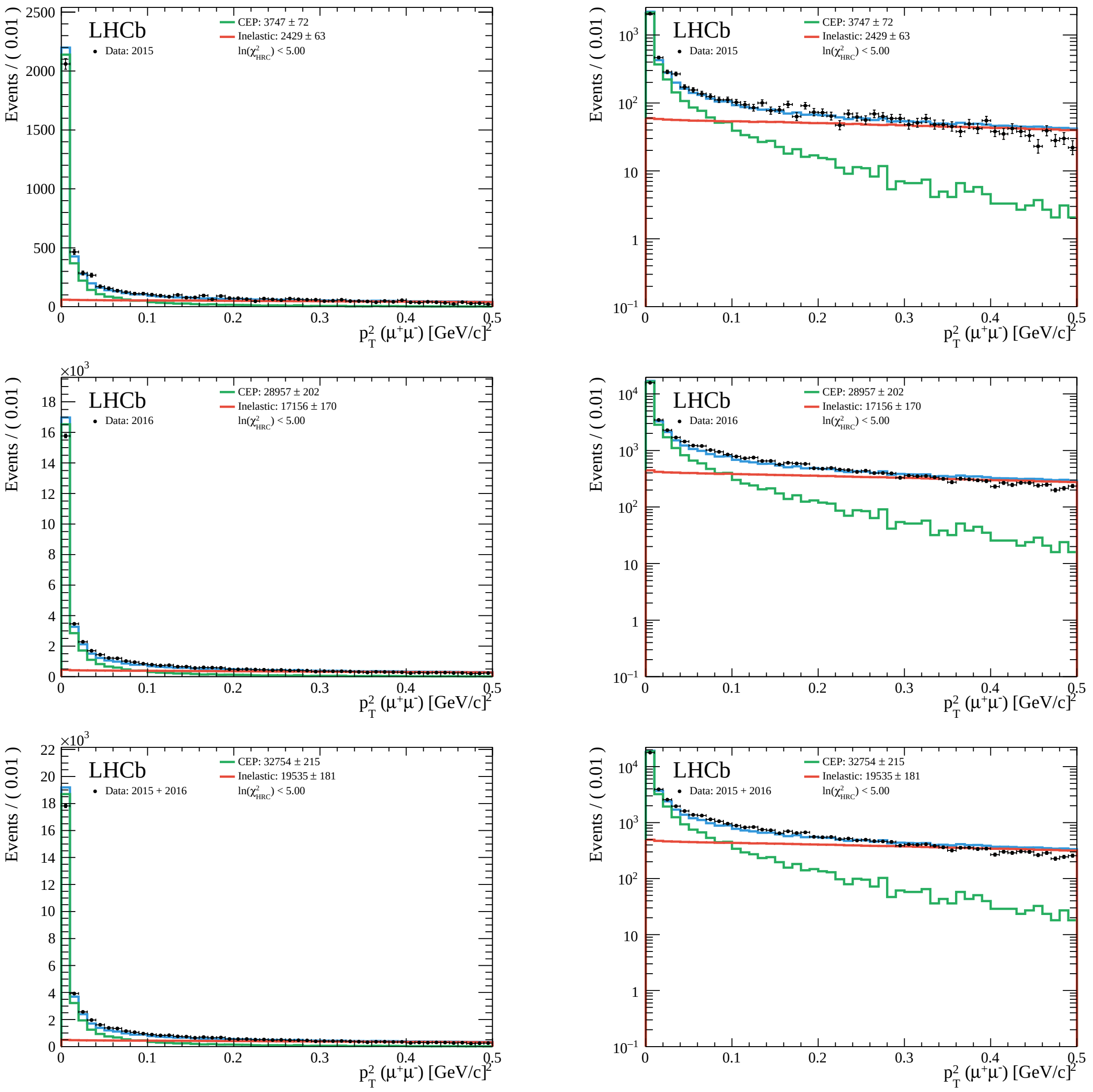

Figure 5.37. An example for the dimuon transverse-momentum-squared fits with a $\ln(\chi^2_{\mathrm{HRC}}) < 5$ cut applied for the 2015 (top), 2016 (middle), and combined 2015 and 2016 (bottom) data in linear (left) and logarithmic (right) scale. The CEP component is fitted with a template extracted from Monte Carlo (green) while the inelastic non-CEP component is fitted with a template extracted from inelastic data (red).

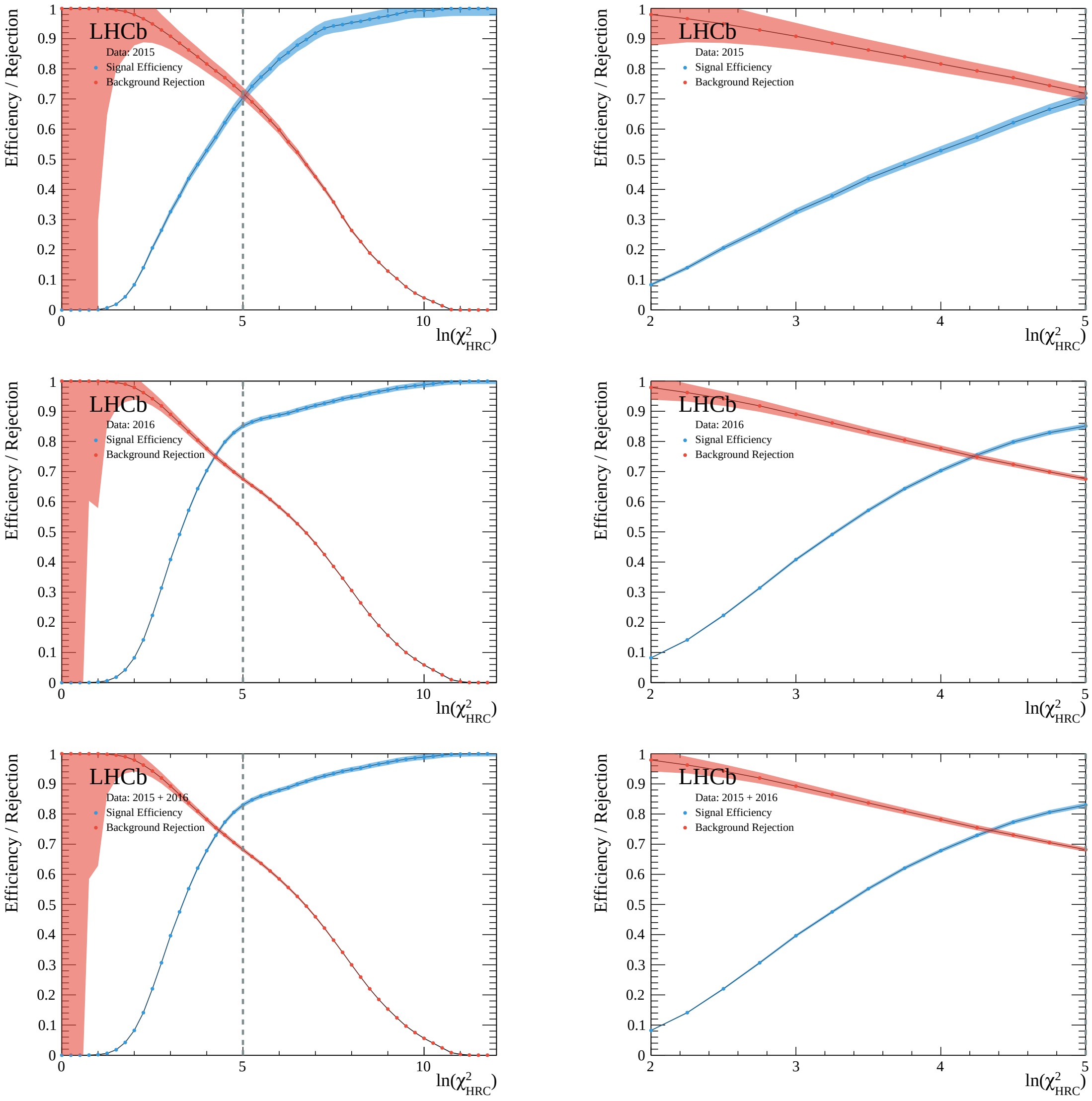

Figure 5.38. CEP-signal efficiency (blue) and background rejection (red) for dimuon production as a function of the limit chosen for $\ln(\chi^2_{\mathrm{HRC}})$ for the 2015 (top), 2016 (middle), and combined 2015 and 2016 (bottom) data. The distribution is reproduced for the range where $\ln(\chi^2_{\mathrm{HRC}})$ has the largest variation (right), $2 < \ln(\chi^2_{\mathrm{HRC}}) < 5$. The upper limit of the cut used in the analysis, $\ln(\chi^2_{\mathrm{HRC}}) < 5$, is marked by the dashed grey line.

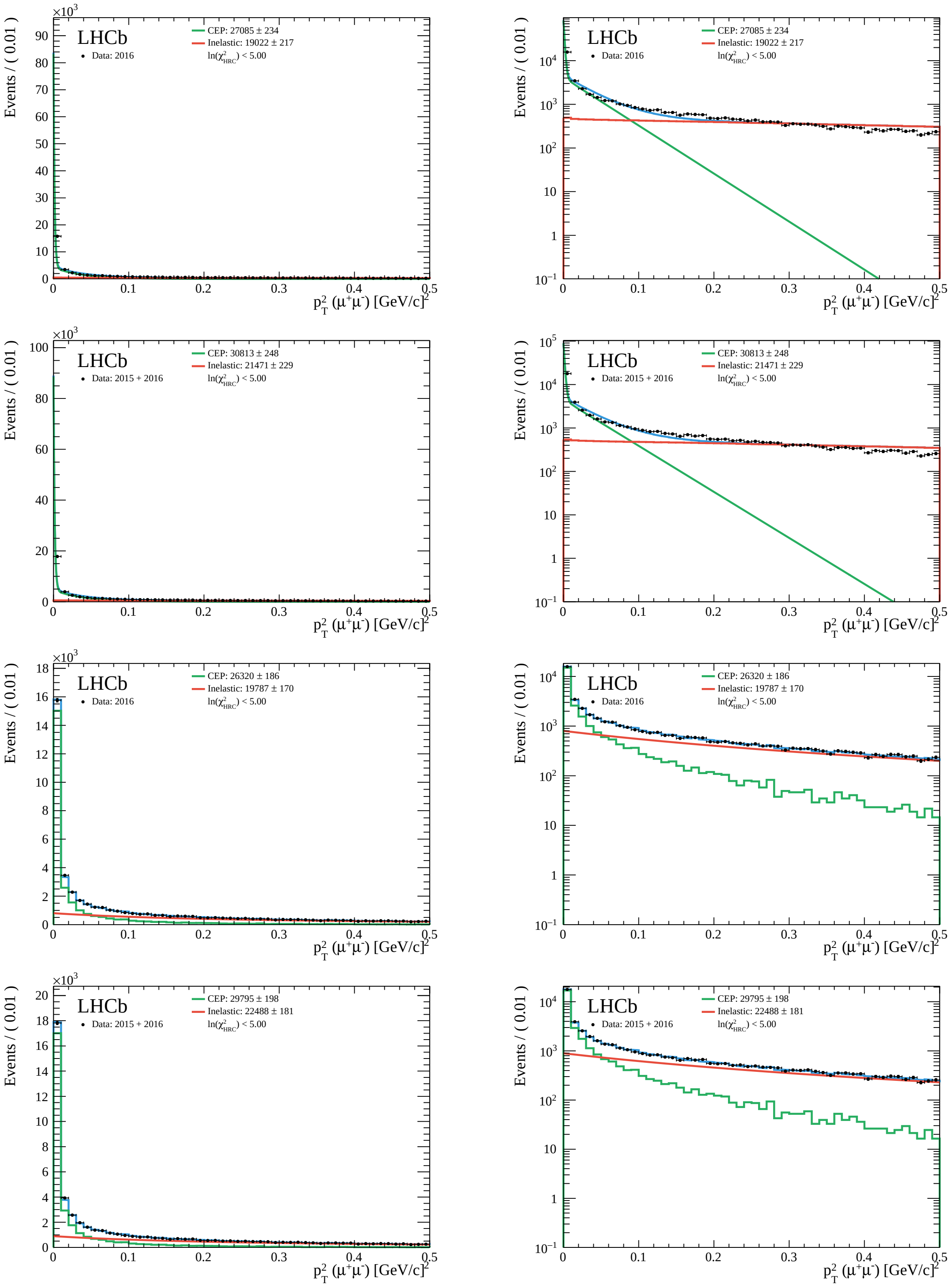

Figure 5.39. Dimuon transverse-momentum-squared fits with a $\ln(\chi^2_{\mathrm{HRC}}) < 5$ cut applied for the 2016-only (first and third row), and combined 2015 and 2016 (second and fourth row) data in linear (left) and logarithmic (right) scale. In the first and second row, the CEP component is fitted with a template extracted from Monte Carlo (green) while the inelastic non-CEP component with Eq. 5.10 (red). In the second and third row, the CEP component is fitted with the sum of two exponentials (green) while the inelastic non-CEP component is fitted with a template extracted from inelastic data (red).

Table 5.10. Summary of $\ln(\chi^2_{\mathrm{HRC}})$ efficiency and background rejection.

$\ln(\chi^2_{\mathrm{HRC}})$	**Efficiency [%]**			**Background Rejection [%]**		
$<$	**2015**	**2016**	**2015 + 2016**	**2015**	**2016**	**2015 + 2016**
0.25	0.0 ± 0.01	0.0 ± 0.002	0.0 ± 0.002	-	-	-
0.50	0.0 ± 0.01	0.004 ± 0.004	0.003 ± 0.003	-	100 ± 134	100 ± 134
0.75	0.019 ± 0.009	0.03 ± 0.01	0.03 ± 0.01	-	100 ± 40	100 ± 42
1.00	0.12 ± 0.05	0.2 ± 0.03	0.2 ± 0.02	100.0 ± 70.3	100 ± 42	100 ± 37
1.25	0.7 ± 0.1	0.6 ± 0.05	0.6 ± 0.05	99.8 ± 35.1	99.8 ± 14.4	99.8 ± 13.4
1.50	1.9 ± 0.2	1.8 ± 0.09	1.8 ± 0.08	99.5 ± 19.6	99.5 ± 8.8	99.5 ± 8.0
1.75	4.4 ± 0.3	4.2 ± 0.1	4.2 ± 0.1	99.1 ± 15.0	99.0 ± 5.9	99.0 ± 5.5
2.00	8.4 ± 0.5	8.2 ± 0.2	8.2 ± 0.2	98.0 ± 10.2	97.9 ± 4.1	97.9 ± 3.8
2.25	14.0 ± 0.6	14.2 ± 0.3	14.1 ± 0.2	96.6 ± 7.8	96.2 ± 3.0	96.3 ± 2.8
2.50	20.6 ± 0.8	22.3 ± 0.3	22.0 ± 0.3	94.9 ± 6.3	94.2 ± 2.4	94.3 ± 2.2
2.75	26.5 ± 0.9	31.4 ± 0.4	30.7 ± 0.4	92.9 ± 5.2	91.8 ± 2.0	91.9 ± 1.8
3.00	32.6 ± 1.1	40.8 ± 0.5	39.6 ± 0.4	90.8 ± 4.4	89.0 ± 1.7	89.3 ± 1.6
3.25	37.8 ± 1.2	49.1 ± 0.6	47.5 ± 0.5	88.5 ± 3.9	86.1 ± 1.4	86.5 ± 1.3
3.50	43.6 ± 1.3	57.1 ± 0.6	55.2 ± 0.6	86.2 ± 3.5	83.2 ± 1.3	83.7 ± 1.2
3.75	48.3 ± 1.4	64.3 ± 0.7	62.1 ± 0.6	84.0 ± 3.1	80.4 ± 1.1	81.0 ± 1.1
4.00	52.9 ± 1.5	70.3 ± 0.7	67.8 ± 0.7	81.6 ± 2.8	77.6 ± 1.0	78.2 ± 1.0
4.25	57.3 ± 1.6	75.5 ± 0.8	72.9 ± 0.7	79.3 ± 2.6	74.8 ± 0.9	75.5 ± 0.9
4.50	62.1 ± 1.7	79.8 ± 0.8	77.3 ± 0.7	77.1 ± 2.4	72.4 ± 0.9	73.0 ± 0.8
4.75	66.6 ± 1.8	82.9 ± 0.8	80.6 ± 0.7	74.5 ± 2.2	69.9 ± 0.8	70.5 ± 0.8
5.00	70.4 ± 1.8	85.1 ± 0.8	83.0 ± 0.8	71.9 ± 2.1	67.6 ± 0.8	68.2 ± 0.7
5.25	74.2 ± 1.9	86.5 ± 0.8	84.7 ± 0.8	69.0 ± 1.9	65.4 ± 0.7	65.9 ± 0.7
5.50	77.3 ± 2.0	87.5 ± 0.9	86.0 ± 0.8	66.0 ± 1.7	63.2 ± 0.7	63.6 ± 0.6
5.75	80.0 ± 2.0	88.1 ± 0.9	86.9 ± 0.8	62.9 ± 1.6	60.8 ± 0.6	61.1 ± 0.6
6.00	83.2 ± 2.	88.7 ± 0.9	87.9 ± 0.8	59.7 ± 1.5	58.2 ± 0.6	58.5 ± 0.5
6.25	85.4 ± 2.1	89.4 ± 0.9	88.7 ± 0.8	55.8 ± 1.3	55.6 ± 0.5	55.6 ± 0.5
6.50	87.9 ± 2.1	90.3 ± 0.9	89.9 ± 0.8	52.4 ± 1.2	52.7 ± 0.5	52.7 ± 0.5
6.75	89.7 ± 2.2	91.1 ± 0.9	90.9 ± 0.8	48.2 ± 1.1	49.6 ± 0.5	49.4 ± 0.4
7.00	91.8 ± 2.3	91.9 ± 0.9	91.8 ± 0.8	44.2 ± 1.0	46.2 ± 0.4	45.9 ± 0.4
7.25	93.5 ± 2.3	92.6 ± 0.9	92.7 ± 0.8	40.1 ± 0.8	42.5 ± 0.4	42.2 ± 0.3
7.50	94.2 ± 2.3	93.3 ± 0.9	93.4 ± 0.8	35.8 ± 0.7	38.5 ± 0.3	38.2 ± 0.3
7.75	94.7 ± 2.3	94.2 ± 0.9	94.2 ± 0.8	30.9 ± 0.6	34.6 ± 0.3	34.1 ± 0.3
8.00	95.3 ± 2.3	94.7 ± 0.9	94.8 ± 0.9	26.4 ± 0.5	30.6 ± 0.2	30.0 ± 0.2
8.25	95.8 ± 2.3	95.2 ± 0.9	95.3 ± 0.9	22.7 ± 0.4	26.4 ± 0.2	25.9 ± 0.2
8.50	96.4 ± 2.4	96.0 ± 0.9	96.0 ± 0.9	18.9 ± 0.4	22.5 ± 0.2	22.0 ± 0.2
8.75	97.0 ± 2.4	96.5 ± 0.9	96.6 ± 0.9	15.8 ± 0.3	18.9 ± 0.1	18.5 ± 0.1
9.00	97.6 ± 2.4	97.1 ± 0.9	97.1 ± 0.9	12.9 ± 0.2	15.7 ± 0.1	15.3 ± 0.1
9.25	98.2 ± 2.4	97.7 ± 0.9	97.7 ± 0.9	10.4 ± 0.2	12.7 ± 0.1	12.41 ± 0.09
9.50	98.9 ± 2.4	98.1 ± 1.0	98.2 ± 0.9	7.7 ± 0.1	10.0 ± 0.07	9.67 ± 0.07
9.75	99.2 ± 2.4	98.5 ± 1.0	98.6 ± 0.9	5.6 ± 0.1	7.8 ± 0.06	7.51 ± 0.05
10.00	99.3 ± 2.4	98.8 ± 1.0	98.9 ± 0.9	4.01 ± 0.07	5.9 ± 0.04	5.60 ± 0.04
10.25	99.4 ± 2.4	99.1 ± 1.0	99.2 ± 0.9	2.75 ± 0.05	4.2 ± 0.03	4.02 ± 0.03
10.50	99.8 ± 2.4	99.5 ± 1.0	99.6 ± 0.9	1.41 ± 0.03	2.5 ± 0.02	2.42 ± 0.02
10.75	99.9 ± 2.4	99.8 ± 1.0	99.8 ± 0.9	$(139 \pm 2)10^{-3}$	$(978 \pm 7)10^{-3}$	$(860 \pm 6)10^{-3}$
11.00	100.0 ± 2.4	99.9 ± 1.0	99.9 ± 0.9	$(312 \pm 6)10^{-4}$	$(333 \pm 2)10^{-3}$	$(290 \pm 2)10^{-3}$
11.25	100.0 ± 2.4	100.0 ± 1.0	100.0 ± 0.9	-	$(544 \pm 4)10^{-4}$	$(468 \pm 3)10^{-4}$
11.50	100.0 ± 2.4	100.0 ± 1.0	100.0 ± 0.9	-	$(909 \pm 7)10^{-5}$	$(781 \pm 5)10^{-5}$
11.75	100.0 ± 2.4	100.0 ± 1.0	100.0 ± 0.9	-	-	-
12.00	100.0 ± 2.4	100.0 ± 1.0	100.0 ± 0.9	-	-	-

Chapter 6

Background and fit model

In this chapter, we construct the simultaneous-fit model of the Δm_{χ_c} and p_{T}^2 distributions of selected CEP χ_c candidates, with and without the HeRSCheL cut applied. The final result for our χ_c cross-section measurement is obtained with the HeRSCheL cut applied, which suppresses the inelastic background. However, in order to understand the effect of the HeRSCheL detector and as a systematic check we present the results of both samples along side one another. We start by introducing a series of background studies through which we quantify and model each background contribution for later use in the fit of CEP χ_c candidates. In Sec. 6.1 we present studies of *combinatorial* background, where erroneously combined particles are matched to emulate our decay signal. In Sec. 6.2 we describe feed-down background where the decay chains of heavier particles, in particular those of $\psi(2S)$ mesons, may contain the final-state particles from our signal-decay mode. The Δm_{χ_c} of many of these decays fall around the range of our signal events, making it an important source of background to model and quantify. The last source of background, discussed in Sec. 6.3, comes from the production of χ_c mesons by *inelastic* processes where we fail to detect rapidity-gap-breaking signatures such as proton dissociation or gluon radiation. Finally, we discuss the fit parameterisation of our CEP χ_c signal and provide a summary of all the fit components in Sec. 6.5.

6.1 Combinatorial background

There are two sources of combinatorial background. Firstly, non-resonant dimuon production from photon-photon fusion can be wrongly matched with a random converted-photon candidate. We will refer to this background as *dimuon* or *continuum combinatorial*. Secondly, a genuine J/ψ meson can be wrongly matched with a random converted photon and mimic our signal. We will refer to this background as *J/ψ combinatorial*.

6.1.1 Continuum-combinatorial background

We estimate the continuum-combinatorial background by fitting the invariant mass of the $\mu^+\mu^-$ system of the events that pass our CEP χ_c selection criteria. This distribution contains contributions from genuine J/ψ mesons and a dimuon continuum that falls with increasing invariant mass. A fraction of this dimuon continuum falls within our 100 MeV/c^2 wide J/ψ mass window centred around the nominal invariant-mass value of the J/ψ, which is set at

$m_{J/\psi} = 3096.900 \pm 0.006$ MeV/c^2 according to the PDG [86]. We estimate this contribution by fitting the invariant mass distribution.

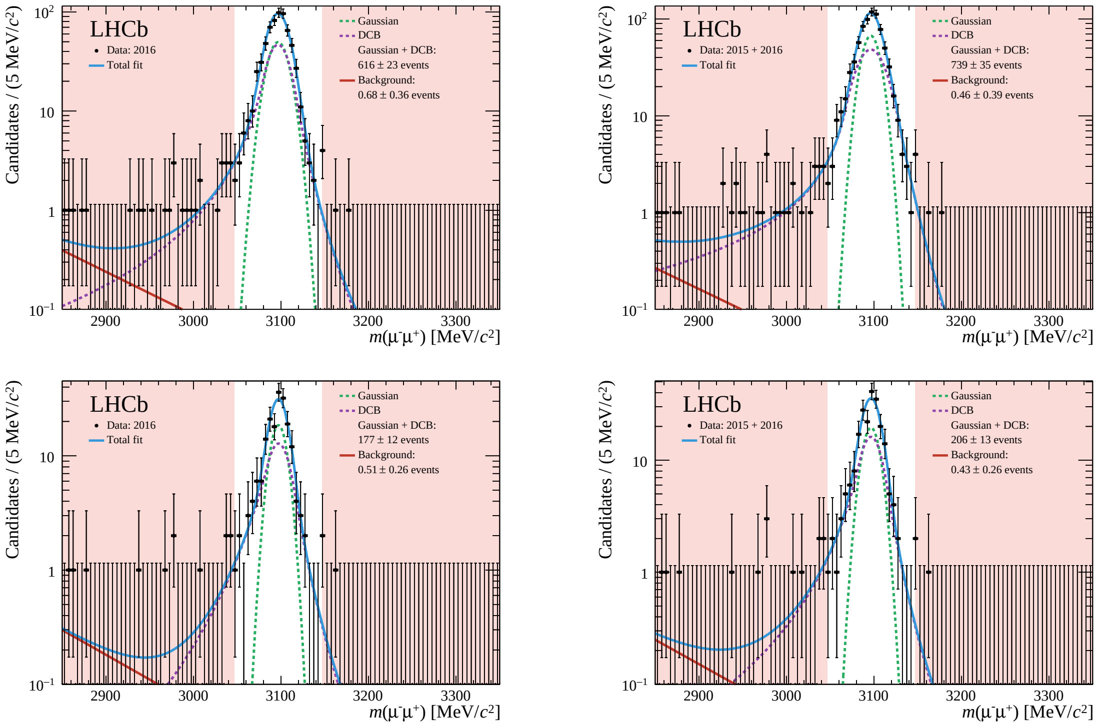

Figure 6.1. Invariant mass of J/ψ mesons from $\chi_c \to J/\psi\,[\mu^+\mu^-]\gamma[e^+e^-]$ for proton-proton collisions at a centre-of-mass energy $\sqrt{s} = 13\,\text{TeV}$ data in logarithmic scale before (top) and after (bottom) the HeRSChel cut is applied, $\ln(\chi^2_{\text{HRC}}) < 5$, for the 2016-only (left), and combined 2015 and 2016 (right) data sets. Events within a 100 MeV mass window around the J/ψ nominal mass are selected. The complementary rejection windows are highlighted in red. A double-sided Crystal Ball (dashed purple) together with a Gaussian (dashed green) is used for the J/ψ candidates and the continuum-combinatorial background is fitted with an exponential (dashed red).

The continuum contribution is modelled with a single exponential,

$$A \cdot e^{\lambda \cdot p_T^2}. \tag{6.1}$$

where A is a normalisation parameter and λ is the slope of the exponential. To fit the J/ψ resonance we use a combination of a double-sided Crystal Ball [137] and a Gaussian with a shared mean parameter, which is the same model used for the comparison of the 2015 and 2016 J/ψ yields presented in Sec. 5.3. As before, the yield ratio of the double-sided Crystal Ball and a Gaussian is fixed to values extracted from CEP χ_c Monte Carlo. Applying this constraint, we perform an unbinned-maximum-likelihood fit of the data samples, the results of which are shown in Fig. 6.1 with and without the HeRSChel cut applied for the 2016-only, and combined 2015 and 2016 data samples. The final values of the fit parameters are detailed in Table 6.1.

Table 6.1. Parameter values of the J/ψ mass fit from CEP χ_c Monte Carlo and data for 2016-only, and combined 2015 and 2016 data sets. Fixed parameters are marked by *.

Variable	**Units**	**Without HeRSCheL**		**With HeRSCheL**	
		2016	**2015 + 2016**	**2016**	**2015 + 2016**
μ	MeV/c^2	3096.7 ± 0.6	3096.4 ± 0.5	3097.2 ± 0.9	3096.6 ± 0.9
α_{Left}	-	1.26 ± 0.09	1.70 ± 0.20	0.90 ± 0.97	1.03 ± 0.13
α_{Right}	-	-1.58 ± 0.16	-1.85 ± 0.23	-1.41 ± 0.26	-1.45 ± 0.25
n_{Left}	-	4.32 ± 2.00	1.36 ± 0.20	4.32 ± 2.00	2.72 ± 0.76
n_{Right}	-	5.83 ± 2.60	11.50 ± 12.33	6.34 ± 4.70	6.26 ± 4.31
σ_{DCB}	MeV/c^2	13.38 ± 0.88	12.84 ± 1.45	13.24 ± 1.65	12.84 ± 1.45
σ_{Gauss}	MeV/c^2	12.07 ± 0.84	9.91 ± 1.33	9.31 ± 1.33	9.91 ± 1.33
$Y_{\text{Gauss}}/Y_{\text{DCB}}$	-	$^*0.818 \pm 0.501$	$^*0.748 \pm 0.408$	$^*0.818 \pm 0.501$	$^*0.748 \pm 0.408$
λ	$[\text{MeV}/c^2]^{-1}$	-0.009 ± 0.007	-0.010 ± 0.008	-0.009 ± 0.008	-0.009 ± 0.008

By integrating the background component of our data fit within our J/ψ selection window, $m_{J/\psi} \pm 50$ MeV/c^2, we estimate 0.46 ± 0.39 (0.43 ± 0.26) continuum-combinatorial-background events in the combined 2015 and 2016 data, and 0.68 ± 0.36 (0.51 ± 0.26) in the 2016-only data without (with) the HeRSCheL cut applied. This demonstrates we have a very clean J/ψ signal with a minimal amount of continuum-combinatorial background. This background is assumed to have a flat Δm_{χ_c} profile.

6.1.2 J/ψ-combinatorial background

J/ψ-combinatorial background comes from the association of genuine J/ψ mesons and a converted photon from another process, or from noise in the calorimeter wrongly interpreted as a photon. To precisely determine the amount of J/ψ-combinatorial background we study a Δm_{χ_c} region where we know the signal is dominated by J/ψ-combinatorial background. From the CEP χ_c Monte Carlo we know not to expect any χ_c signal in the Δm_{χ_c} region above 500 MeV/c^2. From the feed-down study that will be presented in Sec. 6.2, we also know to expect minimal feed-down background in this right-hand side-band. Therefore, any events above this threshold are dominated by J/ψ-combinatorial background with slight contamination from continuum-combinatorial background. We are able estimate the amount of J/ψ-combinatorial background in our sample by fitting events in this right-tail region and extrapolating into our selection window.

To perform the extrapolation we first need to know the shape of the J/ψ-combinatorial background along the entire Δm_{χ_c} range. We model it through a data-driven approach where we mismatch a J/ψ meson from one event with a converted photon from a different event in the CEP χ_c data set. The resulting Δm_{χ_c} distribution falls gently to either side of our signal window as shown in Fig. 6.2, with and without the HeRSCheL cut applied. We will refer to this as the *artificial*-combinatorial background. To fit the distribution, we use a double-sided Crystal Ball to accommodate the tail asymmetry in an unbinned-maximum-likelihood fit where

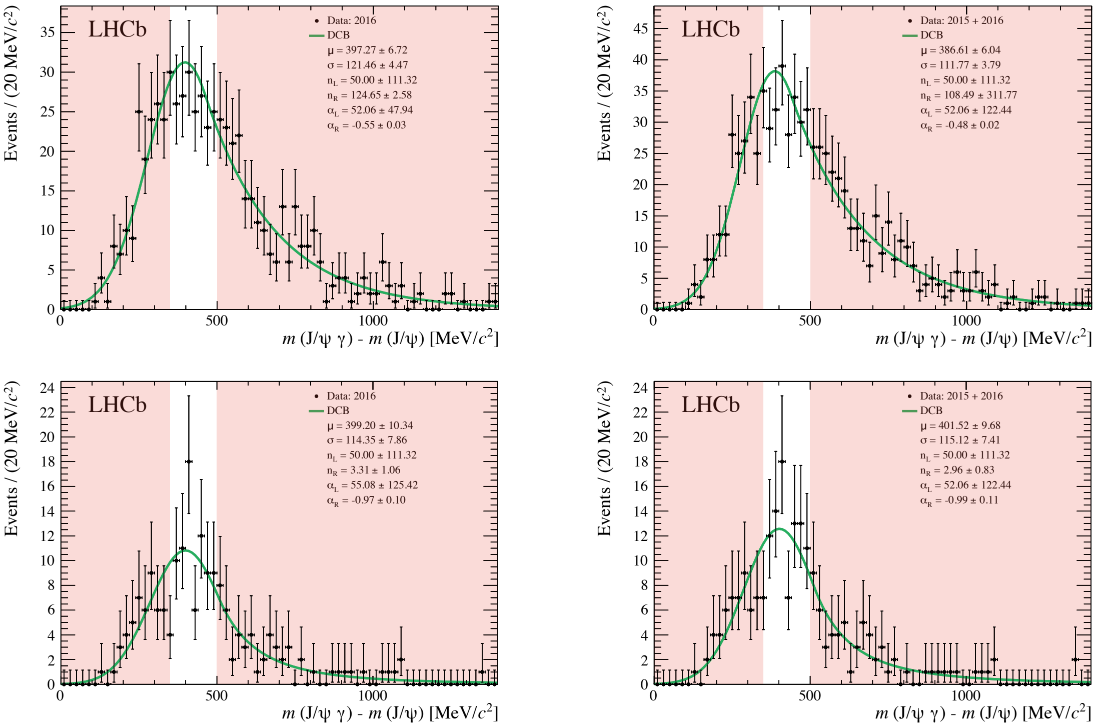

Figure 6.2. Fit of the Δm_{χ_c} distribution of the artificial-combinatorial model before (top) and after (bottom) the HeRSChel cut is applied from the 2016-only (left), and combined 2015 and 2016 (right) data. The distribution is fitted with a double-sided Crystal Ball in green. The vetoed ranges in our CEP χ_c selection are highlighted in red.

all parameters are left floating. The fit is overlaid on Fig. 6.2, and the final-parameter values are summarised in Table 6.2.

In addition to the J/ψ-combinatorial shape described above, we add a uniform distribution for the sub-dominant continuum-combinatorial background such that its integral around our selection window matches the results presented above. In determining the absolute background level from the CEP χ_c sample, the size of the J/ψ-combinatorial background is determined exclusively by the candidates to the right of the signal window. The fit shape of the J/ψ combinatorial is then extrapolated into lower-Δm_{χ_c} values. The maximum-likelihood-fit results of the combinatorial component are shown in Fig. 6.3, with and without the HeRSChel cut applied. The data in the resonant region are not shown as this is signal dominated and not described by the fit model. The fit does not describe the low-Δm_{χ_c}-veto region well since it has an additional contribution from χ_{c0}, which the fit does not account for. By integrating within the selection window we find that we expect 44.97 ± 6.35 (13.25 ± 4.66) J/ψ-combinatorial events in the combined 2015 and 2016 data, and 35.55 ± 5.85 (11.91 ± 4.51) in the 2016-only data without (with) the HeRSChel cut applied. Hence we conclude that HeRSChel suppresses this source of background by around 70%.

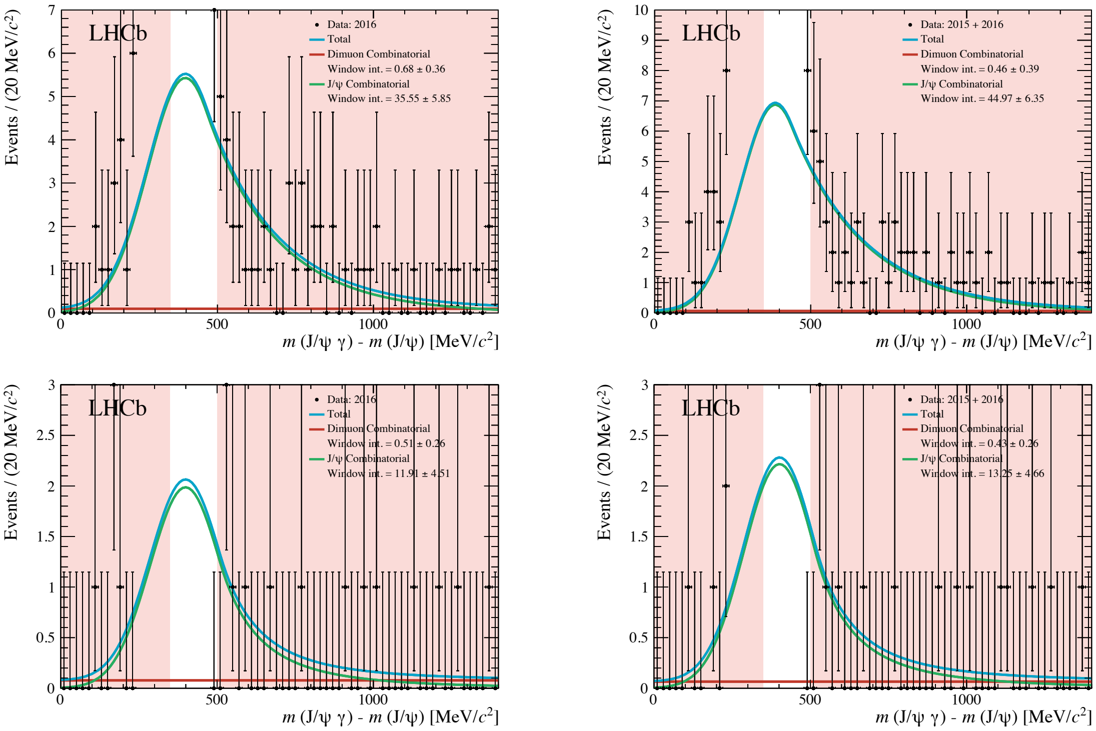

Figure 6.3. Fit of the Δm_{χ_c} distribution from the CEP χ_c selection before (top) and after (bottom) the HeRSChel cut is applied, $\ln(\chi^2_{\text{HRC}}) < 5$, for the 2016-only (left), and combined 2015 and 2016 (right). The y-axis range has been been truncated as to not show the resonant peaks associated with our signal. The Δm_{χ_c} ranges vetoed in the main analysis are highlighted in red. The entries in the resonant region are not shown as they are signal dominated.

Table 6.2. Parameters of Δm_{χ_c} and p_{T}^2 fits of J/ψ-combinatorial background for the 2016-only, and combined 2015 and 2016 data with and without a HeRSChel cut, $\ln(\chi^2_{\text{HRC}}) < 5$, applied.

		Without HeRSChel		**With HeRSChel**	
Variable	**Units**	**2016**	**2015 + 2016**	**2016**	**2015 + 2016**
		Δm_{χ_c} combinatorial			
μ	MeV/c^2	397.27 ± 6.72	386.61 ± 6.04	399.20 ± 10.34	401.52 ± 9.68
σ	MeV/c^2	121.46 ± 4.47	111.77 ± 3.79	114.35 ± 7.87	115.123 ± 7.41
n_{Left}	-	50.00 ± 111.32	50.00 ± 111.32	50.00 ± 111.32	50.00 ± 111.32
n_{Right}	-	124.65 ± 2.58	108.49 ± 311.77	3.31 ± 1.06	2.96 ± 0.83
α_{Left}	-	52.06 ± 47.94	52.06 ± 122.44	55.08 ± 125.42	52.06 ± 122.44
α_{Right}	-	-0.55 ± 0.03	-0.48 ± 0.02	-0.97 ± 0.10	-0.99 ± 0.11
		$p_{\text{T}}^2(J/\psi\,\gamma)$ combinatorial			
a	$[\text{MeV}/c]^{-2}$	-0.58 ± 0.04	-0.56 ± 0.04	-2.78 ± 0.68	-2.60 ± 1.01
b	$[\text{MeV}/c]^{-2}$	-	-	-0.64 ± 0.18	-0.77 ± 0.19
A	$[\text{MeV}/c]^{-2}$	0.44 ± 0.60	0.43 ± 0.42	0.92 ± 0.83	0.82 ± 0.59
B	$[\text{MeV}/c]^{-2}$	-	-	0.14 ± 0.76	0.33 ± 0.62

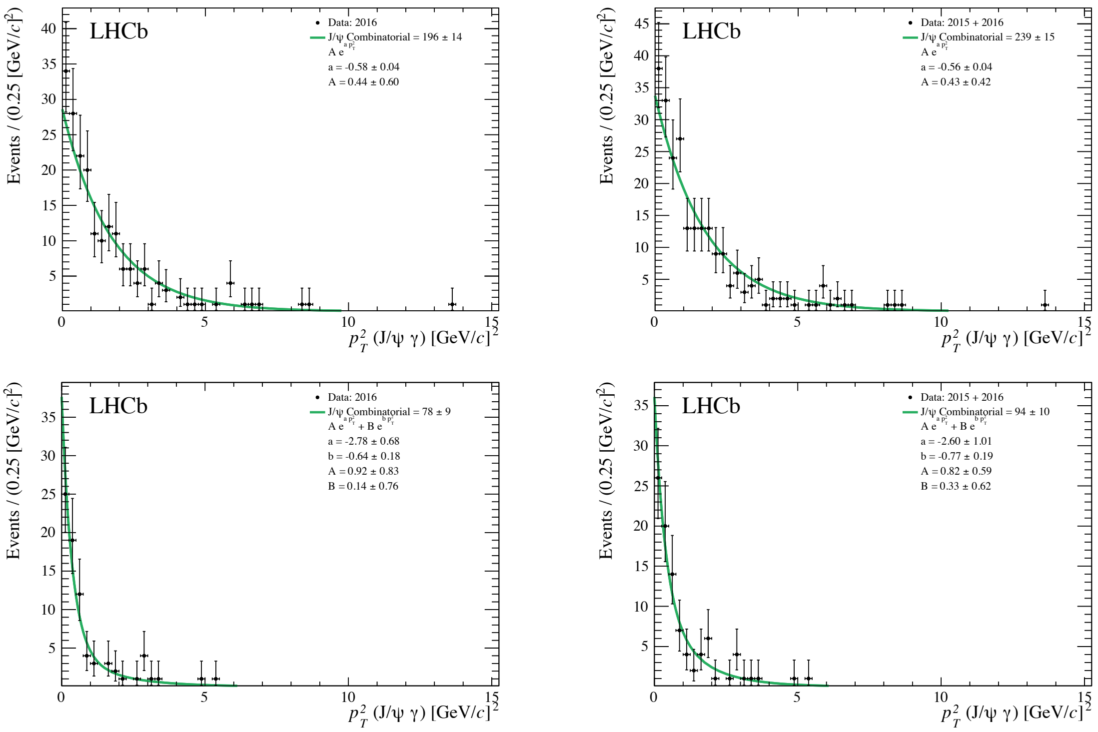

Figure 6.4. Fit of p_{T}^2 distribution of *J/ψ*-combinatorial background modelled by mismatched *J/ψ* mesons and converted photons from different events before (top) and after (bottom) the HeRSChel cut is applied, $\ln(\chi^2_{\mathrm{HRC}}) < 5$, for the 2016-only (left), and combined 2015 and 2016 (right) data with our CEP χ_c selection applied. We use one exponential to fit the p_{T}^2 distribution with all parameters left floating to fit the sample without the HeRSChel cut applied, and the sum of two exponentials to fit the sample after the HeRSChel cut is applied (green).

We can also determine the p_{T}^2 distribution of the $J/\psi\gamma$ background system with this method. Prior to the application of the HeRSChel cut, the shape is well described by a single exponential, $A \cdot \exp(a \cdot p_T^2)$, where A is a normalisation parameter and a is the slope of the exponential. However, once the HeRSChel cut is applied a single exponential is not sufficient to successfully describe the p_{T}^2 distribution. Therefore, we use the sum of two exponentials to fit the p_{T}^2 distribution such that, $A \cdot \exp(a \cdot p_T^2) + B \cdot \exp(b \cdot p_T^2)$, where A and B are normalisation parameters and a and b are the slopes of the exponentials. All parameters are floated during the unbinned-maximum-likelihood fit of both samples. The fit results are shown in Fig. 6.4 and the fit parameter values are detailed in Table 6.2. We use these results to fix the fit parameters and the yield of the Δm_{χ_c}, as well as p_{T}^2, in the CEP χ_c fit.

6.2 $\psi(2S)$ feed-down background modelling

In this section we discuss possible contributions from $\psi(2S)$ feed-down through decays that include an intermediate *J/ψ* meson and a photon. These events are accompanied by one or more particles other than the $J/\psi\gamma$ system and can therefore be rejected by the exclusivity requirement of CEP. However, we expect feed-down contributions from $\psi(2S)$ decays that mimic our signal when one or more of the decay particles are not reconstructed by the main spectrometer, or if we fail to veto them.

6.2.1 $\psi(2S)$ feed-down reconstruction

To calculate the contribution of $\psi(2S)$ feed-down background on our CEP χ_c selection, we use the $\psi(2S) \rightarrow J/\psi X$ Monte Carlo described in Sec. 4.1.4. Here, X represents all possible decay products in a $\psi(2S)$ decay containing a J/ψ meson. The same criteria used for the CEP χ_c selection are applied to the $\psi(2S)$ Monte Carlo. Some of these decays have two or more photons in the final state. This reduces the available phase space and, on average, results in low transverse-momentum photons. As expected from the photon-conversion efficiency results, the reconstruction rate of these events is low. As a result of this and the limited Monte Carlo sample size (100, 000 generated events) fully reconstructing the $J/\psi[\mu^+\mu^-]\gamma[e^+e^-]$ system results in a sample with limited statistical precision. In addition, the Monte Carlo description of the photon-conversion probability and reconstruction may not match the data efficiency well.

To take advantage of the more precise and reliable photon-conversion efficiency measured from data, detailed in Sec. 5.1, we reconstruct only the J/ψ meson while keeping the generator-level information of the photons associated with the decay irrespective of whether the photons convert in Monte Carlo. we later apply our knowledge of the photon-conversion and reconstruction efficiency from data. These decay modes involve more than one photon and the reconstructed-mass distributions vary according to which photon is paired with the J/ψ mesons. The vast majority of the decays involve two photons, however, the $\psi(2S) \rightarrow J/\psi[\mu^+\mu^-]\pi^0[\gamma\gamma]\pi^0[\gamma\gamma]$ decay has four photons, two from each π^0 meson. We save up to four photons involved in the main decay chain, γ_1, γ_2, γ_3, and γ_4, then reconstruct the $J/\psi\gamma$ system for all possible pairs. All bremsstrahlung photons are omitted from this selection process.

The reconstruction resolution of the photons will have an effect on the number of events that fall within our CEP χ_c Δm_{χ_c} selection window, and ultimately the Δm_{χ_c} shape we extract for later use in our CEP χ_c signal fit. These photons are particularly sensitive to resolution effects due to bremsstrahlung radiation and our ability to correct for it. Therefore, to account for detector-resolution effects for the converted photons we use the combined 2015 and 2016 χ_{c2} Monte Carlo introduced in section Sec. 6.5.1. The CEP χ_c analysis selection is applied and we use generator-level information to check that the reconstructed particles belong to our decay. The resolution for each of the four-momentum components is given by subtracting the true value from the reconstructed value. These resolution distributions are shown in Fig. 6.5 for 2015 run conditions. For any given event, the amount of smearing necessary to account for the detector-resolution effects is given by the product of a randomly selected resolution value from the corresponding normalised-momentum resolution distribution, and the absolute value of the true-momentum component of the accompanying photon, which is saved alongside the reconstructed J/ψ in the $\psi(2S) \rightarrow J/\psi X$ Monte Carlo.

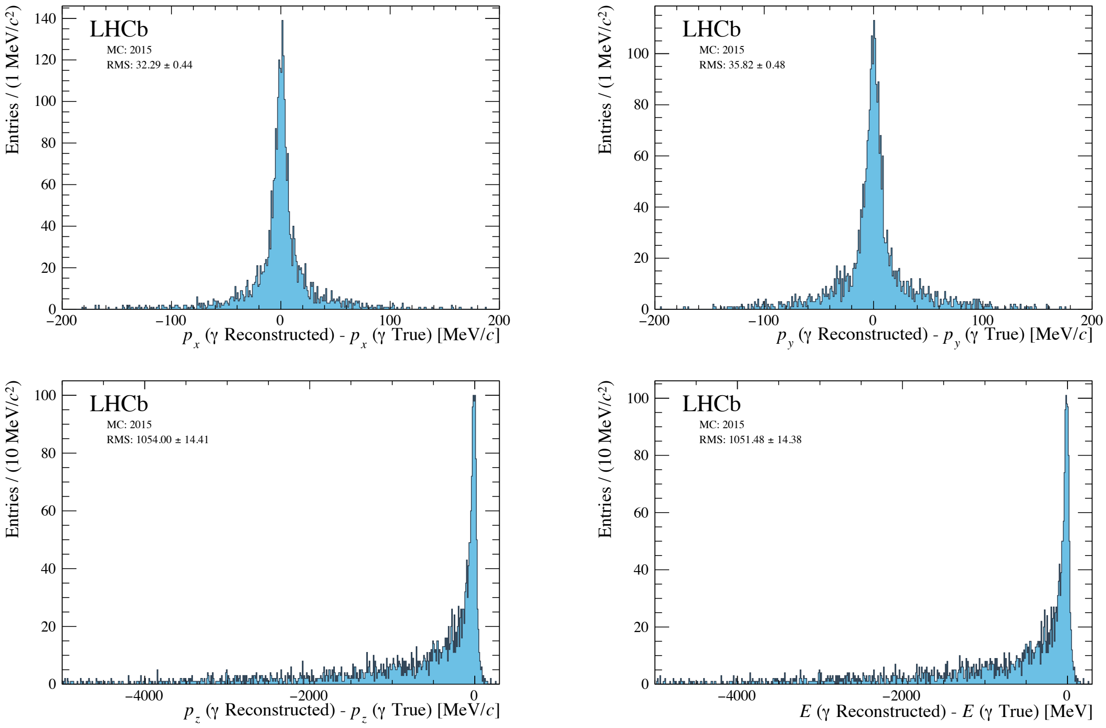

Figure 6.5. Photon-reconstruction-resolution distributions for p_x (top left), p_y (top right), p_z (bottom left), and E (bottom right) using reconstructed CEP χ_{c2} Monte Carlo from pp collisions at a centre-of-mass energy $\sqrt{s} = 13\,\text{TeV}$ for 2015 run conditions.

The resolution of the three-momentum components are not significantly correlated and can be used to smear the momentum of the accompanying photons independently. Similarly, no strong correlations are observed between the energy resolution and the momentum resolution along the x and y-axis. However, there is a strong correlation between the energy resolution and the momentum resolution along the z-axis. As a result of this strong correlation, the energy and momentum along the z-axis can not be randomly smeared simultaneously. Instead, the same randomly selected smear factor is used for both p_z and E. The smeared photon four-vector can now be used to calculate the Δm_{χ_c} together with their corresponding p_{T}^2 distributions, shown in Fig. 6.6.

The difference in the profile of the distributions is due to the nature of the algorithm designed to search for the photons associated with the $\psi(2S)$ meson, namely γ_1 to γ_4. For example, in $\psi(2S) \to \chi_c\gamma$ decays the χ_c mesons tend to appear earlier in the decay list. Therefore, the first photon the algorithm encounters is associated with the χ_c decay, $\chi_c \to J/\psi\gamma$. This is reflected in the presence of the three resonant χ_{c0}, χ_{c1}, and χ_{c2} peaks in invariant-mass-difference distributions in Fig. 6.6 (first row). The second photon encountered by the algorithm would then be the one associated with $\psi(2S)$ decay, $\psi(2S) \to \chi_c\gamma$. This is also reflected as three peaks in the invariant-mass distribution in Fig. 6.6 (second row). However, due to the higher invariant mass of the χ_{c2} meson the phase space available for the photon is lower than that in decays

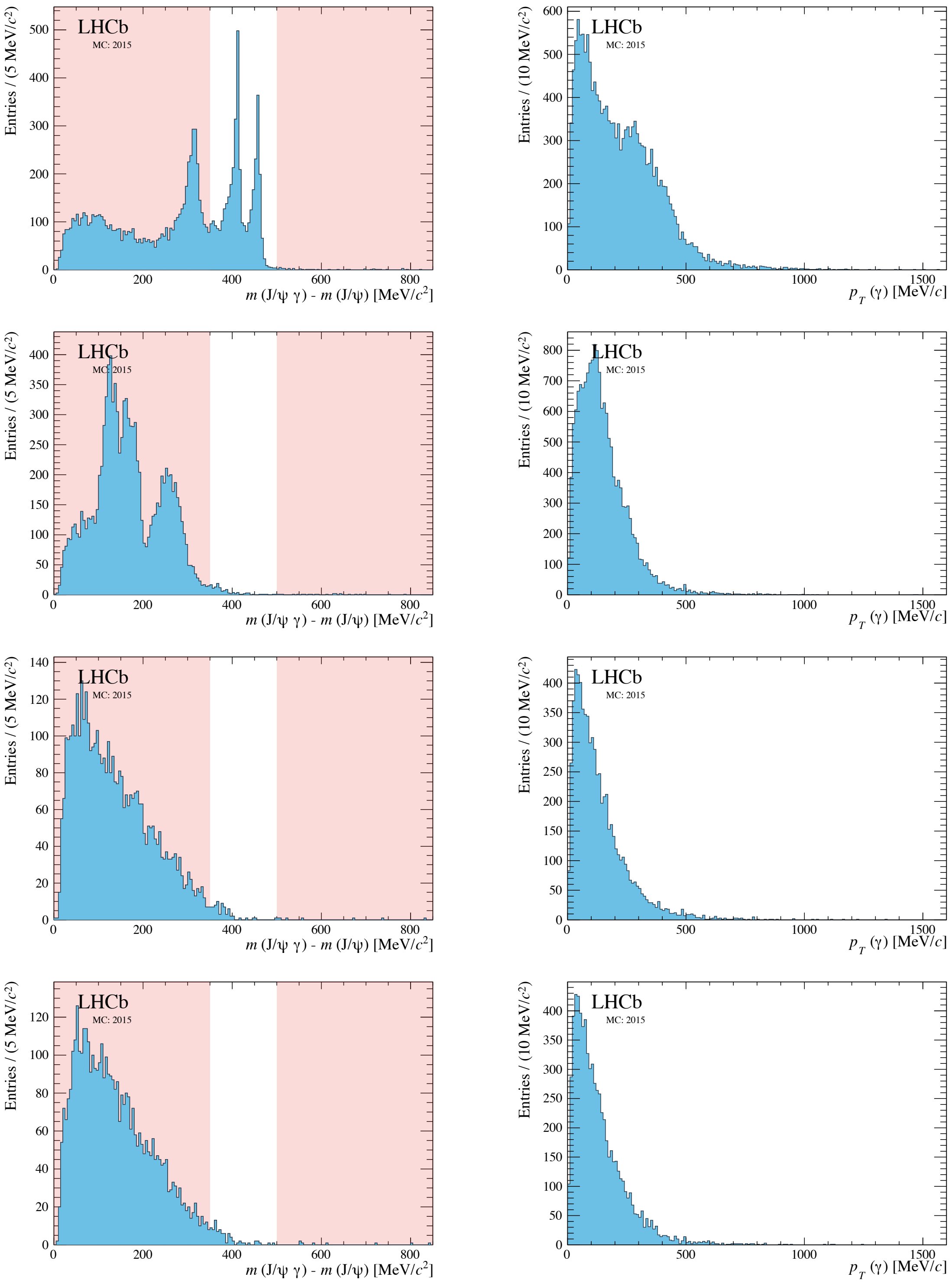

Figure 6.6. Delta-mass (left) and p_{T}^2 (right) distributions of reconstructed J/ψ mesons and generator-level photons prior to conversion and reconstruction, from $\psi(2S) \to J/\psi\,[\mu^+\mu^-]X$ Monte Carlo from pp collisions at $\sqrt{s} = 13\,\mathrm{TeV}$ for 2015 run conditions. Since there are decay modes with more than one photon, we consider four possible combinations displayed separately: γ_1, γ_2, γ_3, and γ_4 from top to bottom. The vetoed Δm_{χ_c} region in the CEP χ_c selection is highlighted in red.

with a χ_{c0}. Therefore, when we reconstruct the $J/\psi\gamma$ system with the second photon the order of the peaks is inverted. That is, the χ_{c2} decay is the one at lower Δm_{χ_c} values followed by χ_{c1} and χ_{c0}. Finally, there are cases where more than one photon appears within the same decay generation such as in $\psi(2S) \to J/\psi\,[\mu^+\mu^-]\pi^0[\gamma\gamma]\pi^0[\gamma\gamma]$. In this case, similar shapes are present in all four Δm_{χ_c} distributions. The Δm_{χ_c} distributions in Fig. 6.6 (rows three and four) come from these decay channels and are also present in the other two plots.

6.2.2 Photon-conversion efficiency and production-mechanism weights

Using the true transverse momentum of the photon, we weight each event by the photon-conversion efficiency as determined in data according to Fig. 5.13 in Sec. 5.1. We multiply this efficiency by a factor of two to account for the dependence of the photon-conversion efficiency on the detector occupancy, so as to be appropriate for CEP-like events, as described in Sec. 5.1.6.

The feed-down background receives contributions from both exclusive and inclusive (i.e. inelastic) $\psi(2S)$ mesons. To model these two contributions, the Monte Carlo kinematics of $\psi(2S)$ mesons are reweighted to match the characteristic kinematics of each production mode according to the results of an earlier LHCb analysis [44], where two exponentials are used to fit the p_{T}^2 $(\psi(2S))$ distribution: one for the inelastic background, B_{I}, and another for the exclusive background, B_{E}. Each shape consists of two parameters: one for normalization, p_0 and p_2 respectively, and another for the slope of the exponential, p_1 and p_3 respectively, such that,

$$B_{\mathrm{I}}(p_T^2) = e^{(p_0+p_1\cdot p_T^2)} \quad \text{and} \quad B_{\mathrm{E}}(p_T^2) = e^{(p_2+p_3\cdot p_T^2)}. \tag{6.2}$$

The experimental fit result of the $\psi(2S)$ study is reproduced in Fig. 6.7. The parameters from these fits are: $p_0 = 3.536 \pm 0.340$, $p_1 = -0.7966 \pm 0.2490\ [\mathrm{MeV}/c]^{-2}$, $p_2 = 5.667 \pm 0.082$, and $p_3 = -6.075 \pm 0.799\ [\mathrm{MeV}/c]^{-2}$.

To perform the re-weighting, the generator-level kinematic information of the $\psi(2S)$ is saved alongside the reconstructed $J/\psi \to \mu^+\mu^-$ mesons. The weights for each case, CEP and inelastic, are calculated by taking the ratio of the $p_{\mathrm{T}}^2(\psi(2S))$ extracted from the $\psi(2S)$ experimental fit results, and the $p_{\mathrm{T}}^2(\psi(2S))$ of the generator-level $\psi(2S)$ Monte Carlo. Furthermore, the inelastic events are assigned an additional weight factor of 0.776, which is the ratio of exclusive-to-inclusive processes measured in an LHCb study of $\psi(2S)$ CEP [44, 141]. Meanwhile the CEP events are assigned a complementary weight factor of $1 - 0.776$, assuring the two backgrounds are produced in the correct proportions. The Δm_{χ_c} distribution of the CEP and inclusive $J/\psi\gamma$ system from $\psi(2S)$ decays, after the selection and weights are applied, is shown in Fig. 6.8 for each of the four photons used to construct the $J/\psi\gamma$ pair.

6.2.3 $\psi(2S)$ feed-down fit and number of expected events

The Δm_{χ_c} distributions are fitted with a kernel estimation PDF (KE PDF), which is an extremely flexible fit method capable of describing the intricate shapes of this background. Since up to four photons are saved for each $\psi(2S)$ meson, the simulated data sets for each $J/\psi\gamma$ pair are treated independently and their fit results are shown in Fig. 6.8. The PDFs are then merged

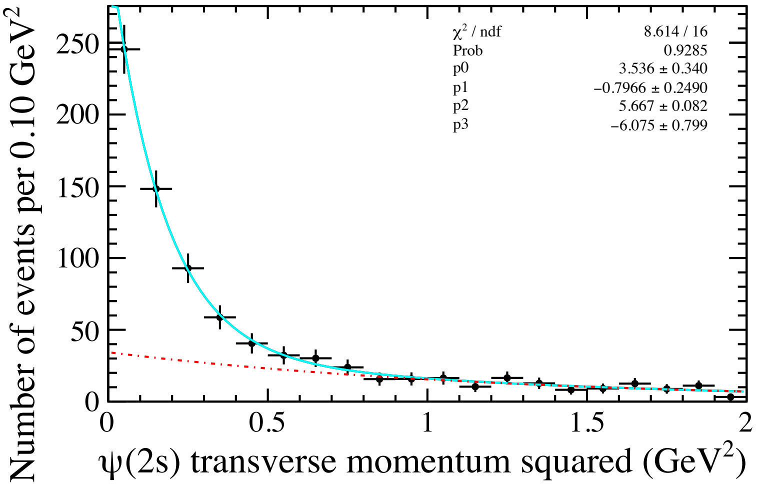

Figure 6.7. Transverse-momentum-squared distribution of $\psi(2S) \to \mu^+\mu^-$ CEP candidates from 2015 pp collisions at a centre-of-mass energy $\sqrt{s} = 13\,\text{TeV}$. The distribution is fitted with two exponentials: one for CEP events and another for the inelastic background in dashed red. The total fit is marked in cyan. Reproduced from Ref. [141].

for both the CEP and inelastic components in proportion to their calculated contribution, as detailed below. The resulting distribution is used as an input for the fit of the CEP χ_c sample.

From the weighted Monte Carlo we can determine an effective efficiency of the selection process, ϵ_s, defined here as the fraction of events that pass the reconstruction and our selection from the 100,000 generated events. This includes the effects of the weights associated with the production mechanism, the reconstruction efficiency of the dimuons, the photon-conversion efficiency, and the multiplicity-correction factor. In the case of CEP production, we have an average-effective efficiency for up to four possible photon combinations of 8.87×10^{-6} within our Δm_{χ_c} selection window, 350 to 500 MeV/c^2. In the case of inelastic production we have an average-effective efficiency of 4.15×10^{-6} within the same range.

The number of expected $\psi(2S)$ feed-down background events, $N(\psi(2S))_{\text{FD}}$, is calculated as follows:

$$N(\psi(2S))_{\text{FD}} = \frac{\mathcal{L} \cdot \sigma(\psi(2S) \to \mu^+\mu^-) \cdot \mathcal{B}(J/\psi \to \mu^+\mu^-) \cdot \mathcal{B}(\psi(2S) \to J/\psi X) \cdot \epsilon_s}{\mathcal{B}(\psi(2S) \to \mu^+\mu^-)}, \qquad (6.3)$$

where $\mathcal{L}$ is the integrated luminosity, $\sigma(\psi(2S) \to \mu^+\mu^-) = 11.1 \pm 1.1 \pm 0.3 \pm 0.4\,\text{pb}$ is the cross-section for the CEP of $\psi(2S)$ reconstructed with two muons within the acceptance of the LHCb experiment ($2 < \eta(\mu^+\mu^-) < 4.5$) [44]. $\mathcal{B}(J/\psi \to \mu^+\mu^-) = (5.961 \pm 0.033)$ % and $\mathcal{B}(\psi(2S) \to \mu^+\mu^-) = (8.0 \pm 0.6) \times 10^{-3}$ are the branching fractions for J/ψ and $\psi(2S)$ decaying into a pair of muons, and $\mathcal{B}(\psi(2S) \to J/\psi\ X) = (61.4 \pm 0.6)$ % is the branching fraction for $\psi(2S)$ mesons decaying into $J/\psi X$ according to the PDG [86]. The total number of expected $\psi(2S)$ feed-down events is calculated for each $J/\psi\gamma$ pair independently and their

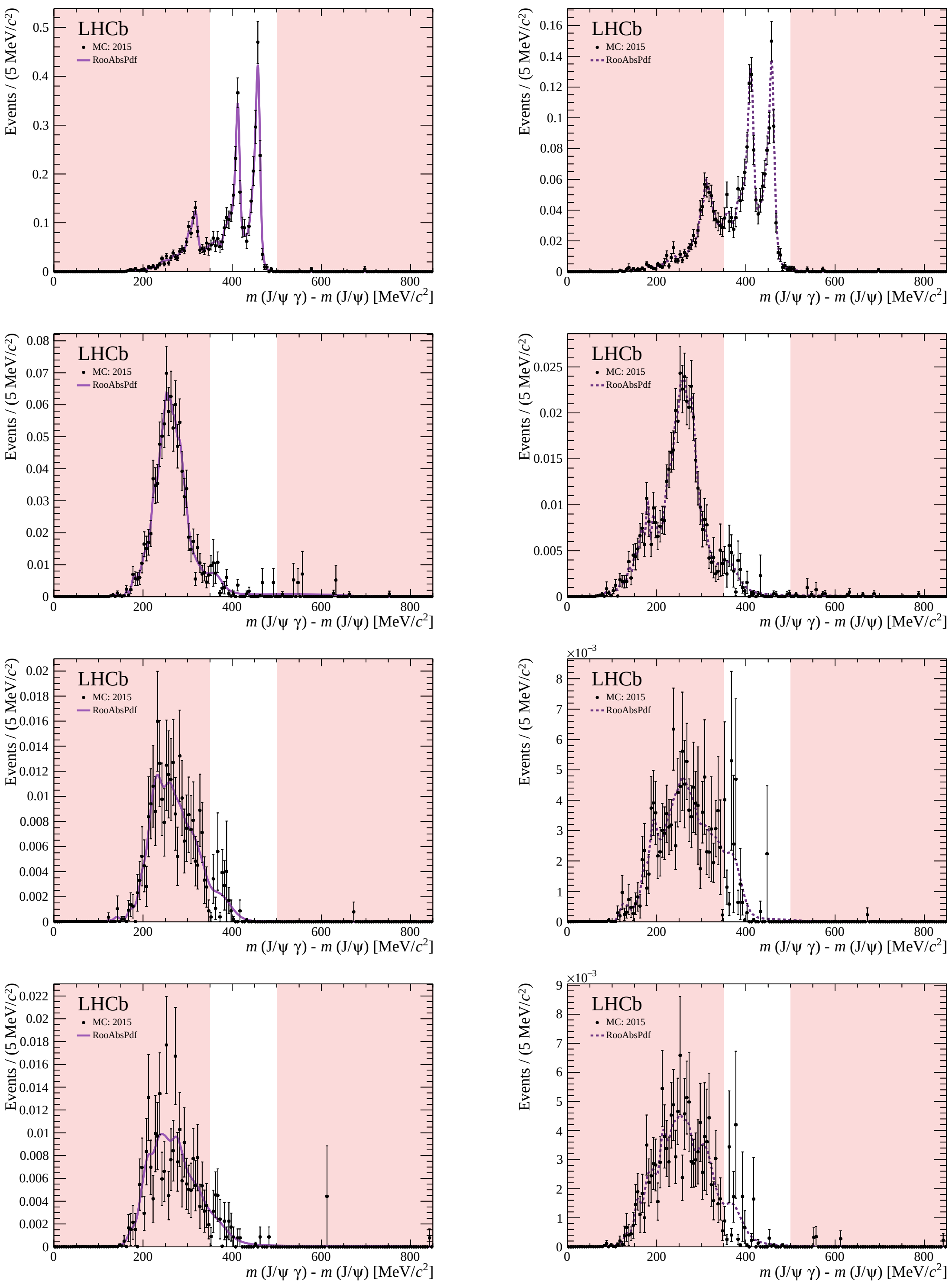

Figure 6.8. Delta-mass of $J/\psi\gamma$ system from $\psi(2S) \to J/\psi\ X$ feed-down using weighted Monte Carlo of pp collisions at a centre-of-mass energy $\sqrt{s} = 13\,\text{TeV}$ to match CEP (left column) and inelastic (right column) experimental $\psi(2S)$ kinematics. This is done for four potentially reconstructible photons, γ_1, γ_2, γ_3, and γ_4, from top to bottom. The distributions are fitted with a kernal-estimator PDF.

Table 6.3. Summary of $\psi(2S)$ feed-down (FD) and combinatorial-background studies including the number of expected background events within the CEP χ_c Δm_{χ_c} selection , 350 to 500 MeV/c^2, for the 2015 (2016), and combined 2015 and 2016 CEP χ_c data, both with and without the HeRSChel cut. The effective-efficiency value, ϵ_s, used in the calculation of the total number of events is also included for 2015 Monte Carlo. Also listed is the total number of events passing the signal selection. Values for the dimuon combinatorial and J/ψ combinatorial background are determined using the 2016-only and combined 2015 and 2016 sample due to the smaller sample size of the 2015-only sample.

Mechanism	**$\ln(\chi^2_{\text{HRC}})$**	**γ_n**	**ϵ_s $\times 10^{-5}$**	**Events 2015 (2016)**	**Total 2015 (2016)**	**Combined 2015 + 2016**
Selected	-	-	-	-	88 (451)	539
	< 5	-	-	-	23 (127)	150
$\psi(2S)^{\text{CEP}}_{\text{FD}}$	-	γ_1	3.45	0.98 ± 0.24 (5.80 ± 1.4)		6.98 ± 5.93
	-	γ_2	0.069	0.0196 ± 0.0058 (0.11 ± 0.03)	1.02 ± 0.61	
	-	γ_3	0.026	0.007 ± 0.003 (0.043 ± 0.015)	(5.97 ± 3.58)	
	-	γ_4	0.027	0.008 ± 0.002 (0.045 ± 0.014)		
$\psi(2S)^{\text{CEP}}_{\text{FD}}$	< 5	γ_1	-	0.69 ± 0.17 (4.91 ± 1.19)		5.80 ± 4.92
	< 5	γ_2	-	0.0138 ± 0.0041 (0.1 ± 0.03)	0.72 ± 0.43	
	< 5	γ_3	-	0.005 ± 0.002 (0.036 ± 0.013)	(5.08 ± 3.05)	
	< 5	γ_4	-	0.005 ± 0.002 (0.039 ± 0.012)		
$\psi(2S)^{\text{In.}}_{\text{FD}}$	-	γ_1	1.58	0.45 ± 0.11 (2.6 ± 0.6)		3.23 ± 2.81
	-	γ_2	0.035	0.01 ± 0.003 (0.058 ± 0.017)	0.47 ± 0.29	
	-	γ_3	0.024	0.007 ± 0.002 (0.04 ± 0.014)	(2.76 ± 1.70)	
	-	γ_4	0.016	0.005 ± 0.002 (0.027 ± 0.009)		
$\psi(2S)^{\text{In.}}_{\text{FD}}$	< 5	γ_1	-	0.32 ± 0.08 (1.8 ± 0.4)		2.20 ± 1.92
	< 5	γ_2	-	0.007 ± 0.002 (0.039 ± 0.011)	0.34 ± 0.21	
	< 5	γ_3	-	0.005 ± 0.002 (0.027 ± 0.009)	(1.86 ± 1.15)	
	< 5	γ_4	-	0.003 ± 0.001 (0.018 ± 0.006)		
$\mu^+\mu^-$ comb.	-	-	-	-	(0.68 ± 0.36)	0.46 ± 0.39
	< 5	-	-	-	(0.51 ± 0.26)	0.43 ± 0.26
J/ψ comb.	-	-	-	-	(35.55 ± 5.85)	44.97 ± 6.35
	< 5	-	-	-	(11.91 ± 4.51)	13.25 ± 4.66

results are summed together to account for the full range of decay modes that contribute to this background. We find a total of 5.97 ± 3.58 (6.98 ± 5.93) CEP $\psi(2S)$ feed-down background and 2.76 ± 1.70 (3.23 ± 2.81) inelastic $\psi(2S)$ feed-down background events within our Δm_{χ_c} selection window in the 2016-only (combined 2015 and 2016) data. Therefore, we expect to see a very small contribution of feed-down events. These results are summarised in Table 6.3.

6.2.4 $\psi(2S)$ feed-down background with HeRSChel

To account for the effects of the HeRSChel cut we use the efficiency for CEP, $\epsilon^{\text{CEP}}_{\text{HRC}}$, and inelastic, $\epsilon^{\text{In.}}_{\text{HRC}}$, events calculated in Sec. 5.6. With these efficiencies, we can scale down the calculated $\psi(2S)$ feed-down background prior to the implementation of the HeRSChel cut, as calculated in Sec. 6.2. For a HeRSChel cut of $\ln(\chi^2_{\text{HRC}}) < 5$, $\epsilon^{\text{CEP}}_{\text{HRC}} = (85.1 \pm 0.8)\%$ $((83.0 \pm 0.8)\%)$ and

$\epsilon_{\rm HRC}^{\rm In.} = (67.6 \pm 0.8)\%$ $((68.2 \pm 0.7)\%)$ for 2016-only (combined 2015 and 2016), we expect to see 5.08 ± 3.05 (5.80 ± 4.92) CEP and 1.86 ± 1.15 (2.20 ± 1.92) inelastic $\psi(2S)$ feed-down events in 2016-only (combined 2015 and 2016) χ_c data after the HeRSChel cut is applied. The results are summarised in Table 6.3.

6.3 Inelastic χ_c background

The background in the CEP χ_c selection is dominated by the inelastic production of χ_c mesons. In this process the proton fragments, or debris from gluon radiation, may leave traces in the main spectrometer. In the case that they do, we are able to suppress the background via our CEP track selection, which requests two long tracks for the two muons associated with the J/ψ, and two downstream tracks for the two electrons used to reconstruct the photon in an otherwise empty detector. However, due to the high longitudinal momentum of the protons, the proton fragments tend to continue their trajectory down the beam line and outside the detector acceptance. We are able to reject some of these high-rapidity inelastic events by looking for activity in the HeRSChel modules. In addition, we can exploit the different transverse-momentum signatures of CEP and inelastic events to determine the contribution of inelastic events we fail to veto by simultaneously fitting the Δm_{χ_c} and $p_{\rm T}^2$ distributions of the χ_c candidates. In particular, this study allows us to determine the following information to later constrain the global CEP χ_c fit necessary to determine the contributions from CEP and inelastic processes:

- The production ratio of inelastic χ_{c1} and χ_{c2} within our Δm_{χ_c} selection window.
- Understand the Δm_{χ_c} fit model for inelastic χ_c candidates.
- Extract the $p_{\rm T}^2$ fit model for inelastic χ_c candidates.

6.3.1 Inelastic data set and selection

To study the inelastic χ_c contribution, we select a sample guaranteed to be inelastic by ensuring events violate the rapidity-gap criteria through the presence of additional tracks, other than those associated with the χ_c decay mode. We use the main analysis χ_c data samples but omit the CEP track-selection criteria used to meet the rapidity-gap criteria and, in its place, we select events that have two downstream tracks for the converted-photon reconstruction and three or more long tracks, two of which are muons from the J/ψ meson reconstruction, and no other tracks. This guarantees we are selecting inelastic χ_c events and associated backgrounds. From this point forth, we will refer to this data set as the $\geq$ 3Long sample. A total of 3099 and 2096 events pass our selection for the 2015 and 2016 data respectively, of which 838 and 778 events fall within our Δm_{χ_c} selection window.

In addition, we apply the HeRSChel cut, $\ln(\chi^2_{\rm HRC}) < 5$, to the $\geq$ 3Long sample to study its effects on the inelastic background. From here on, we will refer to this sample as the $\geq$ 3Long + HRC sample. A total of 187 and 191 events pass our $\geq$ 3Long + HRC selection for 2015 and 2016 data, adding up to a total of 378 for the combined 2015 and 2016 sample. As expected, the HeRSChel cut has reduced the size of this sample significantly compared to the $\geq$ 3Long sample. Of these events, 55 and 60 fall within our Δm_{χ_c} selection window for each year respectively, summing to 115 events for the combined data set.

Recall that the CEP selection has a tight requirement for the maximum number of SPD hits imposed at the hardware-trigger level, and so the multiplicity in these events is still low. The 2015 data set has a larger number of events due to looser requirements on the event multiplicity at the hardware-trigger level, in spite of 2016 being the sample with higher integrated luminosity since higher-multiplicity events are more common. The number of events in the $\geq$ 3Long and $\geq$ 3Long + HRC samples are summarised in Table 6.4.

Table 6.4. Summary of $\geq$ 3Long sample with and without the HeRSChel cut, $\ln(\chi^2_{\text{HRC}})$, including $\psi(2S)$ feed-down and combinatorial-background results for events within the CEP χ_c Δm_{χ_c} selection window, 350 to 500 MeV/c^2, for 2015 (2016), and the combined 2015 and 2016 luminosities. The effective-efficiency value, ϵ_s, used in the calculation of the total number of events is also included for Monte Carlo with 2015 run conditions. Also listed is the total number of events passing the signal selection. Values for the combinatorial background are determined using the 2016-only and combined 2015 and 2016 sample due to the smaller sample size of the 2015-only sample.

Mechanism	$\ln(\chi^2_{\text{HRC}})$	γ_n	ϵ_s $\times 10^{-5}$	**Events 2015 (2016)**	**Total 2015 (2016)**	**Combined 2015 + 2016**
Selected	-	-	-	-	838 (778)	1616
	< 5	-	-	-	55 (60)	115
$\psi(2S)^{\text{In.}}_{\text{FD}}$ $\geq$ 3Long	-	γ_1	0.146	0.041 ± 0.011 (0.243 ± 0.063)	0.05 ± 0.03 (0.29 ± 0.2)	0.33 ± 0.33
	-	γ_2	0.017	0.005 ± 0.002 (0.028 ± 0.01)		
	-	γ_3	0.003	0.0009 ± 0.0003 (0.005 ± 0.002)		
	-	γ_4	0.005	0.0015 ± 0.0006 (0.009 ± 0.004)		
$\psi(2S)^{\text{In.}}_{\text{FD}}$ $\geq$ 3Long +HRC	< 5	γ_1	-	0.03 ± 0.008 (0.164 ± 0.042)	0.04 ± 0.02 (0.19 ± 0.20)	0.23 ± 0.33
	< 5	γ_2	-	0.003 ± 0.001 (0.019 ± 0.007)		
	< 5	γ_3	-	0.0007 ± 0.0002 (0.004 ± 0.001)		
	< 5	γ_4	-	0.0011 ± 0.0004 (0.006 ± 0.002)		
Comb.	-	-	-	-	(439.37 ± 14.56)	1177.77 ± 22.92
	< 5	-	-	-	(52.52 ± 5.58)	90.74 ± 6.54

As well as genuine χ_c events, this samples will also contain combinatorial and feed-down backgrounds. To determine these non-χ_c backgrounds, we repeat the procedures detailed in the two previous sections, Sec. 6.1 and Sec. 6.2, used to model combinatorial and feed-down backgrounds in order to access the pure inelastic χ_c component. Table 6.4 also summarises these contributions to the inelastic sample, the determination of which is detailed in the following sections. As will be seen, the combinatorial background is dominant in this sample.

6.3.2 Combinatorial background in inelastic χ_c sample

To study the combinatorial background in the $\geq$ 3Long and $\geq$ 3Long + HRC samples, we apply the same data-driven approach described in Sec. 6.1.2 to model the J/ψ combinatorial background for the CEP χ_c sample and fit the purely combinatorial Δm_{χ_c} range. Since this method is also sensitive to the much smaller continuum-combinatorial background, we use a single shape to account for both backgrounds. We mismatch J/ψ mesons with converted photons from different events using the $\geq$ 3Long sample, then fit the p_{T}^2 and the Δm_{χ_c} distributions of the $J/\psi\gamma$ system. To model the $p_{\mathrm{T}}^2(J/\psi\gamma)$ distribution of the $\geq$ 3Long sample we use the sum of two exponentials, such that

$$A \cdot e^{-a \cdot p_T^2} + B \cdot e^{-b \cdot p_T^2}, \tag{6.4}$$

where A and B are normalising factors while a and b are the slopes of the exponentials. In the case of the $\geq$ 3Long + HRC sample, we use a single exponential, $A \cdot \exp\left(-a \cdot p_T^2\right)$. The fit results are shown in Fig. 6.9 where we see small contributions from the second exponential in the fit of the $\geq$ 3Long sample.

We use a double-sided Crystal Ball in a maximum-unbinned-likelihood fit to model the Δm_{χ_c} distribution. The fit results are shown in Fig. 6.10. The parameter values for the p_{T}^2 and Δm_{χ_c} fits are summarised in Table 6.5. These shapes are then fixed and used to fit the Δm_{χ_c} and $p_{\mathrm{T}}^2(J/\psi\gamma)$ in the $\geq$ 3Long and $\geq$ 3Long + HRC inelastic χ_c data set, as shown in Fig. 6.11. The data in the resonant region are not shown as this is signal dominated and is not accounted for in this fit model. The normalisation of the fit is based on the combinatoric region above 500 MeV/c^2 and the PDF is extrapolated into our CEP χ_c selection window, 350 to 500 MeV/c^2. Although there is significantly more combinatorial background in this sample compared to the CEP χ_c sample, the data-driven method does an excellent job at modelling this contribution. We see a total of 1177.77 ± 22.92 (90.74 ± 6.54) events in the combined 2015 and 2016 data, and 439.37 ± 14.56 (52.52 ± 5.58) events in the 2016-only data without (with) the HeRSCheL cut applied. These results are summarised in Table 6.4.

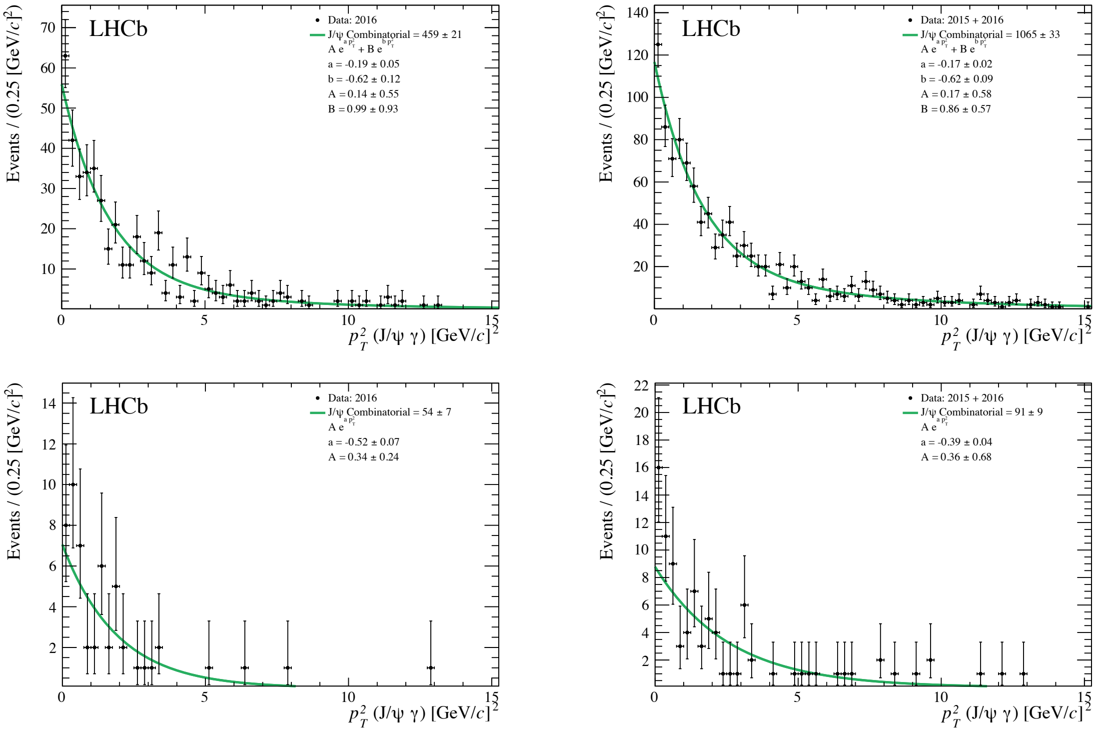

Figure 6.9. Fit of the p_{T}^2 distribution of the artificial-combinatorial background from the $\geq$ 3Long (top), fitted with the sum of two exponentials, and $\geq$ 3Long + HRC (bottom) samples, fitted with a single exponential, for 2016-only (left), and combined 2015 and 2016 (right) data.

Table 6.5. Parameters of Δm_{χ_c} and p_{T}^2 fits of J/ψ-combinatorial background of the $\geq$ 3Long and $\geq$ 3Long + HRC sample for the 2016-only, and combined 2015 and 2016 data.

Variable	**Units**	**Without HeRSChel**		**With HeRSChel**	
		2016	**2015 + 2016**	**2016**	**2015 + 2016**
		Δm_{χ_c} Combinatorial			
μ	MeV/c^2	384.27 ± 4.57	382.86 ± 3.10	439.08 ± 1.34	431.24 ± 11.94
σ	MeV/c^2	112.38 ± 2.80	114.30 ± 1.89	145.89 ± 1.53	143.62 ± 8.13
n_{Left}	-	50.00 ± 111.32	50.00 ± 111.32	50.00 ± 111.32	50.00 ± 111.32
n_{Right}	-	113.85 ± 0.29	107.08 ± 92.53	1.81 ± 0.60	119.16 ± 1.44
α_{Left}	-	62.84 ± 48.13	69.27 ± 126.77	52.06 ± 47.94	52.06 ± 47.94
α_{Right}	-	-0.28 ± 0.01	-0.26 ± 0.01	-0.82 ± 0.01	-0.40 ± 0.03
		$p_{\mathrm{T}}^2(J/\psi\,\gamma)$ Combinatorial			
a	$[\mathrm{MeV}/c]^{-2}$	-0.19 ± 0.05	-0.17 ± 0.02	-0.52 ± 0.07	-0.39 ± 0.04
b	$[\mathrm{MeV}/c]^{-2}$	-0.62 ± 0.12	-0.62 ± 0.09	-	-
A	$[\mathrm{MeV}/c]^{-2}$	0.14 ± 0.55	0.17 ± 0.58	0.34 ± 0.24	0.36 ± 0.68
B	$[\mathrm{MeV}/c]^{-2}$	0.99 ± 0.93	0.86 ± 0.57	-	-

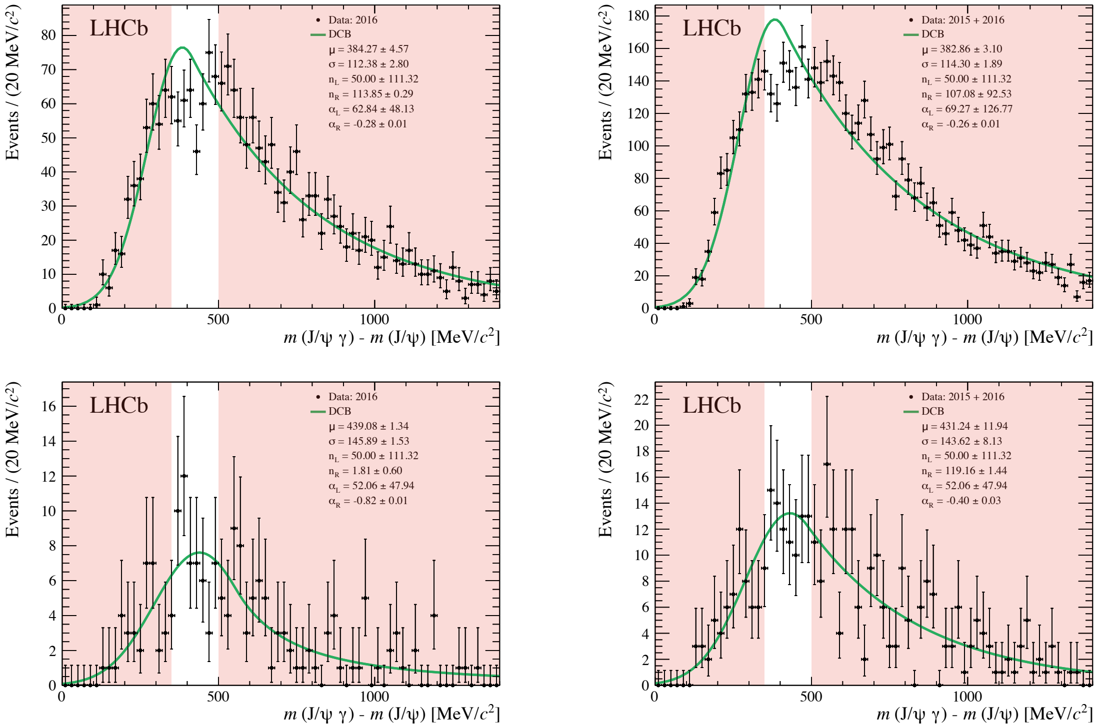

Figure 6.10. Fit of the Δm_{χ_c} distribution of the artificial-combinatorial background using the events from the $\geq$ 3Long (top) and $\geq$ 3Long + HRC (bottom) sample for the 2016-only (left), and combined 2015 and 2016 (right) data. The distributions are fitted with a double-sided Crystal Ball. The vetoed range of our CEP χ_c selection is highlighted in red.

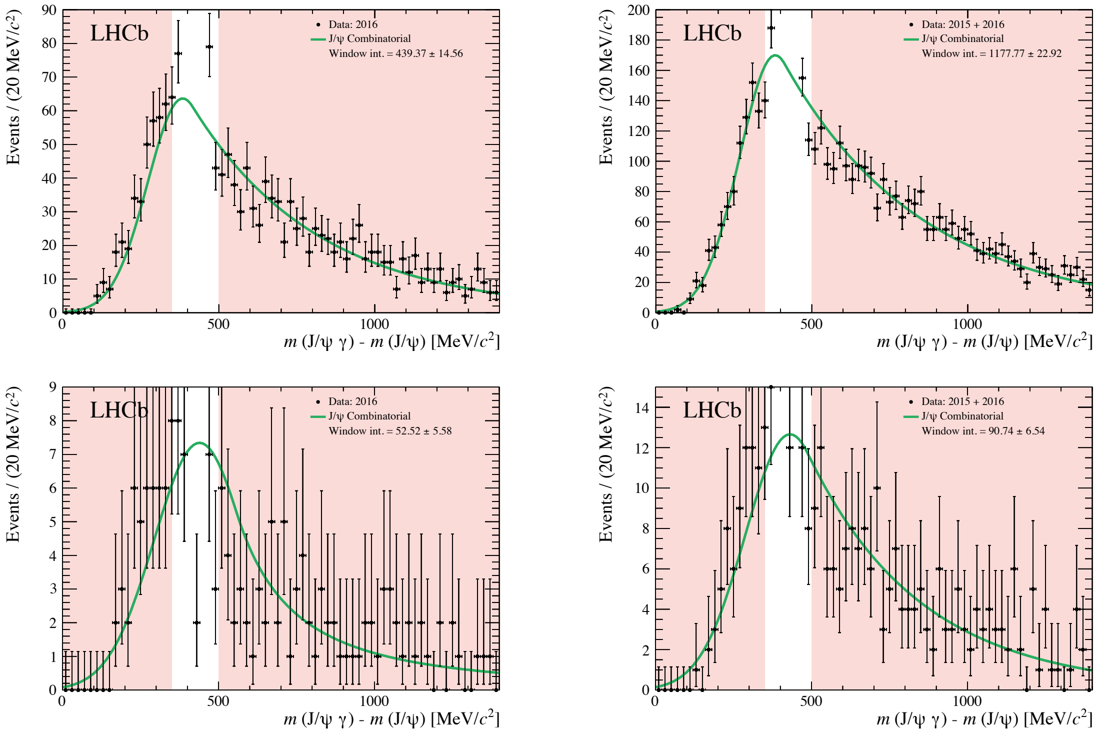

Figure 6.11. Fit of the Δm_{χ_c} distribution of inelastic $\chi_c \to J/\psi\,[\mu^+\mu^-]\gamma[e^+e^-]$ decays from the $\geq$ 3Long (top) and $\geq$ 3Long + HRC (bottom) sample for the 2016-only (left), and combined 2015 and 2016 (right) data. The y-axis range has been been truncated as to not show the resonant peaks associated with our signal. The distributions are fitted with a double-sided Crystal Ball. The vetoed range of our CEP χ_c selection is highlighted in red.

6.3.3 $\psi(2S)$ feed-down background in inelastic χ_c sample

To calculate the number of expected inelastic $\psi(2S)$ feed-down background events in the $\geq$ 3Long sample, as well as extract an invariant-mass fit shape, we use the same procedure detailed in Sec. 6.2 using the $\psi(2S) \rightarrow J/\psi\, X$ Monte Carlo. Our selection is identical with the exception of the track selection where we replace the CEP track selection criteria with that of the $\geq$ 3Long sample, by requiring that an event has one or more long tracks on top of the two long muon tracks and two downstream electron tracks. We apply the weights associated with the photon-conversion efficiency as well as the weights necessary to match the experimental p_{T}^2 $(\psi(2S))$ results of inelastic $\psi(2S)$ mesons. From this, we expect 0.33 ± 0.33 events in the combined 2015 and 2016 data set, and 0.29 ± 0.20 in the 2016-only sample. We account for the effects of the HeRSChel cut by scaling the results in Sec. 6.3.3 by $\epsilon_{\mathrm{HRC}}^{\mathrm{In.}}$. After performing this procedure, we find that we expect a total of 0.23 ± 0.33 inelastic $\psi(2S)$ feed-down events in the combined 2015 and 2016 data, and 0.19 ± 0.20 events in the 2016-only data. These results are summarised in Table 6.4 for each of the $J/\psi\gamma$ combinations. To extract the PDFs, we apply the resolution effects to the photon's kinematics before reconstructing the $J/\psi\gamma$ system. As before, the p_{T}^2 shape is fixed according to the inelastic $\psi(2S)$ component presented in the results of the J/ψ and $\psi(2S)$ CEP measurement [44].

6.3.4 Inelastic χ_c background fit

We model each of the inelastic χ_c resonant peaks with a double-sided Crystal Ball and use the CEP χ_c Monte Carlo samples described in Sec. 4.1 to constrain the fit parameters. The CEP χ_c selection criteria are applied to the reconstructed Monte Carlo and generator-level information is used to verify each reconstructed particle in the event matches its type and position within the $\chi_c \rightarrow J/\psi\,[\mu^+\mu^-]\gamma[e^+e^-]$ decay chain. To extract the resonant shapes, we use an unbinned maximum-likelihood fit on the Δm_{χ_c} distribution while floating all shape parameters. The flexibility of the double-sided Crystal Ball allows for an adequate description of the asymmetric shape, which results from the energy loss of the electrons to bremsstrahlung radiation. The fit results are shown in Fig. 6.12 and the final values of the fit parameters are summarised in Table 6.6.

In the fit of the $\geq$ 3Long sample, the two double-sided Crystal Balls for the χ_{c1} and χ_{c2} contributions are joined together into a single composite shape. This allows us to simplify the model of the inelastic p_{T}^2 contribution to a single shape and a single yield parameter shared between the mass and p_{T}^2 shapes, thereby improving the fit's stability. The Monte Carlo fit results are used to constrain the ratio of the widths of the χ_c resonances in the data fit, providing some flexibility for resolution differences between data and Monte Carlo. The mean value of the χ_{c1} is fixed relative to the mean value of the χ_{c2} according to the mass difference between χ_{c1} and χ_{c2} mesons. These mean values are expected to be slightly lower than the nominal values, which are 3510.67 ± 0.05 MeV/c^2 and 3556.17 ± 0.07 MeV/c^2 [86]. This is due to bremsstrahlung radiation. The tail parameters, on the other hand, are completely fixed according to the Monte

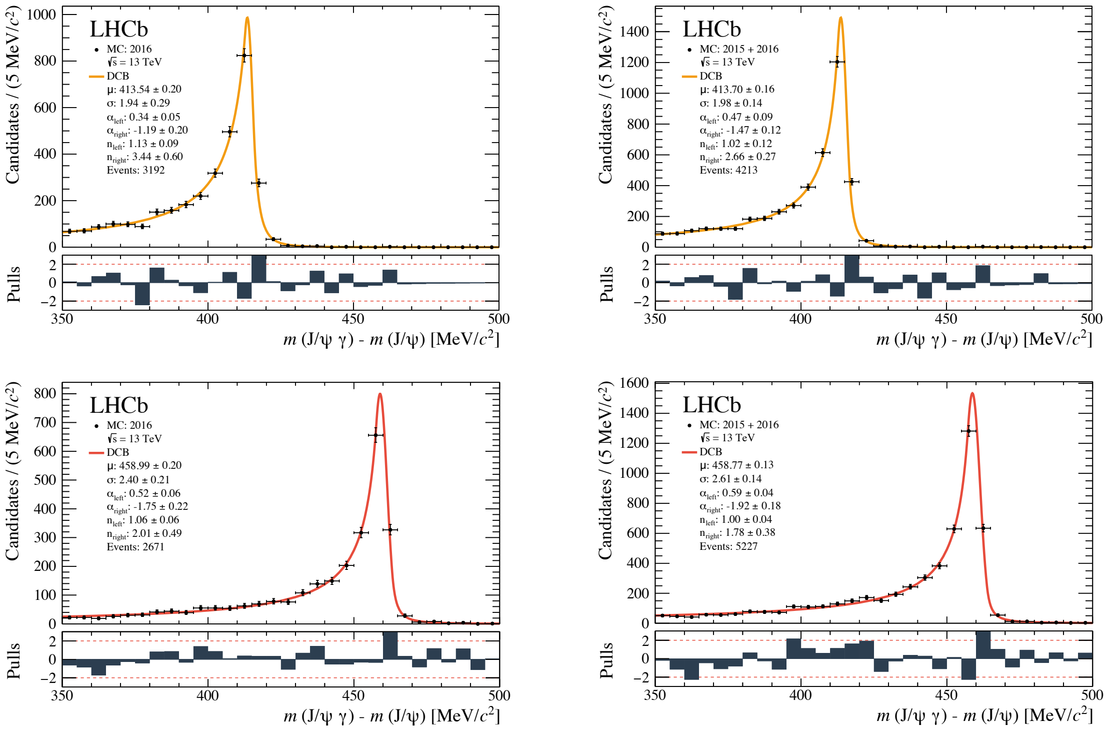

Figure 6.12. Fit of the Δm_{χ_c} distributions of CEP χ_{c1} (top) and χ_{c2} (bottom) Monte Carlo from pp collisions at a centre-of-mass energy of $\sqrt{s} = 13\,\text{TeV}$ generated with SuperChic v2 for the 2016-only (left), and combined 2015 and 2016 (right) run conditions. The Monte Carlo is reconstructed using converted photons and the CEP χ_c selection is applied before the distributions are fitted with a double-sided Crystal Ball with all parameters left floating. The lower panels show the pulls.

Table 6.6. Summary of the parameter values pertaining to the fit parameters of the double-sided Crystal Balls used to fit the Δm_{χ_c} distributions of CEP χ_{c1} and χ_{c2} mesons from the 2016-only, and combined 2015 and 2016 Monte Carlo of pp collisions at centre-of-mass energy $\sqrt{s} = 13\,\text{TeV}$.

		χ_{c1}		χ_{c2}	
Parameter	**Units**	**2016**	**2015 + 2016**	**2016**	**2015 + 2016**
μ	MeV/c^2	413.54 ± 0.20	413.70 ± 0.16	458.99 ± 0.20	458.77 ± 0.13
σ	MeV/c^2	1.94 ± 0.29	1.98 ± 0.14	2.40 ± 0.21	2.61 ± 0.14
α_{Left}	-	0.34 ± 0.05	0.47 ± 0.09	0.52 ± 0.06	0.59 ± 0.04
α_{Right}	-	-1.19 ± 0.20	-1.47 ± 0.12	-1.75 ± 0.22	-1.92 ± 0.18
n_{Left}	-	1.13 ± 0.09	1.02 ± 0.12	1.06 ± 0.06	1.00 ± 0.04
n_{Right}	-	3.44 ± 0.60	2.66 ± 0.27	2.01 ± 0.49	1.78 ± 0.38

Carlo results. For the p_{T}^2, we use the sum of two exponentials (Eq. 6.4) where all parameters are left floating for the Monte Carlo unbinned-simultaneous-maximum-likelihood fit. The Δm_{χ_c} and p_{T}^2 fit results are shown in Fig. 6.13 while the values of the floated parameters are summarised in Table 6.7. From these fit results we are able to extract two important pieces of information. The first is the yield ratio of the inelastic χ_{c1} to χ_{c2} mesons, $\chi_{c1}/\chi_{c2} = 0.91 \pm 0.16$ for 2016-only data, and $\chi_{c1}/\chi_{c2} = 0.83 \pm 0.14$ for the combined 2015 and 2016 data. In addition, we can determine the p_{T}^2 shape parameter and fix them in our simultaneous fit of the CEP χ_c sample.

Finally, we perform a simultaneous fit of the Δm_{χ_c} and the p_{T}^2 distributions of the inelastic χ_{c1} and χ_{c2} candidates in the $\geq$ 3Long + HRC sample. Because this sample is much smaller, on account of the HeRSChel cut, we fix the width of the double-sided Crystal Ball to the fit results of the $\geq$ 3Long sample, detailed in Table 6.7. The Δm_{χ_c} and p_{T}^2 fit results are shown in Fig. 6.14. As before, we extract the χ_{c1} to χ_{c2} production ratio for later use in the CEP χ_c fit: for the combined 2015 and 2016 data, $\chi_{c1}/\chi_{c2} = 2.50 \pm 2.37$ and $\chi_{c1}/\chi_{c2} = 2.11 \pm 1.76$ for 2016-only data. We use these values to constrain the ratios of the CEP χ_c fit of our samples with the HeRSChel cut applied. However, we repeat the fit with the ratio determined with the larger $\geq$ 3Long sample as a systematic check. The results of this study are presented in Sec. 7.1 along side the fit results of the CEP χ_c sample. The production ratios and the values of floated parameters are summarised in Table 6.7 for both $\geq$ 3Long + HRC and $\geq$ 3Long samples.

We observe a total of 20 ± 6 (29 ± 9) inelastic χ_c events in the 2016-only (combined 2015 and 2016) data. This compares to 365 ± 26 (526 ± 37) events prior to the HeRSChel cut, corresponding to a 5.46 ± 1.68 (5.51 ± 1.75) percent retention of inelastic χ_c events for the 2016-only (combined 2015 and 2016) data. This suggests that HeRSChel is successfully eliminating inelastic events. Finally, we use the fit results of the p_{T}^2 distribution to fix the parameters in the CEP χ_c fit.

As a systematic check we repeat the fit using a single exponential, Eq. 6.1, to model the p_{T}^2 distribution from the combined contribution of inelastic χ_{c1} and χ_{c2} mesons. From the fit of the Δm_{χ_c} we obtain χ_c yield ratios consistent with the results presented above, $\chi_{c1}/\chi_{c2} = 0.88 \pm 0.18$ (1.49 ± 1.15) for 2016-only data, and $\chi_{c1}/\chi_{c2} = 0.83 \pm 0.14$ (1.78 ± 1.44) for the combined 2015 and 2016 data without (with) the HeRSChel cut applied. All floated parameters are summarised in Table 6.7.

Unlike the combinatorial and feed-down background, the amount of inelastic χ_c background expected in the CEP χ_c sample is not presented in this section as it is determined together with the amount of CEP χ_c signal in the simultaneous fit of the CEP χ_c sample. The results of the CEP χ_c sample fit are presented in detail in Chapter 7.

Table 6.7. Floated parameter values of Δm_{χ_c} and p_{T}^2 fits of $\geq$ 3Long and $\geq$ 3Long + HRC sample for the 2016-only, and combined 2015 and 2016 data. Results are shown for the case where the p_{T}^2 of inelastic χ_c candidates is modelled with one and with two exponentials.

			1 Exp.		**2 Exp.**	
Variable	**Units**	$\ln(\chi^2_{\mathrm{HRC}})$	**2016**	**2015 + 2016**	**2016**	**2015 + 2016**
			Δm_{χ_c} **Inelastic**			
σ	MeV/c^2	-	3.00 ± 0.51	3.41 ± 0.51	3.09 ± 0.53	3.49 ± 0.64
μ	MeV/c^2	-	457.97 ± 0.60	458.13 ± 0.54	458.05 ± 0.62	457.98 ± 0.68
		< 5	456.58 ± 1.66	455.79 ± 1.84	455.94 ± 1.69	455.86 ± 2.08
χ_{c1}/χ_{c2}	-	-	0.88 ± 0.18	0.83 ± 0.14	0.91 ± 0.16	0.83 ± 0.14
		< 5	1.49 ± 1.15	1.78 ± 1.44	2.11 ± 1.76	2.50 ± 2.37
			$p_{\mathrm{T}}^2(J/\psi\,\gamma)$ **Inelastic**			
a	$[\mathrm{MeV}/c]^{-2}$	-	-0.17 ± 0.01	-0.16 ± 0.01	-0.06 ± 0.03	-0.07 ± 0.03
		< 5	-0.11 ± 0.04	-0.11 ± 0.04	-0.08 ± 0.06	-0.07 ± 0.05
b	$[\mathrm{MeV}/c]^{-2}$	-	-	-	-0.38 ± 0.08	-0.36 ± 0.09
		< 5	-	-	-2.54 ± 2.38	-1.45 ± 1.57
A	$[\mathrm{MeV}/c]^{-2}$	-	0.46 ± 0.65	0.46 ± 0.65	0.04 ± 0.56	0.15 ± 0.52
		< 5	0.46 ± 0.23	0.57 ± 0.21	0.02 ± 0.76	0.02 ± 0.84
B	$[\mathrm{MeV}/c]^{-2}$	-	-	-	0.37 ± 0.80	0.91 ± 0.51
		< 5	-	-	0.28 ± 0.59	0.23 ± 0.86

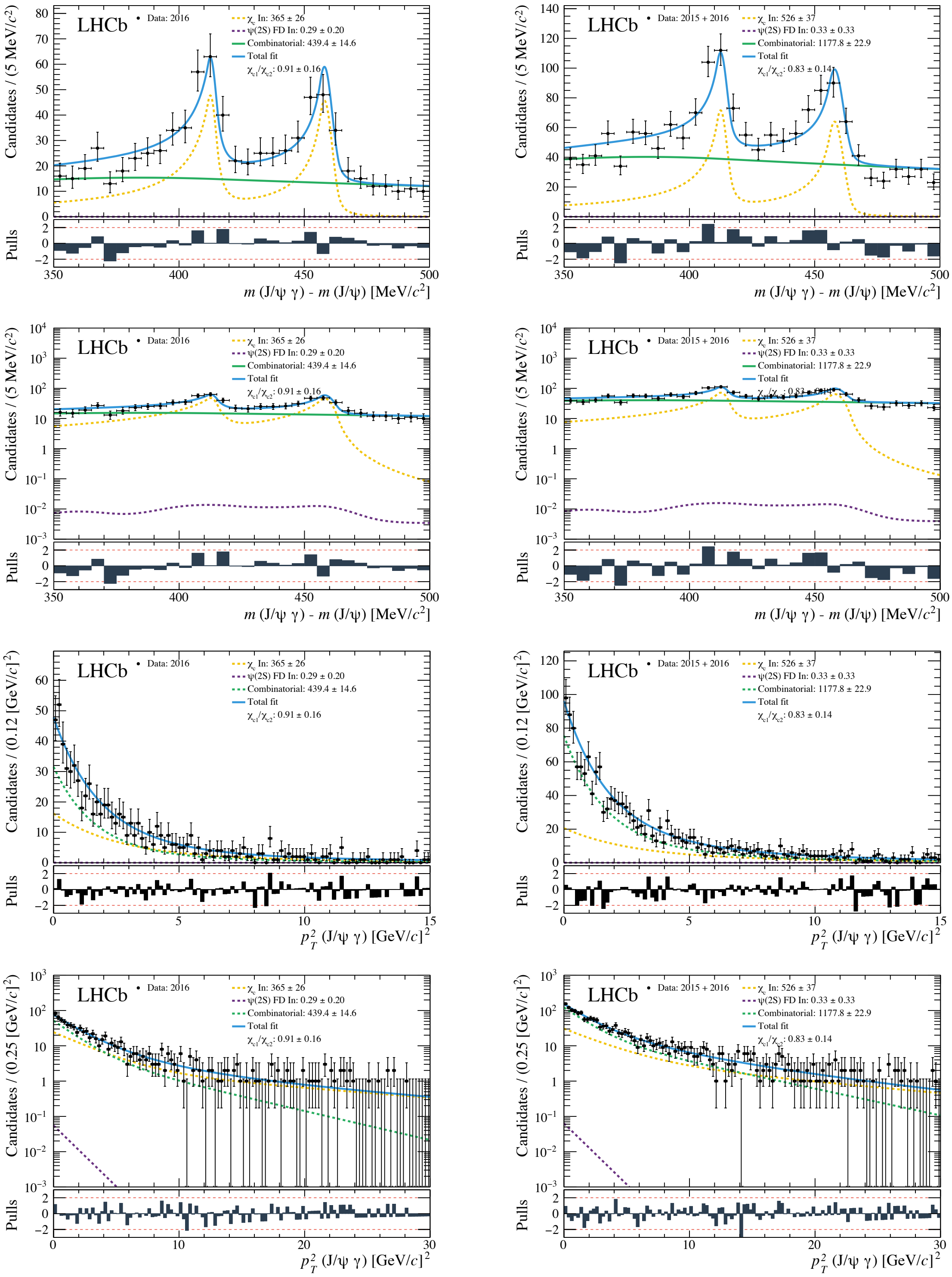

Figure 6.13. Fit of the Δm_{χ_c} (first and second row) and p_{T}^2 (third and fourth row) distribution of χ_c candidates from the $\geq$ 3Long sample in linear (first and third row) and logarithmic scale (second and fourth row) for the 2016-only (left), and combined 2015 and 2016 (right) data. The p_{T}^2 distribution is modelled by a single shape composed of two exponentials for the inelastic χ_{c1} and χ_{c2} mesons. Note that the x-axis scales are different for the linear and logarithmic versions for the p_{T}^2 distribution. The lower panels show the pulls distributions.

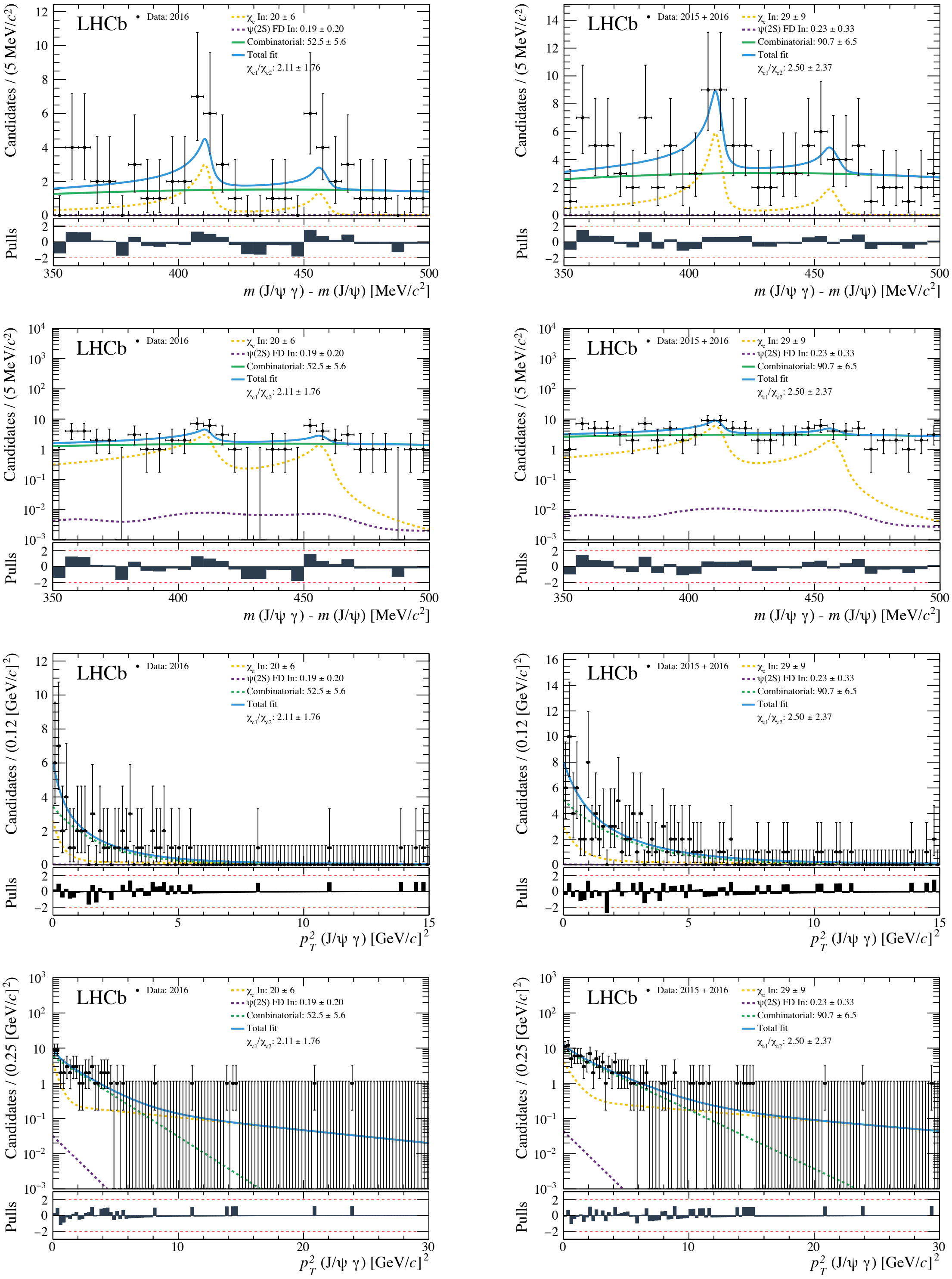

Figure 6.14. Fit of the Δm_{χ_c} (first and second row) and p_{T}^2 (third and fourth row) distribution of χ_c candidates from the $\geq 3\text{Long} + \text{HRC}$ sample in linear (first and third row) and logarithmic scale (second and fourth row) for the 2016-only (left), and combined 2015 and 2016 (right) data. The p_{T}^2 distribution is modelled by a single shape composed of two exponentials for the inelastic χ_{c1} and χ_{c2} mesons. Note that the x-axis scales are different for the linear and logarithmic versions for the p_{T}^2 distribution. The lower panels show the pulls distributions.

6.4 Background summary

In this section, we summarise the results of the background studies necessary to model our CEP χ_c selection data with and without the HeRSChel cut applied. Table 6.8 lists the expected contributions of the combinatorial and feed-down components in our CEP χ_c selection.

Using the CEP χ_c data set we were able to model the J/ψ-combinatorial by mismatching J/ψ mesons with converted photons from different events. We combined this with a flat distribution for the continuum combinatorial such that it matches the measured background under our selected J/ψ mesons. We used this model to fit the Δm_{χ_c} distribution based on the purely combinatorial side-band and extrapolate into our signal range. The Δm_{χ_c} and p_{T}^2 PDFs for the combinatorial background are shown in Fig. 6.2 and Fig. 6.4 with and without the HeRSChel cut, respectively. The fit parameters are detailed in Table 6.2.

We modeled $\psi(2S)$ feed-down by applying weights to CEP $\psi(2S)$ Monte Carlo to match the $\psi(2S)$ kinematics of CEP and the inelastic production mechanism, and to account for photon-conversion efficiency. The transverse-momentum of these photons tends to be softer and as a result have a lower effective-reconstruction efficiency, making this our smallest background. The final Δm_{χ_c} PDFs for the $\psi(2S)$ feed-down background are shown in Fig. 6.8 and p_{T}^2 shapes are extracted from the CEP J/ψ and $\psi(2S)$ LHCb paper [44]. We observe that ninety-six percent of these background events originate from $\psi(2S) \to \chi_c\gamma$ decays.

The inelastic χ_c background is not included in Table 6.8 as its yield and exact shape are determined concurrently with the CEP χ_c signal in a two-dimensional fit of the Δm_{χ_c} and p_{T}^2. By selecting events with three or more long tracks we were able to select a χ_c sample guaranteed to be inelastic. We were able to isolate the inelastic signal and extract crucial information from the fit including the yield ratio between χ_{c1} and χ_{c2}, as well as the $p_{\mathrm{T}}^2(\chi_c)$ shape for these events. Since the Δm_{χ_c} shapes of the inelastic and CEP χ_c signal are assumed to be identical, it is crucial to have a good model for the inelastic p_{T}^2 necessary to determine the contribution of the CEP signal and the inelastic background. The final Δm_{χ_c} and p_{T}^2 PDFs for the χ_c inelastic background are shown in Fig. 6.13 and Fig. 6.14. The values of the floated parameters are summarised in Table 6.7.

6.5 CEP χ_c fit model

A simultaneous unbinned maximum-likelihood fit is performed on the Δm_{χ_c} and p_{T}^2 spectrum of CEP $\chi_c \to J/\psi[\mu^+\mu^-]\gamma[e^+e^-]$ candidates on the $350 < \Delta m_{\chi_c} < 500\,\mathrm{MeV}/c^2$ and $p_{\mathrm{T}}^2(\chi_c) < 30\ [\mathrm{MeV}/c]^2$ range, for 2016-only, and combined 2015 and 2016 data. This fitting method allows us to determine the contribution of inelastic χ_c background events from our CEP signal. We fit the Δm_{χ_c} distribution with a model composed of seven components: the CEP χ_{c1} and χ_{c2} signal, a single inelastic χ_c shape accounting for both inelastic χ_{c1} and χ_{c2} background, J/ψ-combinatorial background, continuum-combinatorial background, as well as CEP and inelastic $\psi(2S)$ feed-down background. Of these shapes, only the CEP χ_c signal and the inelastic χ_c

Table 6.8. Summary of the number of expected background events in our CEP $\chi_c \to J/\psi\,[\mu^+\mu^-]\gamma[e^+e^-]$ selection sample between our Δm_{χ_c} selection window, 350 to 500 MeV/c^2, with and without the HeRSChel cut applied, $\ln(\chi^2_{\rm HRC}) < 5$. The values are presented for the 2016-only, and combined 2015 and 2016 data. This table does not include the important contribution from inelastic χ_c events, which is determined in the final fit to the signal sample.

Component	**No $\ln(\chi^2_{\rm HRC})$ Cut**		**With $\ln(\chi^2_{\rm HRC}) < 5$ Cut**	
	2016	**2015 + 2016**	**2016**	**2015 + 2016**
$\mu^+\mu^-$ combinatorial	0.68 ± 0.36	0.46 ± 0.39	0.51 ± 0.26	0.43 ± 0.26
J/ψ combinatorial	35.55 ± 5.85	44.97 ± 6.35	11.91 ± 4.51	13.25 ± 4.66
$\psi(2S)^{\rm CEP}_{\rm FD}$	5.97 ± 3.58	6.98 ± 5.93	5.08 ± 3.05	5.80 ± 4.92
$\psi(2S)^{\rm In.}_{\rm FD}$	2.76 ± 1.70	3.23 ± 2.81	1.86 ± 1.15	2.20 ± 1.92

background have free parameters and yields in the fit. All other background shapes and yields are fixed according to results detailed in previous sections of this chapter. Each of these Δm_{χ_c} shapes is accompanied by a $p_{\rm T}^2$ distribution that shares the same yield parameter. All $p_{\rm T}^2$ shapes are fixed according to data, Monte Carlo, or previous studies from the LHCb experiment. Table 6.9 provides a summary of all the fit components, their shapes, the parameters that are floated, and a brief description of how each shape is calculated and constrained. The fit is performed with and without a HeRSChel cut applied.

6.5.1 Invariant-mass-difference parameterisation

CEP χ_c fit model

The CEP χ_{c1} and χ_{c2} resonances are each fitted with a double-sided Crystal Ball [137]. To help constrain the fits to the CEP χ_c data, the values of the tail parameters are fixed ($\alpha_{\rm Left}$, $\alpha_{\rm Right}$, $n_{\rm Left}$, and $n_{\rm Right}$) to the values obtained from the CEP χ_c Monte Carlo fit results, shown in Fig. 6.12 and Table 6.6 where they were first presented as part of the inelastic χ_c background study in Sec. 6.3.4. In addition, the width of χ_{c1} and χ_{c2} are described by a single free parameter, $\sigma(\chi_{c2})$, whereby the width of χ_{c1} is fitted by taking $\sigma(\chi_{c2})$ times the ratio of the χ_{c1} to χ_{c2} width extracted from the Monte Carlo fit results. Similarly, the mean value of χ_{c1} is constrained relative to the mean of χ_{c2} by the difference of the nominal-mass value of χ_{c1} and χ_{c2} according to the PDG [86]. Finally, all yield values are floated and shared with the corresponding $p_{\rm T}^2(J/\psi\gamma)$ shape.

Inelastic χ_c fit model

The Δm_{χ_c} shapes for the CEP χ_{c1} signal and the inelastic χ_{c1} background are assumed to be identical. The same applies to χ_{c2}. That is, the tails are fixed to CEP χ_c Monte Carlo results and the resonances share the same floated width and mean parameters as their CEP counterparts. However, in the case of the inelastic χ_{c1} and χ_{c2} background, the two double-sided Crystal Balls are joined together into a single composite shape. This allows us to simplify the

Table 6.9. Summary of the simultaneous-fit strategy of the CEP χ_c sample. Yield values (Y) between corresponding Δm_{χ_c} and p_{T}^2 shapes are shared.

Fit Component	**Dist.**	**Fitted Shape**	**Floated Values**	**Model Description**
CEP χ_{c1}	Δm_{χ_c}	DCB	μ^*, σ^*, Y	- Fixed tails and constrained σ to CEP χ_{c1} MC fit results.
	p_{T}^2	Eq. 6.5	Y	- Fixed shape to CEP χ_{c1} MC fit results.
CEP χ_{c2}	Δm_{χ_c}	DCB	μ, σ, Y	- Fixed tails and constrained σ to CEP χ_{c2} MC fit results.
	p_{T}^2	Eq. 6.5	Y	- Fixed shape to CEP χ_{c2} MC fit results.
In. χ_c	Δm_{χ_c}	DCB	μ, σ, Y	- Shares shape parameters with CEP χ_c counterparts. χ_{c1}/χ_{c2} Y ratio fixed to $\geq$ 3Long Δm_{χ_c} fit results.
	p_{T}^2	Eq. 6.4	Y	- Shape fixed to $\geq$ 3Long p_{T}^2 fit results
$\psi(2S)_{FD}^{CEP}$	Δm_{χ_c}	KE	-	- Modelled from $\psi(2S) \to J/\psi X$ MC. Yield calculated with Eq. 6.3.
	p_{T}^2	Eq. 6.2	-	- Parameters fixed from LHCb CEP J/ψ and $\psi(2S)$ paper [44].
$\psi(2S)_{FD}^{In.}$	Δm_{χ_c}	KE	-	- Modelled from $\psi(2S) \to J/\psi X$ MC. Yield calculated with Eq. 6.3.
	p_{T}^2	Eq. 6.2	-	- Parameters fixed from LHCb CEP J/ψ and $\psi(2S)$ paper [44].
$\mu^+\mu^-$ Com.	Δm_{χ_c}	Horizontal line	-	- Yield calculated from fit to $m(J/\psi)$ in CEP χ_c sample.
	p_{T}^2	Eq. 6.1, 6.4	-	- Same p_{T}^2 shape used as in J/ψ combinatorial.
J/ψ Com.	Δm_{χ_c}	DCB	-	- Shape for Δm_{χ_c} and p_{T}^2 are fixed to fit result of mismatched J/ψ and γ from CEP χ_c sample.
	p_{T}^2	Eq. 6.1, 6.4	-	- Yield extrapolated from fit to χ_c $\Delta m_{\chi_c} > 500$ MeV/c^2 tail.

* Parameters floated relative to their corresponding parameter in the CEP χ_{c2} shape.

model of the inelastic p_{T}^2 contribution to a single shape and a single yield parameter shared between the mass and p_{T}^2 shapes, thereby improving the fit's stability.

These assumptions were studied and validated using our inelastic-control sample, $\geq$ 3Long and $\geq$ 3Long + HRC, as described in Sec. 6.3. The fit results of the control sample are shown in Fig. 6.13 (Fig. 6.14) before (after) the HeRSChel cut is applied. From these results, we see that the shapes extracted from the CEP χ_c Monte Carlo sample describe the distribution successfully. In addition, we extract the yield ratio of the two resonances, χ_{c1}/χ_{c2}, to constrain the χ_c yield ratio of our CEP χ_c fit. The yield ratios are summarised in Table 6.8.

$\psi(2S)$ feed-down fit model

Two fixed shapes are used to model the CEP and inelastic $\psi(2S)$ feed-down. Each PDF is composed of four contributions, one for each of the possible $J/\psi\gamma$ combinations from $\psi(2S) \to J/\psi\,[\mu^+\mu^-]X$ decays, where X stands for all possible particles in $\psi(2S)$ decays accompanied by an intermediate J/ψ meson. The shapes and their contributions, within our delta-mass window, are calculated in Sec. 6.2.3 using 2015 $\psi(2S) \to J/\psi\,[\mu^+\mu^-]X$ Monte Carlo together with results from the LHCb CEP $\psi(2S)$ paper [44] and the photon-conversion efficiency, described in Sec. 5.1. The shapes are extracted with KE fits, shown in Fig. 6.8. The contributions of this background are summarised in Table 6.3 and are fixed according to these results for the CEP χ_c fit.

Continuum-combinatorial fit model

The contribution from non-resonant continuum combinatorial is measured in Sec. 6.1.1 by fitting the invariant-mass distribution of the J/ψ mesons in our CEP χ_c selection within a 100 MeV/c^2 mass window centred about the nominal J/ψ mass value. The yields within our Δm_{χ_c} window, 350 to 500 MeV/c^2, are found to be very small. They are summarised in Table 6.3, and used to fix their contributions in the CEP χ_c fit. We assume the Δm_{χ_c} distribution of this small background to be uniformly distributed and model it with a horizontal line.

J/ψ-combinatorial fit model

The second class of combinatorial background is composed of true J/ψ mesons wrongly matched with a converted photon. This background is modelled with a data-driven method where J/ψ mesons from one event are matched with converted photons from another event and fitted with a double-sided Crystal Ball. The shape is then completely fixed according to the fit results of this artificial background, shown in Fig. 6.2. The parameters are summarised in Table 6.2.

The yield within our Δm_{χ_c} selection window is calculated by fitting the Δm_{χ_c} range of our CEP χ_c candidates above 500 MeV/c^2, a region dominated by combinatorial background, and extrapolating into our Δm_{χ_c} selection window. When performing the fit, we account for the small contribution from dimuon continuum. This process is detailed in Sec. 6.1.2. The yields for each data sample are summarised in Table 6.3.

6.5.2 $p_{\mathrm{T}}^2(\chi_c)$ parameterisation

CEP χ_c fit model

In a similar way to the Δm_{χ_c} model, the parameters of the CEP χ_c p_{T}^2 distribution are all fixed according to the results of a maximum-likelihood fit on fully reconstructed CEP χ_c Monte Carlo. The $p_{\mathrm{T}}^2(\chi_c)$ distribution for each of the χ_c mesons is different and deviates from a single exponential due to reconstruction efficiencies, differences in spin-structure of each $gg \to \chi_{c1,2}$ vertex, as well as effects of spin-survival factor: a measurement of how likely the proton is to survive the interaction. As a result, a flexible parametrization is needed to model the CEP $p_{\mathrm{T}}^2(\chi_c)$ component where all the parameters are floated:

$$\exp(a \cdot p_{\mathrm{T}}^2)\left(b + c \cdot p_{\mathrm{T}}^2 + d \cdot (p_{\mathrm{T}}^2)^2 + e \cdot (p_{\mathrm{T}}^2)^3\right). \tag{6.5}$$

The results of the fit are shown in Fig. 6.15 and the final value of the fit parameters are summarised in Table 6.10.

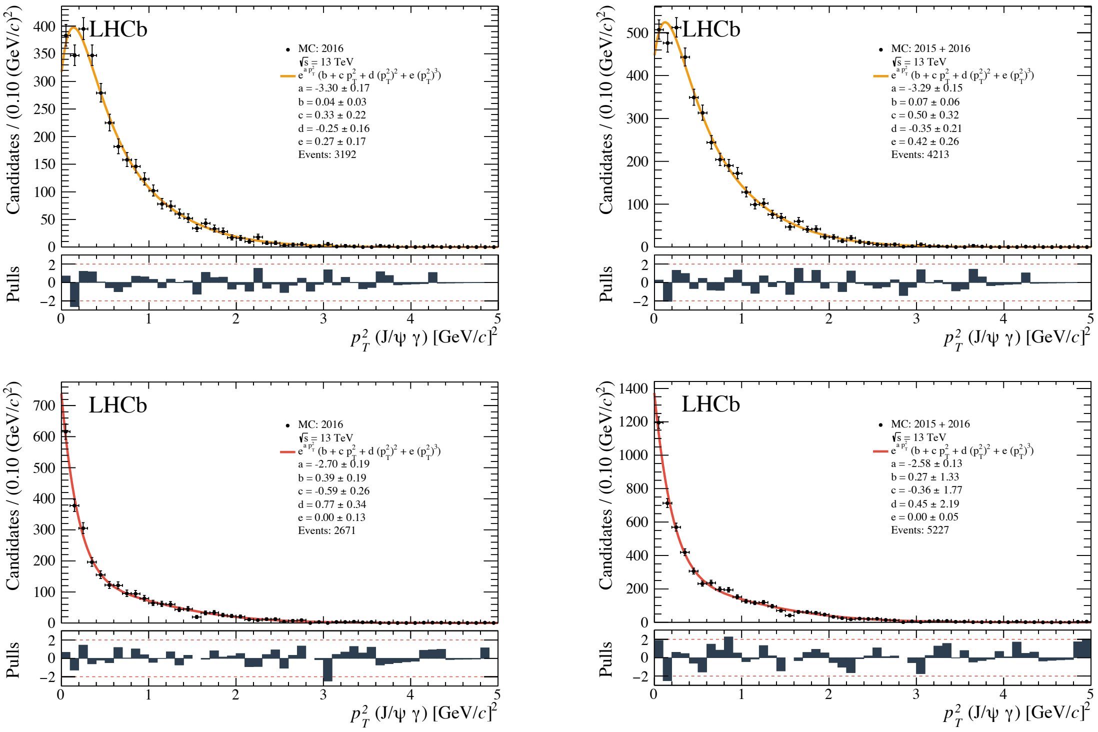

Figure 6.15. Fit of the p_{T}^2 distributions of CEP χ_{c1} (top) and χ_{c2} (bottom) Monte Carlo reconstructed with converted photons for the 2016-only (left), and combined 2015 and 2016 (right) run conditions for pp collisions at a centre-of-mass energy $\sqrt{s} = 13\,\mathrm{TeV}$ generated with SuperChic v2. The distributions are shown within the Δm_{χ_c} selection widow, 350 to 500 MeV/c^2. The distributions are fitted with Eq. 6.5. The lower panels show the pulls.

Table 6.10. Summary of the final parameter values pertaining to the fit parameters of the p_{T}^2 distributions of CEP χ_{c1} and χ_{c2} Monte Carlo reconstructed with converted photons for the 2016-only, and combined 2015 and 2016 data from pp collisions at a centre-of-mass energy $\sqrt{s} = 13\,\mathrm{TeV}$.

		χ_{c1}		χ_{c2}	
Parameter	**Units**	**2016**	**2015 + 2016**	**2016**	**2015 + 2016**
a	$[\mathrm{MeV}/c]^{-2}$	-3.30 ± 0.17	-3.29 ± 0.15	-2.70 ± 0.19	-2.58 ± 0.13
b	$[\mathrm{MeV}/c]^{-2}$	0.04 ± 0.03	0.07 ± 0.06	0.39 ± 0.19	0.27 ± 1.33
c	$[\mathrm{MeV}/c]^{-4}$	0.33 ± 0.22	0.50 ± 0.32	0.59 ± 0.26	-0.36 ± 1.77
d	$[\mathrm{MeV}/c]^{-6}$	-0.25 ± 0.16	-0.35 ± 0.21	0.77 ± 0.34	0.45 ± 2.19
e	$[\mathrm{MeV}/c]^{-8}$	0.27 ± 0.17	0.42 ± 0.26	0.0 ± 0.13	-0.00 ± 0.05

Inelastic χ_c fit model

As with the Δm_{χ_c} fit model, the $\geq$ 3Long and $\geq$ 3Long+HRC samples are used to determine the p_{T}^2 distribution for the inelastic χ_c mesons. The fit of the inelastic-control samples is detailed in Sec. 6.3. The combined $p_{\mathrm{T}}^2(J/\psi\gamma)$ for χ_{c1} and χ_{c2} contributions are fitted with a single shape composed of the sum of two(one) exponentials for the sample without(with) the HeRSChel cut applied. The fit results are shown in Sec. 6.3.4 and the fit parameters are detailed in Table 6.7.

The results are used to fix the shapes of the inelastic χ_c component in the CEP χ_c simultaneous fit while floating the yield shared with its Δm_{χ_c} counterpart.

$\psi(2S)$ feed-down-background fit model

The shapes associated with the $\psi(2S)$ feed-down are taken from observations detailed in a CEP study of J/ψ and $\psi(2S)$ mesons in pp collisions at $\sqrt{s} = 13\,\text{TeV}$ in the LHCb experiment [44] where inelastic and CEP $p_{\text{T}}^2(\psi(2S))$ is modelled with an exponential, Eq. 6.2. Their fit results for this study are reproduced in Fig. 6.7. The same shapes are used for all data samples, before and after the HeRSChel selection is applied. The yields are shared and fixed to the values described for the invariant-mass-difference counterpart.

Combinatorial-background fit model

As with the Δm_{χ_c} model, the p_{T}^2 combinatorial background has two contributions: continuum combinatorial and J/ψ combinatorial. As the minor continuum-combinatorial contribution is very small, we model all combinatorial background with the same p_{T}^2 distribution of the J/ψ combinatorial background described below, but keep their contributions separate.

The p_{T}^2 shape associated with combinatorial background is determined using the same data-driven study used to ascertain the Δm_{χ_c} distribution of this background, described in Sec. 6.1. The selection for the p_{T}^2 model is restricted to events that fall within the Δm_{χ_c} selection window, 350 to 500 MeV/c^2. In this case, the p_{T}^2 shape prior to the HeRSChel cut is well modelled by a single exponential, Eq. 6.1, with fit results shown in Fig. 6.4. However, once the HeRSChel cut is applied, a small contribution from a second exponential is required, Eq. 6.4. These fit results are shown in Fig. 6.4. Both fits are performed with all parameters floated. These parameters are then fixed and fitted to the CEP χ_c data where the yields are shared and fixed to the same value as the Δm_{χ_c} counterpart. The parameter values are summarised in Table 6.2.

Chapter 7

Results and assignment of systematic uncertainties

We present the simultaneous fit results of the Δm_{χ_c} and p_{T}^2 distributions of our CEP χ_c selection, with and without the HeRSCheL cut applied in Sec. 7.1. We then perform a validation study of the fit model in Sec. 7.2 to assess its stability. In addition, we present a series of studies that rely on these fit results. These studies include the calculation of a global photon-conversion efficiency for our selected CEP χ_{c1} and χ_{c2} candidates, as well as their yields corrected for this efficiency, described in Sec. 7.3. We also perform a stability study of the HeRSCheL cut in Sec. 7.4. A description of the luminosity determination for single-interaction crossings is presented in Sec. 7.5. We finish with the cross-section calculation of CEP χ_{c1} and χ_{c2} in Sec. 7.6 and the assignment of systematic uncertainties in Sec. 7.7.

7.1 CEP χ_c fit results

To fit the CEP χ_c sample, we combine the signal and background components described in Chapter 6 into a single composite probability-density function, with which we perform an unbinned simultaneous maximum-likelihood fit of the Δm_{χ_c} and p_{T}^2 distributions of the selected χ_c candidates. The fit results are shown in Fig. 7.1 and Fig. 7.2, respectively, before and after the HeRSCheL cut is applied, $\ln(\chi^2_{\mathrm{HRC}}) < 5$, for the 2016-only, and combined 2015 and 2016 data. The final values for the floated fit parameters and yields are shown in Table 7.1. We observe 0.00 ± 18.6 (0.00 ± 26.5) CEP χ_{c1} events, 176.69 ± 17.96 (229.71 ± 19.85) CEP χ_{c2} events, and 227.03 ± 19.22 (249.74 ± 20.23) inelastic χ_c events in the 2016-only (combined 2015 and 2016) data prior to the HeRSCheL cut. When the HeRSCheL cut is applied we observe 13.27 ± 6.84 (9.41 ± 7.24) CEP χ_{c1} events, 75.34 ± 10.84 (96.30 ± 12.32) CEP χ_{c2} events, and 19.71 ± 6.68 (24.47 ± 7.50) inelastic χ_c events.

The measured width of the χ_c mesons prior to the HeRSCheL cut is slightly larger than expected compared to the χ_c Monte Carlo fit, while the measured value with the HeRSCheL cut applied is in good agreement with the Monte Carlo fit. To check that this does not lead to significantly different results, we repeat the fit while fixing the χ_{c1} and χ_{c2} width to the value predicted by Monte Carlo. The χ_{c1} width is 1.94 ± 0.29 (1.98 ± 0.14) and that of χ_{c2} is 2.40 ± 0.21 (2.61 ± 0.14) MeV/c according to Monte Carlo for 2016-only (combined 2015 and 2016) data. We measure 1.44 ± 19.03 (2.89 ± 11.07) CEP χ_{c1} events, 169.34 ± 18.08 (220.75 ± 20.04) CEP χ_{c2} events, and 226.20 ± 19.89 (248.15 ± 20.85) inelastic χ_c events in the 2016-only (combined 2015 and 2016) data. Although fixing the widths of the resonant peaks leads to slightly different yields, they are consistent with the results presented above. This highlights the benefits of performing the study with the HeRSCheL sample which has a much smaller inelastic χ_c background.

In addition, as a systematic check, we repeat the fit of the sample with the HeRSCheL cut applied while fixing the yield ratio of the inelastic χ_{c1} and χ_{c2} components according to the ratio determined with the $\geq$ 3Long sample; a measurement which benefits from a larger sample size and smaller errors, as shown in Sec. 6.3.4. We measure 14.11 ± 6.89 (10.66 ± 7.25) CEP χ_{c1} events, 75.84 ± 10.98 (96.43 ± 12.34) CEP χ_{c2} events in the 2016-only (combined 2015 and 2016) data. Therefore, we assign a 6% (13%) systematic uncertainty to the fit with the HeRSCheL cut applied.

Table 7.1. Summary of fit parameter results for the simultaneous fit of the Δm_{χ_c} and p_{T}^2 of χ_c candidates in the 2016-only, and combined 2015 and 2016 data before and after the HeRSCheL cut, $\ln(\chi^2_{\mathrm{HRC}}) < 5$, is applied.

Parameter	**Units**	$\ln(\chi^2_{\mathrm{HRC}})$	χ_{c1}		χ_{c2}	
			2016	**2015 + 2016**	**2016**	**2015 + 2016**
Gaussian mean	MeV/c^2	-	-	-	458.26 ± 0.66	457.59 ± 0.59
		< 5	-	-	458.19 ± 0.80	457.70 ± 0.95
Gaussian width	MeV/c^2	-	-	-	4.40 ± 0.59	4.76 ± 0.58
		< 5	-	-	2.74 ± 0.31	3.66 ± 0.80
$N_{\mathrm{CEP}}(\chi_c)$	-	-	0.00 ± 18.6	0.00 ± 26.5	176.69 ± 17.96	229.71 ± 19.85
		< 5	13.27 ± 6.84	9.41 ± 7.24	75.34 ± 10.84	96.30 ± 12.32
Parameter	**Units**	$\ln(\chi^2_{\mathrm{HRC}})$	**2016**		**2015 + 2016**	
$N_{\mathrm{In.}}(\chi_c)$	-	-	227.03 ± 19.22		249.74 ± 20.23	
		< 5	19.71 ± 6.68		24.47 ± 7.50	

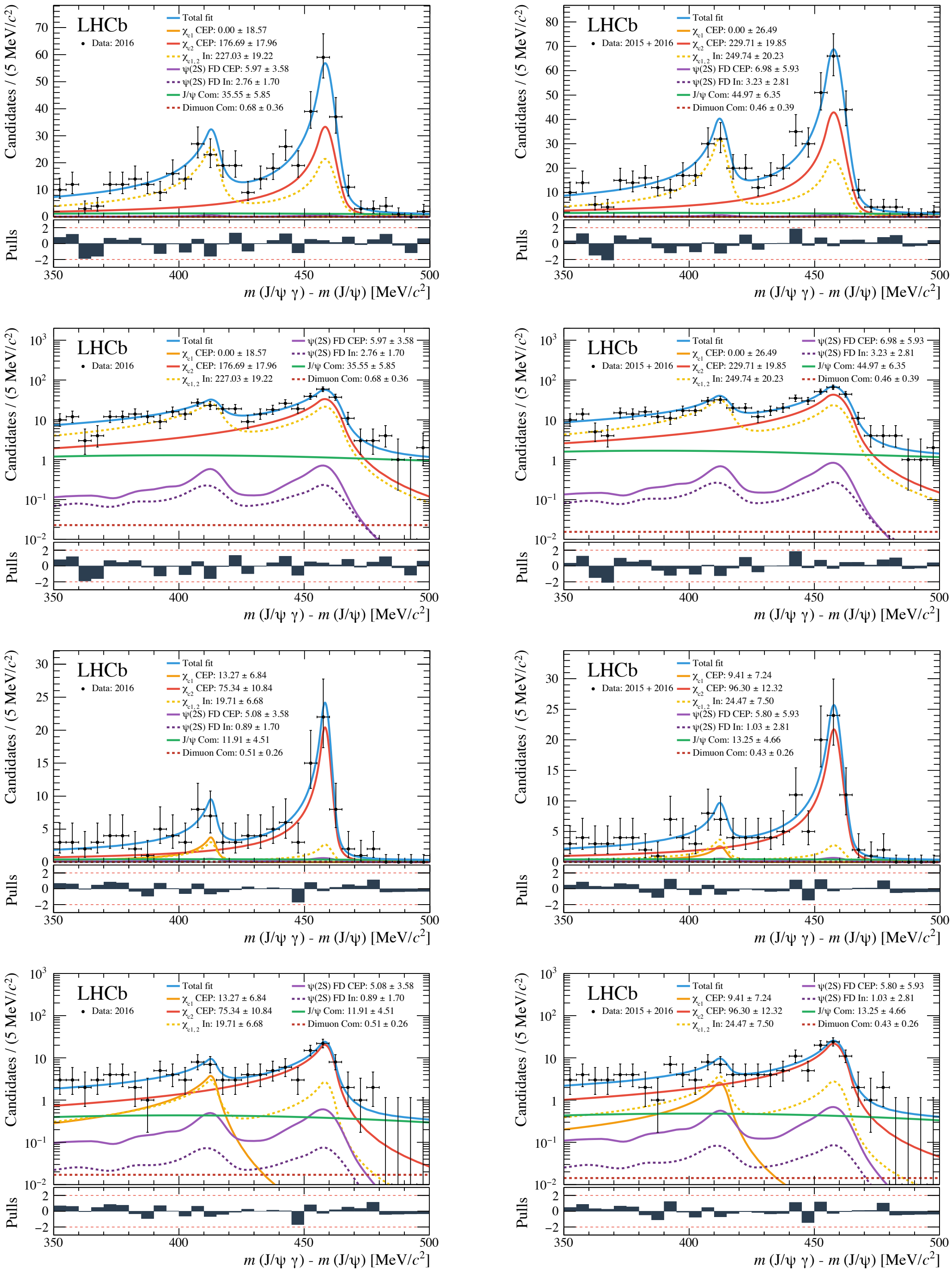

Figure 7.1. Delta-mass component of two-dimensional fit of the invariant mass of χ_{c1} and χ_{c2} candidates for the 2016-only (left), and combined 2015 and 2016 (right) data before (first and second row) and after (third and fourth row) the HeRSChel cut, $\ln(\chi^2_{\text{HRC}}) < 5$, is applied. The distributions are shown in linear (first and third row) and logarithmic (second and fourth row) scale. The overall fit is shown in solid blue, the CEP χ_{c1} component in solid orange, the CEP χ_{c2} component in solid red, the inelastic χ_c sample in dashed yellow, the continuum-combinatorial background in dashed-dark red, the J/ψ combinatorial background in green, the CEP $\psi(2S)$ feed-down in solid purple, and the inelastic $\psi(2S)$ feed-down in dashed purple. The lower panels show the pulls distributions.

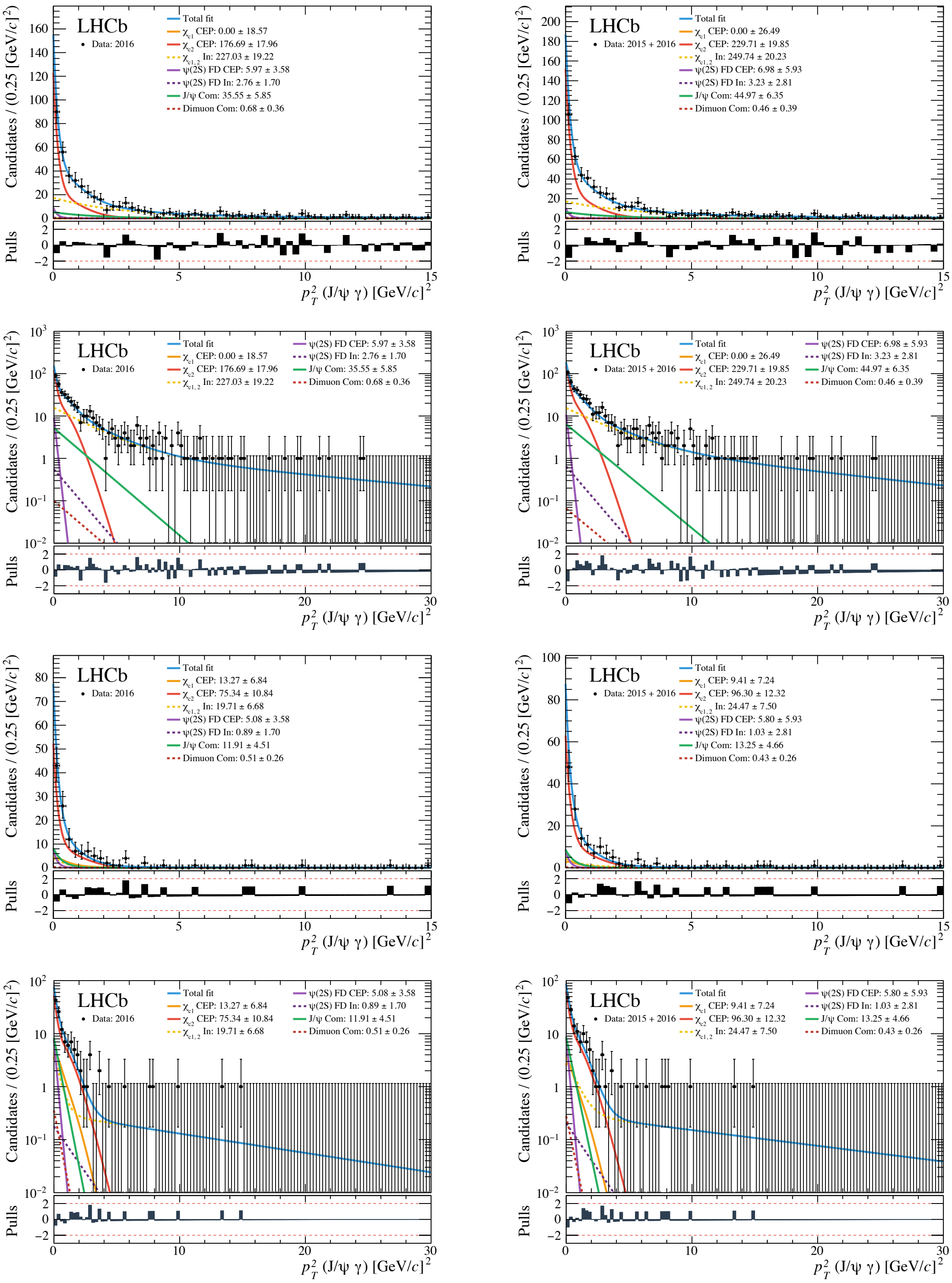

Figure 7.2. Transverse-momentum-squared component of two-dimensional fit of the invariant mass of χ_{c1} and χ_{c2} candidates for the 2016-only (left), and combined 2015 and 2016 (right) data before (first and second row) and after (third and fourth row) the HeRSChel cut, $\ln(\chi^2_{\rm HRC}) < 5$, is applied. The distributions are shown in linear (first and third row) and logarithmic (second and fourth row) scale. The overall fit is shown in solid blue, the CEP χ_{c1} component in solid orange, the CEP χ_{c2} component in solid red, the inelastic χ_c sample in dashed yellow, the continuum-combinatorial background in dashed-dark red, the J/ψ combinatorial background in green, the CEP $\psi(2S)$ feed-down in solid purple, and the inelastic $\psi(2S)$ feed-down in dashed purple. Note that the x-range is different between the linear and logarithmic plots. The lower panels show the pulls distributions.

7.2 CEP χ_c fit-validation study

The fit is validated to make sure it is well-behaved and returns unbiased results. This is done by taking the fit results obtained from the data, and generating pseudo-experiments with the fitted PDF to match the data-set sizes of the CEP χ_c selection. We generate ten thousand *toy-data* sets for each of the four samples: the 2016-only, and combined 2015 and 2016 samples with and without the HeRSCheL cut applied. The toy-data sets are then fitted with the same model originally used for the CEP χ_c sample. However, because the mean value of the χ_{c1} yield is close to zero the χ_{c1} yield is allowed to take negative values in order to prevent the fit from reaching the limit of the floating range. In all cases, the fits complete successfully with a small percentage of cases ($\sim 1\%$) where the covariant matrix is forced to be positive definite.

The pull distributions for the toy studies are shown in Fig. 7.3 (Fig. 7.4) before (after) the HeRSCheL cut is applied and the pulls' mean and width values are summarised in Table 7.2. For the most important parameters, which are the yields of the CEP χ_{c1} and χ_{c2} contributions, we see satisfactory results with indications of small biases at the $\sim 5\%$ level and error underestimation. We assign this as a systematic uncertainty to the CEP χ_{c1} and χ_{c2} yield. We also see that the pulls for the χ_{c2} mean and width parameters have widths $\sim 20\%$ bigger than one both with and without the HeRSCheL cut. After the HeRSCheL is applied the width and inelastic χ_c yield develops a bias of 0.24 ± 0.01 (0.19 ± 0.01) and 0.17 ± 0.01 (0.18 ± 0.01), respectively, for the 2016-only (combined 2015 and 2016) data. Other parameters have a bias of up to nine percent.

In addition, given that the fit of the CEP χ_c sample without the HeRSCheL cut applied yields zero CEP χ_{c1} mesons, we further check the validity of the fit model and its ability to extract the CEP signal by repeating the procedure detailed above for this data sample. However, this time we artificially inflate the CEP χ_{c1} sample by a known amount and check that the fit is capable of retrieving the number of injected CEP χ_{c1} events. We inject 13.27 (9.41) CEP χ_{c1} events in order to match the number of events observed in the fit results of the sample with the HeRSCheL cut applied for the 2016-only (combined 2015 and 2016) data. As before, we generate ten thousand toy-data sets and fit them using the same model. The CEP χ_{c1} yields of the fits are shown in Fig. 7.5 (top row). We observe a mean CEP χ_{c1} yield of 11.48 ± 0.12 (12.77 ± 0.12) with 17% (15%) of the pseudo experiments yielding less than zero CEP χ_{c1} events. We repeat the process two more times with larger signals: once with fifty CEP χ_{c1} events injected, shown in Fig. 7.5 (middle row) and once more with one-hundred injected events, shown in Fig. 7.5 (bottom row). We observe a mean yield of 52.34 ± 0.14 (55.76 ± 0.14) and 102.47 ± 0.15 (99.33 ± 0.15), respectively for the 2016-only (combined 2015 and 2016) data, with zero pseudo experiments with CEP χ_{c1} yield lower than zero. Therefore, we have shown that the fit model is well-behaved and capable of successfully extracting the CEP signal. However, when the signal is small it is not uncommon for the fit, in the presence of a large background, to yield values near zero. This highlights the importance of the reduction of the inelastic background through the use of HeRSCheL.

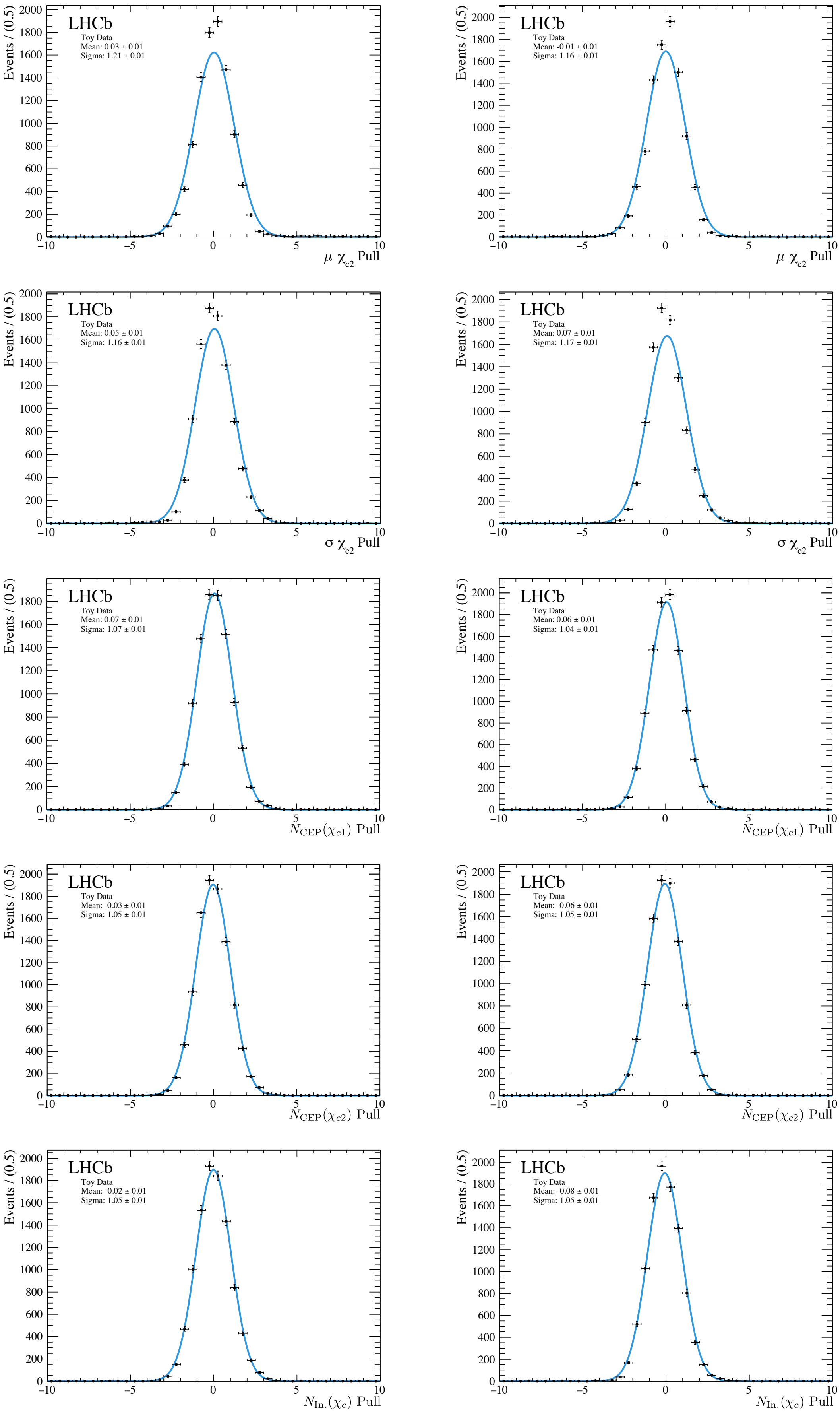

Figure 7.3. Pulls from toy studies for the 2016-only (left), and combined 2015 and 2016 (right) data before the HeRSCheL cut is applied.

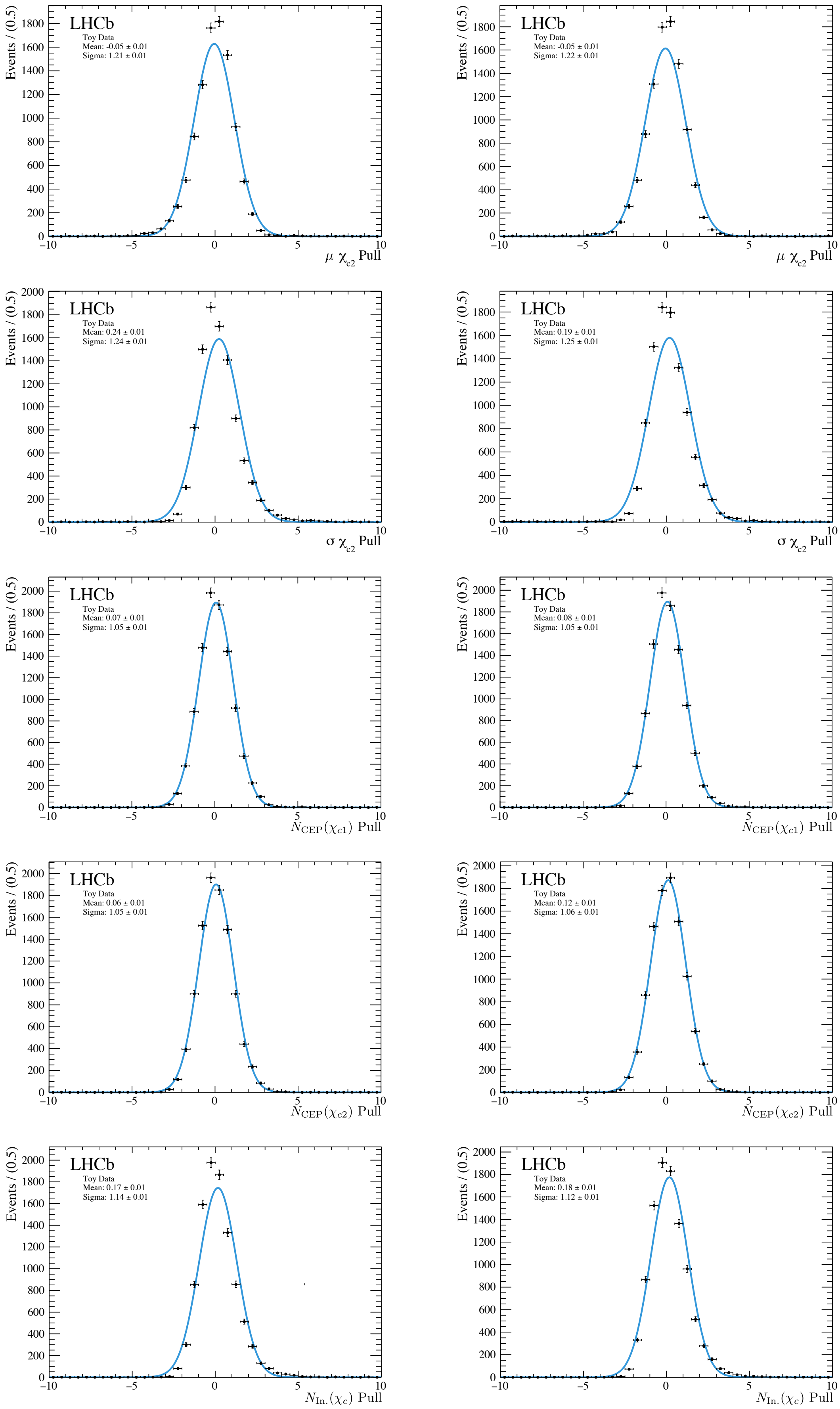

Figure 7.4. Pulls from toy studies for the 2016-only(left), and combined 2015 and 2016 (right) data after the HeRSChel cut is applied.

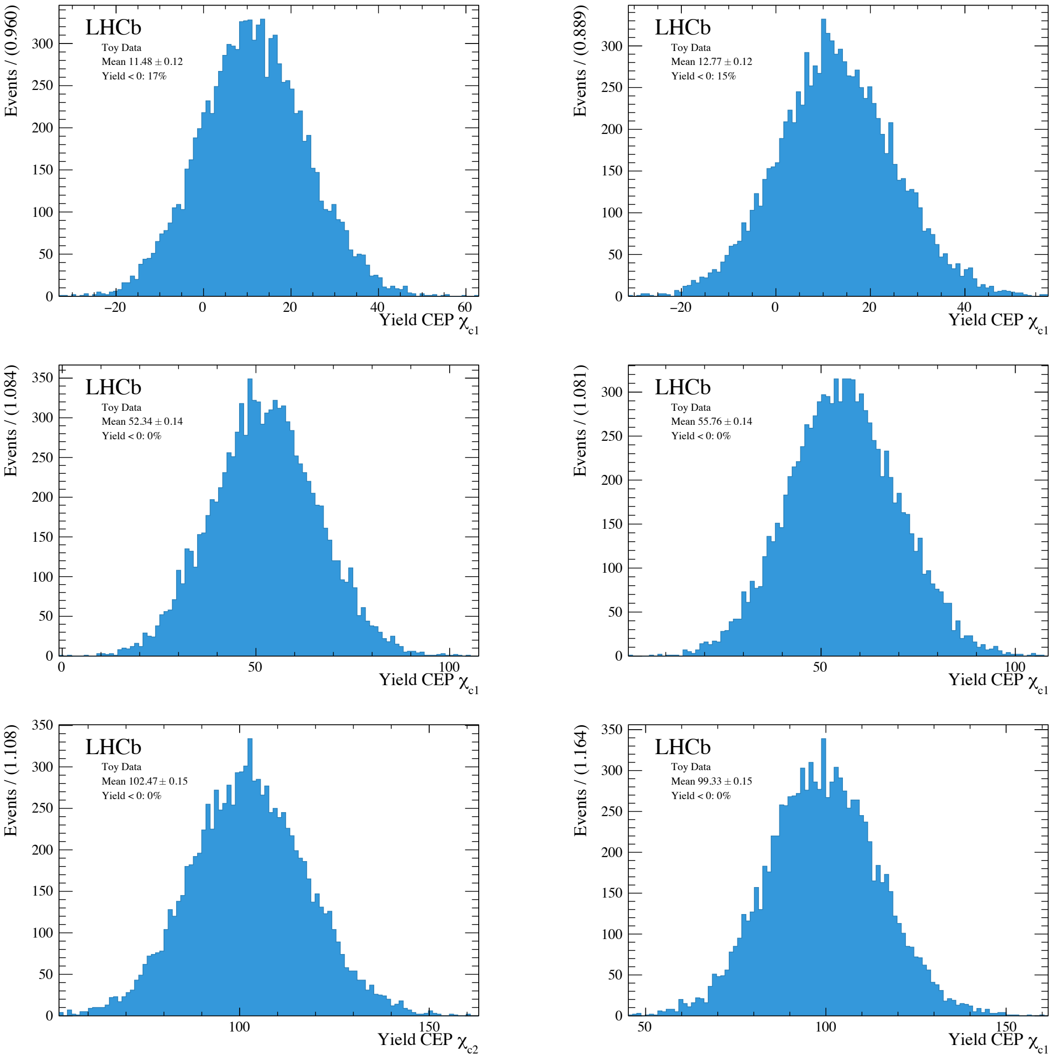

Figure 7.5. CEP χ_{c1} yields of toy studies for the 2016-only (left), and combined 2015 and 2016 (right) data without the HeRSCheL cut is applied. The toy data distributions have been injected with 13.27 and 9.41 CEP χ_{c1} events for the 2016-only and combined 2015 and 2016 data (top row), as well as 50 (middle row) and 100 (bottom row) CEP χ_{c1} events.

Table 7.2. Summary of pull results from toy studies used to validate the fit to the CEP χ_c sample.

Parameter	**Units**	$\mathbf{ln(\chi^2_{HRC})}$	**Mean**		**Width**	
			2016	**2015 + 2016**	**2016**	**2015 + 2016**
μ (χ_{c2})	MeV/c^2	-	0.03 ± 0.01	-0.01 ± 0.01	1.21 ± 0.01	1.16 ± 0.01
		< 5	-0.05 ± 0.01	-0.05 ± 0.01	1.21 ± 0.01	1.22 ± 0.01
σ (χ_{c2})	MeV/c^2	-	0.05 ± 0.01	0.07 ± 0.01	1.16 ± 0.01	1.17 ± 0.01
		< 5	0.24 ± 0.01	0.19 ± 0.01	1.24 ± 0.01	1.25 ± 0.01
$N_{\text{CEP}}(\chi_{c1})$	-	-	0.07 ± 0.01	0.06 ± 0.01	1.07 ± 0.01	1.04 ± 0.01
		< 5	0.07 ± 0.01	0.08 ± 0.01	1.05 ± 0.01	1.05 ± 0.01
$N_{\text{CEP}}(\chi_{c2})$	-	-	-0.03 ± 0.01	-0.06 ± 0.01	1.05 ± 0.01	1.05 ± 0.01
		< 5	0.06 ± 0.01	0.12 ± 0.01	1.05 ± 0.01	1.06 ± 0.01
$N_{\text{In.}}(\chi_c)$	-	-	-0.02 ± 0.01	-0.08 ± 0.01	1.05 ± 0.01	1.05 ± 0.01
		< 5	0.18 ± 0.01	0.18 ± 0.01	1.14 ± 0.01	1.12 ± 0.01

7.3 Applying the photon-conversion-efficiency correction to the fit results

To apply the photon-conversion-efficiency correction to the χ_c data-fit results we calculate a global photon-conversion efficiency for χ_{c1}, $\varepsilon_{\gamma\to e^+e^-}^{\text{Global}(\chi_{c1})}$, and χ_{c2}, $\varepsilon_{\gamma\to e^+e^-}^{\text{Global}(\chi_{c2})}$, that also accounts for the multiplicity correction factor described in Sec. 5.1.6. The correction that is applied must be appropriate for the photon transverse-momentum distribution of the signal in our sample. We do this by studying the impact of the efficiency function determined from data on the CEP χ_c Monte Carlo described in Sec. 4.1. We apply the selection criteria previously referred to as the reconstructed J/ψ selection, where we reconstruct all the J/ψ mesons while saving the generator-level information of the accompanying photon from the $\chi_c \to J/\psi\gamma$ decay. The sample is truth matched and the selection criteria related to the J/ψ meson used in the CEP χ_c analysis are applied, while omitting the selection criteria related to the photon. The reader is reminded that the p_T^2 function used to fit the data derives from a fit to this same χ_c Monte Carlo sample (see Table 6.5.2).

We apply resolution effects to the generator-level kinematics of the photon using the method described in Sec. 6.2.1. With the resolution effects applied, we are able to calculate the Δm_{χ_c} distribution of the $J/\psi\gamma$ system and apply our selection window. The events that pass this selection are the denominator for our global-efficiency calculation. A total of 702451 ± 838 (1390068 ± 1179) χ_{c1} and 678856 ± 823 (1390717 ± 1179) χ_{c2} events pass our selection criteria for the 2016-only (combined 2015 and 2016) Monte Carlo.

To calculate the numerator we apply the weights for the photon-conversion efficiency as given by the data-driven study, shown in Fig. 5.13, according to the generator-level transverse momentum of the photon. We finally apply an additional factor of two to account for the low-multiplicity improvement in the reconstruction efficiency, as shown in the Sec. 5.1.6 study. After the weights are applied we find 1581 (3129) χ_{c1} and 2100 (4305) χ_{c2} events for 2016-only (combined 2015 and 2016) Monte Carlo. This corresponds to a global-photon-conversion efficiency of 0.2250% (0.2251%) for χ_{c1} mesons, and 0.3094% (0.3096%) for χ_{c2} mesons for 2016-only (combined 2015 and 2016) data. The statistical uncertainties on these values are negligible. Due to its larger mass, the photons from χ_{c2} decays have a larger phase space. On average, this results in photons with a larger transverse momentum and therefore a larger global-photon-conversion efficiency.

7.4 HeRSCheL stability check

We measure 13.27 ± 6.84 (9.41 ± 7.24) χ_{c1} mesons and 75.34 ± 10.84 (96.3 ± 12.32) χ_{c2} mesons using our simultaneous-fit method with a HeRSCheL cut of $\ln(\chi^2_{\text{HRC}}) < 5$ applied to 2016-only (combined 2015 and 2016) data. When corrected for the HeRSCheL efficiency, using the results from the study presented in Sec. 5.6, this corresponds to 15.59 ± 8.04 (11.34 ± 8.72) χ_{c1} mesons and 88.53 ± 12.77 (116.04 ± 14.88) χ_{c2} mesons, or a combined signal of 104.12 ± 15.10 (127.38 ± 17.25) CEP χ_c mesons. These numbers may be compared to the results obtained with no HeRSCheL cut, which are 0 ± 18.57 (0 ± 26.49) χ_{c1} mesons and 176.69 ± 17.96 (229.71 ± 19.85) χ_{c2} mesons, or 176.7 ± 25.8 (229.7 ± 33.1) CEP χ_c mesons in total. There is a difference of 72.6 ± 29.9 (102.3 ± 37.3) in the determined number of χ_c decays between the two measurements, which are different from zero with a significance of 2.4 (2.7) standard deviations.

The instability in results suggests some systematic bias in one or both of the measurements. A priori we expect the results obtained with the HeRSCheL cut to be more reliable because of the lower level of inelastic background. A plausible hypothesis is that the understanding of the inelastic background behaviour is imperfect, and this leads to biases in the separation between background and signal estimations in the simultaneous fit. This effect would be most marked in the measurement without the HeRSCheL cut, where the estimated proportion of inelastic background is $(51 \pm 6)\%$ ($(47 \pm 5)\%$), in contrast with $(16 \pm 5)\%$ ($(16 \pm 5)\%$) in the measurement that benefits from the HeRSCheL cut. The observed difference between the two results can be explained if $(32 \pm 13)\%$ ($(41 \pm 15)\%$) of inelastic background in the no-HeRSCheL case is wrongly attributed as signal by the fit. Such a misassignment would have a much smaller effect in the sample after the HeRSCheL cut, resulting in a migration of 6.3 ± 4.5 (10.0 ± 4.8) background candidates from the background to the signal sample for the 2016-only (combined 2015 and 2016) data.

To test this hypothesis, we repeat the measurement with a HeRSCheL cut applied at different working points and monitor the consistency of the results. We place tighter requirements on HeRSCheL to increase signal purity of $\ln(\chi^2_{\text{HRC}}) < 4$ and $\ln(\chi^2_{\text{HRC}}) < 3$. With the background recalculated, we repeat the simultaneous fits of the Δm_{χ_c} and p_{T}^2, the results of which are shown in Fig. 7.6 and Fig. 7.7, for $\ln(\chi^2_{\text{HRC}}) < 4$ and $\ln(\chi^2_{\text{HRC}}) < 3$, respectively. The combined yield of CEP χ_{c1} and χ_{c2} mesons is summarised in Table 7.3 for $\ln(\chi^2_{\text{HRC}}) < 5, 4,$ and 3, before and after being corrected for the HeRSCheL efficiency, as well as fit results with no HeRSCheL cut. The corrected yields are consistent among the different HeRSCheL working points, suggesting that the understanding of the signal efficiency is reliable, and that any imperfections in the understanding of the residual inelastic background has a small impact once HeRSCheL is applied. Noting this, and the initial change in results when moving from the no-HeRSCheL case, we assign a systematic uncertainty of ±40% to the measurement of the inelastic χ_c mesons for both the 2016-only data, and the combined 2015 and 2016 data. In the case of the χ_c sample with the $\ln(\chi^2_{\text{HRC}}) < 5$ this corresponds to a systematic uncertainty of 40% (74%) for χ_{c1} yields in the 2016-only (combined 2015 and 2016) data. The effect of this systematic is reduced significantly for the calculation of the χ_{c2} yields due to the greater CEP purity in this region, as explained above, which has a systematic uncertainty of 3.4% (2.9%) for 2016-only (combined 2015 and 2016) data. In addition, we take the largest differences between the corrected χ_c yields using our nominal HeRSCheL cut, $\ln(\chi^2_{\text{HRC}}) < 4$, and the systematic studies using $\ln(\chi^2_{\text{HRC}}) < 4$ and $\ln(\chi^2_{\text{HRC}}) < 3$ as the systematic uncertainty associated with our HeRSCheL cut, which corresponds to a 5% (6%) uncertainty for 2016-only (combined 2015 and 2016) data.

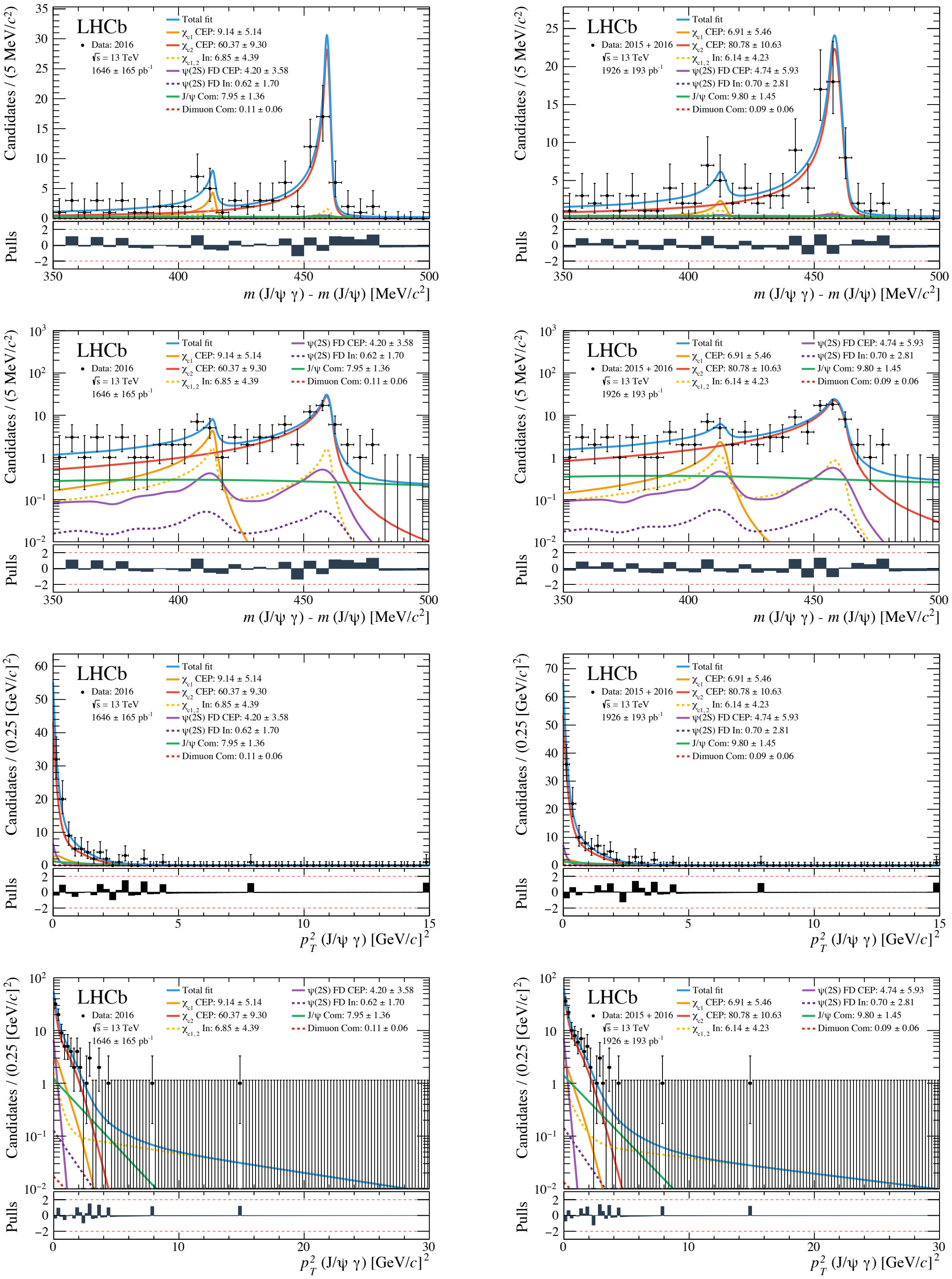

Figure 7.6. Two-dimensional fit of the Δm_{χ_c} (first and second row) and p_{T}^2 (squared) distribution of CEP χ_{c1} and χ_{c2} candidates for the 2016-only (left), and combined 2015 and 2016 (right) data, after the HeRSCheL cut, $\ln(\chi^2_{\mathrm{HRC}}) < 4$, is applied. The distributions are shown in linear (first and third row) and logarithmic (second and fourth row) scale. The overall fit is shown in solid blue, the CEP χ_{c1} component in solid orange, the CEP χ_{c2} component in solid red, the inelastic χ_c sample in yellow, the continuum-combinatorial background in broken-dark red, the J/ψ combinatorial background in green, the CEP $\psi(2S)$ in solid purple, and the inelastic $\psi(2S)$ in broken purple. The lower panels show the pulls.

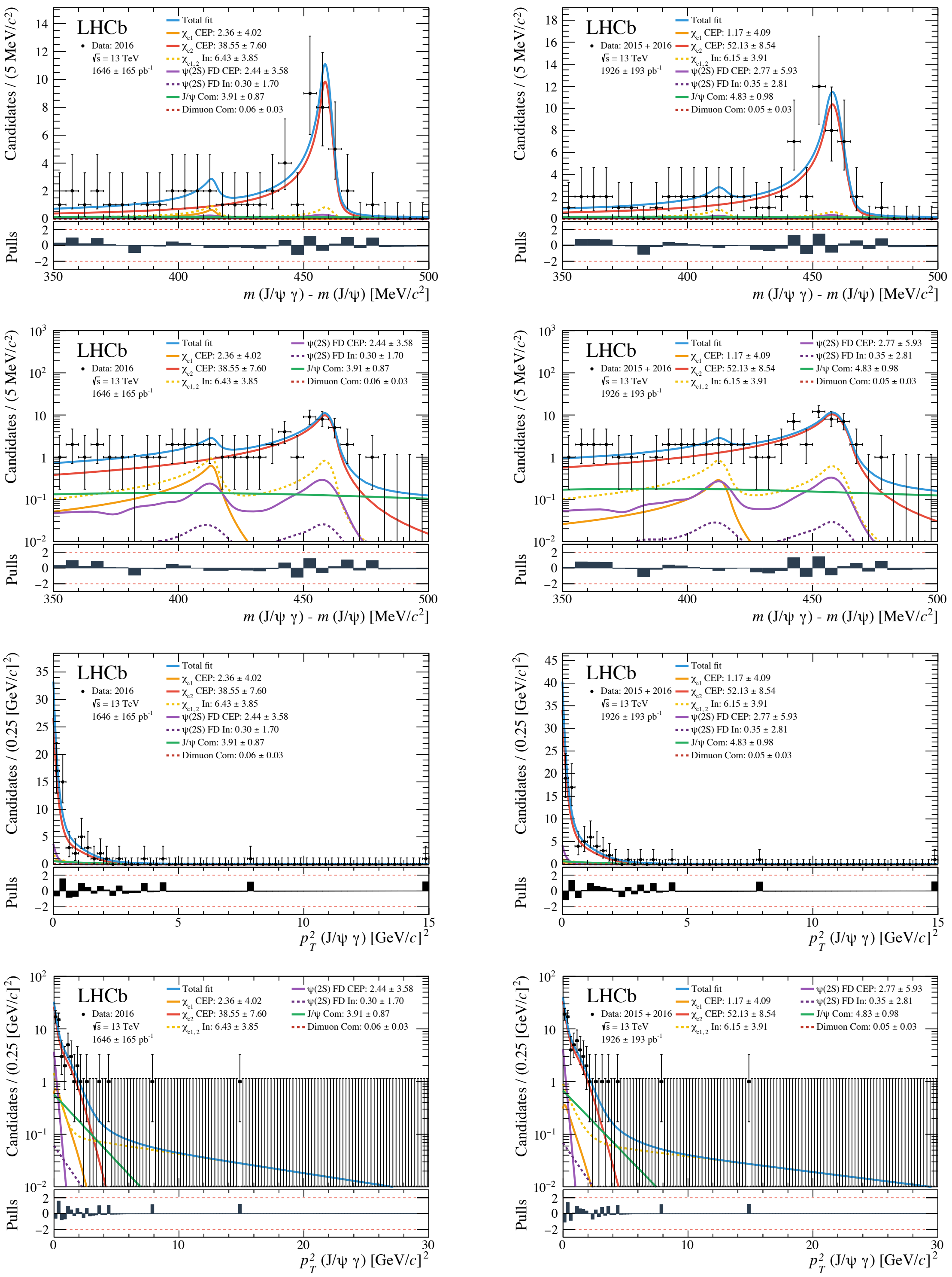

Figure 7.7. Two-dimensional fit of the Δm_{χ_c} (first and second row) and p_{T}^2 (squared) distribution of CEP χ_{c1} and χ_{c2} candidates for the 2016-only (left), and combined 2015 and 2016 (right) data, after the HeRSChel cut, $\ln(\chi^2_{\mathrm{HRC}}) < 3$, is applied. The distributions are shown in linear (first and third row) and logarithmic (second and fourth row) scale. The overall fit is shown in solid blue, the CEP χ_{c1} component in solid orange, the CEP χ_{c2} component in solid red, the inelastic χ_c sample in yellow, the continuum-combinatorial background in broken-dark red, the J/ψ combinatorial background in green, the CEP $\psi(2S)$ in solid purple, and the inelastic $\psi(2S)$ in broken purple. The lower panels show the pulls distributions.

Table 7.3. Combined CEP χ_{c1} and χ_{c2} yields before and after HeRSCheL cut correction.

Year	$\ln(\chi^2_{\mathrm{HRC}})$	**Eff. [%]**	$N_{\mathrm{CEP}}(\chi_c)$	**Corrected** $N_{\mathrm{CEP}}(\chi_c)$
2016	No Cut	100	176.69 ± 25.83	176.69 ± 25.83
	< 5	85.1 ± 0.8	88.6 ± 13	104.1 ± 15.1
	< 4	70.3 ± 0.7	69.5 ± 13	98.9 ± 15.2
	< 3	40.8 ± 0.5	40.9 ± 13	100.2 ± 21.1
$2015 + 2016$	No Cut	100	229.7 ± 33.1	229.7 ± 33.1
	< 5	83.0 ± 0.8	105.7 ± 13	127.4 ± 17.3
	< 4	67.9 ± 0.7	87.7 ± 13	129.2 ± 17.7
	< 3	39.6 ± 0.5	53.3 ± 13	134.5 ± 23.9

7.5 Luminosity determination

To calculate the total integrated luminosity, $\mathcal{L}_{\mathrm{Total}}$, for each sample we sum over the integrated luminosity of all processed runs such that,

$$\mathcal{L}_{\mathrm{Total}} = \sum_{\mathrm{run}} \mathcal{L}^{\mathrm{run}}. \tag{7.1}$$

The integrated luminosity is taken from the latest calibration which has an uncertainty of 2% [142]. For a small number of runs, less than one percent of the total, the new calibration is not available and we use an older calculation of the integrated luminosity. We validate the assigned integrated luminosity for these additional runs by checking that the number of CEP-like J/ψ events is as expected when compared to the well calibrated bulk of the data. The total-integrated luminosity for 2015 is $284 \pm 6\,\mathrm{pb}^{-1}$ and $1637 \pm 33\,\mathrm{pb}^{-1}$ for 2016. This results in a total-integrated luminosity of $1921 \pm 38\,\mathrm{pb}^{-1}$ for the combined 2015 and 2016 data.

However, since we are interested in CEP events that appear in isolation, we have to calculate the fraction of events that have a single interaction per beam-crossing, $\epsilon_{\mathrm{Single}}$. The average number of interactions per beam-crossing, μ, is calculated on a run-by-run basis and stored in the run database. Assuming proton-proton interactions during beam crossings follow Poisson statistics, we can calculate $\epsilon_{\mathrm{Single}}$ per run such that,

$$\epsilon_{\mathrm{Single}} = \mu e^{-\mu}. \tag{7.2}$$

As a result, the single interaction total integrated luminosity is given by,

$$\mathcal{L}^{\mathrm{Total}}_{\mathrm{Single}} = \sum_{\mathrm{run}} \epsilon^{\mathrm{run}}_{\mathrm{Single}} \mathcal{L}^{\mathrm{run}}. \tag{7.3}$$

The total-integrated luminosity for single-interaction events is $105 \pm 2\,\mathrm{pb}^{-1}$ and $606 \pm 12\,\mathrm{pb}^{-1}$ for the 2015 and 2016 runs, respectively. Summing up to $711 \pm 14\,\mathrm{pb}^{-1}$ for the combined 2015 and

2016 data. This implies an average value of $\langle\mu\rangle = 1.099$ (1.1007) and $\langle\epsilon_{\mathrm{Single}}\rangle = 0.3662$ (0.3661) for 2015 (2016).

7.6 Cross-section calculation

The product of the integrated cross-section and the branching fraction for CEP $\chi_{cn} \to J/\psi\,[\mu^+\mu^-]\gamma$ production with muons in the pseudorapidity region $2 < \eta_{\mu^+\mu^-} < 4.5$ is given by

$$\sigma^{(2<\eta_{\mu^+\mu^-}<4.5)}_{\chi_{cn}\to J/\psi\,[\mu^+\mu^-]\gamma} = \frac{N_{\mathrm{CEP}}(\chi_{cn})}{\mathcal{L}^{\mathrm{Total}}_{\mathrm{Single}} \cdot \varepsilon_{\mathrm{HRC}} \cdot \varepsilon^{\mathrm{Global}(\chi_{cn})}_{\gamma\to e^+e^-} \cdot \varepsilon^{\mathrm{Global}}_{\mu\mu} \cdot \varepsilon_{m(J/\psi)} \cdot \varepsilon_{\Delta m(\chi_{cn})} \cdot \varepsilon_{\mathrm{SPD}}}, \tag{7.4}$$

where $n = 1, 2$ corresponding to χ_{c1} and χ_{c2} mesons respectively. The CEP χ_c yields, $N_{\mathrm{CEP}}(\chi_{cn})$, are calculated in Sec. 7.1 and the determination of the integrated luminosity for single-interaction crossings, $\mathcal{L}^{\mathrm{Total}}_{\mathrm{Single}}$, is detailed above in Sec. 7.5. The efficiency associated with the HeRSCheL figure-of-merit cut, $\varepsilon_{\mathrm{HRC}}$, is described in Sec. 5.6.3 and Sec. 7.4; the photon-conversion efficiencies, $\varepsilon^{\mathrm{Global}(\chi_{c1})}_{\gamma\to e^+e^-}$ and $\varepsilon^{\mathrm{Global}(\chi_{c2})}_{\gamma\to e^+e^-}$, are presented in Sec. 5.1 and Sec. 7.3. The muon reconstruction efficiency, $\varepsilon^{\mathrm{Global}}_{\mu\mu}$, is presented in Sec. 5.2. The efficiency associated with the J/ψ mass window, $\varepsilon_{m(J/\psi)}$, is discussed in Sec. 5.3; the efficiency associated with the χ_c delta-mass cut, $\varepsilon_{\Delta m(\chi_{cn})}$, is described in Sec. 5.4, and the efficiency associated with the SPD requirements at hardware-trigger level, $\varepsilon_{\mathrm{SPD}}$, is discussed in Sec. 5.5. The total efficiency, $\varepsilon_{\mathrm{Total}}(\chi_{cn})$, is given by the product of all efficiencies such that,

$$\varepsilon_{\mathrm{Total}}(\chi_{cn}) = \varepsilon_{\mathrm{HRC}} \cdot \varepsilon^{\mathrm{Global}(\chi_{cn})}_{\gamma\to e^+e^-} \cdot \varepsilon^{\mathrm{Global}}_{\mu\mu} \cdot \varepsilon_{m(J/\psi)} \cdot \varepsilon_{\Delta m(\chi_{cn})} \cdot \varepsilon_{\mathrm{SPD}}. \tag{7.5}$$

The values of these parameters are summarised in Table 7.4 for both 2016 data, and the combined 2015 and 2016 data. This leads to the product of the integrated cross-section and the branching fraction results of

$$\sigma^{(2<\eta_{\mu^+\mu^-}<4.5)}_{\chi_{c1}\to J/\psi\,[\mu^+\mu^-]\gamma} = 21.5 \pm 11.1 \pm 10.3\,\mathrm{pb} \tag{7.6}$$

$$\sigma^{(2<\eta_{\mu^+\mu^-}<4.5)}_{\chi_{c2}\to J/\psi\,[\mu^+\mu^-]\gamma} = 83.1 \pm 12.0 \pm 21.4\,\mathrm{pb} \tag{7.7}$$

for 2016-only data, and

$$\sigma^{(2<\eta_{\mu^+\mu^-}<4.5)}_{\chi_{c1}\to J/\psi\,[\mu^+\mu^-]\gamma} = 13.9 \pm 10.7 \pm 11.0\,\mathrm{pb} \tag{7.8}$$

$$\sigma^{(2<\eta_{\mu^+\mu^-}<4.5)}_{\chi_{c2}\to J/\psi\,[\mu^+\mu^-]\gamma} = 99.6 \pm 12.7 \pm 27.7\,\mathrm{pb} \tag{7.9}$$

for the combined 2015 and 2016 data where the first uncertainty is statistical and the second systematic, with sources discussed in Sec. 7.7. The results from the 2016-only and combined 2015 and 2016 data are compatible with one another. We will use the results from the full data set to determine our nominal values.

As we do not observe a significant number of χ_{c1} mesons, we calculate an upper limit of the product of the cross-section and the branching fraction at a ninety-percent confidence level. To do this, we perform a similar procedure as the one used to check the stability of the simultaneous Δm_{χ_c} and p_{T}^2 fit model, presented in Sec. 7.2. As before, we generate a series of ten-thousand toy studies using the fit results to the data. However, this time we manually set the yield of χ_{c1} mesons to zero. We fit the generated distributions with the same model used to fit the CEP χ_c sample and use the result to determine the χ_{c1} yield value for which ninety-percent of the toys return. In doing so, we account for the systematic uncertainties presented throughout the thesis and summarised in Sec. 7.7. We determine this value to be 13.2 ± 10.2 events, which compares to a nominal value of 9.41 ± 7.24 events as calculated with the HeRSCheL cut applied. Therefore, the product of the cross-section and the branching fraction of CEP $\chi_c \to J/\psi\,[\mu^+\mu^-]\gamma$ within a ninety-percent confidence interval is $19.5 \pm 15.0 \pm 15.4$ pb, which compares to our nominal value of $13.9 \pm 10.7 \pm 11.0$ pb.

Table 7.4. Summary of the fitted-signal yields, integrated luminosity for single-crossing interactions, and efficiencies necessary for the calculation of the product of the cross-section and the branching fraction of CEP $\chi_c \to J/\psi\,[\mu^+\mu^-]\gamma$ production in proton-proton collisions at centre-of-mass energies of $\sqrt{s} = 13$ TeV at the LHCb experiment with muons in the $2 < \eta_{\mu^+\mu^-} < 4.5$ pseudorapidity region.

Variable	**2016**	**2015 + 2016**
Yield$(\chi_{c1})_{\mathrm{CEP}}$	13.3	9.4
Yield$(\chi_{c2})_{\mathrm{CEP}}$	75.3	96.3
$\mathcal{L}_{\mathrm{Single}}^{\mathrm{Total}}$	606 pb^{-1}	711 pb^{-1}
$\varepsilon_{\mu\mu}^{\mathrm{Global}}$	0.635	0.631
$\varepsilon_{m(J/\psi)}$	0.954	0.955
$\varepsilon_{\Delta m(\chi_{c1})}$	0.885	0.892
$\varepsilon_{\Delta m(\chi_{c2})}$	0.944	0.926
$\varepsilon_{\gamma\to e^+e^-}^{\mathrm{Global}(\chi_{c1})}$ $(\times 10^{-2})$	0.225	0.225
$\varepsilon_{\gamma\to e^+e^-}^{\mathrm{Global}(\chi_{c2})}$ $(\times 10^{-2})$	0.309	0.310
$\varepsilon_{\mathrm{SPD}}$	0.994	0.950
$\varepsilon_{\mathrm{HRC}}$	0.851	0.830
$\varepsilon_{\mathrm{Total}}(\chi_{c1})$ $(\times 10^{-2})$	0.0988	0.0928
$\varepsilon_{\mathrm{Total}}(\chi_{c2})$ $(\times 10^{-2})$	0.148	0.136

We compare our results with theoretical predictions of the Durham model as implemented in SuperChic v4 [85]. SuperChic calculates the $gg \to \chi_c$ vertex to leading order. Therefore, we select three leading-order parton distribution functions for the calculation: `CT14` ($\alpha_S(M_Z^2) = 0.118$) [143], `MSHT20` ($\alpha_S(M_Z^2) = 0.13$) [144], and `NNPDF 3.1` ($\alpha_S(M_Z^2) = 0.13$) [145]. The theoretical predictions are shown in Table 7.5, where the uncertainties are statistical from the simulation calculation. `CT14` and `MSHT20` PDFs are calculated from global fits to data from multiple experiments, including fixed target experiments, HERA, Tevatron, and Run 1 LHC data collected at 7 TeV and 8 TeV. `NNPDF 3.1`, on the other hand, uses a neural network trained

Table 7.5. Measurements of the product of the cross-section times the branching fraction for the full data set (combined 2015 and 2016 data) together with predictions in pb for CEP $\chi_c \to J/\psi\,[\mu^+\mu^-]\gamma$ production in the rapidity region $2 < \eta_{\mu^+\mu^-} < 4.5$ for pp collisions at a centre-of-mass energy $\sqrt{s} = 13$ TeV, using SuperChic v4 [85] for three `LO` PDFs: `CT14` ($\alpha_S(M_Z^2) = 0.118$) [143], `MSHT20` ($\alpha_S(M_Z^2) = 0.13$) [144], and `NNPDF 3.1` ($\alpha_S(M_Z^2) = 0.13$) [145].

Source	**Order**	$\alpha_S(M_Z^2)$	$\sigma^{(2<\eta_{\mu^+\mu^-}<4.5)}_{\chi_{c1}\to J/\psi\,[\mu^+\mu^-]\gamma}$	$\sigma^{(2<\eta_{\mu^+\mu^-}<4.5)}_{\chi_{c2}\to J/\psi\,[\mu^+\mu^-]\gamma}$	$\sigma_{\chi_{c2}}/\sigma_{\chi_{c1}}$
`CT14`	`LO`	0.118	26.03 ± 0.12 [pb]	71.98 ± 0.34 [pb]	2.77 ± 0.02
`MSHT20`	`LO`	0.130	48.48 ± 0.20 [pb]	138.24 ± 0.51 [pb]	2.85 ± 0.02
`NNPDF 3.1`	`LO`	0.130	6.42 ± 0.27 [pb]	16.16 ± 0.08 [pb]	2.52 ± 0.11
Measurement	-	-	$13.9 \pm 10.7 \pm 11.0$[pb]	$99.6 \pm 12.7 \pm 27.7$ [pb]	$5.11 \pm 3.98 \pm^{+14.21}_{-2.22}$
90% C.L.	-	-	$19.5 \pm 15.0 \pm 15.4$ [pb]	-	-

with genetic algorithms to calculate PDFs. The measured results are compatible with the theoretical predictions given the large uncertainties in the PDF distribution. This measurement is particularly susceptible to the gluon PDF at low Bjorken-x and Q^2 where the PDF is not well determined. For example, the uncertainty of the gluon PDF of NNPDF at low Bjorken-x is approximately fifty percent. As is evident, the nominal value of the theoretical predictions can vary significantly depending on the choice of PDF. At such low scales, the uncertainty of the perturbative predictions can be off by a factor of four or five. We expect improvement in the PDFs as new studies are incorporated into the global studies, such as those conducted with data from the LHC at a centre-of-mass energy $\sqrt{s} = 13\,\text{TeV}$.

However, several of the uncertainties associated with the calculation of the PDFs as well as some of the systematic uncertainties in our measurement will cancel when we take the ratio of the cross-sections. The ratio of the theoretical calculations of the product of the cross-section and the branching fraction of χ_{c2} and χ_{c1} also exhibit small PDF dependence, as shown in Table 7.5. We measure a ratio of $\sigma_{\chi_{c2}}/\sigma_{\chi_{c1}} = 5.11 \pm 3.98 \pm^{+14.21}_{-2.22}$, which hints at a higher result than theoretical predictions by approximately a factor of 2.6. However, our measured value and theoretical predictions are in agreement within one standard deviation. As a reminder, the large statistical uncertainty in this observable is due to the low number of observed χ_{c1} mesons while the large systematic uncertainty is dominated by the misassignment of inelastic χ_{c1} background.

7.7 Assignment of systematic uncertainties

The systematic uncertainties associated with the cross-section calculation are summarised in Table 7.6 and briefly discussed below in order of significance. The origin of most of these sources of potential bias, and the assigned uncertainty has already been discussed in earlier chapters.

The most significant systematic uncertainty for the cross-section calculation of CEP χ_c production is related to the photon-conversion efficiency, described in Sec. 5.1, where we calculate

Table 7.6. Summary of systematic uncertainties for the cross-section calculation of CEP $\chi_c \to J/\psi\,[\mu^+\mu^-]\gamma[e^+e^-]$ production.

Source	**2016**		**2015 + 2016**	
	$\boldsymbol{\chi_{c1}}$	$\boldsymbol{\chi_{c2}}$	$\boldsymbol{\chi_{c1}}$	$\boldsymbol{\chi_{c2}}$
$\varepsilon_{\gamma\to e^+e^-}^{\text{Global}(\chi_{cn})}$	22%	22%	22%	22%
Inelastic background	40%	3%	74%	3%
Inelastic χ_{c1}/χ_{c2} ratio	6%	6%	13%	13%
$\varepsilon_{\mu\mu}^{\text{Global}}$	7%	7%	5%	5%
ε_{HRC}	6%	6%	5%	5%
ε_{SPD}	4%	4%	5%	5%
Fit bias	5%	5%	5%	5%
$\varepsilon_{\Delta m(\chi_{cn})}$	4%	2%	4%	3%
$\mathcal{L}_{\text{Single}^{\text{Total}}}$	2%	2%	2%	2%
$\varepsilon_{m(J/\psi)}$	$< 1\%$	$< 1\%$	$< 1\%$	$< 1\%$
$\varepsilon_{\text{Total}}$	48%	26%	79%	28%

the efficiency using a high-multiplicity sample and extrapolate in to a CEP-like, low-multiplicity, environment. As a systematic check, we vary the binning and fit model used in the extrapolation and assign a 20% systematic uncertainty for both the 2016-only, and combined 2015 and 2016 data. The dominant systematic uncertainty in the normalisation of the efficiency is a relative ±8% associated with the knowledge of the number of D^{*0} mesons produced in the sample. Summing the systematic uncertainty components in quadrature, we obtain a total systematic uncertainty associated with the photon-conversion and reconstruction efficiency of 21.5%.

The next most prominent systematic uncertainty is associated with the fit model and the difficulties inherent with determining the contribution of inelastic χ_c background. When comparing the yields with and without the HeRSChel cut applied we observe a shift in results that we attribute to a 40% misassignment of inelastic χ_c events as CEP χ_c events, a procedure described in Sec. 7.4. This translates into a systematic uncertainty of 40.0% (74.3%) for χ_{c1} yields and 3.4% (2.9%) for χ_{c2} yields in 2016-only (combined 2015 and 2016) data. The effect of this systematic is reduced significantly for the calculation of the χ_{c2} yields due to the greater CEP purity in this region.

We include an additional systematic uncertainty associated with the determination of the inelastic χ_{c1}/χ_{c2} ratio used to constrain the CEP χ_c mass fit. The ratio used in the CEP χ_c sample without the HeRSChel cut applied is extracted from the simultaneous fit of the invariant-mass and transverse-momentum distribution of the $\geq$ 3Long sample, while the ratio for the CEP χ_c sample with the HeRSChel cut applied is determined from a fit to the $\geq$ 3Long + HRC sample. These two samples yield different results. Therefore, as a systematic check we repeat the fit of the CEP χ_c sample with the HeRSChel cut applied using the ratio determined with the $\geq$ 3Long sample, which benefits from a larger sample size. We assign the difference in CEP yields as the systematic for an uncertainty of 6% (13%) for the 2016-only (combined 2015 and 2016) data.

The largest source of systematic uncertainty in the muon reconstruction efficiency, described in Sec. 5.2, comes from the extrapolation of the muon-reconstruction efficiency from 2015 to 2016 data. Although reasonable, the assumption that there is no significant difference in the detector's muon-reconstruction performance is not perfect. As a result, we allocate the full correction required to match 2016 results as a systematic uncertainty to the reconstruction efficiency. This corresponds to 7% (5%) for the 2016-only (combined 2015 and 2016) data.

The largest systematic uncertainty with the HeRSChel efficiency calculation, presented in Sec. 5.6.3, is associated with the dimuon fit used to separate the CEP from the non-CEP contributions. To test this, we vary the signal model and background independently then recalculate the efficiency for our working point, $\ln(\chi^2_{\mathrm{HRC}}) < 5$. We find the biggest contribution to the systematic originating from the signal model, and assign this difference as the full systematic for an uncertainty of 6% (5%) for 2016-only (combined 2015 and 2016) data. In addition, stability checks are reported in Sec. 7.4, which showed no significant changes when varying the cut on $\ln(\chi^2_{\mathrm{HRC}})$.

To assign a systematic to the efficiency associated with the SPD hardware trigger requirement, detailed in Sec. 5.5, we vary the mean number of hits expected in the SPD from each muon and electron in our model and recalculate the efficiency. We take the largest difference from our nominal efficiency as the systematic uncertainty , and assign a 4% (5%) uncertainty to the SPD efficiency of 2016-only (combined 2015 and 2016) data.

We validate the Δm_{χ_c} and p_{T}^2 simultaneous fit of our CEP χ_c candidates by performing a series of toy studies, as presented in Sec. 7.2. From the pull distributions we see that there is a small bias in the order of $\sim 5\%$ in the CEP χ_{c1} and χ_{c2} yields. We assign this fit bias as a systematic uncertainty.

We calculate the efficiency associated with the Δm_{χ_c} cut, described in Sec. 5.4. In this case, the biggest limitation does not come from the fit model, but instead from the photon-conversion-efficiency corrections. As a result, we calculate the cut's efficiency using both Monte Carlo and data driven photon-conversion efficiencies and compare the difference in results. We assign an uncertainty of 3.8% (4.0%) for χ_{c1} and 1.7% (2.7%) for χ_{c2} for the 2016-only (combined 2015 and 2016) data.

For the determination of the single-interaction integrated luminosity we use the latest calibration sample which has an uncertainty of 2%. We validate the small number of runs, where the calibration is not available, less than one percent of said runs, by making sure the number of CEP-like J/ψ mesons matches the assigned integrated luminosity.

To calculate a systematic uncertainty for the efficiency of the J/ψ mass-window cut, described in Sec. 5.3, we vary the signal model and repeat the fit used to calculate the efficiency. We take the difference as the systematic uncertainty and assign a 0.4% (0.3%) uncertainty to the 2016-only (combined 2015 and 2016) data.

The total systematic uncertainty is the quadrature sum of all the sources of uncertainty detailed above and leads to a relative systematic uncertainty of 48% (79%) for the χ_{c1} and 26% (28%) for the χ_{c2} cross-section-times-branching-fraction calculation for the 2016-only (combined 2015 and 2016) data. This corresponds to an absolute systematic uncertainty of 10.2 pb (10.9 pb) for the χ_{c1} and 21.4 pb (27.7 pb) for the χ_{c2} cross-section-times-branching-fraction calculation.

CHAPTER 8

Summary and outlook

We presented a study of the CEP of χ_{c1} and χ_{c2} mesons using proton-proton collisions at a centre-of-mass energy of $\sqrt{s} = 13\,\text{TeV}$, using data collected with the LHCb experiment during the 2015 and 2016 runs corresponding to single-interaction integrated luminosities of $711\,\text{pb}^{-1}$. The study was performed through the χ_c meson's radiative decay into $J/\psi\,[\mu^+\mu^-]\gamma[e^+e^-]$ where the muons from the J/ψ decay are measured within the pseudorapidity region $2 < \eta_{\mu^+\mu^-} < 4.5$.

To obtain the best possible χ_c mass resolution we used converted photons, taking advantage of the improved momentum resolution from the tracking information of the electrons. As a result, we have been able to clearly separate contributions from χ_{c1} and χ_{c2} mesons. However, this came at the cost of a smaller event yield when compared to a sample reconstructed with photons detected by the electromagnetic calorimeter. Using converted photons also meant that having a clear understanding of the photon-conversion and reconstruction efficiency was crucial to the success of this analysis. Consequently, we developed a unique data-driven method using $D^{*0} \to D^0[K^\pm\pi^\mp]\gamma$ decays through which we measured the photon-conversion and reconstruction efficiency of photons with transverse-momentum as low as $200\ \text{MeV}/c$. These events are normally accompanied by a large number of particles, resulting in a high detector occupancy. Therefore, the procedure required the extrapolation of the results into a low multiplicity environment typical of CEP, giving rise to our primary systematic uncertainty.

We enforced the characteristic double rapidity-gap criteria of CEP by selecting low-multiplicity events at the trigger level and requiring that there are no additional tracks in the forward and backward direction within the main spectrometer's acceptance. In addition, we used HeRSCheL to reject events accompanied by proton dissociation, gluon radiation, multiple scattering, or pile-up. HeRSCheL has proven to be a powerful tool for the study of CEP that allows us to significantly reduce inelastic background while retaining CEP signal. To determine the performance of the HeRSCheL figure of merit, we used a sample of CEP dimuons; a well understood CEP process. The observed signal retention and background rejection in the CEP χ_c sample were in good agreement with the calibration sample, even though our signal had two additional final-state particles. In addition, we observed stable and consistent results across different HeRSCheL figure of merit working points.

To separate the CEP χ_c signal from inelastic χ_c background contributions we failed to veto through our low-multiplicity selection, exclusivity-track requirements, or HeRSCheL cut, we performed a simultaneous fit of the χ_c meson's delta-mass and transverse-momentum-squared distribution to take advantage of the characteristically low p_{T}^2 of CEP relative to its inelastic counterpart. The signal component shapes are taken from SuperChic simulation while background shapes are taken from simulation, data-driven studies, and previous experimental results, which makes this a model-dependent study. The fit benefits from lower inelastic χ_c background achieved through the implementation of the HeRSCheL cut. However, given the low reconstruction efficiency of events with soft photons we only observe a few χ_{c1} candidates and, as a result, are able to present a ninety percent confidence limit for the product of the cross-section and the branching fraction of χ_{c1} mesons. The product of the cross-section and branching fraction are measured to be

$$\begin{aligned} \sigma^{(2<\eta_{\mu^+\mu^-}<4.5)}_{\chi_{c1}\to J/\psi\,[\mu^+\mu^-]\gamma} &= 19.5 \pm 15.0(\mathrm{stat}) \pm 15.4(\mathrm{syst})\,\mathrm{pb} \quad [90\%\ \mathrm{C.L.}] \\ \sigma^{(2<\eta_{\mu^+\mu^-}<4.5)}_{\chi_{c2}\to J/\psi\,[\mu^+\mu^-]\gamma} &= 99.6 \pm 12.7(\mathrm{stat}) \pm 27.7(\mathrm{syst})\,\mathrm{pb}, \end{aligned} \tag{8.1}$$

where the first uncertainty is statistical and the second is systematic. These results are compatible with theoretical predictions given the large uncertainties.

There are two additional low-multiplicity dimuon samples of comparable size to the 2016 sample collected during the 2017 and 2018 runs that included the HeRSCheL detector. However, crucial information is missing from the D^{*0} sample collected during these run periods, which is necessary for the photon-conversion calibration. Consequently, a new method needs to be developed before we can incorporate the full Run 2 data set into the analysis. The study would greatly benefit from a larger data set. This would allow us to significantly improve the stability of the fit model and increase our sensitivity to the cross-section measurement of χ_c, especially that of χ_{c1}. The larger sample and improved fit stability might in turn allow us to reincorporate the χ_{c0} mass region into our analysis and give us sensitivity to its CEP contribution. In addition, a larger sample would make the cross-sectional measurement as a function of rapidity possible and allow us to shed light on low Bjorken-x physics.

LHCb is undergoing an upgrade period known as the second long-shutdown, which started in 2019 and is expected to end in 2021. This is in preparation for the high-luminosity stage of the LHC (HL-LHC). The LHC was calibrated to accumulate approximately 1.5 and 1.1 visible interactions per bunch crossing during Run 1 and Run 2, respectively. This allowed for the collection of approximately 10 fb^{-1} of data. During Run 3 and Run 4 the LHC will deliver approximately five interactions per bunch crossing at the LHCb interaction point, and is expected to deliver an integrated luminosity of 50 fb^{-1} by the end of Run 3 and Run 4. However, the higher interaction rate means that only three percent of the bunch crossing will correspond to a single interaction compared to the thirty-seven percent for Run 2. As a result, LHCb will only collect a fraction of the single-interaction events during Run 3 and Run 4 compared to the currently available data set. Therefore, the useful sample size is not competitive and the harsher environment would quickly degrade the HeRSChel modules. This in turn means that HeRSChel will not be available for proton-proton runs during this period.

In order to cope with the higher occupancy while maintaining detector performance, key LHCb sub-detectors are being replaced, including the tracking detectors, the RICH detectors, and the VELO. In addition, all trigger lines will be entirely software based and all detectors will be read at 40 MHz. This will allow us to apply more sophisticated selection criteria at trigger level. With the full software trigger it is possible to identify isolated low-multiplicity vertices from CEP even in a bunch crossing with multiple interactions and many other vertices. However, Herschel information cannot be used in this case because we cannot associate the signals in Herschel with the individual vertices.

However, through an alternative method known as proton tagging, we could guarantee the exclusivity requirement of the event in spite of the presence of pile-up. In this process the two interacting protons scatter at small angles, are detected by instrumentation near the beam line and their kinematics are reconstructed. We could then use the information of the proton's momentum loss to calculate the mass of the central system independent of its decay mode. For CEP events, we would expect agreement between this measurement and the mass calculated using information from decay products detected in the main spectrometer, and expect disagreement between the two measurements for background events. In addition, by reconstructing the full kinematics of the event we would be able to constrain the mass calculation of the central system and improve its resolution as well as detect events with missing energy. Currently, however, there are no plans to install proton taggers at LHCb.

The χ_c measurements could be significantly improved by incorporating hadronic decays where candidates can be reconstructed in the K^+K^-, $\pi^+\pi^-$, and p^+p^- final state, as well as decays with a larger number of hadrons in the final state such as $2(\pi^+\pi^-)$, $3(\pi^+\pi^-)$, and $\pi^+\pi^-K^+K^-$. Data were collected in Run 2 with trigger lines sensitive to these decays. This would significantly increase our sensitivity to χ_{c0} production. LHCb is well suited for this study thanks to its strong particle-identification capabilities. The study presented in this thesis has also shown that the multiplicity trigger requirements are sufficiently loose to cope with a four and six particle final state necessary for some of the hadronic studies.

The next test of our theoretical understanding of the DPE mechanism of CEP is the study of the bottomonium counterpart of the χ_c mesons, the χ_b states. Similar to χ_c, there are three states of χ_b with $J^{CP} = 0^{++}$, 1^{++}, and 2^{++} that follow a similar hierarchy. Although it has a smaller cross-section, the χ_b state's higher mass scale places it safely within the perturbative regime. We can apply the knowledge learned in this study to investigate the CEP of χ_b mesons through a similar radiative decay, $\chi_b \to \Upsilon[\mu^+\mu^-]\gamma$. The invariant mass of χ_{b0} and χ_{b1} mesons are within 33 MeV/c^2 of one another, and that of χ_{b1} and χ_{b2} is within 20 MeV/c^2 of one another. As a result, this analysis would also greatly benefit from the use of converted photons to increase the invariant-mass resolution of the χ_b states.

We can also apply the lessons learned to the study of exotic particles, such as the $X(3872)$ state [146–150], which can be studied through the radiative decay into $J/\psi\,[\mu^+\mu^-]\gamma$ or with a more favourable branching fraction into $\psi(2S)[\mu^+\mu^-]\gamma$. This state has an unusually narrow width, with an upper limit of $1.2\,\mathrm{MeV}/c^2$ set at a ninety percent confidence level. Although the quantum numbers have been determined to be $J^{CP} = 1^{++}$ the nature of this particle has yet to be understood.

In summary, we have demonstrated that the LHCb is well equipped for the study of CEP and shown that HeRSCheL plays an important role in background reduction by expanding the sensitivity of LHCb to higher rapidity regions. We have demonstrated the benefits of using converted photons as a mechanism to improve mass resolution at the LHCb. We also conducted an important measurement necessary to test our theoretical understanding of CEP. More importantly, by studying the CEP of χ_c mesons (considered the standard candle of CEP via DPE) we have opened a new frontier for LHCb through which to probe the Standard Model.

Bibliography

[1] R. Devenish, E. P. P. R. Devenish, A. Cooper-Sarkar, and O. U. Press, *Deep Inelastic Scattering*, Oxford University Press, 2004.

[2] M. Thomson, *Modern particle physics*, Cambridge University Press, New York, 2013.

[3] I. J. R. Aitchison and A. J. G. Hey, *Gauge Theories in Particle Physics: A Practical Introduction, Volume 1: From Relativistic Quantum Mechanics to QED, Fourth Edition*, no. v. 1, CRC Press, 2012.

[4] M. Gell-Mann, *A schematic model of baryons and mesons*, Physics Letters **8** (1964), no. 3 214.

[5] J. Matthew Durham, on behalf of the LHCb collaboration, *LHCb measurements of the exotic tetraquark candidate* $\chi_{c1}(3872)$ *in high-multiplicity pp and pPb collisions*, Nucl. Phys. A **1005** (2021) 121918, `arXiv:2002.01551`.

[6] LHCb collaboration, *Observation of structure in the* J/ψ*-pair mass spectrum*, Sci. Bull. **65** (2020), no. 23 1983, `arXiv:2006.16957`.

[7] LHCb collaboration, *Observation of new resonances decaying to* $J/\psi K^+$ *and* $J/\psi\phi$, `arXiv:2103.01803`.

[8] S.-Y. Li *et al.*, *Pentaquark states with the* $QQQq\bar{q}$ *configuration in a simple model*, Eur. Phys. J. C **79** (2019), no. 1 87, `arXiv:1809.08072`.

[9] LHCb collaboration, *Observation of the doubly charmed baryon* Ξ_{cc}^{++}, Phys. Rev. Lett. **119** (2017), no. 11 112001, `arXiv:1707.01621`.

[10] LHCb collaboration, *Observation of* $J/\psi p$ *Resonances Consistent with Pentaquark States in* $\Lambda_b^0 \to J/\psi K^- p$ *Decays*, Phys. Rev. Lett. **115** (2015) 072001, `arXiv:1507.03414`.

[11] LHCb collaboration, *Observation of a narrow pentaquark state,* $P_c(4312)^+$*, and of two-peak structure of the* $P_c(4450)^+$, Phys. Rev. Lett. **122** (2019), no. 22 222001, `arXiv:1904.03947`.

[12] J. C. Ward, *An Identity in Quantum Electrodynamics*, Phys. Rev. **78** (1950) 182.

[13] P. D. Group, *Review of Particle Physics*, Progress of Theoretical and Experimental Physics **2020** (2020) , `arXiv:https://pdglive.lbl.gov`, 083C01.

[14] F. E. Low, *A Model of the Bare Pomeron*, Phys. Rev. D **12** (1975) 163.

[15] I. Y. Pomeranchuk, V. V. Sudakov, and K. A. Ter-Martirosyan, *Vanishing of Renormalized Charges in Field Theories with Point Interaction*, Phys. Rev. **103** (1956) 784.

[16] G. F. Chew and S. C. Frautschi, *Dynamical Theory for Strong Interactions at Low Momentum Transfers but Arbitrary Energies*, Phys. Rev. **123** (1961), no. 4 1478.

[17] P. D. B. Collins, *An Introduction to Regge Theory and High-Energy Physics*, Cambridge Monographs on Mathematical Physics, Cambridge Univ. Press, Cambridge, UK, 5, 2009. doi: 10.1017/CBO9780511897603.

[18] V. Barone and E. Predazzi, *High-Energy Particle Diffraction*, vol. v.565 of *Texts and Monographs in Physics*, Springer-Verlag, Berlin Heidelberg, 2002.

[19] M. Albrow, *Central exclusive production issue: Introduction*, Int. J. Mod. Phys. **A29** (2014) 1402006.

[20] M. G. Albrow, T. D. Coughlin, and J. R. Forshaw, *Central Exclusive Particle Production at High Energy Hadron Colliders*, Prog. Part. Nucl. Phys. **65** (2010) 149, `arXiv:1006.1289`.

[21] A. D. Martin, M. G. Ryskin, and V. A. Khoze, *Forward Physics at the LHC*, Acta Phys. Polon. B **40** (2009) 1841, `arXiv:0903.2980`.

[22] A. B. Kaidalov, V. A. Khoze, A. D. Martin, and M. G. Ryskin, *Central exclusive diffractive production as a spin-parity analyser: From Hadrons to Higgs*, Eur. Phys. J. C **31** (2003) 387, `arXiv:hep-ph/0307064`.

[23] W. Ochs, *The Status of Glueballs*, J. Phys. G **40** (2013) 043001, `arXiv:1301.5183`.

[24] J. R. Forshaw, *Central Exclusive Production at the LHC*, Nucl. Phys. Proc. Suppl. **191** (2009) 247, `arXiv:0901.3040`.

[25] TOTEM, D0, V. M. Abazov *et al.*, *Odderon Exchange from Elastic Scattering Differences between pp and $p\bar{p}$ Data at 1.96 TeV and from pp Forward Scattering Measurements*, Phys. Rev. Lett. **127** (2021), no. 6 062003, `arXiv:2012.03981`.

[26] D. d'Enterria, *Forward Physics at the LHC: within and beyond the Standard Model*, AIP Conf. Proc. **1038** (2008), no. 1 95, `arXiv:0806.0883`.

[27] ATLAS collaboration, *Observation of light-by-light scattering in ultraperipheral Pb + Pb collisions with the ATLAS detector*, Phys. Rev. Lett. **123** (2019), no. 5 052001, `arXiv:1904.03536`.

[28] CDF collaboration, *Observation of Exclusive Electron-Positron Production in Hadron-Hadron Collisions*, Phys. Rev. Lett. **98** (2007) 112001, `arXiv:hep-ex/0611040`.

[29] CDF collaboration, *Search for exclusive Z boson production and observation of high mass*

$p\bar{p} \to \gamma\gamma \to p + \ell\ell + \bar{p}$ events in $p\bar{p}$ collisions at $\sqrt{s} = 1.96$ TeV, Phys. Rev. Lett. **102** (2009) 222002, `arXiv:0902.2816`.

[30] CDF collaboration, *Observation of Exclusive Dijet Production at the Fermilab Tevatron $p^{-}\bar{p}$ Collider*, Phys. Rev. D **77** (2008) 052004, `arXiv:0712.0604`.

[31] CMS collaboration, *Exclusive photon-photon production of muon pairs in proton-proton collisions at $\sqrt{s} = 7$ TeV*, JHEP **01** (2012) 052, `arXiv:1111.5536`.

[32] K. Piotrzkowski, *Study of exclusive two-photon production of $W^{+}W^{-}$ pairs in pp collisions at 7 TeV, and constraints on anomalous quartic couplings in CMS*, PoS **Photon2013** (2013) 026.

[33] S. R. Klein, *Comment on "η_c production in photon-induced interactions at the LHC"*, Phys. Rev. D **98** (2018), no. 11 118501, `arXiv:1808.08253`.

[34] B. R. Gruberg Cazon, *Studies of the Photoproduction of Charm-Anticharm Resonances in Ultra-Peripheral Collisions of Lead Ions in ALICE at the LHC*, PhD thesis, Creighton University, 2015.

[35] B. Pire, F. Schwennsen, L. Szymanowski, and S. Wallon, *Hard Pomeron-Odderon interference effects in the production of $\pi^{+}\pi^{-}$ pairs in high energy gamma-gamma collisions at the LHC*, Phys. Rev. D **78** (2008) 094009, `arXiv:0810.3817`.

[36] U. Gastaldi and M. Berretti, *Decays into $\pi^{+}\pi^{-}$ of the $f_0(1370)$ scalar glueball candidate in pp central exclusive production experiments*, `arXiv:1804.09121`.

[37] STAR collaboration, *Coherent ρ^0 production in ultraperipheral heavy ion collisions*, Phys. Rev. Lett. **89** (2002) 272302, `arXiv:nucl-ex/0206004`.

[38] CMS Collaboration, *Measurement of exclusive $\rho(770)^0$ photoproduction in ultraperipheral pPb collisions at $\sqrt{s_{\mathrm{NN}}} = 5.02$ TeV*, Eur. Phys. J. C **79** (2019) 702. 39 p, `arXiv:1902.01339`.

[39] ALICE collaboration, *Production of the $\rho(770)^0$ meson in pp and Pb-Pb collisions at $\sqrt{s_{\mathrm{NN}}} = 2.76$ TeV*, Phys. Rev. C **99** (2019), no. 6 064901, `arXiv:1805.04365`.

[40] STAR collaboration, *ρ^0 photoproduction in ultraperipheral relativistic heavy ion collisions at $\sqrt{s_{\mathrm{NN}}} = 200$ GeV*, Phys. Rev. C **77** (2008) 034910, `arXiv:0712.3320`.

[41] PHENIX collaboration, *Photoproduction of J/ψ and of high mass $e^{+}e^{-}$ in ultra-peripheral Au + Au collisions at $\sqrt{s_{\mathrm{NN}}} = 200$ GeV*, Phys. Lett. B **679** (2009) 321, `arXiv:0903.2041`.

[42] CDF collaboration, *Observation of exclusive charmonium production and $\gamma + \gamma$ to $\mu^{+}\mu^{-}$ in $p\bar{p}$ collisions at $\sqrt{s} = 1.96$ TeV*, Phys. Rev. Lett. **102** (2009) 242001, `arXiv:0902.1271`.

[43] LHCb collaboration, *Measurement of J/ψ production in pp collisions at $\sqrt{s} = 7$* TeV, Eur. Phys. J. C **71** (2011) 1645, `arXiv:1103.0423`.

[44] LHCb collaboration, *Central exclusive production of J/ψ and $\psi(2S)$ mesons in pp collisions at $\sqrt{s} = 13$ TeV*, Submitted to: JHEP (2018) `arXiv:1806.04079`.

[45] CMS collaboration, *Coherent J/ψ photoproduction in ultra-peripheral PbPb collisions at $\sqrt{s_{\rm NN}} = 2.76$ TeV with the CMS experiment*, Phys. Lett. B **772** (2017) 489, `arXiv:1605.06966`.

[46] ALICE collaboration, *Coherent J/ψ photoproduction in ultra-peripheral Pb-Pb collisions at $\sqrt{s_{\rm NN}} = 2.76$ TeV*, Phys. Lett. B **718** (2013) 1273, `arXiv:1209.3715`.

[47] ALICE collaboration, *Charmonium and e^+e^- pair photoproduction at mid-rapidity in ultra-peripheral Pb-Pb collisions at $\sqrt{s_{\rm NN}} = 2.76$ TeV*, Eur. Phys. J. C **73** (2013), no. 11 2617, `arXiv:1305.1467`.

[48] K. Naskar, on behalf of the CMS collaboration, *Measurement of exclusive Upsilon photoproduction in pPb collisions at $\sqrt{s_{\rm NN}} = 5.02$ TeV with the CMS*, PoS **HardProbes2018** (2019) 180, `arXiv:1903.10811`.

[49] CMS collaboration, *Measurement of exclusive Υ photoproduction from protons in pPb collisions at $\sqrt{s_{\rm NN}} = 5.02$ TeV*, Eur. Phys. J. C **79** (2019), no. 3 277, `arXiv:1809.11080`.

[50] LHCb collaboration, *Measurement of the exclusive Υ production cross-section in pp collisions at $\sqrt{s} = 7$ TeV and 8 TeV*, JHEP **09** (2015) 084, `arXiv:1505.08139`.

[51] Y. Chen *et al.*, *Glueball spectrum and matrix elements on anisotropic lattices*, Phys. Rev. D **73** (2006) 014516, `arXiv:hep-lat/0510074`.

[52] C. J. Morningstar and M. J. Peardon, *The Glueball spectrum from an anisotropic lattice study*, Phys. Rev. D **60** (1999) 034509, `arXiv:hep-lat/9901004`.

[53] V. A. Khoze, A. D. Martin, and M. G. Ryskin, *Can the Higgs be seen in rapidity gap events at the Tevatron or the LHC?*, Eur. Phys. J. C **14** (2000) 525, `arXiv:hep-ph/0002072`.

[54] M. G. Albrow and A. Rostovtsev, *Searching for the Higgs at hadron colliders using the missing mass method*, `arXiv:hep-ph/0009336`.

[55] V. A. Khoze, A. D. Martin, and M. G. Ryskin, *Prospects for new physics observations in diffractive processes at the LHC and Tevatron*, Eur. Phys. J. C **23** (2002) 311, `arXiv:hep-ph/0111078`.

[56] CDF collaboration, *Search for exclusive $\gamma\gamma$ production in hadron-hadron collisions*, Phys. Rev. Lett. **99** (2007) 242002, `arXiv:0707.2374`.

[57] CMS collaboration, *Observation of a New Boson at a Mass of 125 GeV with the CMS Experiment at the LHC*, Phys. Lett. B **716** (2012) 30, `arXiv:1207.7235`.

[58] ATLAS, G. Aad *et al.*, *Observation of a new particle in the search for the Standard*

Model Higgs boson with the ATLAS detector at the LHC, Phys. Lett. B **716** (2012) 1, `arXiv:1207.7214`.

[59] M. Breidenbach *et al.*, *Observed behavior of highly inelastic electron-proton scattering*, Phys. Rev. Lett. **23** (1969) 935.

[60] J. D. Bjorken, *Asymptotic sum rules at infinite momentum*, Phys. Rev. **179** (1969) 1547.

[61] L. D. Broglie, *Xxxv. a tentative theory of light quanta*, Philosophical Magazine Letters **86** (2006), no. 7 411, `arXiv:https://doi.org/10.1080/09500830600914721`.

[62] J. R. Forshaw and D. A. Ross, *Quantum chromodynamics and the pomeron*, vol. 9, Cambridge University Press, 1, 2011.

[63] S. Donnachie, H. G. Dosch, O. Nachtmann, and P. Landshoff, *Pomeron physics and QCD*, vol. 19, Cambridge University Press, 12, 2004.

[64] L. Sestini, on behalf of the LHCb collaboration, *Electroweak boson production at LHCb*, PoS **EPS-HEP2017** (2017) 402.

[65] A. Levy, *Evidence for no shrinkage in elastic photoproduction of J / psi*, Phys. Lett. B **424** (1998) 191, `arXiv:hep-ph/9712519`.

[66] V. A. Khoze, A. D. Martin, and M. G. Ryskin, *Soft diffraction and the elastic slope at Tevatron and LHC energies: A MultiPomeron approach*, Eur. Phys. J. C **18** (2000) 167, `arXiv:hep-ph/0007359`.

[67] L. A. Harland-Lang, V. A. Khoze, M. G. Ryskin, and W. J. Stirling, *Central exclusive production within the Durham model: a review*, Int. J. Mod. Phys. A **29** (2014) 1430031, `arXiv:1405.0018`.

[68] L. A. Harland-Lang, V. A. Khoze, M. G. Ryskin, and W. J. Stirling, *The Phenomenology of Central Exclusive Production at Hadron Colliders*, Eur. Phys. J. C **72** (2012) 2110, `arXiv:1204.4803`.

[69] L. A. Harland-Lang, V. A. Khoze, and M. G. Ryskin, *Central exclusive production and the Durham model*, Int. J. Mod. Phys. A **29** (2014) 1446004.

[70] L. A. Harland-Lang, *Simple form for the low-x generalized parton distributions in the skewed regime*, Phys. Rev. D **88** (2013), no. 3 034029, `arXiv:1306.6661`.

[71] L. A. Harland-Lang, V. A. Khoze, M. G. Ryskin, and W. J. Stirling, *Central exclusive χ_c meson production at the Tevatron revisited*, Eur. Phys. J. C **65** (2010) 433, `arXiv:0909.4748`.

[72] LHC Forward Physics Working Group, *LHC Forward Physics*, J. Phys. G **43** (2016) 110201, `arXiv:1611.05079`.

[73] V. A. Khoze, A. D. Martin, M. G. Ryskin, and W. J. Stirling, *Double diffractive χ meson production at the hadron colliders*, Eur. Phys. J. C **35** (2004) 211, `arXiv:hep-ph/0403218`.

[74] V. V. Sudakov, *Vertex parts at very high energies in quantum electrodynamics*, Zh. Eksp. Teor. Fiz. **30** (1956) 87.

[75] J. C. Collins, *Sudakov form-factors*, Adv. Ser. Direct. High Energy Phys. **5** (1989) 573, `arXiv:hep-ph/0312336`.

[76] M. R. Pelicer, E. G. de Oliveira, A. D. Martin, and M. G. Ryskin, *Absorptive effects and power corrections in low x DGLAP evolution*, Eur. Phys. J. C **79** (2019), no. 1 9, `arXiv:1810.05573`.

[77] V. A. Khoze, A. D. Martin, and M. G. Ryskin, *Insight into Double-Pomeron-Exchange Higgs production and backgrounds*, Phys. Lett. B **650** (2007) 41, `arXiv:hep-ph/0702213`.

[78] H1 collaboration, *Elastic and inelastic photoproduction of J/ψ mesons at HERA*, Nucl. Phys. B **472** (1996) 3, `arXiv:hep-ex/9603005`.

[79] V. A. Khoze, A. D. Martin, and M. G. Ryskin, *Diffraction at the LHC*, Eur. Phys. J. C **73** (2013) 2503, `arXiv:1306.2149`.

[80] L. A. Harland-Lang, V. A. Khoze, M. G. Ryskin, and W. J. Stirling, *Standard candle central exclusive processes at the Tevatron and LHC*, Eur. Phys. J. **C69** (2010) 179, `arXiv:1005.0695`.

[81] J. R. Forshaw, *Diffractive Higgs production: Theory*, in *HERA and the LHC: A Workshop on the Implications of HERA and LHC Physics (Startup Meeting, CERN, 26-27 March 2004; Midterm Meeting, CERN, 11-13 October 2004)*, pp. 466–481, 8, 2005. `arXiv:hep-ph/0508274`.

[82] R. S. Pasechnik, A. Szczurek, and O. V. Teryaev, *Elastic double diffractive production of axial-vector χ_c (1++) mesons and the Landau-Yang theorem*, Phys. Lett. B **680** (2009) 62, `arXiv:0901.4187`.

[83] L. A. Harland-Lang, V. A. Khoze, and M. G. Ryskin, *Exclusive physics at the LHC with SuperChic 2*, Eur. Phys. J. **C76** (2016), no. 1 9, `arXiv:1508.02718`.

[84] L. A. Harland-Lang, V. A. Khoze, and M. G. Ryskin, *Exclusive LHC physics with heavy ions: SuperChic 3*, Eur. Phys. J. C **79** (2019), no. 1 39, `arXiv:1810.06567`.

[85] L. A. Harland-Lang, M. Tasevsky, V. A. Khoze, and M. G. Ryskin, *A new approach to modelling elastic and inelastic photon-initiated production at the LHC: SuperChic 4*, Eur. Phys. J. C **80** (2020), no. 10 925, `arXiv:2007.12704`.

[86] Particle Data Group, P. A. Zyla *et al.*, *Review of Particle Physics*, PTEP **2020** (2020), no. 8 083C01.

[87] Particle Data Group, M. Tanabashi *et al.*, *Review of particle physics*, Phys. Rev. D **98** (2018) 030001.

[88] CDF collaboration, *The CDF-II detector: Technical design report*, .

[89] LHCb Collaboration, *Central Exclusive Dimuon Production at* $\sqrt{s} = 7$ *TeV*, `https://cds.cern.ch/record/1349022`, 2011. LHCb-ANA-2011-033.

[90] S. R. Klein *et al.*, *STARlight: A Monte Carlo simulation program for ultra-peripheral collisions of relativistic ions*, Comput. Phys. Commun. **212** (2017) 258, `arXiv:1607.03838`.

[91] S. R. Klein and J. Nystrand, *Photoproduction of quarkonium in proton proton and nucleus nucleus collisions*, Phys. Rev. Lett. **92** (2004) 142003, `arXiv:hep-ph/0311164`.

[92] P. M. Bjornstad, *Central Exclusive Production of* χ *Mesons at LHCb*, PhD thesis, Manchester U., 11, 2013.

[93] L. Evans and P. Bryant, *LHC machine*, Journal of Instrumentation **3** (2008) S08001.

[94] J. Haffner, *The CERN accelerator complex. Complexe des accélérateurs du CERN*, `https://cds.cern.ch/record/1621894`, Oct, 2013.

[95] LHCb collaboration, *The LHCb detector at the LHC*, JINST **3** (2008) S08005.

[96] LHCb collaboration, *LHCb reoptimized detector design and performance: Technical Design Report*, CERN-LHCC-2003-030. LHCb-TDR-009.

[97] LHCb collaboration, *LHCb Detector Performance*, Int. J. Mod. Phys. **A30** (2015), no. 07 1530022, `arXiv:1412.6352`.

[98] C. Elsasser, $b\bar{b}$ *production at the LHCb experiment*, provided by the LHCb Speakers' Bureau: `https://lhcb.web.cern.ch/lhcb/speakersbureau/html/bb_ProductionAngles.html`, June, 2021.

[99] LHCb Operations Plots, *LHCb Integrated Recorded Luminosity in pp. 2010-2018*, `https://lbgroups.cern.ch/online/OperationsPlots/index.htm`, June, 2018.

[100] LHCb collaboration, *LHCb VELO (VErtex LOcator): Technical Design Report*, CERN-LHCC-2001-011. LHCb-TDR-005.

[101] LHCb collaboration, *LHCb VELO Upgrade Technical Design Report*, CERN-LHCC-2013-021. LHCb-TDR-013.

[102] LHCb collaboration, *LHCb magnet: Technical Design Report*, CERN-LHCC-2000-007. LHCb-TDR-001.

[103] LHCb collaboration, *Silicon strip detectors for the LHCb experiment*, Nucl. Instrum. Meth. **A541** (2005) 83.

[104] LHCb collaboration, *LHCb RICH: Technical Design Report*, CERN-LHCC-2000-037. LHCb-TDR-003.

[105] LHCb collaboration, *LHCb calorimeters: Technical Design Report*, CERN-LHCC-2000-036. LHCb-TDR-002.

[106] K. C. Akiba *et al.*, *The HeRSCheL detector: high-rapidity shower counters for LHCb*, JINST **13** (2018), no. 04 P04017, `arXiv:1801.04281`.

[107] E. Technology, *EJ-200 plastic scintillator*, `https://www.eljentechnology.com/images/stories/Data_Sheets/Plastic_Scintillators/EJ200%20data%20sheet.pdf`, 2021.

[108] H. P. K. K. *Photomultiplier tubeR1828-01*, `https://www.hamamatsu.com/eu/en/product/type/R1828-01/index.html`, 2021.

[109] LHCb collaboration, *LHCb trigger system: Technical Design Report*, CERN-LHCC-2003-031. LHCb-TDR-010.

[110] G. Barrand *et al.*, *GAUDI - A software architecture and framework for building HEP data processing applications*, Comput. Phys. Commun. **140** (2001) 45.

[111] M. Clemencic *et al.*, *Recent developments in the LHCb software framework Gaudi*, J. Phys. Conf. Ser. **219** (2010) 042006.

[112] BRUNEL, The LHCb Event Reconstruction program `http://lhcb-release-area. web. cern. ch/LHCb-release-area/DOC/brunel`.

[113] A. Hoecker *et al.*, *TMVA: Toolkit for multivariate data analysis*, PoS **ACAT** (2007) 040, `arXiv:physics/0703039`.

[114] S. Benson, V. V. Gligorov, M. A. Vesterinen, and J. M. Williams, *The LHCb Turbo Stream*, J. Phys. Conf. Ser. **664** (2015), no. 8 082004.

[115] DAVINCI, The physics analysis software for the LHCb experiment `http://lhcb-release-area. web. cern. ch/LHCb-release-area/DOC/davinci`.

[116] R. Brun and F. Rademakers, *ROOT: An object oriented data analysis framework*, Nucl. Instrum. Meth. **A389** (1997) 81.

[117] LHCb collaboration, *Triger Schemes*, `https://lhcb.web.cern.ch/speakersbureau/html/TriggerScheme.html`, 2021.

[118] M. Clemencic *et al.*, on behalf of the LHCb collaboration, *The LHCb simulation application, Gauss: Design, evolution and experience*, J. Phys. Conf. Ser. **331** (2011) 032023.

[119] I. Belyaev *et al.*, on behalf of the LHCb collaboration, *Handling of the generation of primary events in* GAUSS*, the LHCb simulation framework*, Nuclear Science Symposium Conference Record (NSS/MIC) **IEEE** (2010) 1155.

[120] LHCb collaboration, *The Gauss project*, `http://lhcbdoc.web.cern.ch/lhcbdoc/gauss`, 2021.

[121] D. J. Lange, *The EvtGen particle decay simulation package*, Nucl. Instrum. Meth. **A462** (2001) 152.

[122] P. Golonka and Z. Was, *PHOTOS Monte Carlo: a precision tool for QED corrections in Z and W decays*, Eur. Phys. J. **C45** (2006) 97, `arXiv:hep-ph/0506026`.

[123] GEANT4, S. Agostinelli *et al.*, *GEANT4–a simulation toolkit*, Nucl. Instrum. Meth. A **506** (2003) 250.

[124] T. Sjöstrand, S. Mrenna, and P. Skands, *PYTHIA 6.4 physics and manual*, JHEP **05** (2006) 026, `arXiv:hep-ph/0603175`.

[125] T. Sjöstrand, S. Mrenna, and P. Skands, *A brief introduction to PYTHIA 8.1*, Comput. Phys. Commun. **178** (2008) 852, `arXiv:0710.3820`.

[126] LHCb collaboration, *The Boole project*, `http://lhcb-release-area.web.cern.ch/LHCb-release-area/DOC/boole/`.

[127] LHCb collaboration, *The Moore project*, `http://lhcbdoc.web.cern.ch/lhcbdoc/moore/`, 2021.

[128] G. Zunica, on behalf of the LHCb collaboration, *Design and performance of the LHCb detector and full real-time reconstruction in Run 2 of the LHC*, in *2019 IEEE Nuclear Science Symposium (NSS) and Medical Imaging Conference (MIC)*, 10, 2019. doi: 10.1109/NSS/MIC42101.2019.9059669.

[129] M. De Cian, S. Farry, P. Seyfert, and S. Stahl, *Fast neural-net based fake track rejection in the LHCb reconstruction*, tech. rep., CERN, Geneva, Mar, 2017.

[130] R. Frühwirth, *Application of kalman filtering to track and vertex fitting*, Nuclear Instruments and Methods in Physics Research Section A: Accelerators, Spectrometers, Detectors and Associated Equipment **262** (1987), no. 2 444.

[131] L. Harland-Lang, *Superchic 2 - a monte carlo for central exclusive production*, https://superchic.hepforge.org.

[132] L. A. Harland-Lang, A. D. Martin, P. Motylinski, and R. S. Thorne, *Parton distributions in the LHC era: MMHT 2014 PDFs*, Eur. Phys. J. C **75** (2015), no. 5 204, `arXiv:1412.3989`.

[133] LHCb collaboration, *PID Plots for Conference*, `https://twiki.cern.ch/twiki/bin/view/LHCb/PIDConferencePlots#RICH_AN1`.

[134] LHCb collaboration, *Measurement of the relative rate of prompt χ_{c0}, χ_{c1} and χ_{c2} production at $\sqrt{s} = 7$ TeV*, JHEP **10** (2013) 115, `arXiv:1307.4285`.

[135] LHCb collaboration, *Measurement of the $\chi_b(3P)$ mass and of the relative rate of $\chi_{b1}(1P)$ and $\chi_{b2}(1P)$ production*, JHEP **10** (2014) 088, `arXiv:1409.1408`.

[136] LHCb collaboration, *Measurements of prompt charm production cross-sections in pp collisions at $\sqrt{s} = 13$ TeV*, JHEP **03** (2016) 159, `arXiv:1510.01707`, [Erratum: JHEP05,074(2017)].

[137] T. Skwarnicki, *A study of the radiative cascade transitions between the Upsilon-prime and Upsilon resonances*, PhD thesis, Institute of Nuclear Physics, Krakow, 1986, DESY-F31-86-02.

[138] K. Cranmer, *Kernel estimation in high-energy physics*, Comput. Phys. Commun. **136** (2001) 198, `arXiv:hep-ex/0011057`.

[139] S. P. Baranov, O. Duenger, H. Shooshtari, and J. A. M. Vermaseren, *LPAIR: A generator for lepton pair production*, in *Workshop on Physics at HERA*, 1991.

[140] H1 collaboration, *Elastic and Proton-Dissociative Photoproduction of J/ψ Mesons at HERA*, Eur. Phys. J. C **73** (2013), no. 6 2466, `arXiv:1304.5162`.

[141] LHCb collaboration, *Central exclusive production of J/ψ and $\psi(2S)$ mesons at $\sqrt{s} = 13$ TeV*, , LHCb-ANA-2016-020 V4.0.

[142] LHCb collaboration, *LHCb Luminosity project*, `https://twiki.cern.ch/twiki/bin/view/LHCbPhysics/LHCbLuminosity#LumiRun2Instructions`.

[143] S. Dulat *et al.*, *New parton distribution functions from a global analysis of quantum chromodynamics*, Phys. Rev. D **93** (2016), no. 3 033006, `arXiv:1506.07443`.

[144] S. Bailey *et al.*, *Parton distributions from LHC, HERA, Tevatron and fixed target data: MSHT20 PDFs*, `arXiv:2012.04684`.

[145] NNPDF collaboration, *Parton distributions from high-precision collider data*, Eur. Phys. J. C **77** (2017), no. 10 663, `arXiv:1706.00428`.

[146] Belle collaboration, *Observation of a narrow charmonium - like state in exclusive $B^\pm \to K^\pm\pi^+\pi^- J/\psi$ decays*, Phys. Rev. Lett. **91** (2003) 262001, `arXiv:hep-ex/0309032`.

[147] CDF collaboration, *Analysis of the quantum numbers J^{PC} of the $X(3872)$*, Phys. Rev. Lett. **98** (2007) 132002, `arXiv:hep-ex/0612053`.

[148] LHCb collaboration, *Determination of the $X(3872)$ meson quantum numbers*, Phys. Rev. Lett. **110** (2013) 222001, `arXiv:1302.6269`.

[149] LHCb collaboration, *Study of the lineshape of the $\chi_{c1}(3872)$ state*, Phys. Rev. D **102** (2020), no. 9 092005, `arXiv:2005.13419`.

[150] LHCb collaboration, *Study of the $\psi_2(3823)$ and $\chi_{c1}(3872)$ states in $B^+ \to (J\psi\pi^+\pi^-)\, K^+$*

decays, JHEP **08** (2020) 123, `arXiv:2005.13422`.